UNIVERSITI TEKNIKAL MALAYSIA MELAKA

ESTIMATION OF ELBOW FLEXION TORQUE FROM NMES MMG SIGNALS AND ANTHROPOMETRIC VARIABLES USING GLEO-RFR

RAPHAEL UWAMAHORO

DOCTOR OF PHILOSOPHY

2025

Faculty of Electronics and Computer Technology and Engineering

ESTIMATION OF ELBOW FLEXION TORQUE FROM NMES MMG SIGNALS AND ANTHROPOMETRIC VARIABLES USING GLEO-RFR

Raphael UWAMAHORO

Doctor of Philosophy

2025

ESTIMATION OF ELBOW FLEXION TORQUE FROM NMES MMG SIGNALS AND ANTHROPOMETRIC VARIABLES USING GLEO-RFR

RAPHAEL UWAMAHORO

A thesis submitted
in fulfillment of the requirements for the degree of
Doctor of Philosophy

Faculty of Electronics and Computer Technology and Engineering

UNIVERSITI TEKNIKAL MALAYSIA MELAKA

2025

DECLARATION

I declare that this thesis entitled “ESTIMATION OF ELBOW FLEXION TORQUE FROM NMES MMG SIGNALS AND ANTHROPOMETRIC VARIABLES USING GLEO-RFR” is the result of my own research except as cited in the references. The thesis has not been accepted for any degree and is not concurrently submitted in candidature of any other degree.

Signature :

Name : RAPHAEL UWAMAHORO

Date : 30/09/2025

APPROVAL

I hereby declare that I have read this thesis and in my opinion this thesis is sufficient in terms of scope and quality for the award of Doctor of Philosophy.

Signature :

Supervisor Name : Prof. Ir. Dr. Kenneth Sundaraj

Date : 22/10/2025

DEDICATION

This thesis is dedicated to my family, academic fellows, co-workers and friends.

ABSTRACT

This thesis presents the development of an elbow joint flexion torque (TQ) estimation model that integrates neuromuscular electrical stimulation (NMES) induced mechanomyography (MMG) signals from the biceps brachii (BB) muscle across three forearm postures and four elbow flexion angles, together with anthropometric variables of the arm. 36 healthy male participants received NMES at 30Hz frequency, 110µs pulse width, 30mA current amplitude, 1s ramp time, and a 6s on over 2s off duty cycle, which induced TQ levels below 15% of maximum voluntary isometric contraction (MVIC). 30s recordings of TQ and MMG signals were collected at forearm positions of neutral, pronation, and supination, and at elbow flexion angles of 10°, 30°, 60°, and 90°. In addition, each participant performed voluntary contractions in 3 randomly selected combinations of elbow angle and forearm posture to provide data for torque estimation model validation. MMG, TQ and anthropometric measurements were recorded into a computer through a data acquisition device for offline analysis. 12 MMG features were extracted and assessed for reliability using Two-Way Random Effects, Single Measurement and Absolute Agreement Intraclass Correlation Coefficient ICC (2,1), at 95% confidence interval. Also, 7 anthropometric variables were validated via intra-test percentage reliability (%R) and technical error of measurement (TEM). Further, Grey Relational Degree (GRD) analysis quantified the correlation of MMG and anthropometric++ features with TQ output. These features were subsequently employed to develop a random forest regression (RFR) based TQ estimation model, optimized via the general learning equilibrium optimizer (GLEO) for feature selection and hyperparameter tuning. Test–retest ICC (2,1) values for TQ and MMG ranged from 0.6880 to 0.8230, indicating moderate to high reliability. Forearm posture and elbow angle significantly affected TQ RMS ($p < 0.05$), with notable variations in MMG RMS, MMG MPF and MMG MDF. MMG RMS and TQ RMS increased from 10° to 60° and then declined at 90° ($p < 0.05$), whereas MMG MPF and MMG MDF progressively decreased with increasing joint angle ($p < 0.05$) along the lateral and transverse muscle axes. Since the behaviour of the transverse axis was statistically significant across a majority of postures and angles, data from it was used for model development. GRD analysis showed TQ and MMG correlation coefficients from 0.5734 to 0.8173. The optimized RFR model achieved 33% of feature reduction (from 12 to 8), yielding 6.25% of improvement in the R^2 values (from 0.7228 to 0.7853) and 0.5232 on the testing and validation datasets respectively. Similarly, anthropometric variables exhibited TEM values between 0.0079 and 0.2417, with %R ranging from 97.9294 to 99.9567. GRD analysis showed TQ and anthropometric++ features correlation coefficients ranging from 0.5808 to 0.8708. Anthropometric++ features based RFR model also achieved 33% of feature reduction (from 9 to 6), 6.10% improvement in the R^2 values (from 0.6560 to 0.7170) and R^2 of 0.4437 on the testing and validation datasets respectively. These findings support the integration of MMG and anthropometric features towards enhanced TQ prediction accuracy, with MMG features demonstrating superior performance. This hybrid approach holds significant implications for ergonomic design, assistive technologies, and sports rehabilitation strategies.

PENGANGGARAN TORK FLEKSI SENDI SUKU DARIPADA ISYARAT MMG NMES DAN PEMBOLEHUBAH ANTROPOMETRIK MENGGUNAKAN GLEO-RFR

ABSTRAK

Tesis ini membentangkan pembangunan model penganggaran tork (TQ) sendi siku yang menggabungkan isyarat mekanomiografi (MMG), yang dijana oleh rangsangan elektrik neuromuscular (NMES), dan pembolehubah antropometrik daripada otot biceps brachii (BB) di bawah tiga postur lengan bawah dan empat sudut fleksi siku. 36 peserta lelaki yang sihat telah dikenakan rangsangan elektrik neuromuskular pada frekuensi 30Hz, lebar denyutan 110μs, amplitud arus 30mA, masa tanjakan 1s, dan kitaran tugas 6s aktif berbanding 2s rehat, yang menjana tahap TQ di bawah 15% daripada pengecutan isometrik sukarela maksimum (MVIC). Rakaman 30s bagi isyarat TQ dan MMG dikumpulkan pada kedudukan lengan bawah dalam keadaan neutral, pronasi, dan supinasi, serta sudut fleksi siku pada 10°, 30°, 60°, dan 90°. Selain itu, setiap peserta melakukan pengecutan isometrik sukarela dalam 3 konfigurasi yang dipilih secara rawak untuk menghasilkan data bagi tujuan pengesahan. Pengukuran MMG, TQ and antropometrik direkodkan ke dalam computer melalui sistem perolehan data untuk tujuan analisis luar-talian. 12 ciri isyarat MMG diekstrak dan disahkan menggunakan teknik Kesan Rawak Dua-Hala, Pengukuran Tunggal dan Pekali Korelasi Intrakelas Persetujuan Mutlak ICC (2,1), yang dinilai pada selang keyakinan 95%. Disamping itu, 7 ciri antropometrik dinilai melalui teknik kebolehpercayaan peratusan intra-ujian (%R) dan ralat teknikal pengukuran (TEM). Seterusnya, analisis Darjah Hubungan Kelabu (GRD) digunakan untuk mengukur korelasi ciri MMG dan antropometrik dengan TQ. Ciri-ciri ini kemudiannya digunakan untuk membangunkan model penganggaran TQ berasaskan kaedah regresi hutan rawak (RFR), yang dioptimumkan melalui pengoptimum keseimbangan pembelajaran umum (GLEO) untuk pemilihan ciri dan penalaan hiperparameter. Nilai ujian semula ICC (2,1) untuk TQ dan MMG adalah antara 0.6880 hingga 0.8230, menunjukkan kebolehharapan sederhana hingga tinggi. Postur lengan bawah dan sudut siku memberi kesan ketara pada TQ RMS ($p < 0.05$), dengan variasi ketara dalam MMG RMS, MMG MPF dan MMG MDF. MMG RMS dan TQ RMS meningkat dari 10° hingga 60° kemudian menurun pada 90° ($p < 0.05$), manakala MMG MPF dan MMG MDF berkurangan secara progresif dengan peningkatan sudut sendi ($p < 0.05$) sepanjang paksi lateral dan melintang BB. Memandangkan sifat paksi melintang didapati signifikan secara statistik bagi kebanyakan postur dan sudut, data daripada ia digunakan untuk pembangunan model. Analisis GRD menunjukkan pekali korelasi TQ dan MMG antara 0.5734 hingga 0.8173. Model RFR yang dioptimumkan mencapai pengurangan ciri sebanyak 33% (daripada 12 kepada 8), peningkatan 6.25% dalam nilai R^2 (daripada 0.7228 kepada 0.7853) dan R^2 sebanyak 0.5232 bagi set data pengujian dan pengesahan masing-masing. Begitu juga, pembolehubah antropometri menunjukkan nilai TEM antara 0.0079 hingga 0.2417, dengan %R antara 97.9294 hingga 99.9567. Analisis GRD menunjukkan pekali korelasi TQ dan antropometri antara 0.5808 hingga 0.8708. Model RFR yang dioptimumkan berdasarkan ciri antropometri juga mencapai pengurangan ciri sebanyak 33% (daripada 9 kepada 6), peningkatan 6.10% dalam nilai R^2 (daripada 0.6560 kepada 0.7170) dan R^2 sebanyak 0.4437 bagi set data pengujian dan pengesahan masing-masing. Penemuan

ini menyokong penggabungan ciri MMG dan antropometri ke arah peningkatan ketepatan ramalan TQ, dengan ciri MMG menunjukkan prestasi yang lebih baik. Pendekatan hibrid ini mempunyai implikasi yang signifikan dalam penilaian ergonomik, teknologi bantuan, dan strategi pemulihan sukan.

ACKNOWLEDGMENTS

In the name of the Triune God, the Most Gracious and the Most Merciful. I praise and thank Almighty God for His greatness and for giving me the strength and courage to complete this research.

First and foremost, I would like to express my deepest gratitude to Rwandan government to support the PhD journey through the University of Rwanda, the regional Centre of Excellence in Biomedical Engineering and E-health (UR-CEBE) project.

My appreciation also goes to Prof.Dr.Ir.Kenneth Sundaraj, for all his constructive mentorship, and scientific advice. I am also thankful to Dr. Farah Shahnaz Feroz, who co-supervised this research.

Special thanks go to my parents and siblings with moral support and prayers. I also want to express my gratuture to George Marc Foletia Zeller for her unconditional support. Deepest gratitude to my wife MUTEGWARABA Honorine for her unwavering understanding and support throughout this journey. Unmeasureable gratitude goes to the subjects of this research, and Universiti Teknikal Malaysia Melaka as well as, the UR-CEBE for providing the research platforms. Also, many gratitude to the the Director General of the Minisry of Health, Malaysia, for giving permission to publish the results of this research and the Medical Research and Ethics Committee (MREC) of Malaysia to provide ethical approval for conducting experiment of the data used in this study.

TABLE OF CONTENTS

LIST OF TABLES

LIST OF FIGURES

LIST OF SYMBOLS

%	-	Percentage
±	-	Plus / minus
×	-	Multiplication
°	-	Degree (angle)
µs	-	Microsecond
cm	-	Centimetre
g	-	Gravitational acceleration
Hz	-	Hertz
kg	-	Kilo gram
kHz	-	Kilo Hertz
m	-	Meter
mA	-	Milliamp
mm	-	Millimeter
ms	-	Millisecond
mV	-	Milli volt
N	-	Newton
n	-	Number of subjects
p	-	Significant value
T	-	Time
Ω	-	Ohm

LIST OF ABBREVIATIONS

AB	-	Able bodies
AMMG	-	Acceleration Mechanomyography
ANN	-	Artificial Neural Network
AT	-	Amplitude triangle
AWL	-	Analysis window length
BB	-	Biceps brachii
CDS	-	Contact Displacement Sensor
CNN	-	Convolutional Neural Network
CNS	-	Central Nervous System
CT	-	Contraction Time
DGR	-	Down-going ramp
Dm	-	Maximum Displacement
DMMG	-	Displacement Mechanomyography
EMG	-	Electromyography
FES	-	Functional electrical stimulation
fMRI	-	Functional Magnetic Resonance Imaging
FR	-	Firing rate
FRDA	-	Friedreich's ataxia
FT	-	Frequency triangle
GLEO	-	General Learning Equilibrium Optimizer
GLM	-	Gloss lateral movement
GM	-	Gastrocnemius Medialis
HRT	-	Half relaxation time
ICC	-	Interclass Correlation Coefficient
IED	-	Inter-electrode distance
KMG	-	Kinemyography
KNG	-	Kinemyography

LCE	-	Leg cycling exercise
LDS	-	Laser Displacement Sensor
LFF	-	Low Frequency Fatigue
LFF	-	Low frequency fatigue
LLA	-	Length of the Lower Arm
LSTM	-	Long Short-Term Memory
LUA	-	Length of Upper Arm
MC	-	Muscle contraction
MCS	-	Muscle Contraction Sensor
MDF	-	Median Power Frequency
MEMS	-	Microelectromechanical system
MFCC	-	Mel Frequency Ceptral Coefficient
MFCC	-	Mel frequency cepstral coefficient
ML	-	Machine Learning
MPF	-	Mean Power Frequency
MS	-	Multiple sclerosis
MTU	-	Muscle Tendon Unit
MTU	-	Muscle-tendon unit
MUAP	-	Motor unit action potential
MVC	-	Maximum voluntary contraction
MVIC	-	Maximum Voluntary Isometric Contraction
NIRS	-	Near Infrared Spectroscopy
NIRS	-	Near-infrared spectroscopy
NMB	-	Neuromuscular Blockade
NMES	-	Neuromuscular Electrical Stimulation
PAP	-	Postactivation Potentiation
PAP	-	Post activation potentiation
PDMS	-	Polydimethylsiloxane
PNG	-	Phonomyography
PMT	-	Passive muscle tension
PNMES	-	Percutaneous neuromuscular electrical stimulation

PP	-	Peak to Peak
pT	-	Peak Torque
RF	-	Rectus femoris
RF	-	Relaxation time
RFR	-	Random Forest Regression
RMS	-	Rooty Mean Square
RMSE	-	Root mean square error
SCI	-	Spinal Cord Injury
SOL	-	Soleus
SP	-	Staircase phenomenon
SPI	-	Spinal cord injury
ST	-	Single twitch
SVD	-	Singular Value Decomposition
SVD	-	Singular value decomposition
SVM	-	Support vector machine
SVR	-	Support vector regression
TEM	-	Technical error of measurement
TB		Triceps brachii
TMG	-	Tensiomyography
TMG		Tensiomyography
TOF	-	Train of four
TQ	-	Torque
UGR		Up-going ramp
VL	-	Vastus Lateralis
VMG	-	Vibromyography
VML	-	Vastus Medialis Longus
VMO	-	Vastus Medialis Obliquus
ZCR	-	Zero Crossing Rate

LIST OF APPENDICES

LIST OF PUBLICATIONS

Journal articles with Impact Factor

R Uwamahoro, K Sundaraj, ID Subramaniam,2021. Assessment of muscle activity using electrical stimulation and mechanomyography: a systematic review, *Biomedical engineering online*, Vol. 20, pp. 1-47, IF = 2.9 (2021).

R Uwamahoro, K Sundaraj, SF Farah, 2023. Effect of Forearm Postures and Elbow Joint Angles on Elbow Flexion Torque and Mechanomyography in Neuromuscular Electrical Stimulation of the Biceps Brachii, *Sensors* 23 (19), 8165, IF = 3.9 (2023).

R Uwamahoro, K Sundaraj, SF Farah, 2025. Estimation of elbow flexion torque using Equilibrium Optimizer on feature selection of NMES MMG signals and hyperparameter tuning of Random Forest regression, *Frontiers in Rehabilitation Sciences* 6, 1469797, (2025).

R Uwamahoro, K Sundaraj, SF Farah, (2025). Estimation of elbow flexion torque from anthropometric and NMES MMG variables using random forest regression, *Scientific report* , 15:8038 (2025).

Indexed Journal

R Uwamahoro, K Sundaraj, SF Farah, (2025). Design and Validation of Mechanomyography and Torque Measurement Acquisition System for Skeletal Muscle Function, *SSRG International Journal of Electrical and Electronics Engineering*, 11(12).

Conferences

R Uwamahoro, K Sundaraj, ID Subramaniam, Analysis of upper limb rehabilitation using muscle mechanics:Current and future perspectives using Mechanomyography signals, in 12th Biomedical Engineering International Conference of IEEE (BMEiCON), pp.1-5, (2019).

CHAPTER 1

INTRODUCTION

1.1 Background

Skeletal muscles are essential components of the human locomotor machine, serving as dynamic actuators that generate the force required for the human and animal movement. By acting across skeletal joints, these muscles collectively produce the torque necessary for joint motion through coordinated activation (Campbell *et al.*, 2020).This function provokes the muscle contraction whose intensity is modulated by the level of tasks being conducted as indicated also at Figure 1.1.

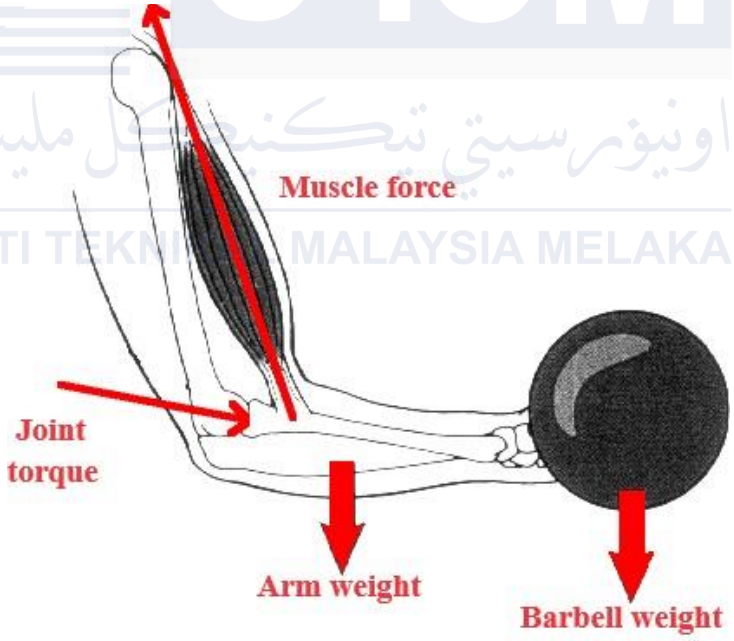

Figure 1.1: Skeletal muscle force contribution in elbow flexion tasks. Online available at https://physics.stackexchange.com/questions/130247/how-muscle-force-work Accessed September, 01, 2025.

Muscle contractions are regulated by the somatic nervous system that regulates the neuromuscular junction (Kozlowska et. al., 2021), ensuring precise transfer of motor

impulses for the control of movements. However, skeletal muscles are frequently subjected to injuries and strain, often resulting from routine occupational activities. Additionally, muscle disuse, neurological disorders, and age-related sarcopenia contribute to movement impairments, coordination deficits, and muscular atrophy (Sirago et al., 2023). Building upon the basic understanding of skeletal muscle function, diving into the critical knowledge of these scenarios is vital for the analysis of muscle status.

Indeed, recent scientific and clinical investigations have increasingly reported the importance of advanced muscle activity assessment techniques in enhancing our understanding of neuromuscular health. Based on anatomically yielded courtesies, engineering applications have been developed. This shift has been motivated by the need for improved diagnostic accuracy, personalized rehabilitation, and more efficient biomechanical modelling towards improved well-being of the population. Muscle activity evaluation not only informs our understanding of healthy motor performance but is also essential in identifying and addressing dysfunctions that arise from injury, disuse, or neurological impairment (J. Li et al., 2024). While these appears variant for different individuals, the growing research interest in health technology development, and personalized medicine, showed a pressing demand for non-invasive, accurate, and real-time methods that can assess muscular function with high fidelity under diverse physiological conditions.

A variety of techniques are employed to assess muscle health conditions and identify the underlying causes of functional impairments, thereby facilitating the development of effective treatment strategies. Common function assessment methods include imaging modalities such as MRI, ultrasound, and near-infrared spectroscopy among others. Each technique offers unique advantages but also presents several limitations. For instance, MRI provides high-resolution structural imaging, but is costly, time-intensive, and unsuitable for

dynamic assessments. Ultrasound, while portable and cost-effective, suffers from limited tissue penetration and requires significant operator expertise for accurate anatomical interpretation (Clevert *et al.*, 2020)imilarly, NIRS is effective for monitoring muscle oxygen saturation but is hindered by low spatial resolution and susceptibility to interference from factors such as skin thickness (Perrey *et al.*, 2024).

1.2. Motivation

Electromyography (EMG) is a widely used technique in measuring electrical activity of muscles with high sensitivity. However, it requires precise electrode placement, can be invasive in some cased, and is prone to interference from external electrical noise. This susceptibility is particular to EMG when combined with neuromuscular electrical stimulation (NMES) essential for muscle re-education. Mechanomyography (MMG) techniques complement the use of EMG by providing mechanical counterparts to muscle activation. MMG detects superficial muscle oscillations resulting from the acceleration of the muscle contraction as reflected at the surface of the skin over the muscle. MMG techniques are classified as phonomyography (PNG), vibromyography (VMG), kinemyography (KNG), and acceleromyography, which are given names according to transducers used for signal recording (Uwamahoro et al., 2019). These transducers include microphone, piezoelectric, laser displacement (Mallegni *et al.*, 2022), accelerometers and vibromyography sensors (Fidali *et al.*, 2024). Of these, accelerometers are particularly efficient due to their light weight, insensitive to NMES, and cost-effective for equipment customization compared to EMG (Uwamahoro et al., 2021).

NMES enables selective activation of targeted muscles, providing precise control over their contribution to joint torque production. This specificity reduces crosstalk from

adjacent muscles, allowing the accurate identification of individual muscle contributions to joint torque production and supports the development of tailored rehabilitation plans (Popesco *et al.*, 2024). Given the muscle activity and torque production at joints, muscle activation is a critical parameter for understanding biomechanical performance. When coupled with MMG, NMES enhances the precision of joint torque assessment, enabling more accurate screening and providing a robust framework for evaluating neuromuscular function. Building upon the established clinical role of NMES in selective activation of targeted skeletal muscle, and the inherent sensitivity of MMG sensors to record mechanical oscillations resulting from muscle contraction, the integrated modality offers immense potential in advanced wearable technology for improved skeletal muscle function screening and rehabilitation paradigms (Shideler *et al.*, 2020). This coupling is further essential for real-time, non-invasive monitoring of the contractile ability of skeletal muscles, which in turn is critical in dynamic, real-world scenarios where rehabilitation protocols must adapt stochastic biomechanical demands.

Acceleration MMG signals mirror the muscle fiber oscillations derived from motor units' recruitment and firing rates, here modulated by the intensity of NMES. With this MMG feedback, wearable systems may obtain intelligent capabilities to interpret mechanical responses of musculoskeletal tissues, thereby supporting the closed-loop control scenarios. Indeed, this closed-loop control enhances the adaptability of assistive orthoses and prosthetic technologies to joint kinematics, joint moments, and limb positioning(Uwamahoro, Sundaraj and Subramaniam 2021). This integrated approach is particularly advantageous for designing targeted interventions, monitoring rehabilitation progress, and improving torque estimation in low levels of muscle activation scenarios such as those accounted for in activities of daily living involving the upper limb muscles. This also improves the fidelity of

assisted intervention in individuals with motor unit's impairment, enabling the patient specific calibration, and adaptive rehabilitation protocols (Ibitoye, Hamzaid, Hasnan, *et al.*, 2016). Overall, integrated NMES and MMG not only refines muscle strength and torque estimation but also improves wearable systems into intelligent platforms facilitating biomechanical decision making, thus promoting efficient skeletal muscle loading, reduced the exposition to overuse injuries and accelerated functional recovery.

The biceps brachii **(**BB) muscle is a primary flexor of the elbow and a key supinator of the forearm, playing a pivotal role in torque generation .It is indispensable for tasks requiring strength, precision, and coordination in both occupational settings and athletic performance (Gwak *et al.*, 2021). Due to its anatomical position and multifunctionality, the BB is frequently studied in research focusing on muscle activation, force production, and neuromuscular coordination. As a bi-articular muscle, the BB contributes to multiple movements including elbow flexion, forearm supination, and shoulder stabilization, making it a versatile muscle for biomechanical studies (Yamamoto *et al.*, 2018). This dual-joint involvement allows researchers to investigate its role in dynamic force generation and intricate coordination of upper limb movements.

Studying the BB muscle in healthy subjects is important for several reasons. First, its accessibility for NMES and MMG recordings makes it an ideal model for investigating muscle function. Second, examining healthy subjects establishes a baseline for normal muscle dynamics, minimizing confounding variables such as injury or pathology, enabling clear insights into muscle behaviours (Brueckner *et al.*, 2018).

Torque measurements at the elbow joint, with a focus on the BB muscle activation, provides valuable insights into muscle function under various conditions of the upper limb geometry (Gerditschke *et al.*, 2024). These assessments help quantifying the BB's

contribution to joint torque during isolated or combined movements, enabling precise evaluation of its performance as shown at Figure 1.2. Such studies are essential for advancing rehabilitation protocols, optimizing prosthesis designs, and improving performance strategies, with potential application in clinical research and intervention.

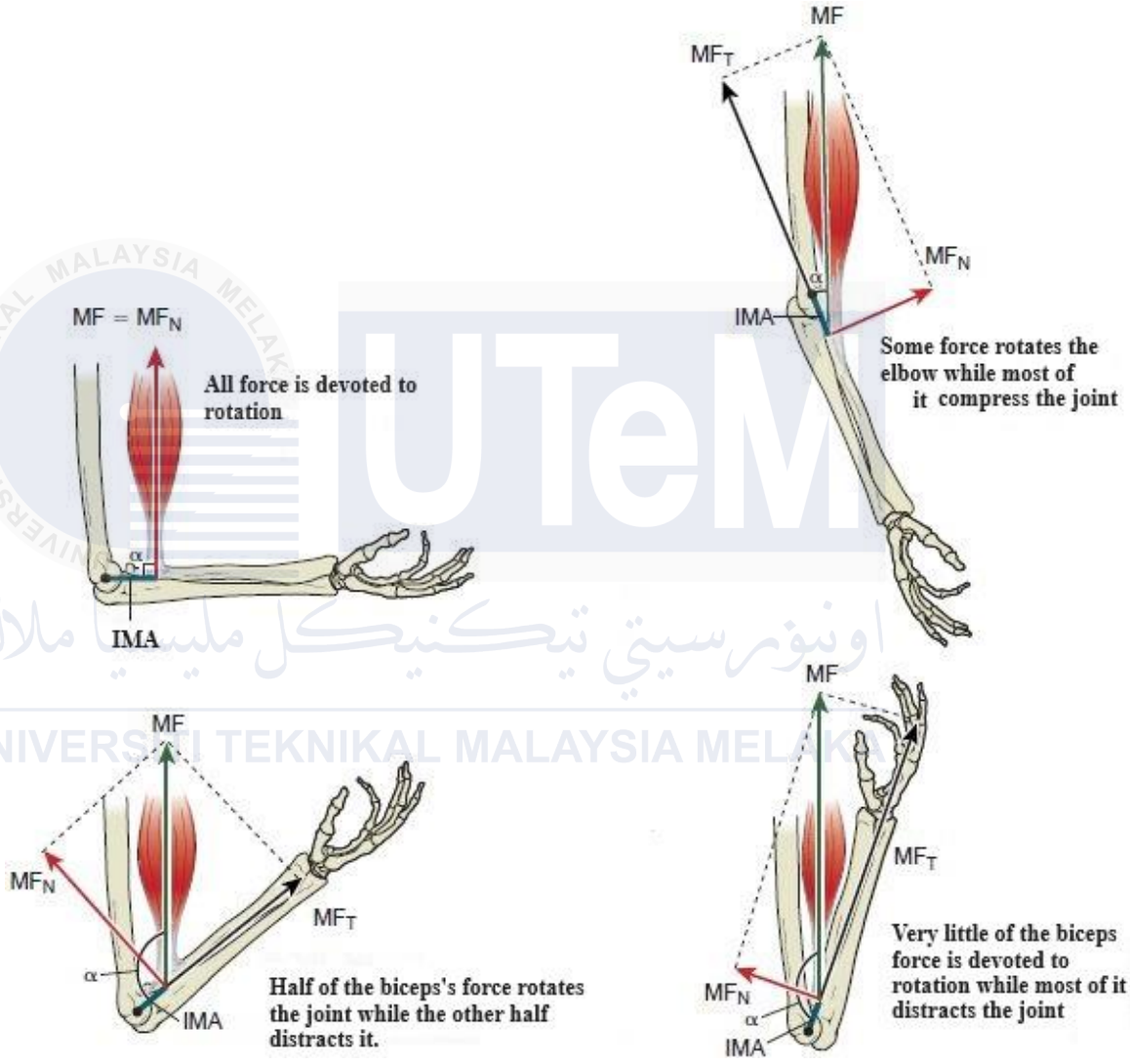

Figure 1.2: Biomechanics of the Biceps Brachii Moment Arm and joint torque generation at different arm's geometry: Online Available at https://in.pinterest.com/pin/1023654190302651222/ Accessed on September, 1st, 2025

To build the foundation for this study, we conducted a comprehensive literature review on muscle activity assessment using NMES and MMG, not limited to the BB muscle

alone. The review explored experimental methodologies used in assessing skeletal muscle function, including variations in muscle groups, stimulation parameters, signal processing methods, and outcome measures. While many studies have centered on large muscle groups such as the quadriceps, few have investigated the BB in a context that combines MMG, NMES, and elbow torque prediction—particularly under varying joint angles and hand postures.

1.3 Problem Statement

The BB muscle is a key muscle involved in elbow flexion and forearm supination, playing a critical role in torque generation during these movements. It also contributes to shoulder stabilization, underscoring its integral role in upper limb functionality. Despite its biomechanical significance, existing studies on torque estimation during elbow flexion primarily focus on overall joint torque, often overlooking the specific contribution of individual muscles. While prior research has demonstrated the potential of MMG over EMG (Bowdle *et al.*, 2020),with notable capacity in detecting the direction of propagation in muscle fibers (Uwamahoro *et al.*, 2021b), the biomechanical effects of the BB muscle under varying joint angles (Ichikawa et al., 2021) and forearm postures (Zimmermann *et al.*, 2025) remain underexplored. Hence, the magnitude of muscle contraction depends on the activation of muscle fibers, which is further modulated by changes in muscle geometry (Zimmermann *et al.*, 2025) . Consequently, the unique architecture and anatomical location of the BB muscle makes it an ideal reference for analysing MMG behaviours across muscle fibers directions.

NMES is recognized as an effective tool for selective activation of specific muscles, facilitating precise limb movement control (Li *et al.*, 2019) as well as generating torque at

the elbow joint (Gonzalez *et al.*, 2018). However, no studies to date have explicitly identified the contribution of specific muscle within a synergistic group acting at joint using NMES. Recent research on NMES and torque predominantly focussed on the lower limb, particularly quadriceps muscles using VMG coupled with Biodex for torque measurement (Ibitoye bet al., 2016). Despite the contribution, muscle-specific analysis has been largely overlooked. Hence, the assessment of elbow joint flexion torque through NMES activation of smaller muscles remains insufficiently explored.

Joint torque is influenced by muscle activation and muscle size (Green and Gabriel, 2012), whereby voluntary muscle activation being directly proportional to muscle size. However, NMES may elicit dynamic responses that are influenced by the electrode attachment on muscle's motor point (Gobbo et al., 2014;Ichikawa et al., 2021). These motor points can shift due to changes in limb geometry, which in turn alter anthropometric parameters such as the middle upper arm circumference (MUAC) and motor point location relative to the upper arm length (LUA) (Paillard, 2018a;Fok et al., 2020). Previous studies have demonstrated the value of incorporating anthropometric measurements as features in torque assessment using machine learning (ML) and deep learning (DL) approaches (Serbest et al., 2023; Moreira et al., 2021), suggesting that dynamic joint torque analyses could provide valuable insights for future research.

ML algorithms have gained prominence over traditional mathematical regression models for joint torque estimation due to their flexibility and capacity to handle complex biological datasets (Yang and Shami, 2020). Effective ML outcomes largerly depends on meticulous hyperparameter tuning and the selection of relevant and non-redundant features (Chandrashekar and Sahin, 2014; Yu and Liu, 2004). Current approaches often use separate feature selection, which can limit the model performance when applied to intricate biological

database (Aljarah *et al.*, 2018). This demonstrates the lack of integral frameworks that simultaneously optimize torqu estimation accuracy.

1.4 Research Hypothesis

The research hypothesizes that:

1) Variations in forearm posture and elbow joint angle induce measurable changes in physiological signals, which are influenced by alterations in muscle geometry. These changes can be unobtrusively monitored using NMES-induced MMG across three muscle fiber axes and corresponding torque measurements. It is believed that a dominant axis will prevail among the longitudinal, lateral, and transverse axes of muscle fiber orientations, indicating a strong correlation between forearm posture, elbow joint angle and torque.
2) While muscle physiology primarily contributes to torque production, the literature claims that anthropometric variables may as well influence torque generation. Both these phenomena arise from distinct etiologies, and are measured differently. Consequently, their combined effects on NMES-induced torque are likely non-overlapping and can be delineated through ML techniques. Hence, it is hypothesized that the application of a general learning equilibrium optimizer (GLEO) for the determination of an ideal feature set from both physiological and anthropometric variables would generate an optimum hybrid feature RFR model for torque estimation.
3) Using AI, reliable elbow joint torque can then be estimated from MMG signals of the dominant axis in muscles. Although the RFR ML model is suited to handle high-dimensional feature set, large features size may introduce redundant and

irrelevant features, which impair the learning ability of the RFR model. Therefore, it is envisaged that the application of a general learning equilibrium optimizer (GLEO) for simultaneous feature selection and hyperparameters tuning will reduce the number of features and optimize the hyperparameters values, thereby leading to an improved performance of the RFR model.

1.5 Research Objectives

The stipulated hypotheses will be achived using these objectives to:

1) investigate the effect of forearm posture and elbow joint angles on elbow flexion torque and MMG elicited by NMES of the BB muscle.
2) analyse the relationship between anthropometric variables and dynamic torque in order to develop torque estimation model that integrate both anthropometric and MMG features.
3) develop a random forest regression (RFR) torque estimation model optimized using a general learning equilibrium optimizer (GLEO) for simultaneous feature selection and hyperparameter tuning based on NMES-induced MMG signals.

1.6 Scope of the Research

Skeletal muscles are vital in occupational activities, with elbow flexors frequently engaged in forearm flexion tasks. The BB muscle serves as a primary elbow flexor, making it indispensable in the development of assistive technology. However, due to the loss of efficient muscle function due to injury, muscle disuse, or several pathologies, NMES was found essential to investigate the status of individual muscle acting at a joint. The torque at the joint can be assessed through myography techniques, thus this research focuses on

estimating elbow flexion torque using MMG signals derived from electrically stimulated BB muscle in healthy male participants.

MMG features characterising the level of muscle activity (RMS) and recruitment pattersn including the mean power frequency (MPF) and median power frequency (MDF) derived from BB muscle fiber axis are employed to evaluate muscle behaviors across different angle and posture configurations. RFR based torque estimation model was developed using MMG features derived from the muscle fibers axis exhibiting the dominant statistically significant variance in MMG amplitude and frequency parameters. The performance of the RFR model was improved by both feature selection and hyperparameter tuning using GLEO.

This research also investigated the influence of anthropometric parameters on torque production, acknowledging that variations in these parameters affect muscle contraction properties and torque generation. The scope of this study extends to the deployment of RFR model that integrated anthropometric and MMG variables for torque modelling with a focus on their applicability in real-world scenarios.

This study was conducted on young healthy male participants to minimize potential biases due to age and sex difference and ensure baseline uniformity. As a foundational investigation into muscle function, the primary elbow flexor was the focus of this work. The findings have significant implications for assessing muscle function and torque production, providing insights that can be applied in the design and development of upper-limb assistive technologies.

1.7 Thesis Outline

Chapter 1 offers a comprehensive overview of the study, outnlining its background ,core concepts and theories that form its foundation. It provides the research objectives, questions that the research aims to answer, while emphasizing the study's significance and contribution to the existing body of knowledge.

Chapter 2 provides a literature review, thoroughly examining the existing techniques for muscle function assessment, with a particular focus on the use of Neuromuscular Electrical Stimulation (NMES) and Mechanomyography (MMG) signals. This section critically reviews previous studies, highlighting the methodologies used, the results obtained, and the identified limitations. Special attention is given to the influence of anthropometric parameters and the characteristics of NMES-MMG signals on torque estimation. The chapter concludes by identifying the research gaps, which serve as the foundation for the objectives of the current study.

Chapter 3 delves into the research methodology, building on the experimental insights gained from the literature review in Chapter 2. It offers a step-by-step explanation of the experimental protocol, including the design, the materials selected, and the procedures followed. The rationale for choosing specific methods and materials is explained, ensuring that the study can be replicated by future researchers. This section also addresses the ethical considerations associated with the study, ensuring compliance with clinical research guidelines.

Chapter 4 focuses on presenting the results of the study in a clear and organized manner, supported by detailed tables, figures, and statistical analyses. The findings are interpreted and discussed, providing insights into their significance and their potential

practical applications. The section also compares the study's results with those of previous research, highlighting any similarities, differences, and novel contributions.

Chapter 5 provides a discussion of the research findings, connecting them to the objectives. This section also addresses the limitations of the study, acknowledging factors that may have influenced the results. Additionally, it suggests future research directions, offering recommendations for further studies that could build on the findings of the current research. The chapter concludes with a summary of the study's contributions to the field.

The next chapter presents a review of previous experimental studies which guided the selection of studies related to the assessment of the BB's function, strength assessment and joint torque estimation from both muscle activation and morphological characteristics.

CHAPTER 2

LITERATURE REVIEW

2.1 Introduction

This chapter presents a literature review on the techniques for the assessment of the skeletal muscle activity using NMES-MMG. It begins with an overview of muscle excitation by the central nervous system, laying the foundation for understanding muscle fibers recruitment under NMES, as detailed in the section 2.4. The chapter then outlines the anatomy and physiology of skeletal muscles, providing a context for subsequent discussions, and explores MMG recording techniques emphasizing their reliability and the insights gained from captured signals. This chapter also examines the mechanism of joint torque generation, muscle strength assessment and presents an extensive review of studies employing MMG for joint torque studies, with a particular focus on techniques applied for elbow flexion torque estimation. The review concludes by identifying research gaps and potential contributions, particularly in the areas of low voluntary contraction torque estimation and the application of metaheuristic optimization algorithms.

2.2 Overview of skeletal muscle

Skeletal muscle comprises multinucleated fibers which are responsible for voluntary movement (Csapo *et al.*, 2020). The bundle of fibers are organized into either pennate or parallel units, influencing the muscle's functional properties and force generation capabilities (Trovato *et al.*, 2016).

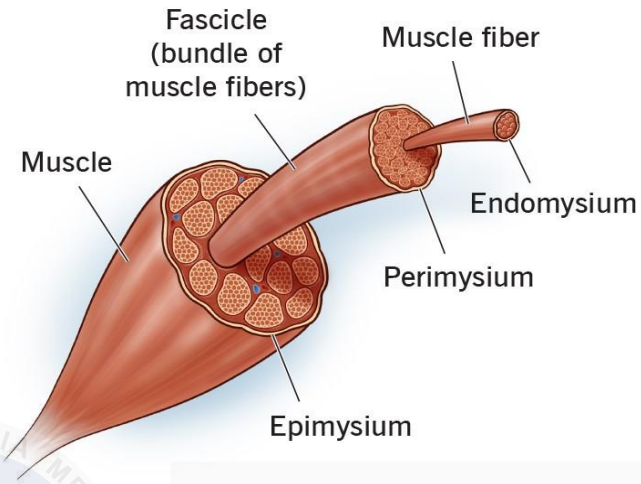

Figure 2.1:Overview of skeletal muscle

Each muscle fiber contains myofibrils (refer to Figure 2.1), which are longitudinally aligned structures composed of repeating contractile units known as sarcomeres (Adewale and Ahn, 2021). Sarcomers in turn consist of two main proteins i.e actin and myosin, that interact through cross-bridge cycling to generate muscle contraction (Trovato *et al.*, 2016).

The sliding filament theory explains the molecular basis of muscle contraction, where the myosin heads bind to actin filaments and pull them toward the sarcomere center. This process leads to a rapid and sustained shortening of sarcomeres, thereby generating force (Pertici *et al.*, 2023). Motor control is initiated at the motor point, where the motor neuron interfaces with the muscle fiber to allow neural regulation. The neuromuscular junction serves as the site for action potential transmission, which triggers the release of calcium ions, synchronizing sarcomere contraction.

2.2.1 Anatomy and physiology of BB muscle

The BB is a prominent muscle of the upper arm, playing a key role in the musculoskeletal system. Anatomically, it comprises two heads: the long head and the short head. The long head originates from the supraglenoid tubercle of the scapula, while the short head originates from the coracoid process of the scapula. Both heads converge to insert into the radial tuberosity of the radius and the bicipital aponeurosis.

Located in the anterior compartment of the upper arm, the BB functions as a powerful flexor of the elbow and a supinator of the forearm. The long head contributes significantly to shoulder stability by keeping the humeral head within the glenoid cavity during arm movements. The short head aids in shoulder flexion and adduction. The muscle's position and attachment points make it crucial for lifting, pulling, and other arm movements that require elbow flexion and forearm rotation. This functional structure of the BB muscle indicates that its length must also be influenced by concentric (shortening) and eccentric (lengthening) occuring along with varying elbow geometry (Arrillaga *et al.*, 2024) , and its contribution in both dynamic and static movements of the upper limb exposes it to injuries, such as tendinopathy and tendon ruptures.

As shown at Figure 2.1, both heads merge into a single muscle belly that inserts into the radial tuberosity of the forearm and the bicipital aponeurosis. The biceps brachii is innervated by the musculocutaneous nerve, which arises from the brachial plexus. The musculocutaneous nerve enters the muscle near the coracoid process, supplying both the long and short heads, facilitating elbow flexion and forearm supination. The nerve's pathway and branches ensure precise control of the BB muscle during various upper limb activities, including lifting and pulling.

Recent studies have highlighted the detailed innervation patterns and functional aspects of the BB muscle. While some earlier research suggested variations in innervation, it is now well-established that the musculocutaneous nerve is the primary nerve for both heads of the BB muscle. This consistent innervation pattern underscores the muscle's role in coordinated upper limb movements and its importance in clinical assessments and interventions.

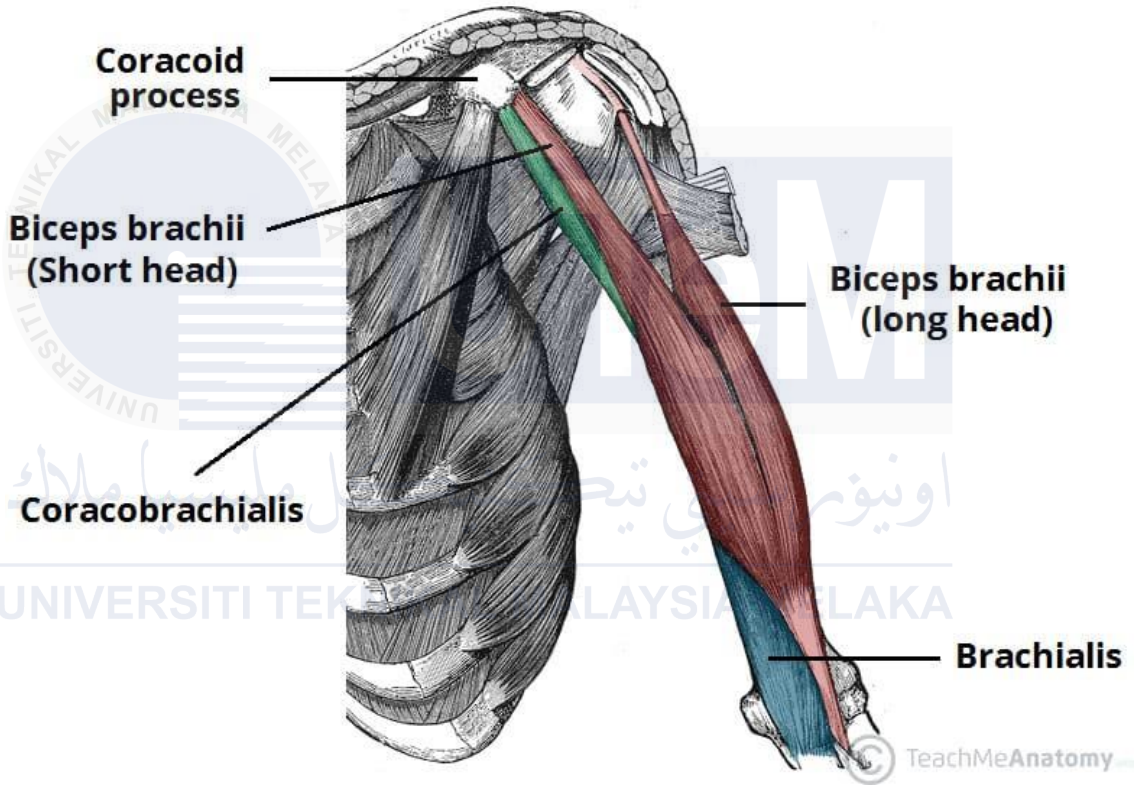

Figure 2.2: Attachment of the BB: Online available at https://teachmeanatomy.info/encyclopaedia/b/biceps-brachii/. Retrieved April 20, 2024.

The functional properties of a muscle, including its contractility and ability to twist, are shaped by the composition of its muscle fibers (Plotkin *et al.*, 2021). Differences in the contractile characteristics between the two heads of the biceps BB are attributable to their distinct fiber compositions (von Werder and Disselhorst-Klug, 2016).

The long head of the BB muscle is composed of a mix of Type I and Type II fibers, whereas the short head predominantly contains Type II fibers (Podgórski *et al.*, 2019), known for their higher twist speed and greater force production, and contribute significantly more power compared to Type I fibers . This difference in fiber composition results in varying twist speeds and force capabilities between the two heads of the BB muscle (Snow and Lanik, 2024).

The predominance of Type II fibers in the short head of the BB makes it particularly effective for high-power, explosive movements. This composition allows the short head to excel in rapid and forceful contractions, while the long head, with its blend of fiber types, offers a balance between endurance and power. The substantial proportion of Type II fibers in the BB highlights its role in activities requiring quick, powerful actions. Consequently, the fiber composition directly influences torque generation, with Type II fibers being crucial for producing the torque needed for swift and forceful elbow flexion and supination. Understanding this fiber distribution is key to appreciating BB muscle's torque generation capabilities during various movements.

2.2.2 Muscle contraction for functional assessment

Like other skeletal muscle, the BB muscle contraction can occur voluntarily or through external stimulation such as NMES (Karamian *et al.*, 2022). During voluntary contraction, the central nervous system (CNS) through upper motor neurons (Menon and Vucic, 2021) transmits neural command signals to the lower motor neurons at the muscle's motor point . The motor point is the specific region of the muscle where the motor neuron interfaces with the muscle fiber, and is the most responsive to neural stimulation (Cabral *et*

al., 2024). Under NMES, a pen electrode is often used to map the motor point by applying small electrical currents and identifying the location that produces the strongest and most localized muscle contraction (refer to Figure 2.3). Once the motor point is identified, NMES electrodes are placed over this region to maximize muscle activation and ensure targeted stimulation (Cheuy *et al.*, 2023).

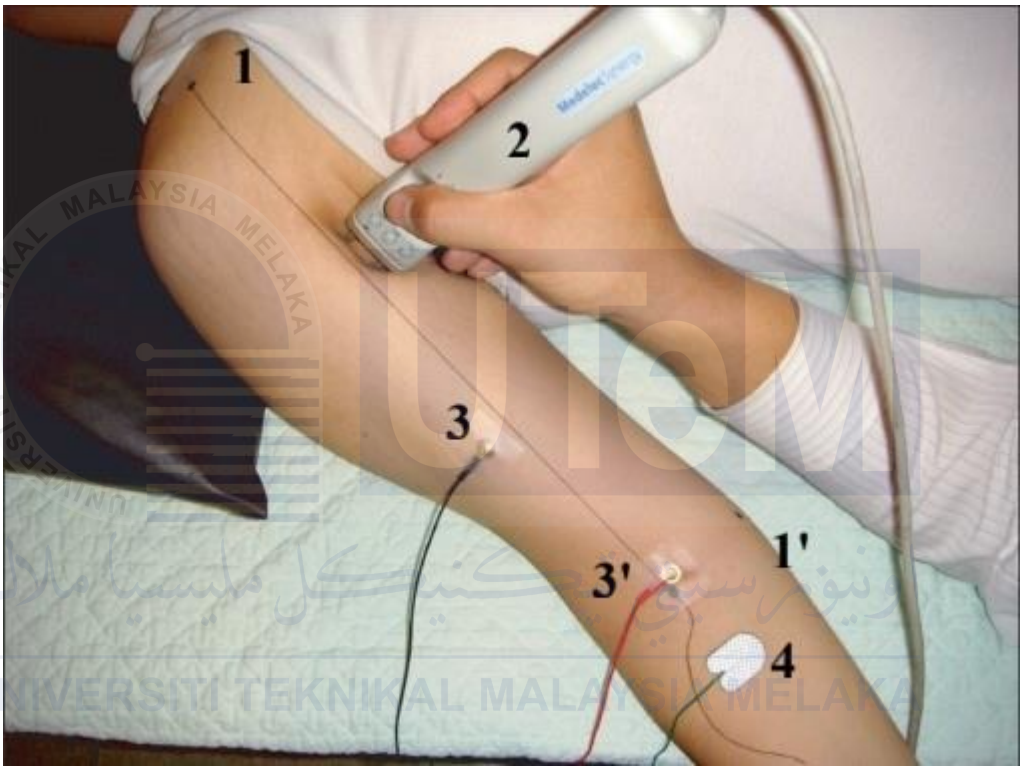

Figure 2.3: Determination of the motor point: 1,1') reference point at the coracoid process and end point of the elbow crease, 2) pen electrode, 3,3') EMG electrodes, 4) stimulation electrode.

2.3. Muscle function assessment using myography techniques

Muscle function can be evaluated using sensor-based, and imaging myography techniques, as well as strength measurement approaches. Sensor-based methods detect electrical or mechanical signals generated during muscle activity, providing real-time data on muscle activation dynamics. Imaging methods offer structural and functional measurement methods, such as dynamometers, load cells, or force plates, quantify the

mechanical force exerted by muscles and the torque output at limb joints though they do not directly capture neural activation or fine control mechanisms.

Imaging-based myography technology focuses on visual analysis of muscle structure and activity. These include ultrasound imaging**,** commonly used to study muscle fiber orientation, pennation angles, and dynamic changes in muscle thickness during contractions (Jin *et al.*, 2024). Advanced applications, such as elastography, assess tissue stiffness by measuring their response to external or internal mechanical forces of muscle activity. Magnetic resonance imaging (MRI) provides high-resolution anatomical details and can measure functional changes, such as muscle activation patterns using functional MRI (fMRI) (Scarapicchia *et al.*, 2017). Near-infrared spectroscopy (NIRS) monitors changes in oxygenated and deoxygenated hemoglobin in muscles, indirectly reflecting metabolic activity (Herold *et al.*, 2018). While imaging techniques are highly informative and often non-invasive, they are costly and require specialized training personnel.

EMG is the most widely used method using invasive or non-invasive sensors to record electrical signals from muscles. Surface electromyography (sEMG) measures the activity of superficial muscles through electrodes placed over the skin, while intramuscular EMG uses fine wire or needle electrodes to target deeper or specific muscle motor units (Guo *et al.*, 2010). MMG is another sensor based methods that measures mechanical vibrations produced by muscle fibers during contraction using accelerometers or piezoelectric transducers. These non-invasive techniques provide real-time data. While EMG can be affected by crosstalk signal from adjacent muscles, MMG is better suited for low-force contractions. MMG offers a broad assessment of muscle function, with negligible skin impedance, does not require the skin preparation (Islam, Sundaraj, Ahmad and Ahamed, 2013), making it particularly valuable for clinical research on skeletal muscle function.

2.3.1 Parameters used for muscle function assessment

Physiological features of myoelectric signals are commonly analyzed in time domain, frequency domain, and time frequency domain. The root mean square (RMS) value serves as an indicator of the intensity of muscle activation, while the mean power frequency (MPF) and the median power frequency (MDF) reflect the rate of muscle fiber recruitment. The zero crossing rate (ZCR) reflects the frequency content and activation patterns during muscle contraction, thereby linking features the spectral characteristics of myographic signal with its temporal behaviors (Jiang *et al.*, 2022).

Acoustic myography provides a robust measurement of the recording of oscillatory muscle activity generated during muscle contractions (Shcherbynina *et al.*, 2020). It has been employed to characterize muscle force production using ZCR, signal energy, spectral centroid (SC), spectral spread (SS), and spectral flux (SFlux), thereby enabling the characterization of physiological state of the muscle under investigation (Udahemuka *et al.*, 2024). As an acoustic signal, MMG has been found particularly valuable for torque estimation (Dzulkifli et al., 2018), with these features offering added potential for characterizing muscle function.

Hjorth mobility parameter is an indicator of the rate of physiological behaviors of muscles, and underscores its potential integration into machine learning algorithms for improving functional assessment in biomedical applications (Alawee *et al.*, 2023).

2.4 NMES and MMG techniques for muscle function assessment

MMG has been established as a crucial tool for evaluating muscle performance. Previous research has demonstrated the reliability of MMG in characterizing the contractile properties of skeletal muscles, particularly when combined with NMES. While several studies have focused primarily on the NMES-induced activation of quadriceps in muscle force and joint torque assessments, the present study broadens the scope to include both upper and lower limb muscles under NMES, offering new insights into the clinical monitoring of smooth muscle activity.

Relevant original research articles were sourced from the Scopus and SpringerLink databases using targeted search keywords, focusing on studies published between 2000 and 2024. These articles were systematically evaluated for inclusion in this review based on eligibility criteria defined in Figure 2.4.

Following a systematic screening, 78 potential studies were retained for analysis, supplemented by 2 additional articles identified from reference lists. These studies were classified into (1) reliability of MMG NMES, (2) fatigue assessment, (3) force measurement, (4) tissue stiffness analysis, (5) torque assessment (6), torque estimation models (7), evaluation of anthropometric parameters for torque estimation (8) , and validation of these techniques for clinical monitoring applications (9) . Each identified study was evaluated for NMES parameter, MMG features, types of sensors used, electrode sites and experimental protocol. Initial search using keywords in Figure 2.4 yielded 64 studies. Further search on torque estimation using myography alone or fused with anthropometric as well as optimization techniques yielded additional 12 studies.

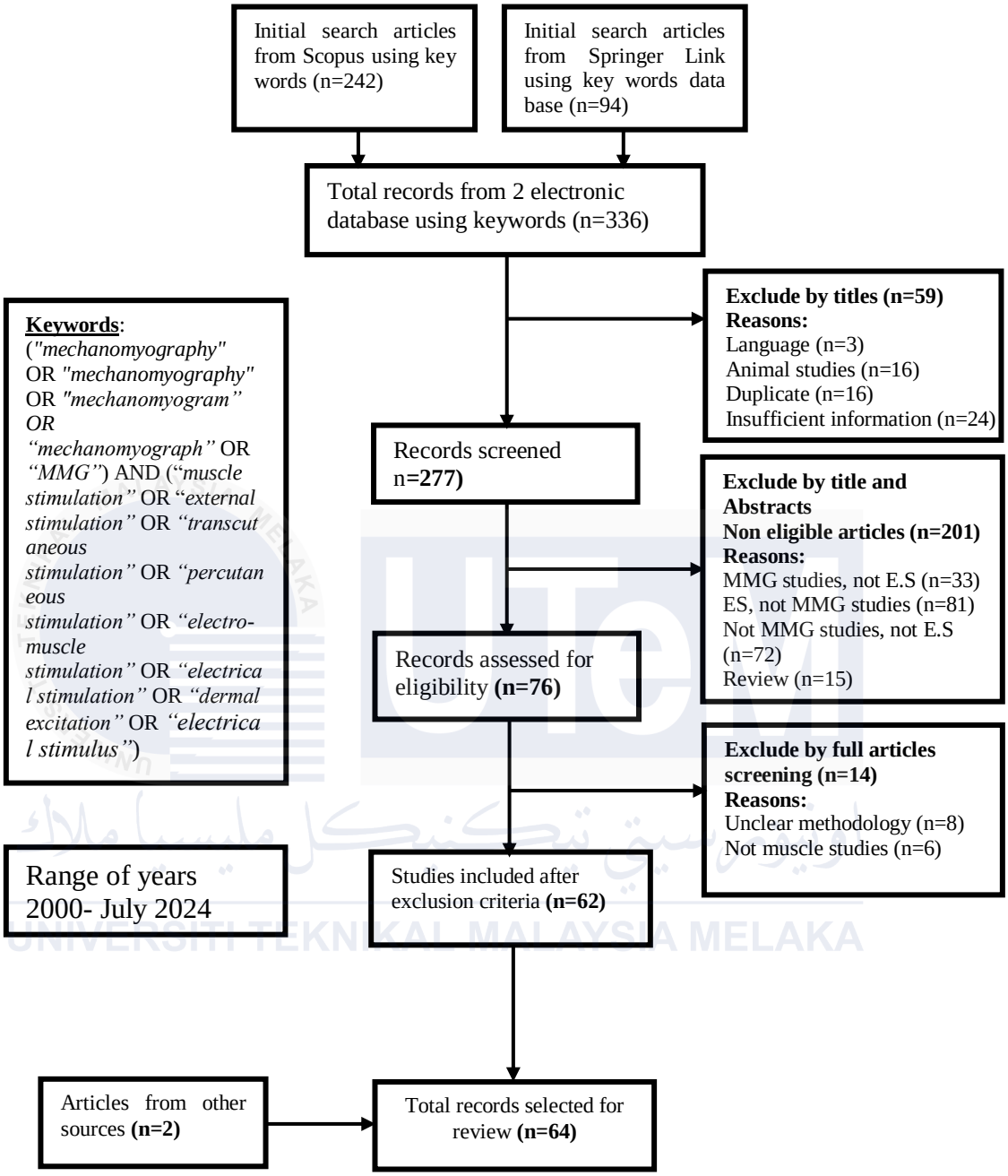

Figure 2.4: Flowchart of article search on NMES and muscles function in myography studies.

2.4.1 Sensors sites

The literature details the identification of proper sensor site for reliable MMG measurements.Using different measurements technologies, the robustness of MMG measurements ensuring the subject safety and physiological significance of the muscle is identified in Table 2.1 as well as in the continuation of this section.

As shown in Table 2.1, four records examined the effects of electrode sites on MMG. One of these studies (Cooper et al., 2014) found that the skinfold thickness can influence the EMG M-waves and MMG gross lateral movement recorded from NMES of vastus lateralis (VL) and rectus femoris (RF) muscles. As a measurement of the muscle belly displacement, the findings obtained in another previous study (Tous-Fajardo *et al.*, 2010) revealed the efficacy of tensiomyography (TMG) in terms of detecting muscle contractile parameters with varying inter-electrode distance (IED). However, due to electrodes repositioning, a decrease in IED from ± 5 to ± 3 cm has been observed to lower the maximum muscle displacement. Thus, these researchers claimed that IED should be maintained during experiments that require electrode repositioning.

In clinical settings, where muscle disuse might lead to physiological weakness, TMG can be used for estimating muscle mass recovery. Using ultrasound scans of the vastus medialis obliquus (VMO) and vastus medialis longus (VML), the thickness and pennation angle were measured, and TMG signals were then obtained at the same measurement site. The authors found that TMG was deemed reliable for the assessment of muscle degradation (Šimunič et al., 2019). Besides, a previous study (Travnik *et al.*, 2013) has showed that the application of a similar twitch type to two separate regions yielded different values of contraction time (TC) values. Thus, TMG can be used to detect the structure and function of

Table 2. 1: Effects of electrodes repositioning on the reliability of MMG data

Study 1: Analysis of the effect of the skinfold thickness on the MMG responses in voluntary and stimulated muscles.					
Author(s)	**Sensor and electrode type**	**Electrode site**	**Dataset**	**Methodology**	**Results and discussion**
(Cooper et al., 2014)	MMG: active miniature accelerometer (EGAS-FS-10-/V05, Measurement Specialties, Inc., Hampton, VA, USA); Force: load cell (LC402, Omegadyne, Inc., Sunbury, OH, USA)	VL and RF	17 healthy male subjects, age 21 ± 2 years, weight 81.9 ± 13.6 kg, height 1.8 ± 0.09 m; and 23 healthy female subjects, age 21 ± 2 years, weight 67.3 ± 8.9 kg, height 1.69 ± 0.07 m)	The stimulation site was determined after M-wave detected with 20 mA. The stimulation increased from 2 to 100 mA. The skinfold thickness was obtained using MMG and EMG electrodes sites and averaged to represent the thickness of each subject. MMG GLM and EMG M-waves, in terms of the log-transformation of EMG-RMS and MMG-RMS-force relationship, were correlated with the skinfold thickness.	The terms and skinfold thickness were not significantly correlated, and a non-meaningful correlation was found among the skinfold thickness, EMG M-waves and MMG GLM.
Remark: A significant relationship was found between the MMG GLM and the skinfold thickness of the VL and RF under non-voluntary contraction.					
Future work: 1. The influence of subcutaneous fat on MMG and EMG signals and the spectral characteristics of the test variables should be investigated. 2. The possible geometrical alteration of subcutaneous tissues and spectral features of EMG, MMG, and force during isometric contractions should be investigated.					

the VML and VMO and should be verified for other muscles.

Study 2: Analysis of the reliability and effect of the inter-electrode distance on TMG parameters					
us-Fajardo et al., 2010)	ES: self-adhesive electrodes (Compex Medical SA, Ecublens, Switzerland); TMG: (GK 40, Panoptik d.o.o., Ljubljana, Slovenia)	Right and left of the VM	18 healthy male subjects, age 22.9 ± 3.8 years, height 171 ± 10 cm, body mass 66 ± 10 kg	A current with 1-ms pulse duration and increases from 50 mA to 11 mA at 10-mA intervals was applied until no increase in the Dm was observed. Rater A positioned the sensors at ±5 cm, marked ±3 cm IED and left the room after removing electrode. Similarly, rater B performed test 2. Rater A then performed tests 3 and 4 with placements at ±5 cm and ±3 cm.	All contractile parameters showed good inter-rate reliability apart from Tr with an ICC of 0.99.
Remark: Dm is provides crucial information in TMG assessment. **Future work:** An experimental confirmation of TMG parameters should be conducted with different subjects, muscles groups and side-to-side					
Study 3: Analysis of the inter-changeability of TMG and ultrasound.					
(Šimunič et al., 2019)	TMG: (TMG-BMC Ltd., Ljubljana, Slovenia)	BF, VMO and VML	10 male subjects, age 24.3 ± 2.6 years	Innervation points were detected using tetanic stimulation (0.1 ms and 10 Hz). TMG parameters were extracted after stimulation with 110 mA at 30 V. The Tc, Dm, and velocity of the radial displacement (Vr) were measured after an ultrasound B-mode scan of the same location.	A significant decrease in thickness and pennation angle makes TMG candidate for early bed test muscle of muscle atrophy.
Remark: The interpretation of muscle contraction based on the modelled muscle shapes depends on twitch contraction. **Future work:** The assessment of muscle contractile functions in terms of angle and inter excitation interval should be investigated.					

Study 4: Analysis of the structure and function of VMO and VML using TMG.					
(Travnik *et al.*, 2013)	ES: self-adhesive anode and cathode (Axelgaard Manufacturing); TMG: (TMG-BMC, Ljubljana, Slovenia)	VML and VMO	mATPase histochemistry: 9 male subjects who experienced sudden death, age 18-44 years; TMG: 15 healthy sedentary male subjects, age 20-37 years	VML and VMO blocks frozen in nitrogen at -196^0 C, were cut into cryostat at -20°C for myofibrillar adenosine triphosphase activity. The muscles fibres were classified into types 1, 3a, 2b, and 2c at different pH levels TMG experiment VML and VMO received 1KHz, monophasic pulse at 1 ms to induce Dm and three 10-s twitches followed	The TMG signal responses of electrical stimulation from two different regions has shown significant difference in T_c, D_m, and T_r and a constant T_d
Remark: The anatomical and histochemical behaviours of VMO and VML are similar, but their biological functions are different. **Future work:** The determination of the biochemical function during voluntary contraction should be further considered.					

The results from the studies on the reliability of muscle function assessment showed that the functionality of TMG to detect the small muscle displacement gave the impression to record muscle contraction at different sensors' positions. Besides, these studies support the contention that the muscle belly displacement signal is influenced by IED. Hence, the interval between sensor positions on muscles should be kept constant in the studies of muscle activities using their mechanics. Further investigation should also shed light on the TMG characteristics considering the changes in muscle dimensions and positions for different tasks and postures.

2.4.2 Stimulation protocol and muscle responses

As presented in Table 2.2, nine studies have been determined to examine the effects of the duration of the stimulation pulse on the muscle contractile properties. The research (Mcandrew et al., 2006) showed that the application of a percutaneous electrical stimulation to the gastrocnemius medialis (GM) between 300 and 500 µs resulted in the displacement of the lateral belly and fixed contractile properties. The authors have recommended that the effects of skin impedance and other physiological moderators should be further examined. In another study (Ohta, 2013), Yoichi Ohta evaluated the effect of nonisometric muscle contraction on joint kinematics and its reliability for detecting MMG responses. In this particular study, it was found that increases in the inter-pulse intervals or the number of stimuli yielded MMG signals that exhibited poor correlation with the changes in the excursion and angular velocity. Similarly, another study (Latella et al., 2019) revealed that the inter-day and inter-stimulus interval and the joint angle have altered the Dm, sustain time, and delay time, even though the obtained TMG parameters were deemed reliable.

The literature also demonstrates that the NMES frequency does not correlate with the MMG frequency response. Papcke et al. (Papcke *et al.*, 2018) reported that during NMES at 5% maximum voluntary isometric contraction, the application of a 20-, 25-, 30-, 35-, 40-, 45-, 50-, 75-, and 100-Hz stimulation frequency did not correlate with any of the three axes analyzed during the Cauchy wavelet-based frequency analysis of MMG signals from the RF. Specifically, the mechanical characteristics of the RF have exhibited a frequency of 20–25 Hz that differs from and is not governed by the stimulation frequency. Hence, the study revealed that a high frequency does not impact the MMG characteristics and, therefore, does not affect the application of MMG in neuroprosthetics.

Postactivation potentiation (PAP) has been determined to be dependent on the joint angle and fiber composition. Specifically, a previous study (Miyamoto *et al.*, 2010) found a difference in the inter-muscle MMG due to PAP of the SOL and GM muscles at the ankle joint. After MVC in the neutral and dorsiflexion directions, a single stimulus was delivered, and a recording uniaxial accelerometer was positioned between two distal and proximal EMG electrodes on each muscle belly. After applying a stimulation protocol similar to that applied in pre-MVC, simultaneous and individual MMG measurements yielded a higher peak-to-peak MMG amplitude from the GM than the SOL in the neutral and dorsiflexion directions. As both muscles were potentiated, it was determined that the magnitude of the PAP depended on the joint angle and composition of fiber types. Another previous study (Shima *et al.*, 2006) used percutaneous NMES of the tibial nerve and twitch torque to evaluate the MMG and EMG responses of the GM. Thus, a positive correlation was found for the MMG PP with both pT and acceleration of twitch torque development (d2T/dt2). Moreover, it was determined that the evoked MMG signals mirror the PAP force and that

the mechanical changes in the muscles are deemed related to an increase in the twitch contraction. These findings reveal the reliability of MMG in characterizing the contractile properties of a muscle after PAP. Moreover, another study (Toca-Herrera et al., 2008) has noted a stable MMG response before and after electrical excitation of non-dominant RF, despite increases in the EMG response and strength. In this particular study, it was suggested that a high exposure time can improve mechanical behaviors. Meanwhile, another study (Mazzinari *et al.*, 2019) has evaluated the onset time, recovery time, and rate of changes in piezoelectric myographic amplitudes after a tetanic stimulation of the ulnar nerve, wherein reductions in the onset and recovery times were observed prior to measured myograph.

Specifically, the wavelet-based intensity analysis was reported to provide insight into the spectral characterization of individual muscle contractile properties. Using both MMG and sEMG, the correlation between the MMG and H-reflexes was determined to support the hypothesis that muscle mechanics may provide insight into muscle recruitment strategy. The authors suggest that future work should evaluate the clinical implication of the MMG signals corresponding to H-reflexes and M-waves (Armstrong, 2014).

Insights from the reliability of muscles recruitment and function monitoring have shown that the stimulation pulse duration (Mcandrew et al., 2006), number of stimuli (Ohta, 2013), pulse rate (Latella et al., 2019) , and joint angles (Travnik et al., 2013; Shima et al., 2006) provide global insights for elucidating the relationship between muscle contraction and recovery of their mechanical properties. Furthermore, the muscle fiber types and joint angles have been identified as two of the factors affecting the PAP (Shima *et al.*, 2006). Because MMG provides useful information on the musculoskeletal system, various MMG features, such as the onset time, recovery time, and relaxation time, should be examined after PAP (Mazzinari et al., 2019; Armstrong, 2014). In contrast, no correlation was found

between the frequency of stimulation and the MMG response (Papcke *et al.*, 2018). Based on this perspective, the reliability of muscle recruitment and mechanical features remains an issue that should be addressed in future studies. In addition, the tissue underlying the skin, viscoelastic properties, and motor tendon units could alter the behaviors of the MMG signal. Therefore, muscle excitation and feature extraction techniques should be verified for outputing repeatable measurements. Interestingly, the variable and fixed contractile properties of the BB muscle's belly for known stimulation pulses were observed. Hence, a new parameter, namely, M + H, from the wavelet intensity analysis using both MMG and sEMG through NMES coupling encourages further verification of the technique for muscle recruitment using the stimulating signal pulses duration and frequencies of different muscles.

2.4.3 Electrodes for NMES and sensors for MMG measurement

As shown in Table 2.3, six studies have been determined to discuss the performance of developed electrodes and sensors in MMG and electrical muscle stimulation settings, further describing their ongoing development. In one study (Ibrahim *et al.*, 2017), a silver (Ag) polydimethylsiloxane (PDMS) composite was developed and used for electrical muscular activation. After fabrication, single and array electrodes were then used to excite the BB muscle. Their functionalities have been evaluated by comparing the MMG signals detected after the NMES of the BB using the newly developed single and array electrodes to the ones detected using commercial NMES electrodes. As per the results, it was shown that the MMG signals obtained with single rather than array electrodes appeared to have a higher range. As such, NMES of a specific muscle by single Ag–PDMS electrode is deemed more effective than array electrodes. Thus, single electrode yields a better signal-to-noise ratio compared with array electrodes. Array electrodes, on the other hand, have been determined

to be crucial for wearable devices, particularly in cases in where nonuniform contact region could be present and where continuous NMES is needed.

Another previous study (Rafolt and Gallasch, 2002) has evaluated the applicability of a galvanometer-attached lever and skin indentor in MMG signal detection. During isometric contraction of the calf muscles, a dynamometer was used to record the surface response 3 cm from the motor point of the GM muscle. The contraction force was then recorded by a load cell. After the application of single-twitch electric intensity, an accelerometer was utilized to detect the target contraction on the skin surface. During evaluation of the effect of indention and muscle contraction, the amplitude RMS showed a proportional increase during contraction; furthermore, constant mean frequencies were observed. The accelerometer and galvanometer amplitudes were then preserved at 200 N, but their double differentiation output reportedly decreased by 9%. A unity cross-correlation coefficient confirmed the validity of using a galvanometer for recording MMG signals.

Interestingly, the availability of different forms of MMG recording devices has encouraged the examination of the validity of a micromachined acceleration sensor for TMG (Zagar and Kri~aj, 2005). Simultaneous recordings, coupled with a linear optical encoder-based displacement sensor and accelerometer, were obtained to acquire the muscle belly displacement at 100 data points per 1 s; in this experiment, a bandwidth of 2300 Hz was observed after a single-twitch square-wave stimulus of the BB. Based on previous studies, the researchers found that the results agreed with the minimal allowable threshold amplitude and a window length of 1 mm. The standard deviation of the double integration of the linear displacement MMG increased over time. The mean relative error, the maximum displacement (Dm), and ½Tr were 0.02 mm, 0.6, and 3 ms, respectively. Therefore, this study has confirmed that the microelectromechanical system (MEMS) accelerometer can be

used to detect short-term small muscle displacement.

Meanwhile, another study (Uchiyama and Shinohara, 2013) has examined the performance of displacement and acceleration transducers using a system identification method, with electrical stimuli as the input and acceleration (AMMG) or displacement (DMMG) as the output. Based on this study, it was determined that DMMG at a natural frequency of 3 Hz was suitable as a longitudinal mechanical feature, whereas AMMG was found to be of advantage when used for reflecting both the longitudinal and transverse mechanical characteristics of muscles, subcutaneous tissue, and the skin.

Table 2. 2: Effects of stimulation signal parameters on muscle contractile responses

Study 1: Analysis of the effect of changes in the duration of stimulation pulses on contractile measures.					
Author(s)	**Sensor and electrode type**	**Electrode site**	**Dataset**	**Methodology**	**Results**
(Mcandrew et al., 2006)	MMG: laser sensor (model LG10A65PU: Banner Engineering, Minneapolis, MN, USA; Class 2, sensing beam with a 670-nm visible red laser, power output = 0.20 mW, beam size = 0.06 mm x 0.8 mm, resolution =10 μm)	BB	10 healthy male subject, age 19-33 years	Stimulation pulses were increased from 50 μ*s* to 500 μ*s* until no further increase in the MMG Dm was detected.	The duration of the pulse impacted the muscle contractions reflected by MMG.
Remark: The lateral displacement and rate of muscle contraction decreased from 50 to 300 μs, and none of the fibres were maximally activated below 300 μs.					
Future work: Other muscles and the effect of skin impedance on other moderators must be evaluated in the future.					
Study 2: Effect of non-isometric muscle activation on joint parameters and MMG					
(Ohta, 2013)	MMG: 9-mm^2 accelerometer (thickness = 4.5 mm, mass = 0.75 g, sensitivity = 500 mV/g where g = 9.8 m/s^2; MP110-10-101, MediSens INS, Japan)	TA	8 healthy male subjects, age (means ± SDs) 27 ± 2.9 years, height 173 ± 9.1 cm, weight 73 ± 5.5 kg	The ankle joint and MMG were measured after one, two, three, four, seven and eight stimulation pulses separated by a 1-5-min rest; the 10-ms (100-Hz) pulses were administered at an inter-pulse interval of 10, 20, 30, 40, 50, 80 and 100 ms.	At different inter-pulse intervals or with different numbers of stimuli, the MMG signals exhibited a poor correlation with the changes in joint kinematics.
Remark: Torque changes should not be considered for the control of the initial joint movement using functional electrical stimulation.					
Future work: Investigate further MMG-derived parameters or sensor fusion techniques to improve early-phase joint movement prediction FES.					

Study 3: Analysis of the effect of the inter-pulse duration on muscle contractile parameters.					
(Latella et al., 2019)	ES: stimulating electrodes (Compex Medical AS, Ecublens, Switzerland); TMG: (BMC Ltd., Ljubljana, Slovenia)	BB	13 male and 2 female subjects, age 29.5 ± 7.4 years, height 176.9 ± 9.2 cm, body mass 78.7 ± 14.9 kg	A 10-s ES was delivered to the BB positioned at 10, 45, 90º with the arm at rest for 10-20 s on 2 separate days. The delay time (Td), contraction time (Tc), sustained time (Ts), relaxation time (Tr) and maximal displacement (Dm) were compared between the 2 days.	The test-retest reliability of TMG parameters was significant for 2 days.
Remark: The interpretation of muscle contraction in terms of modelled muscle shapes depends on twitch contraction. **Future work:** The possible maximal stimulation response should be verified.					
Study 4: Analysis of the effect of submaximal contraction on the MMG response.					
(Papcke *et al.*, 2018)	Accelerometer (13 × 18 mm, 0.94 g; MMA7260Q, Free scale)	RF	13 right-footed healthy male subjects, age 21.3 ± 6.5 years, mass 79.3 ± 6.08 kg, height 179 ± 10.71 cm	The femoral nerve was excited by nine NMES frequencies at 1 KHz modulated at 20, 25, 30, 35, 40, 45. 50, 75 and 100 Hz.	The relationship between NMES frequencies and MMG responses is not linear.
Remark: A high frequency does not impact the mechanomyographic characteristics and thus does not affect for the application of a neuroprosthetic device. **Future work:** Integrating machine learning could help model the nonlinear MMG-NMES relationship for adaptive neuroprosthetic control.					

Study 5: Analysis of the effect of post-activation potentiation on the MMG of synergistic muscles.					
(Miyamoto *et al.*, 2010)	EMG: 11-mm pick-up diameter, 25 mm inter-electrode distance; MMG: uniaxial accelerometer (dimensions = 9 × 9 × 5 mm, mass = 0.75 g, model MP101-10, MediSens, Japan)	MG and SOL	8 male subjects, age (means ± SDs) 26.86 ± 3.7 years, height 176.1 ± 6 6.3 cm, mass 71.2 ± 6 6.1 kg	Before and after a 10-s MVC, a 500-µs pulse was delivered every 1 min for 5 min, and one stimulus was applied after 10 min. The evoked MMG was measured before and after 10-s supramaximal plantar flexion.	The potentiation of both muscles with the plantar flexion angle was investigated. The MG showed a higher MMG amplitude than SOL at DF and NP.
Remark: A 10-s dorsiflexion and neutral position of the MG showed greater potentiation than SOL, but no significant difference in PAP for plantar flexion was found between the two conditions. **Future work:** Expanding the analysis to include bilateral comparisons and dynamic movements may provide deeper insights into muscle coordination during PAP.					
Study 6: Analysis of the effect of post-activation potentiation on MMG.					
(Shima *et al.*, 2006)	MMG: (MP110-10-101, MediSens, Inc., Japan; sensitivity = 500 mV/g where g = 9.8 m/s^2)	MG	10 healthy male subjects, age 25.8 years, height 170.3 ± 4.8 cm, weight 67.8 ± 7.5 kg	After supramaximal stimulation to determine the M-wave and a 10-min rest, three isometric contractions at a 5-s interval were delivered for each twitch stimuli. Twitch contractions were evoked 2, 15, 30, 60 and 180 s after the MVC.	No change in the M-wave was found after MVC. The changes in MMG measured after the evoked twitch contractions reflect changes in muscle contraction.
Remark: After PAP, the evoked MMG-PP represents the contractile properties of the muscle. **Future work:** Future studies should explore the long-term effects of repeated post-activation potentiation (PAP) on MMG characteristics across different muscle groups					

Study 7: Analysis of the intensity and contraction velocities of skeletal muscles.					
(Armstrong, 2014)	MMG: accelerometer (ADXL330, Analogue Devices, Inc., Norwood, MA, USA); EMG: Ag–AgCl electrodes (EL503; Biopac Systems Inc.)	Soleus muscle	3 male and 5 female subjects, age 19 ± 1 years	An H-M recruitment curve was mapped for the soleus muscle by increasing the 0.1-ms square wave at 1.0-5-V increments with a 10-s rest interval until an M-wave was recruited.	The maximum sEMG corresponding to H-reflex and M-waves showed a moderate correlation between HM and MMG_{PP}.
Remark: The time-to-maximum intensity (TTMax) was longer at a low stimulation intensity and declined with increases in the intensity.					
Future work: Further studies should account for the body composition, muscle fibre composition, gender and training.					
Study 8: Effect of unilateral surface stimulation session on the contralateral limb					
(Toca-Herrera et al., 2008)	MMG: 6.5-g accelerometer (K-Beam 8305A; Kistler, Amherst, MA, USA); EMG: Ag/AgCl bipolar surface electrodes (Blue Sensor M-00-S; Medicotest, Ølstykke, Denmark)	RF	36 healthy right-footed male subjects, age 25.8 ± 1.3 years, weight 75.0 ± 2.1 kg, height 178.3 ± 1.1 cm	After stimulation at 100 Hz with a 300-µs pulse duration, a cycle of 10 s on and 10 s off was applied for relaxation of the RF of the non-dominant leg of the 18 RS group for 10 min.	MMG, EMG and MVIC from the dominant leg before and after stimulation showed no changes in the MMG activity of the RF ($p < 0.05$).
Remark: The lack of mechanical changes could be due to the short exposure time to the stimulus.					
Future work: The influence of a long exposure time to the stimulus on the tension, rigidity, mass and length of the muscle should be investigated.					

Study 9: Analysis of the effect of the staircase phenomenon on neuromuscular blockade (NMB) monitoring.					
(Mazzinari *et al.*, 2019)	AMMG (TOF–Watch SX; Organon, Dublin, Ireland)	Abductor pollicis	17 males and 7 females in group C, age 45.9 years, BMI 25.6 kg/m^2; 17 males and 5 females in group S, age 47.9 years, BMI 25.1 kg/m^2	Group C received 2-Hz train of four (TOF) every 15 s over 20 min, and rocuronium was injected into the other hand. Group S was tetanically stimulated (50 Hz, 5 s, and 50 mA).	Prior to acceleromyography, tetanic stimulation resulted into reduced onset and recovery times of AMMD amplitudes.
Remark: SP has no influence on the TOF ratio. **Future work:** The effect of sensitivity on monitoring NMB function should be investigated.					

However, a 3-Hz higher fluctuation was noted for AMMG than DMMG. Although the sensors showed good performance in measuring underlying events, some evidence shows the importance of the transduction rate and sensitive parameters. In another study (Seidl *et al.*, 2017) , it was found that a laser-displacement (LDS) and a contact-displacement sensor (CDS) exhibited satisfactory reliability after four tests conducted over 2 weeks. Despite the recovery Tc and D_{max}, the half-relaxation time ($½T_r$) exhibited poor recovery to its pre-fatigued value during the recovery period. Despite the slower Tc of CDS, it was found that the sensor might detect individual muscle actions, whereas noncontact LDS exhibits some limitations, and this uniformity is thought to limit the inter-changeability of these sensors.

Another study (Mohamad *et al.*, 2017) compared the average, and peak torques measured using a commercial dynamometer, and torque estimated using a muscle contraction sensor (MCS) FES evoked muscle contraction. The results showed that the signals obtained using MCS and dynamometer were strongly correlated, which indicated that these sensors can be used instead. Although some limitations such as different responses of the LDS and CDS, AMMG and DMMG, effectiveness of VMG than MCS in muscle fatigue assessment for SCI population (Ng et al. 2014), there exist proof that confirms their validity in the myographic signal recording. Based on recent insights on selecting MMG sensors (Islam et al., 2013; Talib et al., 2018), experimental verification with similar conditions and recording sites may provide better conclusions. A comparison of MMG recorded using MEMS accelerometer for TMG measurement showed that the MEMS accelerometer is reliable in detecting small muscle displacement. AMMG was found to measure both longitudinal and transverse muscle characteristics and subcutaneous tissues. The lack of fast recovery of ½Tr in LDS and slower CT in CDS favor accelerometers as MMG sensors, while piezoelectric sensors and MCS require further comparisons.

Table 2.3: Overview of the electrodes for NMES and sensors for MMG measurements

Study 1: Validation of Ag-PDMS substrate for the electrostimulation of muscles.					
Author(s)	**Sensor and electrode type**	**Electrode site**	**Dataset**	**Methodology**	**Results and discussion**
(Ibrahim *et al.*, 2017)	Ag-PDMS composite	BB	Not reported	Single and array electrodes composed of Ag/Ag-PDMS and PDMS/OHP substrates were used, and MMG signals were recorded for testing purposes.	The responses were like those obtained with a single commercial electrode, with an average peak of 7000-10000 mV.
Remark: The Ag-PDMS can be bent and stretched, which was a limitation of the Ag-OHP paper electrode. **Future work:** Future work should evaluate the long-term biocompatibility and durability of Ag-PDMS electrodes during repeated NMES sessions.					
Study 2: Evaluation of a lever indentor and a moving magnet galvanometer for MMG recording.					
(Rafolt and Gallasch, 2002)	ES: galvanically isolated stimulator (MYOSTIM); MMG: scanner galvanometer; Force: ankle dynamometer (RAFOLT and GALLASCH, 1996)	Calf muscles	6 healthy subjects	9 stimulation pulses were delivered to achieve a contraction of 70 N, whereas the indentor was adjusted to 0.1, 0.5 and 5 N. Under isometric contraction of the calf muscles, an ankle dynamometer was used to record the surface response from the gastrocnemius muscle.	The amplitudes of MMG-RMS showed direct increases during contraction.
Remark: A unity cross-correlation coefficient confirmed the validity of using a galvanometer for recording MMG signals. **Future work:** Further studies should verify indirect stimulation.					

Study 3: Analysis of the accuracy of an accelerometer for tensiomyography.					
(Zagar and Kri~aj, 2005)	TMG: optical encoder (4 µm, 0.25 mm^{-1}; a spherical tip of 12 mm^{-2}); MMG: displacement accelerometer	BB	Not reported	A single twitch stimulus consisting of a 1-ms, 20-mA square pulse was delivered to the BB using two self-adhesive electrodes. The double integration of the acceleration records was compared with the optical encoder records.	The MEM accelerometer efficiently detects short-term small muscle displacement.
Remark: The difference in D_m recorded from an accelerometer and a displacement sensor and the time parameter must not differ by more than 0.05 mm and 0.5 ms, respectively. **Future work:** A commercially available micromachined holds potential for integration into future compact and flexible systems designed for similar displacement monitoring.					
Study 4: Characterization of muscles and subcutaneous tissues.					
(Uchiyama and Shinohara, 2013)	ES: Ag-AgCl; DMMG: (LK-G80, Keyence, Osaka); AMM: (MP-110-10-101, MediSens, Saitama)	TA	6 healthy males, age 22-25 years	A mono-polar rectangle pulse with a 500 µs in width and an inter-pulse interval of 600 ms was applied.	Good identification of the longitudinal and transversal mechanics of the muscle, subcutaneous tissue and skin was achieved.
Remark: The natural frequency of an acceleration sensor fluctuates more than that of a displacement sensor, but the latter is limited to longitudinal muscle mechanics. **Future work:** The effect of the mass of subcutaneous tissue on the natural frequency should be investigated.					

2.5 Types of muscles function assessment using NMES and MMG

The screening of selected articles analayzed various muscle conditions relevant to daily muscle's function, which are presented in this section.

2.5.1 Fatigue assessment

In total, 18 records have been identified to describe the examination of muscle fatigue using MMG and NMES protocols. Among these 18 studies, 10 articles in Table 2.4 utilized various techniques for the quantification of fatigue, 4 articles in Table 2.5 documented fatigue and muscle physiology, and 4 articles in Table 2.6 reported the relevance of fatigue and endurance. In one study (Blangsted *et al.*, 2005), the development of fatigue was examined at 10% MVC 10min wrist extension during a 20-min pre-experiment and its recovery over 10, 30, 90, and 150 min under low-force contraction. The force analysis was conducted at 1, 20, and 100 Hz. The low-frequency fatigue (LFF) was measured as the response of the ratio of the 20- to 100-Hz of stimulating signal. The EMG RMS and MMG RMS values were observed to increase at the force ratio of 20/100 Hz at 10% maximum MVC within 10 and 30 min of recovery. No significant changes were noted in the 80% MVC test. In addition, no change in the mean power frequency (MPF) values was observed at 5% MVC, whereas a decrease before the experiment at 10% MVC and after 90–150 min was detected. Therefore, these findings reveal that low-force muscle contraction leads to prolonged LFF, as identified by EMG and MMG. These results are supported by (Adamo *et al.*, 2002) where LFF was observed for 2 h after a 5% MVC hand grip for 30 min.

Meanwhile, four studies (Cè et al., 2017;Rampichini et al., 2014;Cè et al., 2014; Cè et al., 2013) have evaluated muscle behavior after fatiguing stimulation for 120 s, followed

by tetanic stimulation at 1, 2, a(Cè *et al.*, 2017)these studies (Cè *et al.*, 2017) evaluated the changes in electromechanical delay components from the GM. The DelayTOT values were determined based on the RMS and MF of the EMG, MMG, and force. All measurements were obtained from a time frame of 250 μs during fatiguing stimulation. During a 120-s stimulation, MMG RMS was noted to show stable patterns over the first 90 s, but then decreased until the end of the stimulation. The MF of MMG presented a strong reduction during the first 10 s; then, it monotonically decreased until the end of stimulation. In contrast, the EMG RMS increased by 40% during the first 70 s before it returned to its initial values, whereas the MF components presented reductions starting after the first 10 s until the end of the stimulation. In this study, various electrochemical and mechanical components were identified, and the researchers reported that the detected delay correlated with the tested EMG, MMG, and force parameters. In addition, the researchers claim that the mechanical events (t MMG-F) provided a highly reliable measure of fatigue. These findings were consistent with those obtained in another study (Rampichini *et al.*, 2014) that investigated the effect of fatigue on the delay in force development (DelayTOT) from GM during 35-Hz fatiguing stimulation for 120 s. Before and after the induction of fatigue, a couple of tetanic stimulations were administered, with a resting interval of 10 min, and the effect of fatigue was indicated by the reductions in pF and MMG PP. The results also showed that fatigue lengthened the delay, which in turn affected its electromechanical and electrochemical components.

Similarly, another study (Cè *et al.*, 2014) has examined the impacts of fatigue on electromechanical delay components and assessed the inter-day and inter-session reliability during relaxation after tetanic and fatiguing stimulation protocols, same as those used in the above-mentioned study (Rampichini *et al.*, 2014). The results demonstrated that the increase

in R − DelayTOT paralleled the increase noted in electrochemical components and the first mechanical component measured after fatigue, whereas the second mechanical component, which was an electromechanical component measured at the onset of the force decay and the negative MMG peak values, did not change. Therefore, a low contribution to the R − DelayTOT was found.

The aims of another study (Cè *et al.*, 2013) were two folds: (1) to examine the correlations between peak-to-peak MMG and force parameters and (2) to validate the interday reliability of mechanical parameters of the MMG signals induced by a tetanic stimulation before and after the NMES to fatigue. The authors reported that pT , MMG PP , R – MMG PP, and the acceleration of force development, the slope, and relaxation decreased after fatiguing stimulation, but the relaxation time (RT), CT, and τ were noted to increase. The relaxation MMG (R−MMGP−P) correlated with the MMG PP , slope, τ, pT, and the acceleration of force development (D2RFD) before and after fatigue. Due to the high intraclass correlation coefficient between the MMG and force parameters obtained from different experimental sessions on different days, it was concluded that the MMG is a viable alternative to force for examining fatigue-induced changes during muscle relaxation (Macgregor, Ditroilo, Smith, Fairweather and Hunter 2016) . Furthermore, (Macgregor et.al, 2016) have examined muscle fatigue based on muscle tension through the temporal and spatial displacement recorded from GM before and after supramaximal stimulation through a process known as TMG. As per the result of this study, a significant ($P < 0.001$) decline was noted in the peak force measured with MVC; thus, it was hypothesized that this decline was in line with the decrease in the TMG Dm ($P = 0.031$). Similarly, the researchers claimed that the passive muscle tension from the plantar flexor increased.

In a previous study (Naeem *et al.*, 2019), the mel frequency cepstral coefficient

(MFCC) and MMG RMS were used to train an SVM classifier for the identification of fatigued and non-fatigued RF, VL, and vastus medialis in SCI. MFCC were then obtained as its time-localized frequency information using short-time Fourier transform of a stationary signal with a window frame of 25 ms. The MFCC features exhibited 90.7% accuracy, whereas the RMS feature only showed 74.5% accuracy.

Meanwhile, three studies (Islam et al., 2018; Jo et al., 2018; Gobbo et al., 2006) also examined muscle fatigue via analyzing torque and MMG p(Islam *et al.*, 2018)e studies (Islam *et al.*, 2018) assessed the MMG responses from the quadriceps muscles to quantify its changes between pre- and post-fatiguing conditions in SCI patients in NMES-evoked cycling. The peak torque and normalized MMG RMS and MMG MPF values showed significant trends between pre- and postelectrical excitation for individual muscles. The researchers also observed a change in the MMG signals as a function of the cycling time for the VL, RF, and VM muscles. Typically, MMG RMS and epT significantly ($P < 0.05$) decrease as the leg cycling exercise increases for the quadriceps groups.

On the other hand, Massimiliano Gobbo and colleagues (Gobbo *et al.*, 2006) have investigated the validity of MMG to assess the fatigue that develops during NMES in rehabilitation services. After a fatiguing stimulation of 50 single twitch and 2 Hz for 25 s, a correlation was found between the mean values of normalized pT % and MMG PP %. It was further reported that pT % and MMG PP % decreased from 100% of their initial values to 50 and 60% for the BB, respectively, and to 43 and 47% for the VL, respectively. In addition, the decreases in pT % and MMG PP % exhibited a different linear correlation. Thus, the introduction of electrical activation of skeletal muscles and MMG responses into assistive technology that involves analysis of torque of a particular muscle remains to be unclear.

Under both artificial ele(Jo *et al.*, 2018)ation and MVC (Jo *et al.*, 2018) examined

the fatigue from the ankle joint and performed a torque analysis. The raw MMG data were then extracted during 30 min of repeated stimulation of the tibialis anterior (TA) muscle, sampled at 1 kHz and bandpass filtered at 8–100 Hz. The amplitude, i.e., convexhull, peak-to-peak, and Lempel–Ziv algorithm, and median and mean frequency-based MMG features were also utilized for the quantification of fatigue of the TA muscle. The ankle joint torque has been used to analyze fatigue after low-pass filtering of the raw torque at a cutoff frequency of 3 Hz. The muscle fatigue was further indicated by a linear decrease in torque during consecutive stimulation patterns. The coefficient of determination (r^2) was 0.7823. However, it was noted that the frequency components of MMG signals demonstrated a weak linear relationship with fatigue. Thus, the use of the stimulation protocol relevant to NMES popular in clinical settings supports the finding that the technique may fit the design of electrical muscle excitation feedback control system, which is useful in assisting week/injured muscles.

Four studies (Krueger et al., 2016; Esposito et al., 2009 ;Ohta et al., 2009;Cè et al., 2008) have been identified to discuss the physiological behaviors after fatigue administration. In one of these studies (Krueger *et al.*, 2016), the authors evaluated the correlation between the temporal and spectral features of MMG from 10 SCI and 10 health volunteers undergoing recovery by NMES. MMG RMS and MMG MF from the analysis of window length were examined. An increase in RMS and a decrease in MF were then observed from both groups. The authors concluded that the temporal features might originate from the increased amplitude of mechanical wave from motor unit coherence, whereas the decrease in MF might be attributed to motor unit adaptation.

On the other hand, two studies (Esposito et al., 2009; Cè et al., 2008) evaluated the effects of stretching on mechanical and electrical responses, wherein both analyses found

constant electrical parameters but a divergence in the mechanical (Cè *et al.*, 2008)these studies (Cè *et al.*, 2008) used a stretching protocol in order to evaluate the changes in the mechanical and electrical properties of EMG and MMG on GM. Significant decreases in the RMS and MF of EMG have been noted, and a conduction velocity was observed after the fatiguing protocol. Similarly, the RMS and peak-to-peak values of MMG were noted to decrease, whereas the speed of electromechanical impulse and the ½Tr increased. The authors claimed that all RMS values of EMG and MMG returned to their pre-fatigued values after stretching, whereas the peak rate of force development, derived acceleration, and the ½Tr showed further reductions. This led the researchers to a conclusion that the application of acute stretching to previously fatigued muscles weakened the mechanical but not the electrical properties.

The study by (Cè *et al.*, 2008) has evaluated the electrical and mechanical manifestations of muscles after a set of six electrical stimulations before and after stretching. The findings are i(Esposito *et al.*, 2009)e study (Esposito *et al.*, 2009), revealing no significant changes in the EMG signal parameters. In addition, the study found reductions in the force acceleration, peak force, and peak-to-peak MMG values, and these reductions were determined to be accompanied by a possible concomitant decrease in muscle stiffness. Moreover, the researchers found a poor correlation between the MMG and force parameters, wherein a bout of acute passive stretching alters the mechanical but not the electrical parameters of electrically stimulated muscles.

Furthermore, the mechanical properties of skeletal muscles were also investigated in a previous study (Ohta *et al.*, 2009), with the aim of characterizing the architectural changes in the human MG under interpolation conditions. Using ultrasound images obtained from electrically excited MG under plantar flexion at 20, 40, 60, 80, and 100% MVC, the

researchers found that superimposed MMG amplitudes exhibited a curvilinear decrease accompanied by a fascicle shortening, with increases in the contraction intensity up to 100% MVC. In contrast, the study argued that the superimposed twitch amplitude decreased linearly with increases in the contraction intensity up to 80% MVC.

Four studies in Table 2.6 (Willingham et al., 2018; Mccully et al., 2019; Decker et al., 2010 ;Connor et al., 2016) have also reported on the use of MMG and fatigue as a reflection of muscle endurance. One study (Willingham *et al.*, 2018) aimed to diagnose the drawback of exercise-based improvements in disabled individuals. Assisted by electrical muscle activation, the walking speed and muscle endurance were compared to the working function and strength. As per the endurance index, the endurance was noted to increase with increases in the walking function in individuals with multiple sclerosis. Similarly, another study (Mccully *et al.*, 2019) highlighted the dependency of the endurance index on MMG recorded from electrical activation of the erector spinae muscle compared with those from the voluntary or muscle oxygen levels. Another study (Decker *et al.*, 2010) has also used different stimulation protocols to examine endurance in SCI-paralyzed patients under different workloads. The authors reported that a high stimulation intensity, compared with the lower intensity, can lead to increased muscle fatigue and hypothesized that the standard co-activation stimulation protocols are less prone to cycling endurance time accounted in NMES-based functional recovery compared with alternative stimulation.

Meanwhile, a previous study (Connor *et al.*, 2016) evaluated the endurance, feeling of fatigue, and mitochondria capacity using NMES, near-infrared spectroscopy (NIRS), and MMG at different age ranges. The forearm flexors of 10 abled bodies and 16 Friedreich's ataxia (FRDA) were electrically stimulated for 3 min at 2, 4, and 6 Hz, with a resting interval of 5 s. MMG indicated a considerable correlation of mitochondrial capacity, disease severity,

and muscle-specific endurance in FRDA. Based on these findings, it can be concluded that the disease frequency and progression in the FRDA population can be monitored.

It was indicated that MMG signals are obtained from muscles, which represent the different physiological conditions of those muscles through fatigue protocols. It is likely that a decrease in spectral component during functional recovery produced by NMES can be due to motor unit adaptation, whereas the increase in MMG RMS might be due to motor unit coherence. In addition, a decline in MMG parameters and torque with an increase in fatiguing NMES demonstrates the usefulness of electrical stimulation and muscle mechanics in determining muscle injury in SCI population. Hence, fluctuation in mechanical features manifested as a muscle response in different experiments requires further exploration. It was also pointed out that LFF might be attributed to low % MVC. However, this was contradictory to other studies as this was identified to be due to the slower ability of muscles to recover their normal activity under low frequency or overlap between signals from damaged and fatigued muscles. The role of muscles mechanics has also been determined using MFCC, which is a feature extraction technique that uses speech signal processing and other nonstationary signals such as EMG classifications and electroencephalography (EEG) (Norali *et al.*, 2017). The literature shows that the developed model exhibited good accuracy in muscle fatigue assessment. The features from MMG also reflect the correlations among muscle endurance, mitochondrial capacity, and diseases severity in FRDA population.

Collectively, the findings show that muscle fatigue should be re-investigated considering overlap between muscle damage and fatigue, the muscle weakness, the overlap between muscle endurance and disease severity as well as the progression in populations other than the FRDA. Thus, muscle mechanics based on MMG has been experimented in NMES exercises but requires further investigation in biofeedback control system required in

Table 2.4 : Assessment of muscle fatigue using MMG and ES

Study 1: Examination of prolonged low-force fatigue due to prolonged low- and high-frequency ES.					
Author(s)	**Sensors and electrode type**	**Electrode site**	**Dataset and electrode sites**	**Methodology/electrical stimulation protocol**	**Results and discussion**
(Blangsted *et al*., 2005)	MMG: uniaxial accelerometer (Bang & Olufsen Technology, Denmark, diameter = 17.6 mm, weight = 2.9 g, 20 pC/ms^{-2}, 0.1 to 800 Hz); EMG: bipolar Ag/AgCl (Blue Sensor N-00-S, Medicotest, Denmark, diameter = 6 mm); Force: Alpha Beam 250N (BLH Electronics, USA)	ECR	3 healthy and 4 healthy male subjects, age 27–54 years, height 1.52–1.84 m, weight 56–92 kg, body mass index: 20.9–27.2 kg/m^2	Arm flexed at 90º, static wrist extension for 10 min at 10% MVC; over 150 min, the subject was administered a 10-s train at 1 Hz, two 2.5-s trains at 20 Hz, and two 2-s trains at 100 Hz s, with a 30-s rest between each train. The ES was adjusted to obtain 30% of the MVC at 100 Hz, each pulse lasted 0.7 s.	LFF showed electromechanical efficiency in the low-force and control experiment for up to 9000 s, as reflected in MMG more than the EMG.
Remark: A low-force test is recommended for fatigue development in muscle and recovery prior to low-force exertion. **Future work:**Fatigue at low force of muscle contraction should be further evaluated.					

Study 2: Analysis of the changes in electromechanical delay components of skeletal muscle exposed to fatigue.					
(Cè *et al.*, 2017)	EMG: model ELSCH004 (OT Bioelettronica, Turin, Italy); MMG: accelerometer (model ADXL103, Analogue Devices, Norwood, MA, USA; weight < 1.0 g, sensitivity = 1000 mV/g, range = ±1.7 g); Force: load cell (model SM-1000 N, Interface, Crowthorne, UK, linear operation between 0 N and 1000N)	GM	20 healthy subjects, age (means ± standard deviations) 23.1 ± 4.2 years, body mass 74.3 ± 11.2 kg, stature 1.77 ± 0.08 m	12 blocks of 10-s stimulation at 35 Hz, pulse duration of 340 us, a duty cycle of 9 s on/1 s off for a duration of 120 s was delivered after 2-Hz, a 5-mA increasing amplitude was administered for motor unit stimulation	All of the delays lengthened the contraction based on different onsets and kinetics. The changes in the cross-bridge and muscle tendon unit (MTU) mechanical properties occurred later compared with the electrochemical events.
Remark: The delay in the lengthening of mechanical events suggests that these were the most affected by fatigue. **Future work:** Further studies are needed to evaluate the electrochemical and electromechanical alternations at the motor tendon units and muscle junctions under fatigue conditions.					
Study 3: Inter- and intra-operator reliability of the measurements and the effects of fatigue on different $\mathbf{Delay_{TOT}}$ components.					
(Rampichini *et al.*, 2014)	MMG: accelerometer (model ADXL103, Analogue Devices, Norwood, MA, USA; weight = <1.0 g; sensitivity = 1,000 mV/g; range = ±1.7 g); Force: Load cell (mod. SM-1000 N, Interface, UK); EMG: linear array of four electrodes (model ELSCH004, OT Bioelettronica, Turin, Italy)	GM	16 healthy male subjects, age (means ± SDs) 25.0 ± 3.9 years, body mass 77.5 ± 13.8 kg, stature 1.79 ± 0.08 m	A biphasic 50-Hz pulse with a 340-µs duration at 110% of the M-wave amplitude was administered during a 3-s tetanic stimulation with a 5-min rest before a fatiguing tetanic pulse of 120 s at 35 Hz was delivered to the GM. The pre-fatiguing pulse was repeated at 1, 2, and 7 min.	The ICC was 0.874–0.996, and the SEM was 0.78 and 6.61% before fatigue. The reliability was 0.781 to 0.981, and the SEM was 1.78 to 8.71%. All the variables were reliable within an inter-parameter operability of 0.847 to 0.999 after fatigue.
Remark: The intra- and inter-operator reliability of individual $Delay_{TOT}$ components increases, and the results provide a valid indication for the monitoring of physiological and pathological changes. **Future work:** Longitudinal research is recommended to assess the effectiveness of this approach in detecting subtle physiological and pathological alterations across multi-center settings.					

Study 4: Effects of fatigue on $Delay_{TOT}$ components and their inter-session and inter-day reliability.					
(Cè *et al.*, 2014)	MMG: accelerometer (model ADXL103, Analogue Devices, Norwood, MA, USA; device weight = <1.0 g; sensitivity = 1000 mV/g; range = ±1.7 g); EMG (model ELSCH004, OT Bioelettronica, Turin, Italy)	GM	17 healthy male subjects, age 24.3 ± 3.4 years, body mass 77.8 ± 14.3 kg, stature 1.79 ± 0.08 m	A biphasic 50-Hz pulse with a 340-µs duration at 110% of the M-wave amplitude was administered during a 3-s duration tetanic stimulation with a 10-min rest before a fatiguing tetanic pulse of 120 s was delivered at 35 Hz to the GM.	**$Delay_{TOT}$**, R-Δt F-MMGp-p, and **DT_{Slow}** were positively correlated. Fatigue changed the duration of the experiment and the start of force decays but had no effect on its duration.
Remarks: 1. Fatigue might prolong R-EMD components, which might indicate physiological recovery after physical or rehabilitation exercises. 2. After fatigue, the constant elongation of the R-Δt MMGR-F without changes in R-Δt F-MMGPP might be due to increases in the spatial relationship between blood vessels and muscle fibres. **Future work:** The reoccupation of the squeezed out interstitial fluid might be attributed to alterations in the return of the MMG signal to baseline.					
Study 5: Evaluation of the reliability of MMG for determining the evoked changes during muscle relaxation.					
(Cè *et al.*, 2013)	MMG: (model 10ADXL103, Analogue Devices, Norwood, MA, USA; weight = <1.0 g; 1000 mV/g; range = ±1.7 g); EMG: (model ELSCH004, OT Bioelettronica, Turin, Italy); Force: (model SM-1000 N, Crowthorne, UK)	GM	23 HV male subjects, age 25.1 ± 3.8 years, body mass 78.2 ± 15.3 kg, stature 1.81 ± 0.05 m	A biphasic 50-Hz pulse for 340 µs at 110% of the M-wave amplitude was administered during a 3-s tetanic stimulation with a 10-min rest before a fatiguing tetanic pulse for 120 s at 35 Hz was delivered to the GM.	High ICC values between the MMG and force parameters was obtained at different experimental sessions on different days.
Remark: The correlation between $R-MMG_{PP}$ and force confirm the effect of mechanisms of muscle fatigue that modify the extent of velocity and force relaxation. **Future work:** Full relaxation of the muscle under voluntary dynamic and isometric contractions should be investigated.					

Study 6: Analysis of the use of TMG and PMT to evaluate peripheral fatigue-induced alterations in mechanical and contractile properties.					
(Macgregor *et al.*, 2016)	ES: (5 cm^2, Axelgaard, USA); Contractile properties detection: TMG (BMC Ltd., Ljubljana, Slovenia)	GM	21 HV male subjects, age (means ± SDs) 21.3 ± 3.4 years, height 182.0 ± 6.1 cm, mass 79.5 ± 10.0 kg	1-ms pulse; amplitude of 20 mA, 10-mA increase to evoke Dm. An inter-pulse rest of 10 s was used to lower both fatigue and potentiation. The fatigue protocol was 15 pulses (1 every 100 ms) at approximately 110 mA over 5 min.	PMT from the plantar-flexor increased, and the TMG Dm decreased, which confirmed muscle stiffness after fatigue.
Remark: A decrease in the TMG Dm is not associated with Vc, but the results are limited to healthy individuals and cannot be applied to non-superficial muscles. **Future work:** Future verification of fatigue changes in various cohorts should be performed.					
Study 7: Prediction of the muscle fatigue in SCI patients using SVM.					
(Naeem *et al.*, 2019)	ES: RehaTrode (HASOMED, Germany); MMG: accelerometer (Sonostics BPS-IIVMG transducers; 20–200 Hz, 30 V/g, 10 g)	VL, RF, and VM	5 SCI patients classified as Class A and B according to ASIAIS	30-min FES cycling at 120 mA, 30 Hz, biphasic, pulse width of 400 ± 400 µs. The MFCC and RMS MMGs were trained and tested based on SVM.	Contractions correctly identified as non-fatigued and fatigued had higher MFCC compared with RMS values.
Remark: Both MFCC and RMS showed that fatigued muscle contractions overlapped with non-fatigued muscle contractions, which resulted in insufficient prediction. **Future work**: 1. Multiple experimental trials and analyses of the effects of the window size of MMG signals should be performed to improve the accuracy of the SVM classifier. 2. The nature of MMG signals that influence physiological properties and the physical environment should be investigated.					

Study 8: Assessment of fatigue based on MMG and torque responses.					
(Islam *et al.*, 2018)	ES: Two 9-cm×15-cm self-adhesive electrode (RehaTrode, HASOMED, Germany); MMG: (Sonostics VMG BPS II Transducer, frequency = 20–200 Hz, sensitivity = 50 V/g)	VL, VM and RF	5 male and 1 female subjects with complete chronic SCI	30 Hz, 400-µs pulse width, 90-120 mA to the quadriceps; 30 Hz, 60-120 mA, 300 µs was used to elicit FES-leg cycling exercise from the quadriceps; and 58-90 mA was applied to the hamstrings for 30 min.	The MMG MPF, MMGrms and FES-cycle time altered similarly to the epT during pre- and post- fatigue in a 2-day test.
Remark: The high fatigability of RF might lead to limited FES-cycling exercises in SCI subjects. **Future work:** The reliability of muscle fatigue assessment during FES-cycling in SCI patients should be further investigated.					
Study 9: Quantification of fatigue under repeated functional electrical excitation.					
(Jo *et al.*, 2018)	MMG measurement device: LIS311, STMicroelectronics, USA	TA	21 healthy male subjects, age 24.0 ± 2.0 years, height 174.1 ± 6.9 cm, weight 75.3 ± 13.2 kg	60 Hz, 240 µs, relaxation times of 0.5 s, 2.0 s, 0.5 s, and 1.0 s. MMG signals were collected for 30 min. During MVC and ES, the torque was measured offline using a dynamometer.	During muscle fatigue, the MMGpp, convex-hull volume, and convex-hull area linearly decreased with decrease in the mean and median frequencies.
Remark: The Lempel-Ziv symbolization technique exhibited the best performance for complex MMG feature reduction. **Future work:** 1. Based on Lempel-Ziv symbolization, further studies should address the required threshold for individuals under FES. 2. Repeated evoked fatigue was under isometric conditions, and isokinetic and/or isotonic conditions should be investigated.					
Study 10: Analysis of the mechanical fatiguing phenomenon that develops during ES in sport training or rehabilitation protocols.					
(Gobbo *et al.*, 2006)	**MMG:** ADXL202JE (Analogue Devices, Inc., Norwood, MA, USA); **EMG: s**ilver bar (diameter = 1 mm, length = 5 mm, inter-electrode = 10 mm); **Force**: load cell (Interface, model SM-100N, operation range = 0 and 100 N)	BB and VL	10 healthy subjects, age 20-50 years	6 potentiation pulses of 100 Hz with a rest of 1 s followed by a fatigue protocol of 50 Hz for 2 s and 2 Hz for 25 s. Normalized MMG and pT were linearly used for fatigue evaluation.	The torque and MMG decreased linearly from 100% of their initial values to 50% and 60% for the BB and to 43% and 47% for the VL, respectively.
Remark: Accurate screening of muscle mechanical fatigue should eradicate muscle tendon unit insertion and joints. **Future work:** MMG need further validation for tracking muscle mechanical fatigue, minimal challenging talk measures such as during electrically stimulated training or rehabilitation sessions.					

Table 2.5: Studies of fatigue and muscle physiology

Study 11: Relationship between temporal and spectral MMG features during fatiguing FES.					
Author(s)	**Sensor and electrode type**	**Electrode site**	**Dataset**	**Methodology**	Results and discussion
(Krueger *et al.*, 2016)	MMG: Freescale MMA7260QMEM triaxial accelerometer, sensitivity = 800 mV/G at 1.5 g	RF and VL	10 HV subjects, age 28.30 ± 6.58 years 10 SCIV subjects, age 32.06 ± 9.68 years	A single pulse at 1 kHz based on a 15% duty cycle was delivered with a rest of 2 to 5 min, and the maximum ES was determined based on the voltage required to vary the knee angle from approximately 90º to 40º.	Both the HV and SCI analyses yielded correlation coefficients of -12 up to -0.82.
Remark: The negative correlation between MMG_{RMS} and MMG_{MF} justify their divergence due to fatigue and motor neuron adaptation. **Future work:** Strategies for differentiating the timing among muscle fibre events during the FES process should be investigated.					
Study 12: Analysis of electrical and mechanical behaviours of stimulated pre-fatigued muscles.					
(Esposito *et al.*, 2009)	EMG: silver bars (diameter = 1 mm, length = 10 mm, inter-electrode = 10 mm); MMG: accelerometer (model ADXL202JE, Analogue Devices, Norwood, MA, USA); Force: load cell (model #SM-200 N, Interface, UK; operation range = 0 and 200 N)	GM	11 healthy male subjects, age 21 ± 2 years, body mass 75 ± 4 kg, stature 1.79 ± 0.06 m	A set of three 50-Hz, 10-100-mA, 307-µs pulses lasting 5 s with a 1-min rest between contractions was delivered before and after the fatiguing protocol (35 Hz for 120 s) and stretching manoeuvres (elongation up to 45 s with 15-s rest periods).	EMG, MMG and force features decreased and recovered after a 420-s rest period. A stretching protocol reduced the MMG and force signals.
Remark: Passive stretching remains questionable during a cooldown routine. **Future work:** Studies on passive muscle tendon units should help verify the force reduction after stretching.					

Study 13: Evaluation of the features of human muscle and mechanomyography from interpolated twitch methods.					
(Ohta *et al.*, 2009)	**MMG:** uniaxial accelerometer (9-mm square, thickness = 4.5 mm, mass = 0.75 g, sensitivity = 500 mV/g where g = 9.8 m/s^2; MP110-10-101, MediSens INS, Japan)	GM	12 male subjects, age 27 ± 2 years, height 0.5 ± 5.2 cm, weight 68.5 ± 9.7 kg	The plantar flexion force was measured at 20%, 40%, 60%, 80% and 100% followed by a supramaximal 1-ms stimulus to the twitch resting torque. The superimposed twitch amplitude, MMG amplitude and ultrasonic images at each force level were recorded.	The superimposed MMG amplitude and the extent of fascicle shortening with increasing intensities showed similar patterns.
Remark: Superimposed MMG might strongly mirror changes in the muscle architecture rather than the twitch amplitude. **Future work**: The degree of slack in the muscle–tendon complex may be estimated using the interpolated twitch methods with ultrasonography, or indirectly through its combination with MMG during low-level voluntary contractions.					
Study 14: Analysis of passive stretching on the electromechanical properties of muscles.					
(Cè *et al.*, 2008)	**EMG**: silver bar electrodes (diameter = 1 mm, length = 10 mm, inter-electrode distance = 10 mm); **MMG**: one accelerometer (ADXL202JE, Analogue Devices, Norwood, MA, USA); **Force:** load cell (model SM-200 N, Interface, UK; operation range = 0 and 200 N)	GM	12 healthy male subjects, age (means ± standard errors) 23 ± 1 years, body mass 76 ± 5 kg, stature 1.79 ± 0.005 m	Six electrical stimulations with a rest period of 5 s between stimulations. The force signal was induced by two impulses of 100 Hz for 307 μs during a 1-s period. The stretching signals during five manoeuvres lasting 45 s with a 15-s rest were obtained.	Acute passive stretching altered the mechanical but not the electrical properties.
Remark: Attention should be paid to the use of MMG to examine stretch-induced changes in the mechanical properties of skeletal muscles. **Future work:** Future study using NMES should assess the influence of different stretching protocols on the relationship between MMG signals and muscle force to enhance MMG's reliability on muscle mechanical properties.					

Table 2.6: Use of MMG for studying endurance and fatigue

Study 1: Analysis of torque and MMG fluctuations at various joint angles.					
Author(s)	**Sensor and electrode type**	**Electrode site**	**Dataset**	**Methodology**	**Results and discussion**
(Mccully *et al.*, 2019)	Triaxal accelerometer-based MMG sensor (WAX3, Axivity, Newcastle upon Tyne, UK)	Erector spinae of the forearm and wrist flexors	5 male and 3 female subjects, age 22.9 ± 2 years, height 1.8 ± 0.1 m, weight 69.8 ± 14.9 kg	Pulses of 25 to 35 mA at pulse durations/intervals of 200/50 µs were delivered, and the muscle twitch contraction was measured. The endurance protocol consisted of 2 Hz, 4 Hz, and 6 Hz (3 min each) with 5 s of no stimulation between each stage.	The EI values were reasonably reproducible, particularly those obtained with the 2- and 4-Hz stimulations.
Remark: In young healthy individuals, the erector spinae muscle has a lower endurance index than the leg muscles. **Future work:** The experiment was conducted on young healthy subjects; thus, the application of the system for evaluating lower back pain in the healthy population should be investigated.					
Study 2: Analysis of the effect of exercise on endurance.					
(Willingham *et al.*, 2018)	Accelerometer-based MMG sensor	GM	56-year-old female with muscle sclerosis	A 3-min, 2-, 4- and 6-Hz stimulation signal was applied, and the endurance index was determined as the percentage of the acceleration at the last stage of the stimulation frequency relative to the peak accelerometer records.	The walking endurance and oxidative capacity were improved.
Remark: These finding address the complex relationship between muscle strength, endurance, and walking function in MS. **Future work:** 1. The effect of voluntary exercises on muscle plasticity and the role of muscle oxidative capacity on assisting individuals with MS should be evaluated. 2. The use of a large sample size for examining the role of muscle plasticity to improve the walking function in people with MS should be investigated.					

Study 3: Evaluation of rider time and virtual distance in SCI.					
(Decker *et al.*, 2010)	ES: two self-adhesive surface electrodes (oval, 2” × 4”); MMG: accelerometers (Entran EGAS, weight = 1 g, 2–150 Hz, gain of 25)	VM, RF and VL	12 SCI subjects, mean age 37 years, height 1.8 m, mass 80.6 kg	An electrical stimulation of 50 Hz for 500 µs was increased to a current of 140 mA to maintain a cadence of 32 RPM over 0.4 s and applied every 1.88s.	An improved FES cycling alternated the activity of synergistic muscles in SCI, and different RMS values of MMG signals were obtained from all the muscles.
Remark: The MMG amplitude decreased due to muscle fatigue and the virtual distance, and both the stimulation and co-activation protocols yielded the same mechanical output.					
Future work: The use of improved stimulation techniques to evaluate improvements during a longer training practice without an external rider should be evaluated.					
Study 4: Analysis of endurance and feelings of fatigue in FRDA.					
(Connor *et al.*, 2016)	MMG: tri-axial accelerometer (WAX-9; Axivity, UK); ES: electrodes (5.08 cm by 10.16 cm, Pro Advantage by NDC)	Forearm flexor	10 healthy subjects, 16 FRDA subjects	The forearm flexor muscles were stimulated with 3 min of ES at 2 Hz, 4 Hz, and 6 Hz with a 5-s rest between stages.	A correlation was found among the mitochondrial capacity, disease severity and muscle-specific endurance.
Remark: People affected by FRDA exhibit lower forearm muscle endurance than ABs.					
Future work: MMG and NIRS measurement methods are correlated with disease severity, and this correlation should be further investigated.					

2.5.2 Force assessment

As presented in Table 2.7, four studies (Esposito et al., 2011a ;Esposito et al., 2011b;Kimura et al., 2003;Yung et al., 2012) have been determined to examine the influence of muscle conditions on force and MMG recorded under NMES. One of these studies (Kimura *et al.*, 2003) has attempted to determine the effect of temperature on contractile parameters using temporal and spectral features of MMG signals. After electrical intensity was delivered to the GM and SOL muscles, the force signals and MMG responses were examined under a controlled temperature. The authors of this study then reported a decrease in the maximum peak force development and relaxation under cooling conditions. In contrast, the CT and ½Tr increased under hypothermia. Further, an increase in M-waves was also noted, which justifies the decreases in the muscle conduction velocity. These findings encourage the use of MMG for screening muscular contractile behaviors under varying physiological circumstances. The use of MMG-, EMG-, and force-based approaches to evaluate the time course of stretching-induced changes in the mechanical and viscoelastic properties of MTU was examined in (Esposito et al., 2011a; Esposito et al., 2011b). The findings ob(Esposito *et al.*, 2011a)tudies (Esposito *et al.*, 2011a) revealed that an increase in the EMD followed a reduction in pF . The time delay between EMG and MMG recovered to its initial value within 15 min, whereas the delay between MMG and force value was maintained for 2 h. These findings only confirmed the effect of stretching and encouraged the use of MMG, EMG, and force as indicators of the recovery of muscle properties after the induction of mechanical stress on the MTU viscoelastic properties. On the one hand, pF and MMG PP did not exhibit recovery, and on the other hand, the short recovery observed in MMG RMS indicated a recovery in the viscoelastic properties of parallel components after a short period (Esposito *et al.*, 2011b). Biomechanical and physiological responses were

also used to evaluate the slowing of fatigue due to changes induced by occupational mechanical exposure. Using various force amplitudes, (Esposito *et al.*, 2011b) applied electrical stimulation quantities to the triceps brachii (TB) at 15% MVC to elicit LFF. Therefore, the subject performed MVC for 5 s, and the force was recorded for 3 s. The authors then concluded that (i) local fatigue might be reduced in individuals performing low-load tasks and (ii) muscle rest does not exert more marked effects than those predicted by variations in the force amplitude. These findings imply that changes in mechanical action with or without rest delay can reduce the rate of fatigue development compared with the development observed under isometric, isotonic, and sustained conditions. Therefore, it was suggested that muscle exposure to time-varying forces might reduce the degree of local fatigue during low-load tasks. The observations described in this review highlighted the relationship of muscle conditions, force, and daily tasks using MMG through NMES. Hence, muscles screening should take into consideration physiological conditions and daily occupational exposure circumstances.

Table 2.7: Overview of studies of force and MMG

Author	Sensor and electrode type	Electrode site	Dataset	Methodology	Results and discussion
Study 1: Analysis of the effect of temperature on MMG and the force response.					
(Kimura *et al.*, 2003)	EMG: Ag-AgCl (diameter = 8 mm, interelectrode distance = 35 mm); MMG: microphone sensor (Daia Medical, Tokyo, Japan; diameter = 10 mm, mass = 5 g); Force: (model LU-00KSB34D, Kyowa, Tokyo, Japan)	SOL and MG	8 healthy male subjects, age (means ± SEs) 23.3 ± 0.5 years, height 173.6 ± 2.7 cm, body mass 71.1 ± 4.6 kg	At temperatures of 34, 15, 20 and 25ºC, a 10-Hz stimulation for 8 s with a 30-s rest between trials was delivered.	Under cooling conditions, the CT and ½T_r increased, and the maximum peak force development (dF/dt) and relaxation (RdF/dt) decreased; in addition, a low RMS of the force fluctuations and low MG and SOL MMG amplitudes were obtained.
Remark: MMG can be used to study the muscle contractile properties under a wide range of physiological conditions. **Future work:** The combined effects of temperature and other physiological factors, such as fatigue or hydration, on MMG and force characteristics should be assesses to enhance the clinical applicability of MMG in monitoring muscle function under diverse conditions.					
Study 2: Analysis of the effect of changes in contractile and viscoelastic properties due to EMD.					
(Esposito *et al.*, 2011a)	MMG: accelerometer (model ADXL202JE, Analogue Devices, Norwood, MA, USA); EMG: four silver bar electrodes; Force: (model SM-200 N, Interface, UK; operation range = 0 and 200 N)	MG	16 healthy male subjects, age 24 years, body mass 75 ± 2 kg, stature 179 ± 2 cm	A supramaximal stimulation followed by a rest time of 10 min was delivered while the ankle was positioned at 20º. Before and after stretching, a set of three tetanic stimulations was delivered and followed by 15 min to 2h s of rest.	During recovery, the delay between EMG-MMG returned to pre-stretching values within 900 s, and Δt MMG-F remain lengthened for 7200 s.
Remark: Significant lengthening of the EMD was observed, possibly due to changes in the MTU stiffness. **Future work:** The involvement of parallel and series elastic components in the lengthening of Δt MMG-F, sites and duration of the MTU deformation after stretching should be examined.					

Study 3: Analysis of the use of MMG, EMG and force approaches to evaluate the time course of stretching-induced changes in mechanical and viscoelastic properties of MTUs.					
(Esposito *et al.*, 2011b)	MMG: mono-directional accelerometer (model ADXL202JE, Analogue Devices, Norwood, MA, USA); EMG: three Ag-AgCl electrodes	MG	11 healthy male subjects, age (means ± SDs) 22 ± 1 years, body mass 77 ± 5 kg, stature 1.78 ± 0.05 m	Stimulation with an amplitude of 10-100 mA, a pulse duration of 307 µA, and lasting for 5 s to 1 min at 50 Hz was followed by 110% supramaximal stimulation and rest for 600 s. A tetanic stimulation was delivered every 5 s for 15 min and followed by 2 h of rest.	The MMG-RMS recovered to the pre-stretching values, and the MMG-PP and P^F values remained low. No difference in the EMG response was found between the two experiments ($p > 0.05$).
Remark: No significant differences in the control parameters for the EMG, MMG and force features were found during the stimulation sets and during the 2-h recovery period. **Future work:** The rule of transverse MTUs based on the MMG amplitude should be studied.					
Study 4: Analysis of the effects of the amplitudes in the force variation between force and local fatigue using biomechanics and physiological measures.					
(Yung *et al.*, 2012)	ES: grass model S48; EMG: bipolar surface electrodes (Ag– AgCl electrodes, Ambu Blue Sensor N, Denmark); MMG: (Bruel and Kjaer 4507 ± 70 g)	TB	15 healthy male subjects, age 24 ± 4 years, mean height 177.7 ± 4.9 cm, weight 75.8 ± 8.7 kg	EMG, MMG, and blood flow velocity recordings of the triceps were collected at 2-min intervals during supramaximal fatiguing stimulation (20 and 100 Hz, pulse duration of 50 µs and train duration of 1 s) and at baseline. Test contraction at 15% of the force was exerted for 12 s.	Changes in mechanical action with or without rest delayed and reduced the rate of fatigue development compared with those observed under isometric, isotonic and sustained conditions
Remark: Force variation at different amplitudes might yield slower fatigue responses under a set time course than those observed during sustained low-level contractions. **Future work:** Exploration of the use of NMES to simulate time-varying force patterns in low-load occupational tasks, assessing its potential to reduce fatigue and enhance muscle recovery compared to sustained or static stimulation protocols.					

2.5.3 Muscle stiffness assessment

Using MMG and NMES, six studies (Uchiyama and Tomoshige, 2017; Longo et al., 2016; Matsue, Yuto, 2000; Chiyama and Aito, 2018;,;Ukawa and Chiyama, 2016).Uchiyama et al., 2015;Ukawa and Chiyama, 2016) in Table 2.8 have been identified to examine muscle stiffness. One of these studies (Uchiyama *et al.*, 2015) has utilized evoked MMG signals from voluntary MMG and walking acceleration in order to estimate stiffness. Combined with the undamped natural frequency, the mass of the VL estimated as 0.99% of the subject's weight was also used in an attempt to estimate stiffness. The result was then compared with the stiffness estimated using the identification technique, wherein muscle stiffness was found to exhibit a prior relationship with both workload and power.

Furthermore, the analysis on the synchronous averaging of evoked MMGs in a previous study (Uchiyama and Tomoshige, 2017) was performed through identifying both longitudinal and transverse muscle stiffness from MMG signals obtained via electrical activation of the peroneal nerve. A capacitor microphone and a differential circuit were used for recording purposes. The stiffness was measured from a natural frequency, assuming that the mass of the TA muscle equals 0.2% of the participant's weight. In another study (Ukawa and Chiyama, 2016), the singular value decomposition (SVD) was used in determining the transfer function from stimulated to evoked MMG signals. The velocity MMG yielded two natural frequency components denoted as f1 and f2: f1 mirrored the longitudinal stiffness, which was approximated to the values in the displacement and acceleration MMG systems, and f2 was determined from the velocity MMG and was found to be similar to the natural frequency of the acceleration MMG system. The resulting value was then regarded as the transverse muscle stiffness but was not estimated from MMG signals. The displacement and

acceleration MMG yielded three natural frequencies, which were denoted as f1, f2, and f3, and no significant difference was obtained between the natural frequencies from velocity and displacement MMG.

In the same study (Ukawa and Chiyama, 2016), electrical stimuli were transcutaneously delivered to the VL muscle while the participants were asked to pedal an ergometer. The mass of the muscle and the coefficient of the transfer function estimated using SVD, which was performed as described in another previous study (Uchiyama and Tomoshige, 2017) , were used to estimate the muscle stiffness and viscous characteristics under low power output (Chiyama and Aito, 2018). The authors then observed a progressive increase in muscle stiffness as the pedal rate also increased. The stiffness was approximated at $p < 0.025$, with a decision coefficient of 0.984. However, the viscous coefficient was determined to not increase. A possible reason for these findings is the rubbing between active and inactive muscle fibers due to the force exerted in direct proportion to the velocity. Clearly, this study has examined the muscle activity using EMG and found that EMG RMS showed changes at different pedaling rates in various subjects. In contrast, similar mean EMG RMS values were found at 40, 60, and 80 rpm. Thus, future studies should elucidate the mechanism underlying the associations among muscle stiffness, viscous coefficients, and muscle function.

More recently, another study (Matsue and Yuto, 2000) has examined the stiffness obtained based on the GM dependency on gait speed. During treadmill training, stimulated and nonstimulated MMGs were recorded from the GM, and the evoked MMG signals were then used to identify the stiffness index based on the corresponding natural frequencies. The researchers reported that the frequencies and thus the stiffness increased as the gait speed increases.

The authors of a previous study (Cè *et al.*, 2008) have also used changes in the joint angle torque to estimate stiffness. The responses from electrical excitation of the GM, namely, the EMG, MMG, and torque, were recorded to estimate the muscle stiffness before and after static stretching. After dividing the information into electrochemical and mechanical components, the offline R−DelayTOT was determined based on the force, EMG, and MMG signals recorded at PT . A decrease in the main electromechanical component was then observed as the joint angle increased before and after static stretching. This study has also determined that during muscle relaxation, an increased dorsiflexion angle could be attributed to joint stiffness rather than the electrochemical process.

Authors of this study have further demonstrated that the anthropometric features and geometry of the limbs can contribute to joint stiffness and found that the frequency components increased as stiffness increases (Ukawa and Chiyama, 2016), even though the so-called viscous coefficient did not seem to vary. In addition, the changes in the joint angle torque after stretching tasks have exhibited a progressive decrease in electromechanical delay components with increases in the joint angle at pT (Longo *et al.*, 2016). As has been discussed in a previous study (Jarocka *et al.*, 2011), the effects of inactive and active muscles on the viscous coefficient (Uchiyama *et al.*, 2015), subcutaneous tissue (Matsue and Yuto, 2000), MTU stiffness, and joint angles should be considered in further studies (Longo *et al.*, 2014). It can be concluded that the anthropometric, electrochemical, and mechanical components, daily physical tasks, and geometry of the muscles are of importance in terms of estimating muscle stiffness using myographic signals.

Table 2.8: The use of ES and MMG on the assessment of muscle stiffness

Study 1: Analysis of muscle stiffness at various workloads, cadences, and power levels.					
Author(s)	**Sensor and electrode type**	**Electrode site**	**Dataset**	**Methodology**	**Results and discussion**
(Uchiyama *et al.*, 2015)	MMG: capacitor microphone (MXE-4758; Primo, Tokyo, Japan); ES: 10-mm diameter Ag-AgCl (Vitrode J-150; Nihon Kohden)	VL	8 able subjects, age 21–24 years	The subjects pedalled an electrically braked ergometer set to 47 W. Stimulation pulses were delivered at 30º with 3-, 2- and 1.5-s inter-pulse intervals and a constant power of 40, 60, and 80, respectively.	With the knee angle set to 80º, the muscle stiffness was in direct proportion to the workload and power.
Remark: The muscle stiffness progressively increased with increases in the pedalling rate. **Future work:** The effect of non-active and active muscles on the viscous coefficient and the muscle response after the application of various phases per cycle should be investigated.					
Study 2: Estimation of the muscle stiffness from evoked MMG.					
(Uchiyama and Tomoshige, 2017)	ES: Ag-AgCl electrodes (F-150S; Nihon Kohden); DMMG: capacitor microphone (MX-E4758; Primo, Tokyo, Japan; weight = 0.78 kg, sensitivity = -43 ± 3 dB at 1 kHz, gain = 0.5 to 4000 Hz); AMMG: (MP-110-10-101, MediSens, Saitama, Japan)	TA	7 healthy male subjects, aged 22-24 years	A monopolar pulse with a 500-µs width and an inter-pulse interval of 1 s was applied in each trial and repeated five times.	No significance difference was found between the natural frequencies from the velocity and displacement obtained by MMG.
Remark: The velocity measured with a differential circuit reached a steady state value in a short time, and motion is thus recommended. **Future work:** The transverse muscle stiffness should be further estimated.					

Study 3: Analysis of muscle strength.					
(Chiyama and Aito, 2018)	MMGs: capacitor microphone (MX-E4758; Primo, Tokyo, Japan); ES: Ag-AgCl surface electrodes (F-150S, Nihon Kohen)	GM	8 healthy male subjects, age 22-24 years	The subject was asked to pedal at speed of 3 km/h with a gait cycle of 1.8, 1.5, 1.2, and 1.1 s, and a monopolar rectangular pulse width of 500 µs and an amplitude of 20-mA was applied.	A progressive increase in muscle stiffness was detected with increases in the pedalling rate.
Remark: The stable viscous coefficient was attributed to the friction effect from active and non-active fibres. **Future work:** The cause of the stable viscous coefficients should be investigated.					
Study 4: Analysis of the stiffness of the gastrocnemius muscle and the waking speed.					
(Matsue, Yuto, 2000)	ES: Ag-AgCl (F-150S, Nihon Kohden); MMG: capacitor microphone (MX-E4758; Primo, Tokyo, Japan)	GM	8 healthy male subjects, age 22-24 years	Stimulation for 500 µs with a 20-mA amplitude was delivered to the GM while the subject walked on a treadmill at 2, 3,4, 5 km/h with a gait cycle of 1.8, 1.5, 1.2, and 1.1 s.	The stiffness was indicated by an increase in the natural frequencies f1 and f2, which increased with increases in the gait speed.
Remark: A constant natural frequency f3 is likely caused by subcutaneous tissue. **Future work:** The natural frequency corresponding to the soleus muscle should be further studied, and the natural frequency of GM should be clarified.					
Study 5: Analysis of the effect of static stretching (SS) on joint angle stiffness.					
(Longo *et al.*, 2016)	EMG: silver bars (model ELSCH004, diameter = 1 mm, length = 10 mm, inter-electrode distance = 10 mm, OT Bioelettronica, Turin, Italy); MMG: accelerometer (model ADXL202JE, Analogue Devices, Norwood, MA, USA); Force: load cell (model SM-2000 N, Interface, UK; 0-2000 N)	GM and GL	19 healthy male subjects, age (mean ± SD) 24 ± 3 years, body mass 76.4 ± 8.9 kg, stature 1.78 ± 0.09 m	MMG, EMG and force signals were recorded before and after SS. The joint stiffness and the force from plantar flexors were measured after a supramaximal +10% tetanic stimulation (3 s, 50 Hz, 10-100 mA, and 304 µs) applied at 0°, 10° and 20°.	The SS and joint stiffness increased with increases in the joint angle.
Remark: The increase in dorsiflexion with $R - Delay_{TOT}$ might be due to joint stiffness. **Future work:** Investigation of variations in joint angle and stimulation parameters on MMG and force responses across populations					

2.5.4 Torque assessment

As presented in Table 2.9, nine studies (Miyamoto and Oda, 2005; Orizio et al., 2008) (Orizio et al., 2013; Koren et al., 2015;Ibitoye, Hamzaid, Abdul Wahab, et al., 2016 Oza et al., 2017;chiyama and Sakai, 2013 ; Dzulkifli et al., 2018; Shima et al., 2007) have reported that torque is mirrored by the MMG features from electrically contracted muscles. The studies by (Miyamoto and Oda, 2005) used a combination of MMG and torque signals in determining the dependency of the contractile properties of a muscle on its length. The BB was electrically stimulated using 10- and 30-Hz fused and unfused tetanic stimulation, and then, evoked flexion torque was measured at six joint angles ranging from 75° to 150° at 15° increments. The RMS values of both the torque and MMG signals obtained with different stimulation frequencies confirmed the reliability of MMG for evaluating the contractile properties of muscles. In addition, the findings have demonstrated that the torque fluctuates with variations in the muscle length (Table 2.10).

Some researchers (Shima *et al.*, 2007) have examined the effects of aging on muscles through a comparison of MMG and EMG features with torque's profiles. The muscles of old and young individuals were subjected to electrical stimulation before and after 10 s and then less than 100% MVC, wherein both MMG and PT were observed to have been significantly increased, but the M-waves remained steady. However, no effect of aging was detected. During voluntary contraction, the MMG and EMG profiles in young and old men exhibited similar shapes, which indicated that the electrical and mechanical properties of voluntary or artificial stimulation of muscles exhibited different behaviors at different ages.

Many studies have used a combination of MMG and torque signals in an effort to characterize muscle mechanics. Using short and long stimulation pulses, the detected MMG and torque signals yielded two transfer functions, and these functions were analyzed to

characterize the TA muscle joints. After stimulation intensity was delivered, the torque was determined offline based on the tension recorded from the foot and ankle lever arm. Therefore, the in vivo mechanical properties of muscle joints obtained using short stimulation protocols were obtained from MMG and torque signals (Orizio *et al.*, 2008). An analysis of the torque, MMG, and EMG signals obtained under NMES with triangular trains with varying frequencies and amplitudes has yielded the muscle input/output relationship of the TA under static contraction and thus showed the module of muscle force production (Orizio *et al.*, 2013). The relationship between the stimulation frequencies yielded the average torque, MMG, and EMG signals for each 5% of the Δ frequency range from 2 Hz (0%) to 35 Hz (100%). As per experimental results, an additional torque corresponds to an increase in the extra-muscle displacement (MMG) during down-going ramp (DGR) rather than upgoing ramp (UGR) for both frequency and amplitude triangles. In addition, the authors suggest that stimulation parameters close to physiological quantities indicate the influence of intrinsic muscle factors on additional torque and MMG signals.

However, the findings obtained in a previous study (Koren *et al.*, 2015) have been deemed controversial. The longitudinal torque and transverse TMG have yielded differences in the contractile parameters of the VL. Therefore, these findings indicate that the TMG mechanical responses can reflect the intrinsic contractile parameters of skeletal muscles.

A study conducted a year later (Ibitoye, Hamzaid, Abdul Wahab, *et al.*, 2016) used computational intelligence to solve the complex mathematical computation derived in the above-mentioned studies (Koren *et al.*, 2015).

Using MMG PP, MMG RMS, the knee angle, and the levels of NMES parameters, the SVR was trained to predict torque; then, the knee torque was in line with the dynamometer readings. The high correlation and reduced root mean square error only

confirmed the efficiency of the developed technique in terms of estimating the knee torque and the accuracy of the laboratory results. Similarly, the variability in the neurological function of SCI patients determined in this study (Ibitoye et al., 2016) was addressed using artificial intelligence, which was p(Dzulkifli *et al.*, 2018) study (Dzulkifli, Hamzaid, Glen M Davis, *et al.*, 2018). After delivering electrical impulses to the quadriceps muscle groups of three SCI subjects, the knee torque estimated using a dynamometer was significantly correlated with the ANN-predicted torque. Therefore, the authors highlight the usefulness of ANN for real-time torque estimation.

Thereafter, the methods were further validated in a later study (Oza *et al.*, 2017). Using increasing stimulation amplitudes, the peak-to-peak torque was obtained from an average of the 20 highest data points, and the M-wave, H-reflex, and MMG responses were also determined using the peak-to-peak amplitudes. Thus, the combination of M-waves and H-reflexes was proposed for estimation of the plantar flexion torque using Cybex 6000. The study then introduced the M + H parameter, which was strongly correlated with the twitch torque and MMG. Hence, the study was able to determine that MMG was not affected by stimulus artifacts and is thus recommended for estimating the maximal twitch torque. This pioneering work on NMES and mathematical models continues to guide research in the characterization of muscles, particularly small muscles. Using SVD, the transfer function between torque and MMG reported by a previous study (Uchiyama and Sakai, 2013) showed that the activity of small, thin, and parallel muscle fibers can be mathematically modelled through a combination of DMMG and AMMG. The studies support the use of muscle mechanics, anthropometry, and age difference for characterizing the muscle torque. ML (Ibitoye, Hamzaid, Abdul Wahab, et al., 2016; Dzulkifli et al., 2018) was also used and support the hypothesis that sophisticated signal processing need future MMG exploration.

Table 2.9: MMG and joint torque

Author(s)	Sensor and electrode type	Electrode site	Dataset	Methodology	Results and discussion
Study 1: Analysis of torque and MMG fluctuations at various joint angles.					
(Miyamoto and Oda, 2005)	Torque: strain gauge (model LURA-100NSA1, Kyowa Electronic Instruments, Japan); MMG: microphone sensor (QTEC, Japan; diameter = 8 mm, mass = 5 g)	BB	9 healthy male subjects, age (mean ± SE) 24.5 ± 1.1 years, height 171.3 ± 2.8 cm, weight 68.1 ± 2.6 kg	A 10 Hz, 5-s train at 30 Hz was applied at each angle to familiarize the subject with the pain induced by the tetanic stimulation. The elicited torque at 75, 90, 120, 135 and 150º was measured and was analysed based on recorded MMG signals. A 100-µs pulse duration was provided to ensure an increase in the muscle contraction with torque.	The MMG amplitude was correlated with the CT and the half-relaxation time and reflected the changes in torque relaxation observed with increases in the muscle length.
Remark: The correlation of the MMG amplitude with the half-relaxation and contraction times indicates that MMG is a valid tool for monitoring changes in the contraction features of skeletal muscle.					
Future work: MMG to be applied for the characterize the development of fusion and dynamic changes in muscle contractile properties across varied stimulation frequencies and intensities in both healthy and clinical populations.					
Study 2: Analysis of the effect of age and muscle mechanics.					
(Shima *et al.*, 2007)	MMG: 9-mm square with a thickness of 4.5 mm and a mass of 0.75 g (MP110-10-101; MEDiSENS, Tokyo, Japan; sensitivity = 500 mV/g); EMG: (1.5 - 1 cm; Kendall-LTP, Chicopee, MA, USA)	TA	10 young male subjects, age 27.1 ± 3.8 years (range 21–33 years), height 174.2 ± 7.7 cm, weight 78.7 ±7.8 kg; 10 old male subjects, age 79.0 ± 2.5 years (range 75–83 years), height 171.4 ±5.7 cm, weight 79.2 ± 10.2 kg	The M wave was detected after delivering a 400-V pulse with a width of 50 µs and a current intensity of 70-150 mA. The pT was assessed after a supramaximal twitch and a 30-60-s rest.	The electrical and mechanical features of muscles that are either electrically or voluntary induced are affected in different manners by ageing.
Remark: The MMG and EMG patterns presented similar shapes in young subjects and were altered in the old population.					
Future work: Assess MMG and EMG across muscles, contraction types and age to understand neuromuscular decline in aging					

Study 3: Analysis of muscle features during long and short stimulation protocols.					
(Orizio *et al.*, 2008)	MMG: laser-distance sensor (M5 L/20, MEL Mikroelektronik, Germany, range = ±10 mm, sensitivity = 1 V/mm, linearity = 0.6%, resolution < 6 µm, bandwidth = 0–10 kHz); EMG: two bar electrodes (1 cm × 1 mm × 1 mm); Force: load cell (Interface, model SM-100 N, operating range = 0 –100 N)	TA	14 healthy male subjects, age 20-35 years	12.5-s short duration pulses (0.4, 6.0, 1.0, 4.5, 1.8, 3.0, and 2.5 Hz) and 6-s pulses (0.4, 0.6, 0.8, 1.0, 1.2, 1.4, 1.6, 1.8, 2.0, 2.5, 3.0, 4.0, 5.0, and 6.0 Hz) with a 300-s rest between pulses to avoid fatigue.	A similar transfer function from the torque and laser-detected MMG signal resulted in a decline in the sinusoidal amplitude and a phase shift in the torque and MMG.
Remark: The torque and laser MMG recordings yielded similar transfer functions, which validates the use of MMG for screening the mechanical properties of muscle tendons units.					
Future work: Elicitation of the whole motor nerve can be used to investigate the shortening of non-active muscle fibres.					
Study 4: Model of human muscle using a triangular frequency and an amplitude train					
(Orizio *et al.*, 2013)	MMG: laser distance sensor (M5 L/20, MEL Mikroelektronik, Germany, range = ±10 mm, bandwidth = 0–10 kHz, linearity = 0.6%); EMG: pair of silver bar electrodes; Force: load cell (model SM-100N, Interface Inc, Scottsdale, AZ, USA; operation range = 0-100 N)	TA	10 healthy male subjects, age 23-35 years	Increase from 2 to 35 Hz over 7.5 s or decrease from 35 Hz to 2 Hz over 7.5 s; the amplitude was increased from V_{min} to V_{max} and decreased from V_{max} to V_{min}. The mean torque, MMG and EMG for each 5% in the Δ frequency range of 2 Hz (0%) to 35 (100%) Hz were used to determine the stimulation frequency and additional muscle torque.	Under DGR, the amplitude and frequency triangle are in line with the additional torque and muscle displacement.
Remark: Bypassing the CNS, the additional torque and MMG are induced by the intrinsic muscle property.					
Future work: The number of subjects needs to be increased to validate the EMG behaviours in DGR and UGR induced by a frequency triangle.					

Study 5: Analysis of contractile parameters from the TMG and the torque twitch response in human VL muscle.				
(Koren *et al.*, 2015)	TMG: displacement sensor (G40 digital-optical comparator, TMG-BM Ltd., Slovenia); Force: transducer (TSD121C, BIOPAC Systems Inc., USA)	VL	19 healthy male subjects, age 46.1 ± 17.8, body mass 78.4 ± 12.7 kg, height 1.74 ± 0.05 m, BMI 26.0 ± 4.2 kg/m^2	1-ms pulse current separated by 10 s from the motor threshold to the maximum stimulation current at incremental steps of 5 mA, with a maximum stimulation amplitude of 10 mA -100 mA.	Based on TMG, the force inter-method correlation was significant with Ts and Tr but not significant with other parameters.
Remark: TMG-measured contractile parameters are shorter during the contraction phase due to their dependence on intrinsic muscle properties.					
Future work: Future work should explore the relationship between TMG-derived parameters and muscle force across different contraction types and intensities to enhance the interpretation of TMG in clinical and athletic settings.					
Study 6: Prediction of NMES-evoked knee torque using SVR					
(Ibitoye, Hamzaid, Abdul Wahab, *et al.*, 2016)	ES: 9×15-cm^2 self-adhesive electrodes (Hasomed GmbH, D 39114, Magdeburg, Germany); MMG: accelerometer (Sonostics BPS-II VMG transducer, sensitivity = 30 V/g)	RF	8 healthy male subjects, age 23.4 ± 1.3 years, body mass 70.4 ± 5.8 kg, height 1.72 ± 0.05 m	Square-wave 30-Hz pulses with a 400-µs duration were applied; the current amplitude was increased from 20 mA to 80 mA over a duration of 48 h, and a recovery time of 10 min was established after each trial.	A high prediction accuracy with a coefficient of determination of $R^2 = 94\% - 89\%$ and a low RMSE of 9.48-12.95 was obtained.
Remark: The study was limited to healthy volunteers.					
Future work: The model should be examined with disabled subjects, and normal and fatigued knee extensors during standing or itinerant tasks should be classified.					

Study 7: Analysis of twitch torque and reliability of recruitment curves.					
(Oza *et al.*, 2017)	ES: self-adhering stimulating electrodes (1 × 1 cm); MMG: accelerometer (EGAS-FS-10-/VO5, Measurement Specialties Inc., Hampton, VA, USA)	Soleus	16 subjects, age 23.5 ± 1.9 years, body mass 71.1 ± 10.6 kg, height 173.4 ± 8.0 cm	A pulse (1 ms, 100-400 V, and 2-100 mA) was administered with increments of 0.5-2 mA to detect the maximum H-reflex and decreases in the H-reflex. Thereafter, an increment of 2-5 mA was applied to localize the plateau in the M-wave amplitude; a rest period of 3 to 5 s was applied between stimuli, and four to seven stimuli were included in each individual pulse.	A strong test-retest reliability with $p > 0.05$ was found over days. A low coefficient of variation for MMG_{max} with the maximal stimulation intensity and torque was found.
Remark: A new parameter, M+H, exhibited a strong correlation with the twitch torque and MMG. **Future works:** 1. The gross lateral movement of muscles under voluntary contractions should be investigated. 2. Comparisons of M-wave and H-reflex should be performed, and features related to the soleus and gastrocnemius muscles after treatment should be investigated.					
Study 8: System identification of muscle with parallel fibres.					
(Uchiyama and Sakai, 2013)	ES: Ag–AgCl surface electrodes (F-150S, Nihon Kohden, Tokyo); DMMG: capacitor microphone (MX-E4758, Primo, Tokyo); AMMG: MP-110-10-101 (MediSens, Saitama); Force: FlexForce A201-1 (Nitta, Osaka)	Abductor pollicis brevis	6 healthy male subjects, age 21-25 years	The median nerve was electrically stimulated with a 500-µs rectangular pulse at an interval of 1 s and a bandwidth of -3Db; the pulse was repeated 20 times.	Muscles with parallel fibres can be modelled by a 6^{th}-order model using system identification of DMMG and AMMG.
Remark: The abductor pollicis brevis presented a higher frequency than the tibialis anterior, which might be due to the anatomical structure. **Future work:** The effect of the anatomical properties of the tibialis anterior and abductor pollicis brevis on the natural frequency should be verified.					

Study 9: Prediction of the muscle torque using ANN					
(Dzulkifli, Hamzaid, Glen M Davis, et al., 2018)	Torque: dynamometer (Biodex Medical system Shirley, NY, USA); ES: 9×15-mm^2 self-adhesive electrodes; MMG: transducer (Sonostics BPS-II VMG, sensitivity = 30 V/g)	Right and left GM	8 SCI volunteers with ISNCSCI classes A and B, 3 for training and 5 for testing	30 Hz, 200-µs duration and 100-mA amplitude; the MMGrms, MMG ZC and torque were recorded with a knee angle of 30º	The ANN-based prediction using MMG and dynamometer recordings were close with a p-value of 0.33.
Remark: MMG-RMS- ZC showed higher prediction than RMS alone. **Future work:** Other MMG features and other ANN models should be investigated.					

2.5.4.1 Torque estimation models

MMG signals based torque estimation has been carried out using voluntary and electrically stimulated contraction. Relevant research applied various artificial intelligence-based regresion techniques such as statistical regression (polynomial regressions), ML and deep learning models (for example :Table 2.8). Furthermore, metaheureustic algorithms have been applied in machine learning optimization, thus imporved performance of machine learning models can be observed by tuning hyperparameters and features optimization by relevance and redundancy identification.

The initial part of section section 2.5.4 generalizes the torque meassurement techniques. The current continuation addresses machine learning models for torque estimation using both NMES and voluntary contraction and highlights metaheurestic approaches that have been used for both features and hyperparameter tuning and concludes by the highlights of considerations for selected hyperparameter tuning algorithm used in this study.

Table 2. 10: Torque\strength estimation using MMG parameters

Study 1: TQ estimation using extreme boost algorithm					
Author(s)	**Sensor**	**Muscle**	**Method**	**Model validation**	**Results and discussion**
(Xie *et al.*, 2020)	Adxl 335 accelerometer	Quadriceps femoris of 7 subjects	**AI model:** Extreme gradient boost model, quadratic polynomial model (Linear regression model). **Features:** 18 features (RMS, VAR, LOG RMS,difference absolute SD, ZC Reduced to 3 by permutation for performance evaluation. MPF, MNF,variance of the central frequency, frequency variance, 1st, 2nd snd 3rd spectrum moments, root mean square power spectrum, wavelet packet energy(time-frequency) **Metaheuristic algorithm:** NA	7 subjects per 1 group with a frequency of 1Hz used for training and 7 people, 8 groups at 0.5 Hz used for testing. T-test used to evaluate the performance of both models at different frequency, time and fatigue states.	No significance difference between the 2 models.
Remark: The improved estimation accuracy by the reduction of features by 3. **Future work:** Further analysis of features relevance and redundancy as well as the hyperparameters tuning should determine specific features and hyperparameters of the models.					

Study2: Knee flexion extension TQ estimation of the femoral muscles using arrays of MMG signals					
(Hondo and Tsuji, 2022)	ADXL 335 accelerometer	RF of 5 subjects	**AI model:** SVR(RBF-kernel) **Features:** RMS and PTP **Metaheuristic algorithm:** NA	R^2 of 70 % & 30 % 0.91 both tr+test.(4 channels) Validation: 4 channels vs 1 channel MMG, and 2 channels EMG.	Conventional single channel MMG gave R^2 of 0.46 and 0.44 and the 4 channels gave R^2 of 0.91. MMG are feasible counterpart to EMG
Remark: Multi-channel MMG dataset improved the SVR performance. **Future work:** Additional features, determination of their relevance and redundancy and hyperparameters tuning need to be evaluated for improvement of the model's performance					
Study3: TQ estimation from quadriceps using IGWO-SVR					
(Li et al., 2021)	ADXL 335 accelerometer	RF, VM, VL from 4 subjects	AI model: SVR **Features:** RMS, MAV, ZC, MPF, and SE (Sample entropy). **Metaheuristic algorithm:** IGWO	RMSE, MAPE, R (Corr. Coef.) were used to verify the accuracy and compare the IGWO-SVR model on BPNN, GRNN, SVR, GS-SVR, PSO-SVR, and GWO-SVR. 90% and 10 % of data were used for training and testing.	The introduction of IGWO-SVR improved MSE, MAPE, and R. The SVR along with IGWO becomes more reliable for MMG and force relationship.
Remark: The Knee joint strength estimation is essential baseline to guide the control of limb joint assistive equipment **Future work:** Motion angular velocity, body posture, other algorithms used for other muscles and application to the lower limb motion intentions is required.					

Study 4: Estimation of knee joint TQ using ICS-SVR					
(Z. Li et al., 2022)	ADXL 335 accelerometer	VL, VM, RF from 5 subjects	**AI model:** SVR **Features:** RMS, Kurtosis, SD, SSC, MAV, ZC, WL, WPE, MPF, MDF, Energy (WP1,2,34,5,6,7,8). Nonlinear dynamic feature (Lempel ziv zomplexity(LZC), SampEnt, ApEn, FuzzyEn, DistEn, box counting fractal dimension (FD), Lyapuno exponent (Lyap Exp) **Metaheuristic algorithm:** ICS algorithm	Performance based on particle swarm optimization (PSO), gray wolf optimization (GWO), ICS algorithm, and compared to classical machine learning (BPNN, ELM, CS-SVR).	ICS-SVR yielded R^2 of 0.9966. The proposed ICS algoritm showed improved R^2 , convergence rate, and convergence accuracy during model optimization.
Remark: Metaheuristic algorithm improved the accuracy, but ICS exhibited the highest improved accuracy. **Future work:** Further feature selectin, redundancy analysis and hyperparameter tuning need to be determined for further improvement.					
Study 5: Estimation of knee joint TQ from NMES-MMG					
(Ibitoye, Hamzaid, Abdul Wahab, *et al.*, 2016)	Sonostics BPS-II VMG transducer, sensitivity 30 V/g	RF	**AI model:** SVR **Features:** RMS, PTP **Metaheuristic algorithm:** Hybrid immune algorithm for hyperparameter combination	RMSE, R^2 and R	Model development on 7:3 ratio showed a high-test regression coefficient R^2 of 0.89 as well as a low RMSE.
Remark: NMES-MMG not previously investigated. A good performance was observed from RMS, PTP features alone. **Future work:** Additional features determination, and further metaheuristic algorithms are believed to improve the model's prescribe.					

Study6: Assessment of the association between NMES-MMG and TQ at different knee joint angle					
(Ibitoye, Hamzaid, Hasnan, *et al.*, 2016)	Sonostics BPS-II VMG transducer, sensitivity 30 V/g	RF	**AI model:** SVR **Features:** RMS, PTP **Metaheuristic algorithm: NA**	RMSE, R^2 The positive relationship between the NMES-MMG and torque	Moderate to hight reliability of MMG and TQ reveals the suitability of MMG to track mechanical changes in muscles.
Remark: The positive correlation between MMG and torque signals generated by NMES indicates that MMG could serve as a reliable indicator for assessing muscle torque or functional status. **Future work:** The relationship of joint angle on NMES-MMG and TQ should be further investigated.					
Study 7: TQ estimation using MMG signals for the development of Upper Extremity Exosuit					
(Shi et al., 2022)	IMU	Brachioradialis of 3 subjects	**Model:** RFR **Features**: RMS, MPF, SampleEn **Metaheuristic algorithm:** NA	RMSE, R^2.Model was trained and tested on 2 separate subjects. The model was validated on unseen dataset of the 3rd subject data.	Estimation results show the strength of the exosuit for upper limb control. Elimination of artefacts due to cable motion or cale driven system may reduce the artefacts.
Remark: A high R^2 was obtained when utilizing the biological data of trained Subject 1 and Subject 2. **Future work:** Training the model on multiple subjects may capture more variability to yield a robust model.					

Study 8: Estimation of knee Joint Force Using MMG and SVR-IGWO					
(Li et al., 2021)	ADXL 335	VM, VL, and RF 6 healthy subjects	**Model:** LSTM, BPNN, and SVR **Features:** RMS, kurtosis, SD, SSC, MAV, ZC, waveform length; MPF, MDF, WPE, energy of every frequency band (WP1, WP2, WP3, WP4, WP5, WP6, WP7, WP8), Lempel-Ziv Complexity (LSC), SampEn, ApEn, FuzzyEnt, distribution entropy (DistEn), box-counting fractal dimension (FD), and largest Lyapuno exponent (LyapExp) **Metaheuristic algorithm:** IGWO	NRMSE, MAPE, and R	SVR-IGWO 's test results fit the actual values well, and the performance metrics are highly noticeable than other methods tested here.
Remark: Using the IGWO-SVR may preserve the reliable method to investigate complex, nonlinear relationship between the MMG and TQ. **Future work:** 1. The use of a single muscle with less crosstalk and raining the network more time may improve the model's regression accuracy 2. Use of swarm intelligence metaheuristic algorithms are required to optimize the performance of machine learning, thus may improve accuracy of muscle force estimation.					

2.5.4.2 Anthropometry and torque estimation

Muscle strength can be determined by muscle activation and physiological factors. MMG signal has been utilized for the assessment of muscle stiffness and strength estimation and remained inaffected by the NMES, and physical milieu of electrode positioning. A cross spectrum investigation has shown that MMG is highly sensitive to difference in fiber type composition than EMG (T. W. Beck *et al.*, 2009). While neuromuscular pathology such as muscle weekness hinder the torque ouput, the use of NMES has shown positive relationship with torque during muscle streghthening (Son et al., 2014). Hence, the positive linear correlation of NMES parameters and amplitude of MMG with torque parameters in pathological subjects highlights the the potential of the use of MMG for torque estimation (Ibitoye, Hamzaid, Hasnan, *et al.*, 2016).

Muscle physiology also was examined per conditions of angle and twished stimulation, where the findings suggest MMG to be reliable to track the changes in muscle contraction properties and torque fluctuation during unfused contractions (Miyamoto and Oda, 2005). Also, the forearm posture was reported to change the middle upper arm circomference (MUAC) and the muscle fibers relocation underneath NMES electrodes. Hence, it is required to investigate the relationship between physiological manufestations occuring during muscle geometry, which also may provide further proxies on the anthropometric measurements as factors of torque estimation.

The increase in muscle strength along with muscle thickness induced by NMES training suggests that MMG signals from NMES are also best predictor of torque. This finding is inline with the outcomes of the study by Irsa, where MMG RMS and MUAC were positively correlated with the torque (Talib et al., 2021) observed a strong prediction of wrist flexion torque from anthropometric variables namely the length of lower arm (LLA) , length

of upper arm (LUA), the weight, the height, and arm circumferences using polynomial regression (Green and Gabriel, 2012). Despite the prediction capability, the stastistical regresison techniques can be challenging especially in multi degrees of freedom. Hence, artificial intelligence applied to torque estimation using anatomical segments of ankle, knee, hip, neck joint, , lower leg, upper leg, trunc, and head segments showed improved estimation (Serbest *et al.*, 2023). Studies also used the ankle joint angle, angular velocity, acceleration, walking speed, body height and mass, foot and junk length, gender and age to predict ankle joint torque, which was further fused with EMG of the TA and the GL to develop LSTM and CNN (Moreira et al., 2021). The results show that the body size is appropriate to be used for joint torque estimation (Table 2.11).

Table 2.11: Studies on torque estimation using anthropometric variables

Study 1: Prediction of forearm flexion, pronation, and supination tasks using MMG			
Author(s)	**Anthropometric parameters**	**Method**	**Results and discussions**
(Talib *et al.*, 2022)	MUAC, arm length, weight, height, BMI, SKT	**AI model:** Linear regression **Features:** arm length, MUAC, age, weight, height, BMI, SKT, MMG RMS **Metaheuristic algorithm:** NA	The MUAC exhibited a weak moderate correlation with torque at 40%, 60%, 80% and 100% level of exercise efforts.
Remark: Low level of muscle contraction and insights relating anthropometrics and MMG with torque information should are crucial in the torque modelling **Future work:** Machine learning, metaheuristic algorithms along with anthropometry and MMG parameters may improve the prediction accuracy shown by mathematical regression.			
Study 2: Kinematic, speed and anthropometric variable to estimate ankle joint torque			
(Moreira et al., 2021)	ankle joint angle, angular velocity, acceleration, walking speed, body height and mass, foot and junk length, gender and age	**AI model:** LSTM, CNN **Features: NA** **Metaheuristic algorithm/optimization:** LOSOCV	The predictability of the CNN was observed statistically significant at low walk speed. Unl;ike EMG, the addition of body mass and height did not improve the TQ prediction ability.
Remark: Improved TQ estimation capability after the introduction of EMG recalls further considerations of myography signals along with anthropometry for TQ modelling. **Fuure work:** Subjects' variability per anthropometric and age range, as well as muscle activity should be addressed for AI powered assistive devices.			

Study 3: Anthropometry and EMG as predictors of arm muscle strength			
(Green and Gabriel, 2012)	Arm segments lengths, arm joint circumferences, weight, and height.	AI: Multiple regression **Metaheuristic algorithm/ optimization:** NA	Circumference showed a strong prediction than lengths in male than female. Inconsistent variability of the prediction ability by the introduction of lengths, or circmferences as well as EMG on muscle strength.
Remark: The lower estimation ability from the addition of muscle activation to anthropometric prediction equation may have been caused by the considering overall muscle efforts rather than individual muscle model. **Future work:** Anthropometric variables can be combined with muscle activation to improve torque estimation.			
Study 4: Anthropometrics and electromyography as predictors for maximal voluntary isometric wrist torque: Considerations for ergonomists			
(Chimera *et al.*, 2021)	Hand thickness, forearm circumference and ECR activation or hand thickness, elbow circumference	**AI model:** Pearson correlation coefficients assessed **Features:** NA **Metaheuristic algorithm/ optimization:** NA	Body circumference, muscle size, and muscle activation showed high wrist force output than both limb length and coactivation.
Remark: Anthropometry and muscle strength relationship are crucial for workspace design in activity of daily leaving requiring wrist and drip motions. **Future work:** Consideration of specific anthropometric variables for specific strength modelling and low muscle efforts.			

Study 5: Joint torque estimation using anthropometric and kinematic data			
(Serbest *et al*., 2023)	anatomical segments of ankle, knee, hip, neck joint, lower leg, upper leg, trunc, and head segments	**AI model:** FFBPNN, multi-layer perceptron **Metaheuristic algorithm/ optimization:** 7:1.5:1.5	Joint TQ were predicted with high accuracy using a varied training dataset collected from individuals across four distinct BMI categories and varying physical attributes.
Remark: The optimization of the ANN machine learning model demonstrates that enhanced prediction accuracy is driven not only by the quality of the training data but also by the effectiveness of the optimization technique employed.			
Future work: Other machine learning models along with hyperparameter optimization techniques need to be verified.			

2.6 Application of NMES and MMG for muscle function assessment

MMG can reportedly be used in real-time clinical monitoring (Trager et al., 2006; ; Hemmerling, 2015; Salminen et al., 2016; Watanabe et al., 2016;Wessell et al., 2016;Deffieux et al., 2008). Table 2.12. The authors of a related study (Wessell *et al.*, 2016) were able to detect an MMG response of the target nerve to a specific stimulation current to verify the rate of nerve root decompression, wherein a decrease in the stimulation threshold of ≥ 1 mA was observed in 98% of the test subjects. The affected nerve root maintained a stimulus threshold of 1 mA following decompression but exhibited an increase in the amplitude of the MMG signal response. The technique can thus adequately guide a surgeon in cases in which decompression is deemed uncertain. Furthermore, two other studies (Trager et al., 2006; Hemmerling, 2015) verified the validity of KMG and PMG in neuromuscular monitoring. Prior to general anesthesia, the ulnar nerve has received supramaximal train-of-four stimulation for every 12 s at 0–70 mA. Based on the concordance correlation coefficient, the recovery of NMB determined using KMG and PMG agreed with that obtained based on the MMG response. In contrast, the features of KMG appear to exhibit a high TOF ratio in NMB monitoring. Some researchers have compared the KMG data recorded using a Datex M-NMT MechanoSensor with EMG data recorded with a Datex ElectroSensor and found a higher recovery in terms of TOF % with KMG compared with EMG. However, the researchers stated that the 90% recovery rate of KMG makes it less preferable for NMB than EMG. Thus, further validation of these findings in clinical settings is needed (Salminen *et al.*, 2016).

In another study (Deffieux *et al.*, 2008), the BB was stimulated with a programmable function generator providing a 1-ms pulse, and 3D images were synchronously acquired through ultrafast acquisition in the transverse plane at each position. The Tc and 1/2Tr

matched the in vitro and in vivo surface MMG responses. In addition, the muscle fiber bundle was retrieved and agreed with the echogenic architecture of the muscle. Further, the researchers argued that the technique can be used to remedy the inability of diffusion tensor imaging in providing the mechanical function of a muscle, allowing for easy recruitment of muscle fibers. Therefore, the authors encourage further verification of the validity of myography-based screening of the functions of other muscles.

Several of the available techniques for respiratory assessment have been determined to involve maximal inspiratory and expiratory mouth pressures. After electrical excitation of the phrenic nerve, the MMG responses from the contracted diaphragm correlated with the respiratory muscle strength and provided higher sensitivity than the conventional method.

Electrically induced mechanomyograms reflect inspiratory muscle strength in young or elderly subjects (Watanabe *et al.*, 2016). Altogether, the techniques of MMG, KMG, and PMG through NMES are presented as interesting tools to evaluate muscle behaviours in clinical setting with no physical efforts. Taking advantage of the myographic signals from NMES to monitor specific muscle status, more research is needed to verify the functions of other muscles.

Table 2. 12 : Miscellaneous application of NMES and MMG for muscle function assessment

Study 1: Analysis of surgical monitoring.					
Author(s)	**Sensor and electrode type**	**Electrode site**	**Dataset**	**Methodology**	**Results and discussions**
(Wessell *et al.*, 2016)	MMG: (SentioMMG, Sentio, LLC, Wixom, MI, USA)	VM, TA, BF and gastrocsoleus	15 subjects with herniated nucleus pulposus (HNP), 31 subjects with lateral recess stenosis	The stimulation current was measured beyond 1 mA after passing a ball-tripped sterile probe onto the surgical field. MMG signals were recorded to indicate the lowest current at which a motor action potential was measured. The stimulation current was increased to evoke MMG.	The affected nerve root maintained a stimulus threshold of 1 mA following decompression but exhibited an increased MMG amplitude.
Remark: The method is adequate fir root decompression and provides direct feedback to the surgeon.					
Future work: The threshold change among patients with acute and chronic impingement should be studied, and the valuable measurements obtained from advanced IONM MMG for quantifying changes in health pre- and post-decompression and their relationship to post-operative clinical outcomes should be investigated.					

Study 2: Analysis of neuromuscular monitoring.					
(Hemmerling, 2015)	MMG: piezo-electric (diameter = 1.6 cm, model 1010, Grass Instruments, Astro-Med, Inc., West Warwick, RI, USA; frequency = 2.5 Hz to 5 kHz, output = 20–40 mV)	Adductor pollicis and VM	4 male and 8 female subjects, age 47 ± 21 years, weight 75 ± 8 kg, height 165 ± 12 cm	Mivacurium was injected for 5 min after the ulnar nerve and IM branches of the femoral nerve were supramaximally stimulated for 12 s with a 70-mA maximum current using a constant current stimulator. Acoustic signals were recorded from both muscles.	The control twitch amplitude of the adductor pollicis was more significant than that of the VM.
Remark: The VM was associated with a shorter onset time, a less pronounced maximal effect and more rapid recovery of the NMB compared with the adductor pollicis. **Future work:** The presence of fat layer recall further filtering during NMB monitoring procedures					
Study 3: Comparison of KMG and EMG for clinical monitoring.					
(Salminen *et al.*, 2016)	EMG: Datex^{TM} electrosensor; KMG: KMG sensor (Datex M-NMT MechanoSensor^{TM})	Adductor pollicis	27 female subjects, age 18-65 years	NMB was measured after injection of anaesthesia, and NMT was measured after supramaximal stimulation for 5 min with 5-s pulses at 50 Hz; the Bland-Atman method was used to determine the difference between MMG and EMG.	KMG overestimated the EMG due to variation from 65% to 100%, and these sensors cannot be used interchangeably.
Remark: KMG and EMG sensors cannot be used interchangeably **Future work:** The use of KMG for monitoring a clinical endpoint should be verified.					

Study 4: Analysis of diaphragm contractility using MMG.					
(Watanabe *et al.*, 2016)	ES: (Neuropack MEB-9100, Nihon Kohden Inc., Tokyo, Japan); MMG: accelerometer (MPS110, MediSens Inc., Saitama, Japan)	Right phrenic nerve	21 young subjects, age 22.5 ± 3.2, height 165.3 ± 78.6 m, weight 56.5 ± 8.1 kg; and 20 elderly subjects, non-smokers, age 70.9 ± 4.4 years, height 157.9 ± 8.2 m, weight 53.4 ± 8.5 kg, smokers, age 74.2 ± 5.9 years, height 154.8 ± 9.1 m, weight 51.4 ± 9.1 kg	The MMG signals from a contractile diaphragm were recorded after stimulation of the phrenic nerve. The correlations between diaphragmatic MMGs and respiratory parameters were assessed using Pearson correlation coefficients (significant if $p < 0.05$).	The correlations between diaphragmatic MMGs and respiratory parameters were significant ($p < 0.05$). Despit these results, no clear standard MMG sensors assembly available for clinical validation.
Remark: Diaphragmatic MMG was strongly correlated with inspiratory muscle strength and might reflect the diaphragmatic contractility more directly and with higher sensitivity than the conventional method.					
Future work: Validating diaphragmatic MMG in clinical populations, assessing its effectiveness in monitoring rehabilitation over time, and advancing its technological development for standardized, practical use.					

2.7 Summary

This literature review critically examines existing studies on muscle activity screening using myography signals, identifying notable research gaps that warrant further exploration. Building upon this foundation, the thesis formulates hypotheses and contributes to advancements in torque assessment techniques for the upper limb, focusing on refining methodologies to enhance accuracy and reliability.

The measurements of joint torque using myographic signals depends on various biomechanical factors, such as the number of muscles acting on a joint and their dynamic coordination. These lead to enormous information, which motivated recent studies investigating the potential of wearable technology and advanced algorithms to address these complexities. For instance, study (Yang and Yin, 2020) highlighted the feasibility of using gaussian processes with wearable smart shoes to estimate joint torques in lower-limb exoskeletons, providing robust modelling under dynamic conditions. Similarly, LSTM networks was applied to predict lower-limb joint angles and moments using EMG data, showcasing its potential to bypass traditional force plates and motion capture systems (Truong *et al.*, 2023). Despite these advancements, the role of individual-specific biomechanical parameters, such as muscle architecture and tendon elasticity, in influencing torque prediction accuracy remains underexplored. Also, most studies focus on lower-limb dynamics with small, homogeneous populations, limiting generalizability, where upper-limb dynamics, crucial for daily occupational tasks, have received less attention. Here, the synergistic activity of muscles like elbow flexors warrants further investigation to assess individual muscle contributions to joint torque. Another investigation (von Werder and Disselhorst-Klug, 2016) also quantified synergistic activity of the BB muscle and brachioradialis using EMG signals based on the fine tuning and load bearing torque tasks.

The study found a synergistic activity during the load bearing and claimed different control strategy during fine tuning tasks. Further, study (Shi et al., 2022) estimated the elbow flexion torque, based on MMG but the isolation of the muscle to its synergies was not considered. Hence, targeting individual elbow flexor muscle activation using NMES can refine further findings on torque estimation**.** For example, the BB's superficial location and large cross-sectional area allow precise electrode placement, enabling effective stimulation and signal acquisition. Its distinct motor unit recruitment patterns ensure predictable torque responses, and isolating BB activation minimizes interference from synergistic muscles, enhancing the accuracy and specificity of torque estimation models.

The quality of MMG signals on torque estimation also is a critical issue, when dealing with prosthesis or exoskeleton requiring a clean signal. Muscle activation levels play a pivotal role, with MMG responses exhibiting nonlinear behaviors at different contraction intensities. Low muscle activation, often targeted in NMES studies, may produce distinct MMG signatures compared to maximal voluntary contractions (MVC) (Flodin et al., 2022), necessitating models to account for such differences.

Variations in MMG data acquisition protocols, including sensor placement and filtering parameters, can influence the signal quality and model generalizability. The authors of one study on TMG found that a decrease in inter-electrode distance from ±5 to ±3 cm (Tous-Fajardo *et al.*, 2010). Despite no study has verified this effect using NMES-MMG integration, findings suggest that consistent electrode positioning is critical to maintain data integrity during myography studies (Talib et al., 2019).

MMG signals are influenced by the propagation of muscle vibrations along the longitudinal, lateral and transverse axis of muscle fibers. This recording necessitates a triaxial accelerometer for comprehensive signal acquisition along muscle fiber axis and can

provide a more robust representation of muscle activity. However, some torque estimation studies used vibromyography (Ibitoye et al., 2016), which lack the significance of the MMG features across muscle fibers directions. Other studies use analogue sensors like the ADXL-335, which, despite being widely accessible, suffer from low signal-to-noise ratio (SNR). Additionally, while lower-limb applications are frequently analysed, the lack of systematic evaluation of directional MMG components and torque estimation highlights a significant gap. Another critical limitation is the absence of consensus on the contributions of MMG signals from longitudinal, lateral, and transverse axes in extracting MMG feature on joint torque modelling, leaving unanswered questions about the relative importance of these directions. This multidirectional analysis is essential to account for fiber behaviour on MMG and torque and identify dominant muscle fiber's axis.

Joint torque correlate with muscle volume (Anon, 2001), and postural settings such as joint angle significantly influence the shape and length of the BB muscle, warranting further verification (Gonzalez *et al.*, 2018). The literature on biomechanics showed that joint angle impacts muscle fiber length, contraction velocity, and the motor unit's recruitment, which in turn alters the MMG signal amplitude and frequency characteristics. For example, mid-range elbow angles of 60°, optimize actin-myosin overlap and increase MMG amplitude, while extreme angles (10° or 90°) reduce torque due to suboptimal fiber alignment. MMG frequency components, such as MPF, also shift with angle, reflecting changes in motor unit recruitment patterns. Conversely, at extreme angles, either extended or flexed, suboptimal fiber alignment reduces MMG amplitude, reflecting lower torque output. Studies have demonstrated that MMG frequency components also vary with joint angle, with shifts in MPF indicating changes in motor unit recruitment patterns. These findings highlight the necessity of considering muscle geometry (joint angle and posture) in

muscle activation protocols for torque modelling.

The forearm posture influences the muscle activity (Gerditschke *et al.*, 2024), and further modulates MMG signals due to the presence of synergistic contributions. During voluntary elbow flexion, pronation increases the activation of the brachialis muscle, while supination emphasizes the BB, generating posture-specific MMG profiles critical for torque estimation. Research indicates that spinal excitability is affected by joint angle even under controlled arm posture and elbow angle conditions (Forman *et al.*, 2019). Another study also found that the level of muscle contraction is influenced by the optimal motor points (Gobbo *et al.*, 2014), which are likely to shift with angle beyond NMES electrode attachment (Ichikawa et al., 2021). Considering these factors can clarify the postural dependencies of MMG responses for improved torque quantification.

Anthropometric variables, including weight, height, BMI, skinfold thickness, MUAC and segment lengths, further modulate MMG responses and torque production. For example, the musculoskeletal strength can be determined by the contractile proteins measured by the cross-sectional area (CSA) of the muscle (Kim *et al.*, 2014), which is in turn modulated by the MUAC. Additionally, the variation in MUAC following changes in elbow joint angle or forearm posture affect the mechanical advantage of the BB muscle, thus altering sarcomere lengths. Consequently, these modifications influence the formation of cross-bridges between actin and myosin filaments, crucial for muscle contraction. As the alignment of muscle fibers shifts with different angles, torque output is modified due to changes in actin-myosin overlap and mechanical leverage (Kleiber *et al.*, 2015), affecting torque output and MMG signal characteristics. Therefore, the MUAC, which correlates with muscle mass, affects the amplitude and frequency of MMG signals, with greater muscle mass typically producing stronger signals, but further modulated by posture and contraction intensity in voluntary

muscle activation (Fok *et al.*, 2020). However, while the muscle contraction by NMES depends on stimulation density per muscle fiber arrays, these findings warranty analysis of MUAC in NMES based MMG and torque experiments.

Skinfold thickness introduces MMG signal attenuation (Santos *et al.*, 2021). Typically, increased skinfold thickness dampens signal transmission, particularly in deeper muscle layers. It may come that the attenuation of MMG be the result of the tissue underneath the sensor undergoing geometrical changes with joint angle. The authors indicated a negative correlation of RMS-MMG from voluntary contraction with both torque and muscle activity changing with elbow joint angle (Shi *et al.*, 2021). Similar findings were accounted for using NMES in animal study (Frangioni *et al.*, 1987). These mechanisms resulting from the change in muscle morphology may be the outcomes of motor unit control strategies, such as the recruitment of additional motor units and the increase in rate coding (Cooper et al., 2014). Although (Forman et al., 2024) focused on the geometrical changes of muscle, it is conceivable that alterations exist within the subcutaneous fat overlaying the muscle. With this variation, correlation between the skinfold thickness and the torque under the condition of both angle and posture may provide further clarity on torque assessment.

Upper arm length directly influences MMG amplitude and torque generation by altering muscle fiber recruitment and mechanical leverage. Longer upper arms often require greater muscle force to achieve equivalent torque due to the increased moment arm. This can result in higher MMG amplitudes, as muscle fibers must work harder to compensate for the mechanical disadvantage. Conversely, shorter upper arms may generate higher torque at lower MMG amplitudes due to improved leverage efficiency. Research by Irsa and colleagues (Talib *et al.*, 2022) highlighted that those anthropometric variations, including limb length, significantly affect MMG signals during isometric contractions. Additionally,

(Green and Gabriel, 2012) observed that torque prediction models incorporating arm length as a feature improved estimation accuracy, supporting the importance of individualization in biomechanical analyses. These findings underline the necessity of including arm length in wearable device calibration for precise torque estimation and injury prevention. However, NMES introduces additional variables, such as electrode placement and stimulation parameters, which can affect muscle fiber recruitment patterns differently from voluntary contractions. In addition, the relationship between upper arm length, MMG signals, and torque generation may vary, as recruitment depends on the stimulation current and its ability to activate deeper or more distal fibers (Paillard, 2018). Studies exploring upper arm length specifically under NMES are limited, and further investigation is needed to determine how anthropometric differences modulate MMG and torque responses in electrically induced muscle contractions. Accounting for these anthropometric and postural variations is essential to developing robust MMG-based torque estimation models.

Taken together, the inherent magnitude attenuation with the sensor mass, adipose tissue and lower frequency band (5 to 100 Hz) of MMG signals motivated further research to map muscle efforts and evoked contractions (Santos *et al.*, 2021), leveraging MMG and joint torque production (Uwamahoro et al., 2021). Indeed, feature engineering methods often prioritize time- and frequency-domain features, overlooking nonlinear or fusion-based metrics that better represent complex muscle dynamics. The literature reports no significant correlation between stimulation frequency and MMG variables (Papcke *et al.*, 2018) highlighting dynamic contractile properties of the BB muscle under predefined stimulation parameters. This perspective should be concluded along with the investigation of the repeatability of MMG responses measured from NMES.

Building on these advantages, a recent study employed the RMS and zero crossing

rate (ZCR) features from MMG signals of the BB and brachioradialis muscles to estimate elbow flexion force using ANN and multiple linear regression achieving a prediction accuracy of 0.883 (Youn andKim, 2011). Another study (Shi et al., 2022) developed a RFR model to map MMG and elbow joint torque levels, leveraging RMS, MPF, and sample entropy features, achieving 0.6828 accuracy on an unseen dataset. The study in (Li et al., 2021) integrated RMS, mean absolute value, ZCR, MPF, sample entropy, and band energy features. Complementing these efforts, research in (Z. Li et al., 2022) expanded the features set by incorporating MMG frequency band energy, wavelet packet energy, and approximate and fuzzy entropy features and achieved reduced RMSE. Despite these advancements, further exploration of the acoustic (Nagineni et al., 2018) and Hjorth features (Shah et al., 2022) is essential. However, inclusion of additional features escalates computational complexity, emphasizing the need to assess feature relevance and redundancy (Yu and Liu, 2004).

The assessment of redundant and relevant features are classified into filter methods that rank the features based on the data characteristics; wrapper methods that use ML algorithms to select significant features; and embedded techniques that integrates both feature selection and model predictions in a single process (Chandrashekar and Sahin, 2014). These integration necessitate metaheuristic algorithms which dynamically adjust the search agent based on objective function (Yang and Shami, 2020). EO, a physics-inspired algorithm, has outperformed traditional metaheuristic methods (Faramarzi *et al.*, 2020). Hence, algorithm combining both feature selection and redundancy analysis, along with hyperparameter tuning of machine learning models could provide further generalization.

Most presented methods validate ML models using experimental datasets,

demonstrating their effectiveness in controlled settings. However, extending validation to real-world data is crucial to assess model robustness and generalizability under practical conditions. Real-world scenarios often introduce variability that is not present in experimental datasets, such as differences in sensor placement or user behaviours. Incorporating such data into validation processes can enhance the reliability and applicability of torque estimation models.

The study by (Shi et al., 2022) in which a RFR model was employed to map MMG and elbow joint torque levels reveals the model's capability to handle complex biological datsets. However, the author relied on significant features from only 3 participants and the absence of subject variability may have biased the outcomes. Despite the RFR hyperparamters such as *Mtrees*, *Ntrees*, and sample size tuned around default values, inconsistent model performance was also noted from default parameterization (Huang and Boutros, 2016). Therefore, RFR model from carefully tuned hyperparameters and relevant no-redundant MMG features may improve the model prediction performance.

In the next chapter, the above identified gaps in the literature will be investigated by designing a suitable methodology to achive the objectives of this thesis. This will be described in details.

CHAPTER 3

METHODOLOGY

3.1 Introduction

This chapter details the methodologies employed in this research, which are the data collection, data preprocessing techniques, feature extraction, methods for statistical and reliability analysis, and for elbow flexion torque estimation model development as depicted in Figure 3.1.

3.2 Ethical statement

This study was approved by the local Medical Research and Ethics Committee, (MREC), Ministry of Health, Bangsar, Kuala Lumpur, Malaysia (Ref No: NMRR-20-2613-56796) refer to Appendix F. The experimental procedures adhere to the ethical guidelines outlined in the Declaration of Helsinki for human subjects' research (Parums, D.V, 2024). The experiment was conducted at the laboratory of the Faculty of Electronics and Computer Technology and Engineering, Universiti Teknikal Malaysia Melaka (UTeM), Malaysia with a licensed medical physician that supervised and approved the entire experimental process.

3.3 Participants

36 healthy, untrained, right-handed male participants with a mean age of 22.24 yrs, height of 172.00 cm, and weight, of 67.01 kg, volunteered for this study. None of the participants had a history of neuromuscular disorders, prior surgical procedures or implanted source of electrical signals. Each participant provided a signed consent form after receiving a detailed explanation regarding the purpose of the study and the experimental procedures

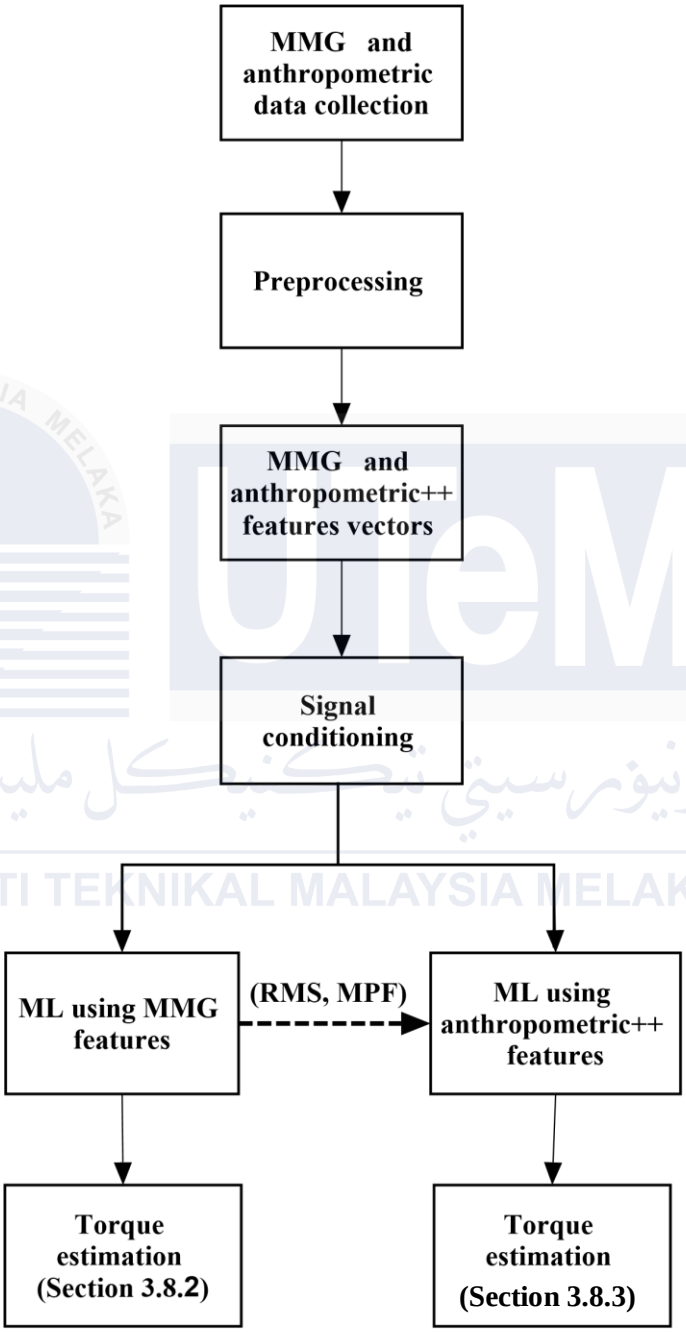

Figure 3. 1: Flowchart of the methodology stipulated in the research.

(Appendix B). The sample size was sufficient to test the hypotheses as approved by the Medical Research Ethics Committee. Male participants were specifically selected due to their typical higher force steadiness and lower variation in motor unit action potential and inter-pulse interval compared to females. The participants' age range was considered to minimize its influence on NMES, as the literature suggests age-related effects on MMG responses (Cogliati *et al.*, 2020).

3.4 Experiment design

The fundamental aspect of the current section is to identify and characterize the biomechanical manifestation of the BB muscle accounted for during NMES at varying upper limb geometry. The initial part highlights the basic characteristics of the BB muscle such as appearance, shape and the anatomical and physiological structure, the generation of mechanical activity of the muscles and how these signals are generated by electrical stimulation of the BB muscle.

3.4.1 Equipment

3.4.1.1 Anthropometric measurement

The weight was measured using (Type SECA 861 Hamburg, Germany), and the height was recorded using a (Type SECA 225, Hamburg, Germany) stadiometer. MUAC was measured with a HOLLESTA Body Mass Index Retractor Tape, while the SKT at the BB muscle was recorded using a digital skin-fold thickness calliper (ABD digital body fat calliper, range 0−50 mm, resolution 0.1 mm, accuracy of ± 0.2 mm, Shanghai ENOVO Industrial Ltd., China).

3.4.1.2. Measurement of MVIC

A push-pull dynamometer (SF−200, range = 0.5−200 N, resolution = 0.01 N, 100 – 200 V, Aliyiqi, Mainland China, China) was used to measure the MVIC in the neutral, pronation, and supination postures of the forearm. The lever arm was defined as the forearm length which was maintained under resistive load using a Velcro strap as illustrated in Figure 3.10.

3.4.1.3. Muscle Electrical stimulation

A certified MDA-registered transcutaneous NMES (EMS7500, V2U Healthcare Pte. Ltd., Singapore) (Appendix C), was used to deliver electrical intensity to the BB muscle for elbow flexion. This device (refer to Figure 3.2), powered by a 9 V battery, features two isolated channels with an optimal load of 500 Ω per channel and delivers an asymmetric biphasic square pulse. It allows for an adjustable frequency range of 2−50 Hz in 1 Hz increments, a pulse amplitude of 0−80 mA, a pulse ramp of 0−8 s, a contraction time of 0−90 s, and a relaxation time of 2− 90 s. The device provides 3 user-defined treatment modes −constant, synchronous, and alternate modes each adjustable from 1− 60 s or continuous. Lightweight and compact, with dimensions of 3.98" (L) × 2.40" (W) x 0.96" (H), the device is easy to wear during task performance. Stimulation intensity is delivered via 40 × 40 mm self-adhesive electrodes, connected by a 45" lead wire jack.

Figure 3. 2: Neuromuscular electrical stimulation device (Online available at https://www.herculife.com/product/modalities/electrotherapy/herculife-comfy-stim-digital-ems-tens.html. Retrieved April 20, 2024).

3.4.1.4. MMG sensor

MMG signals were recorded using a digital microelectromechanical triaxial (X, Y, Z) accelerometer ADXL313 (SparkFun, Colorado, USA; weight < 2.6 g; resolution = 10−13 bit; g range = ± 0.5 − ± 4 g; bandwidth = 0 to 3.125 – 1600 Hz; sensitivity = 1024 LSB/g for any g range; dimensions = 5 mm × 5 mm × 1.45 mm LFCSP package; voltage rating = 3.3 V), which effectively captures muscle fiber contractions propagating in three axes (Figure 3.12).

ADXL313 has a scaling factor of 3.9 mg/LSB, corresponding to ±0.5 g for an 8-bit register and provides both static and dynamic acceleration signals. As this study focuses on dynamic information, the output of the sensor was adjusted by averaging a set of 30 samples for each axis (X, Y, Z) while the sensor remained stationary at any elbow geometry defined by forearm posture and elbow joint angle.

3.4.1.5. Torque transducer

A force transducer (FS2050 Compression LC1500 GRAM, TE Connectivity, Schaffhausen, Switzerland; full-scale range = 15 Nm; span = 1 – 4 V; zero offset = 1 V; voltage rating = 5 V) was employed to measure the force applied at a constant lever arm across all subjects. Following the manufacturer's guidelines, a calibration function was established as shown in equation (3.1). The torque acquisition system recorded the voltage corresponding to incremental addition of weights ranging from $5 \times 10^{-5} - 2$ kg (Figure 3.3) resulting in a calibration curve depicted in Figure 3.5.

$$\text{Weight (kg)} = \left(\frac{\text{Sensor output} - \text{Zero offset}}{\text{Sensitivity}}\right) \times 10^{3} \quad (3.1)$$

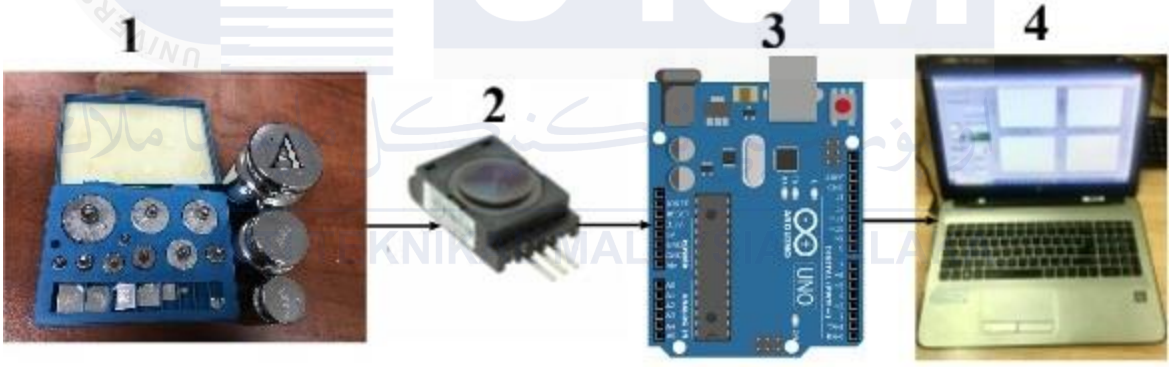

Figure 3.3: Setup for calibrating the force sensor includes : 1) set of calibrating weights, 2) the force transducer, 3) ATMEGA 328 microcontroller, and 4) computer for visualization, calibration and data recording.

3.4.1.6. Interfacing firmware and hardware

The acceleration and force transducers were interfaced through an Arduino Uno R3 (ATMega 328 processor; analogue input/output pins = 14; input voltage = 7−12 V; output voltage = 3.5 V and 5V; analogue input pins = 6; pulse width modulation pins = 6) microcontroller. The three-axis acceleration and force signals were synchronized using a

custom LabVIEW program at a sampling rate of 1000 Hz. Data was stored on a personal computer (64-bit operating system on Windows 11, 12th Gen Intel(R) Core (TM) i7-12700 2.10 GHz) for subsequent analysis. The synchronous operation of the torque and MMG sensors was achieved by configuring an ADC for the force sensor and using the I^2C interface for ADXL313. This synchronization was implemented using timers and registers, employing a compare match register and prescaler as detailed in equation (3.2).

$$\text{Prescaler Value} = \frac{\text{ADC clock}}{\text{Desired Sample Rate}} + 1 \tag{3.2}$$

where the ADC clock is set to 16 MHz, the desired sample rate of MMG and TQ signals is 1000 Hz, and the Prescaler ranges from 0 to 256 for the 8-bit Timer 1.

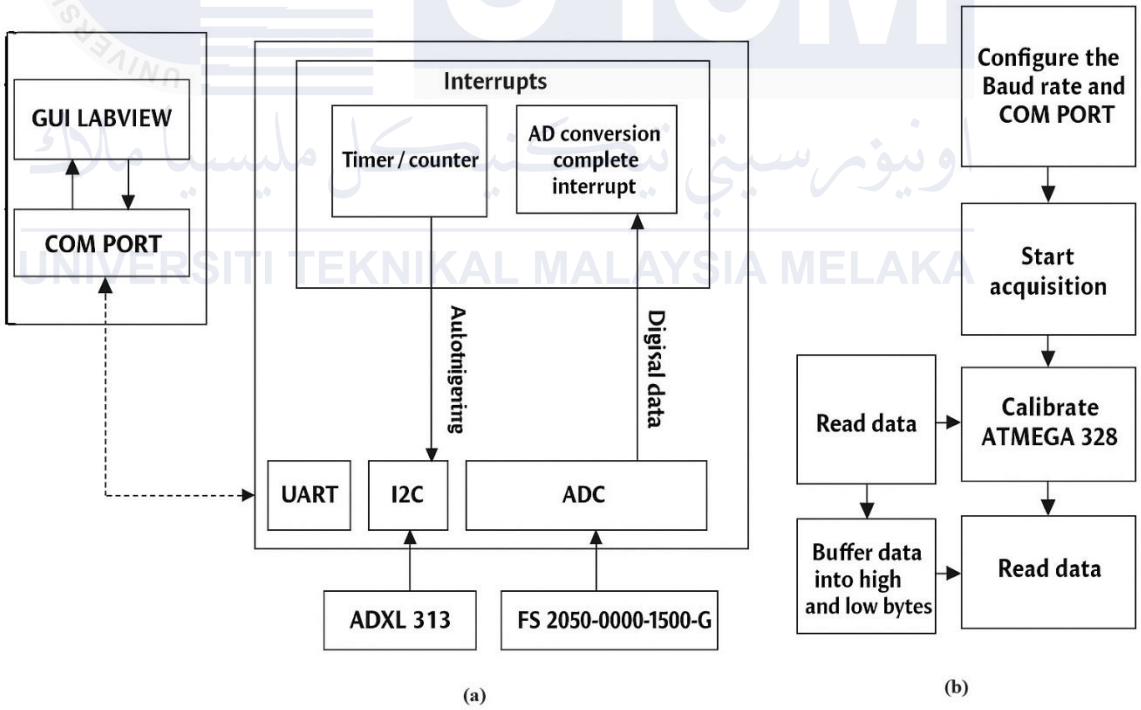

Figure 3.4: (a) Flow diagram of the acceleration and torque data acquisition unit and (b) Read and write process. The software (a) and hardware (b) architectures obtrusively and simultaneously record the acceleration and torque signals. The system includes functionality for selecting the COMPORT of the microcontroller, acknowledging the receipt of sensors' data on the personal computer, visualizing the sensor readings, calibrating the data, and start and stop the recording process on the computer.

Figure 3.6 illustrates the elbow flexion force and acceleration data along the longitudinal, lateral, and transverse axes, denoted as Xacc, Yacc, and Zacc, respectively. The figure also displays the command buttons used to start and stop data acquisition, perform calibration, and store the data. These commands are executed through the software process, as indicated in Figure 3.b, where panel (b) specifically demonstrates the initiation of acquisition, calibration, and data recording.

3.4.1.7 Software and graphical user interface

The functionality of the ADXL313 accelerometer was enabled by accessing its internal registers via the Wire.h library for I^2C communication programmed in C++. This allowed the Arduino to configure the device and accurately capture acceleration data across the X, Y, and Z axes, along with torque data through ADC configurations (Figure 3.4).

The calibration of the accelerometer for MMG data acquisition, as well as the recording of both MMG and torque data, was performed using a custom-developed graphical user interface in the LabView programming environment (LabVIEW program (NI LABVIEW 2021, 64-bit, National Instrument, Austin, TX, USA) as shown in Figure 3.6. The acceleration data across all three axes and force signals were displayed and stored on a personal computer for subsequent statistical analysis using SPSS (IBM version 25.0, 64-bit, SPSS Inc., NY, USA). Signal processing and machine learning model development were conducted in MATLAB® 2021b (MathWorks Inc., USA).

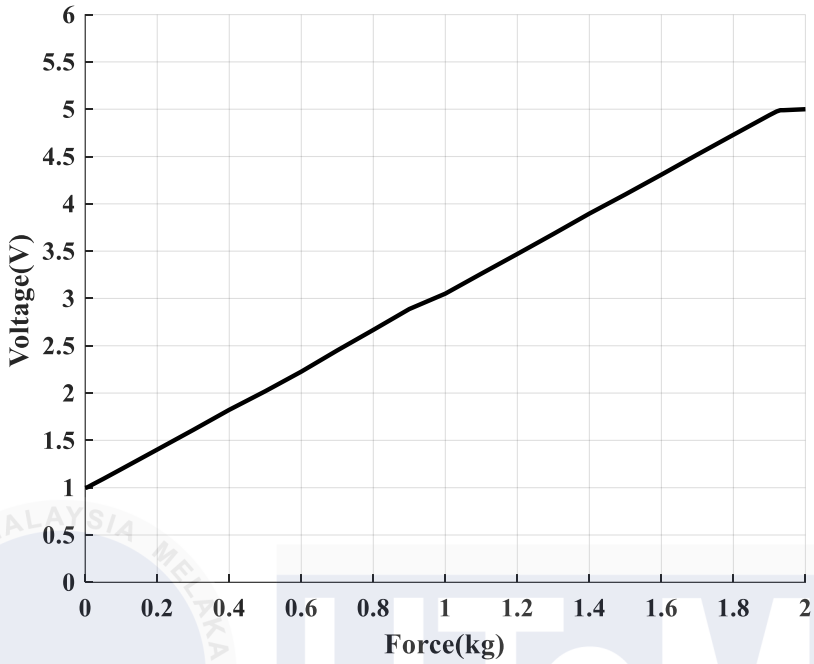

Figure 3.5: Calibration of the torque sensor.

Figure 3.5 illustrates the relationship between force and voltage, obtained by incrementally adding weights to the load cell. With each successive weight addition, the corresponding voltage output was recorded, demonstrating a linear trend between the applied force (in kilograms) and the measured voltage (in volts).

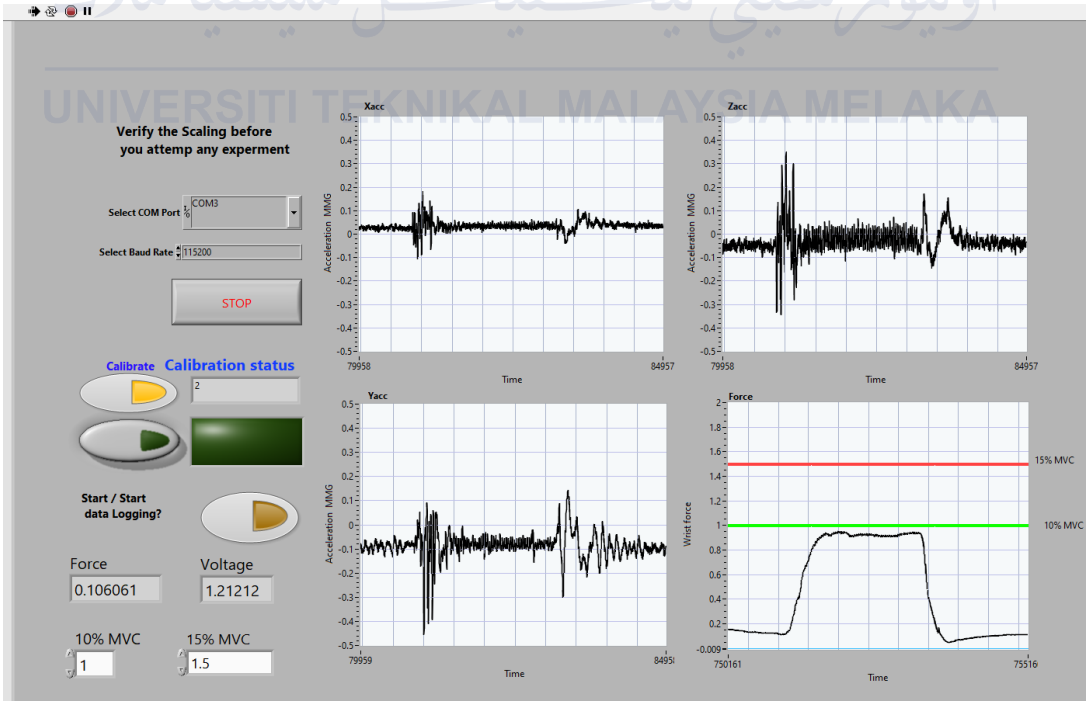

Figure 3.6: The Graphical user interface of the data acquisition device involves the configuration of the board rate to match the microcontroller's configuration, selection of the

COM PORT, start and stop acquisition button, control for data logging and the visualization of the numerical and graphical representations of muscle activity and strength information.

3.4.2 Protocol

The experiment was conducted over three separate sessions, with an intersession interval of 24−36 hours. In the first session, participants were familiarized with the NMES sensation and performed maximal muscle contractions following the recording of anthropometric parameters. The second session involved recording NMES-MMG and torque data. In the third session, isometric submaximal elbow flexion MMG and torque data were captured at three randomized forearm postures and four elbow joint flexion angles.

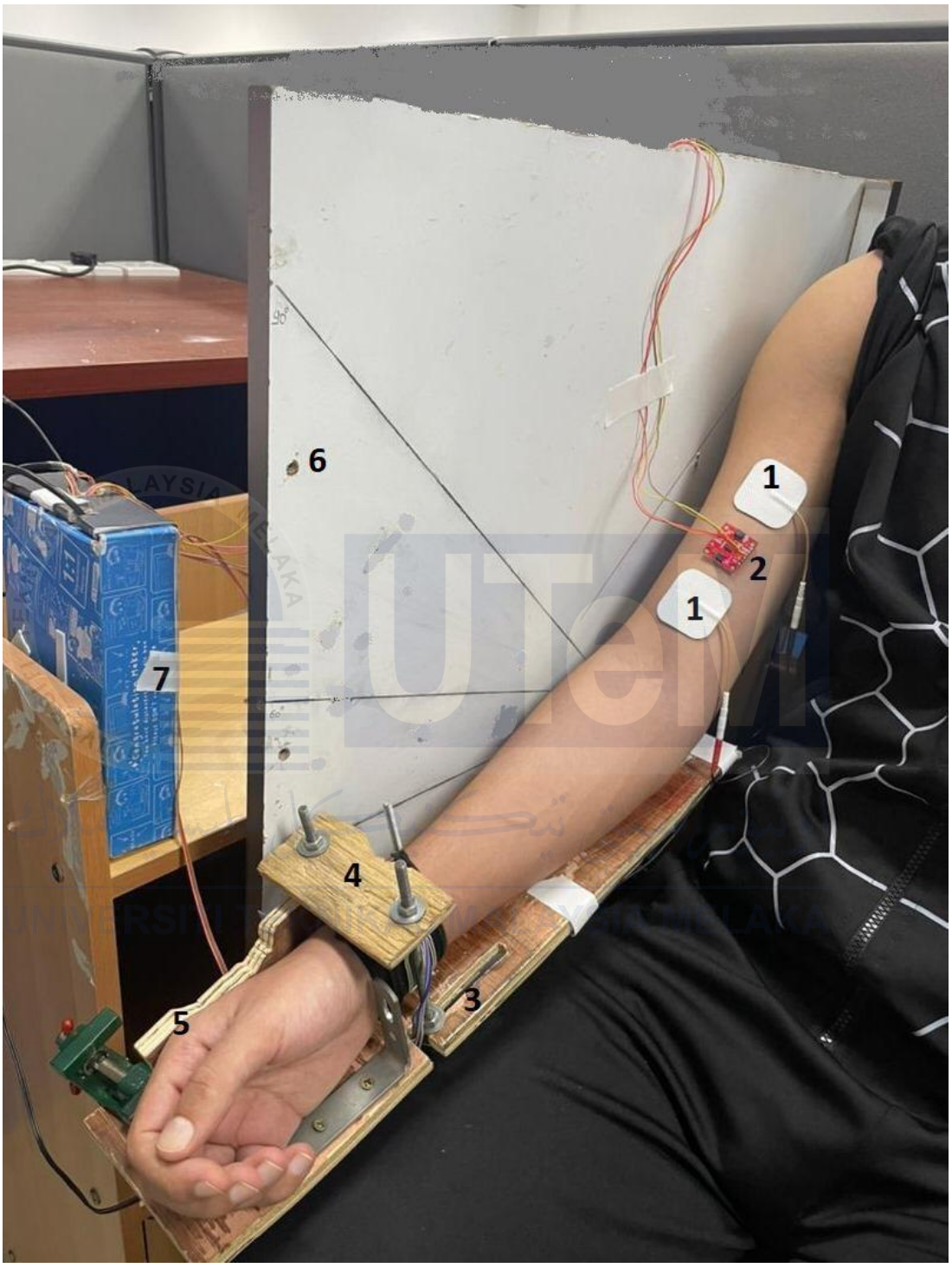

Figure 3.7:Experimental setups of data acquisition for acceleration and torque data acquisition : 1) NMES electrodes, 2) MMG sensor, 3) adjustable elbow rest and fixture for posture, 4) support of the force sensor cuff (placed underneath), 5) fixture of the hand/wrist from flexion, extension abduction, and adduction, 6) fixture for the adjustable elbow joint angle, 7) force and acceleration data acquisition device.

3.4.2.1 Familiarization and consent form

Upon their arrival at the experiment site, participants were briefed about the purpose of the research and provided with detailed explanations and training on the experimental procedures and the equipment involved. Informed consent was obtained from all the participants before their involvement in the study. This session took about 10 minutes.

3.4.2.2 Personal and anthropometric details

Information for each participant was recorded in the bio-section of their respective recording file (Appendix B). Anthropometric variables were measured during the three experimental sessions, following the standard operating procedures established by the International Society for the Advancement of Kinanthropometry (ISAK), with validation by an on-site medical physician. The LUA was measured from the deltoid tubercle to the olecranon process, while the LLA was measured from the olecranon process to the styloid process of the ulna. The MUAC was measured at the middle point between the acromion process to the olecranon process, with the elbow joint maintained at 90°. The SKT was measured at the midpoint between the acromion process (bony point on the shoulder) and the olecranon process, on the anterior aspect of the upper arm with the subject standing and their arm relaxed at their sides. The body weight was recorded with the participant wearing light clothing and no shoes, and the height was measured barefoot using a mounted telescopic stadiometer (Figure 3.8).

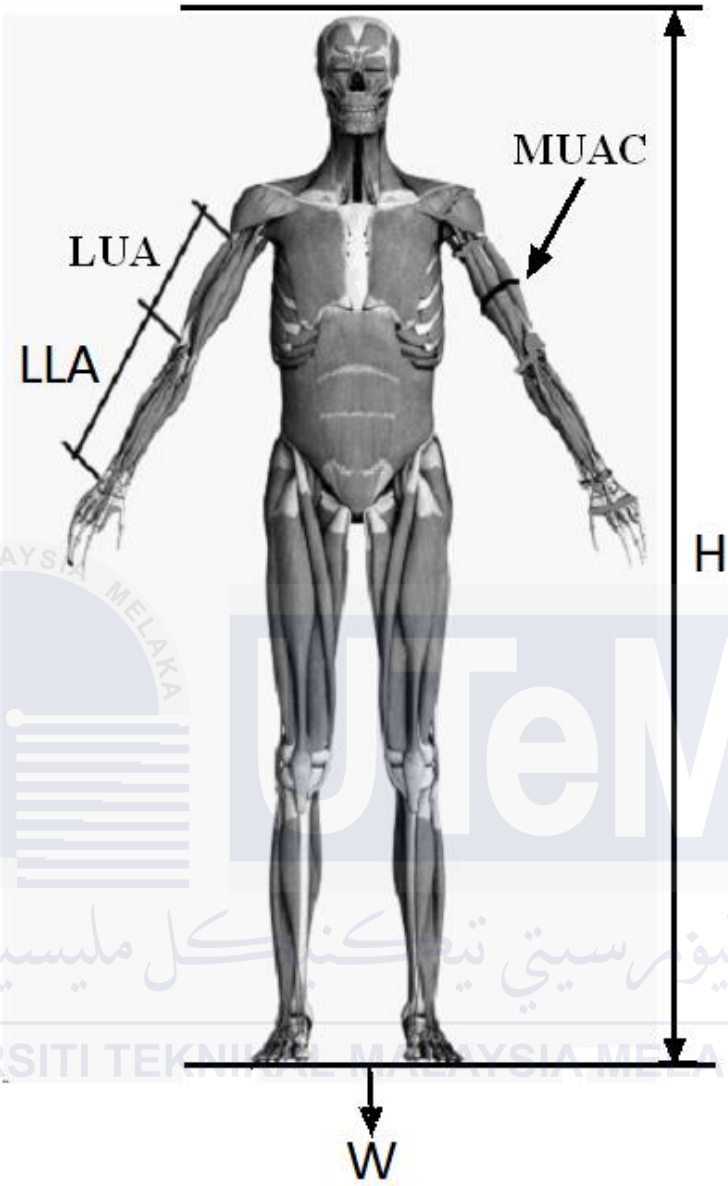

Figure 3.8: Anthropometric measurement lengths, circumference and height(Green and Gabriel, 2012).

3.4.2.3 Determination of MVIC

The subjects sat upright with their back supported and feet flat on the floor. The upper arm was positioned parallel to the torso, with the elbow bent at approximately 90° between the forearm and the arm. The shoulder abduction angle was measured using a digital goniometer and was maintained at about $3-4°$ throughout the experiment. A hand orthosis

was used to restrict any sudden wrist flexion, extension, adduction, or abduction. The wrist was secured to the hook of the push-pull dynamometer, which served as a resistance load during elbow flexion (Figure 3.10). The subject exerted maximum force to flex the elbow while avoiding any movement at the joint or muscle group and maintaining consistent efforts throughout the 3−5 s contraction as trained (refer to section 3.4.2.1). MVIC was then measured for isometric forearm flexion in neutral, pronation and supination hand postures. Muscle recovery was ensured with a 5-min rest between consecutive trials and a 10-min between consecutive postures (Figure 3.9). Verbal encouragement was provided throughout the contraction to promote maximal effort, and the force output was continuously monitored by the experimenter. The trial was repeated if any deviations above 5% between two consecutive trials were observed, and confirmed by independent observers.

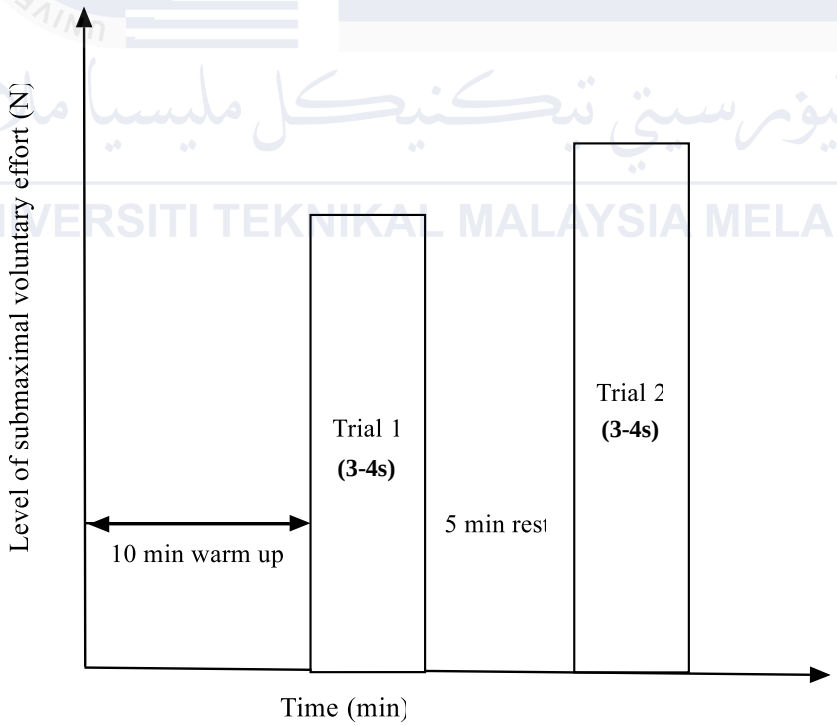

Figure 3.9: Determination of MVIC of elbow flexion in neutral, pronation and supination, where N is the efforts in Newtons.

Figure 3.10: Elbow flexion with the forearm in the Neutral, pronation, and supination along with the dynamometer displaying measurement both before and after the application of force.

3.4.2.4 Anatomical location of BB muscle

The anatomical location of the BB muscle was identified by palpating the midline of the muscle, approximately one-third of the distance from the shoulder to the elbow. The long head of the BB muscle originates from the supraglenoid tubercle of the scapula, runs down the arm and inserts into the radial tuberosity exhibiting parallel fascicles. In contrast, the short head which exhibits both parallel and pennate fascicles, originates from the coracoid process of the scapula and also inserts into the radial tuberosity. Consequently, the longitudinal axis of the BB is defined as the line joining its origin and insertion points into the radius. The transverse axis runs perpendicular to both the longitudinal and lateral axes, captures vertical movement relative to the plane of the muscle, and extends from the anterior (front) to the posterior (back) side of the arm. The lateral axis runs across the muscle from the medial (inner) to the lateral (outer) side of the arm, perpendicular to the longitudinal axis (Figures 3.12 and 3.13).

3.4.2.5 MMG sensor placement

The sensor was attached to the most prominent part of the muscle belly, avoiding tendinous regions and maximising the sensitivity of the sensor to the mechanical activity generated along the length of the muscle fibers (Park, Byung Kyu, et al.,2007). MMG accelerometer was affixed to the belly of the biceps brachii muscle, positioned midway between the upper lateral portion of the acromion border and the proximal lateral head of the radius (Hunter *et al.*, 2012) using double-sided adhesive tape (3MTM VHBTM 4920, Center St. Paul, MN, USA).

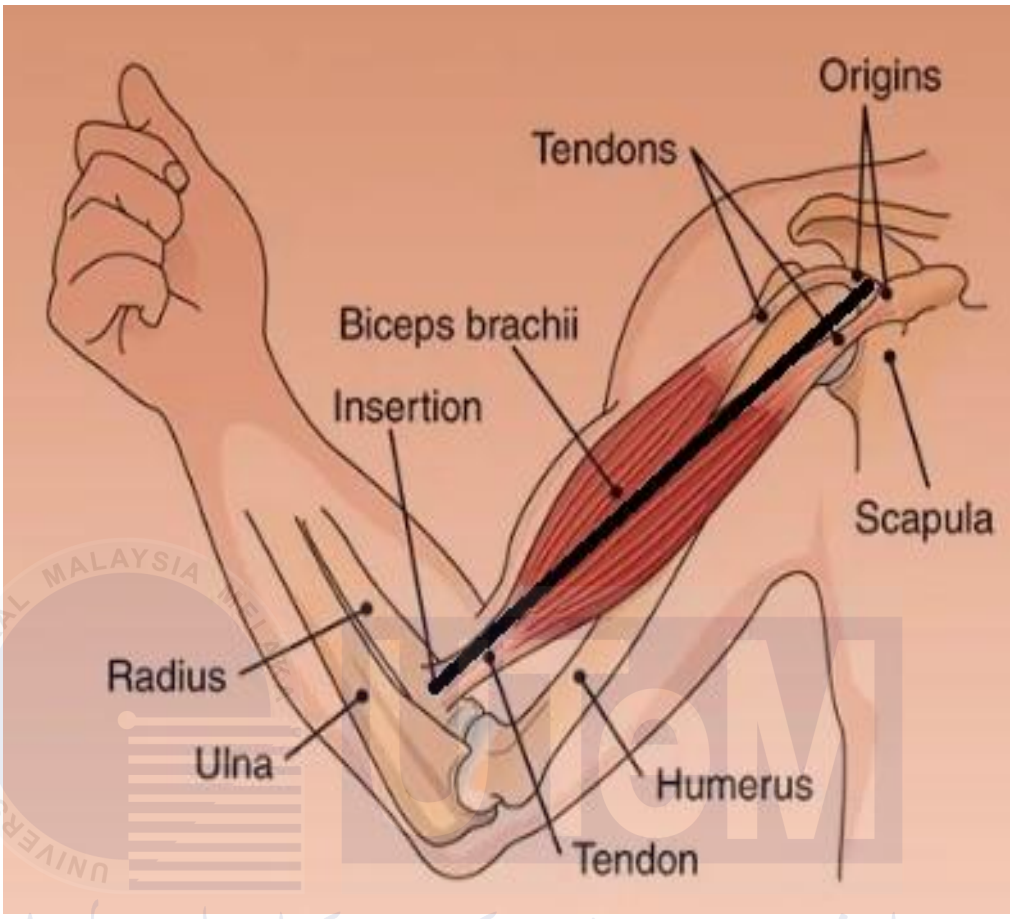

Figure 3.11: Origine, insertion and anatomical position of the BB muscle (https://flexfitnessapp.com/blog/bad-bicep-genetics/).

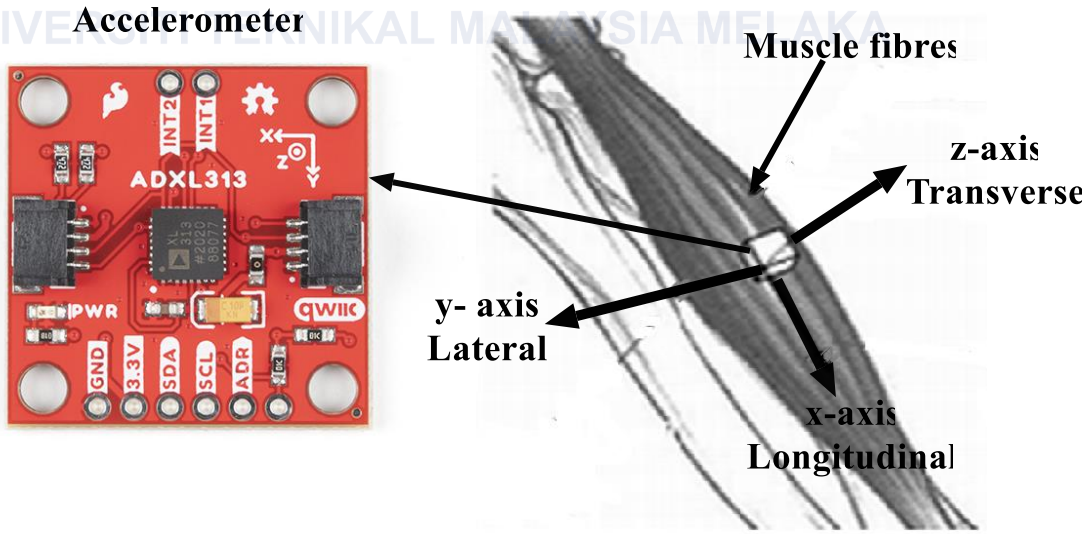

Figure 3.12: Alignment of MMG sensor with axis of muscle fibers in the longitudinal, lateral and transverse axes (Islam *et al.*, 2014b).

3.4.2.6 Attachment of NMES electrodes over the muscle

Electrode placement for BB muscle stimulation for elbow flexion used the acromion mark at the shoulder as a reference point (Figure 3.11). The negative electrode was attached to the muscle belly (black lead) while the positive electrode was attached closer to the elbow crease by the on-site physician (Figures 3.7 and 3.13). The stimulation electrode was placed approximately 5 cm away from the centre of the MMG sensors targeting both the distal tendon and the area of overlap between the Pectoralis major and Deltoid (Hunter *et al.*, 2012). The minimum inter-electrode distance was determined to be 5 cm which exceeds the nominal interelectrode distance of 4 cm. This spacing ensures maximum muscle displacement and prolonged contraction time (Wilson *et al.*, 2019). Additionally, this distance allows sufficient space for the ADXL313 sensor to be securely attached to the muscle for precise detection of muscle contractions. The NMES electrodes used were self-adhesive, ensuring muscle contraction at maximum comfort for the subjects (https://www.axelgaard.com/App/Anatomy/Elbow%20Flexion).

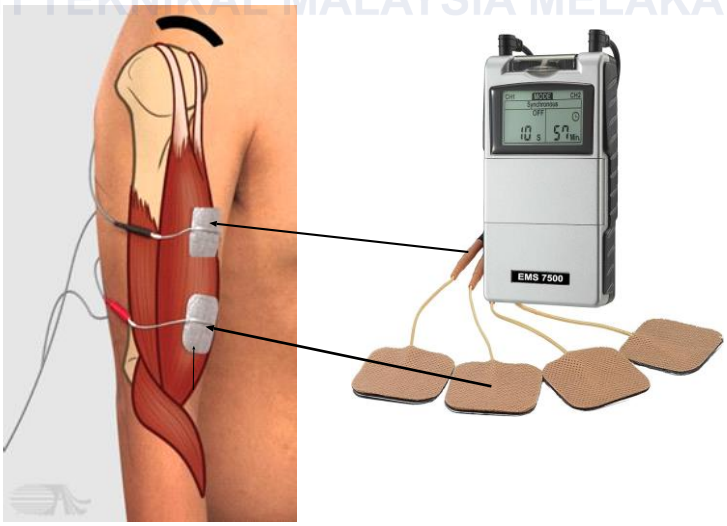

Figure 3.13: Placement of electrodes for electrical stimulation at the BB muscle (https://www.axelgaard.com/App/Anatomy/Elbow%20Flexion.Retrieved on April, 24, 2024).

3.4.2.7 Positioning of the torque sensor

The participant sat on a custom-made chair with the forearm positioned in a randomized posture. The torque sensor setup involves securing a compression force sensor FS2050-000-1500-G at the wrist using a customized armband placed beneath a wrist cuff (Figure 3.7). The wrist was strapped to ensure a standardized forearm length for all participants, maintaining consistency during elbow flexion. Postures were randomized between neutral, pronation, and supination positions. This setup ensured that NMES effectively compressed the transducer under the wrist cuff during the muscle contractions for elbow flexion. The torque transducer is powered by a 5VDC source from the data recording computer and connected to ADC ATMEGA328 for data acquisition via customized C++ firmware. The GUI was developed in LabVIEW to control the data acquisition process, allowing for seamless monitoring and manipulation of data during the experiment.

3.4.3 Data recording

Anthropometry data of each participant recorded in section 3.4.2.2 was considered prior to the application of electrodes for NMES and the placement of MMG and TQ sensors. Hence, MMG and TQ data were collected from participant in accordance with approved ethical experimental procedures.

3.4.3.1 MMG and torque data

A minimum of 24–36 hours after the initial session to determine the MVIC and NMES sensation, each subject received NMES to elucidate the MMG and torque signals at levels below 15% of their equivalent MVIC. Under the guidance of the on-site physician, participants performed elbow flexion stretching exercises with a 2 kg weight using their right arm. After a 10-min rest, the experiment proceeded using the postural and angle settings established during the familiarization session, with the subject seated in the experimental chair (Figure 3.7). The placement of electrodes on anatomical landmarks was ensured using a semi-permanent indelible marker. The same medical physician applied NMES electrodes, MMG and force sensors to the pre-marked body sites. The NMES protocol applied a frequency of 30 Hz, a biphasic electrical pulse of 110 µs, ramp time (Up and Down) of 1s, ON time of 4 s, OFF time of 2 s, and current amplitude of 30 mA, delivered to each subject for 30 s (refer to Figure 3.14). A 5-min rest was given between two consecutive trials, and a 10-min rest was provided between different postures or angles to minimize the electrically elicited torque development and post-activation potentiation. NMES electrodes and MMG sensors remained in situ throughout the experiment to limit the data variability. The order of postures and angles were randomized, and subjects were blinded to specific selections made at the start of the NMES trials. Accelerations and torque data were recorded and saved for the subject for future analysis. The data was validated by analysing the power spectrum and frequency against RMS magnitude obtained from experimental recording trials (Figure 3.15), which confirmed dominance in the recorded signals. The NMES MMG, and torque experiment procedure is depicted in Figure 3.16.

The experiment was terminated under several conditions: failure to reach the target

torque level, insufficient muscle activation, signs of muscle fatigue, subject discomfort, or signal degradation. The on-site medical physician verified that no harm occurred to the subject during the experiment and no adverse effects were reported during the trials.

The NMES experiment consisted of 12 configurations combining 4 angles and 3 forearm postures resulting in datapoints per subject per trial sampled at 1 kHz. Each trial involved recording data for a single angle and posture over 30 s duration, ensuring comprehensive coverage of all postural and angular combinations during the experiment (Figure 3.15).

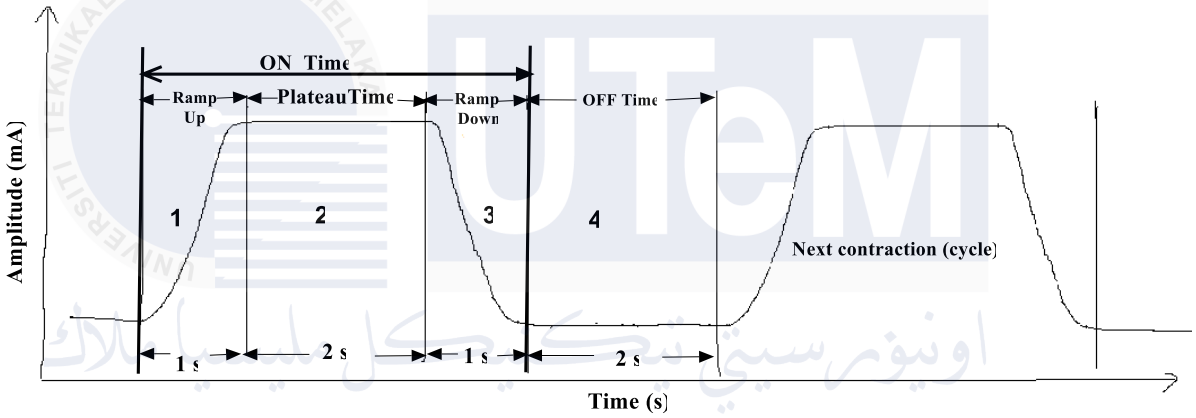

Figure 3.14: Examples of NMES parameter settings for four phases of muscle contraction cycles are denoted as Ramp-up time (1), Plateau Time (2), ramp-down Time (3) and OFF Time (4). Each recording trial involves five muscle contraction cycles of 6 s each, which involve the ON Time for 4 s and OFF Period of 2 s. Application of these stimulation parameters setting generated the muscle activation and torque signals shown in Figure 3.20.

3.4.3.2 MMG and torque data for validation experiment

The third session of the experiment was conducted 24−36 hours after the NMES session. Each subject was assigned 3 configurations of elbow joint angle and forearm posture, ensuring that all participants covered the 12 configurations in equal proportions. Before beginning the experiment, participants performed stretching exercises and adopted postural

and angle settings determined in the familiarization session and the NMES session (section 3.4).

The subject was then guided by the experimenter to perform cyclic elbow flexion with the generated torque level displayed on the computer positioned 1 m directly in front of the subject. Each trial lasted 15 s, with a 5-min rest between consecutive trials and a 10-min rest between different angle-posture configurations . Accelerations and torque data were sampled at 1000 Hz, while MMG data was validated by analysing the power spectrum. Once validated, the data was saved on the hard drive of the computer for subsequent analysis. The steps involved in validation data acquisition are depicted in Figure 3.17 and 3.19. A typical example of a torque signal recorded during the validation session is shown at Figure 3.18.

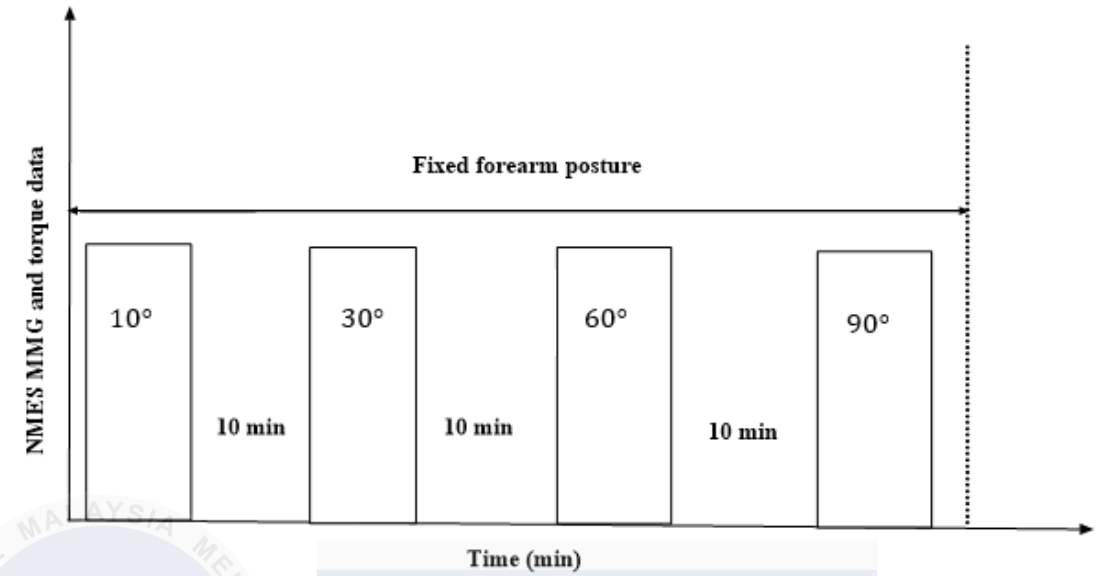

(a)

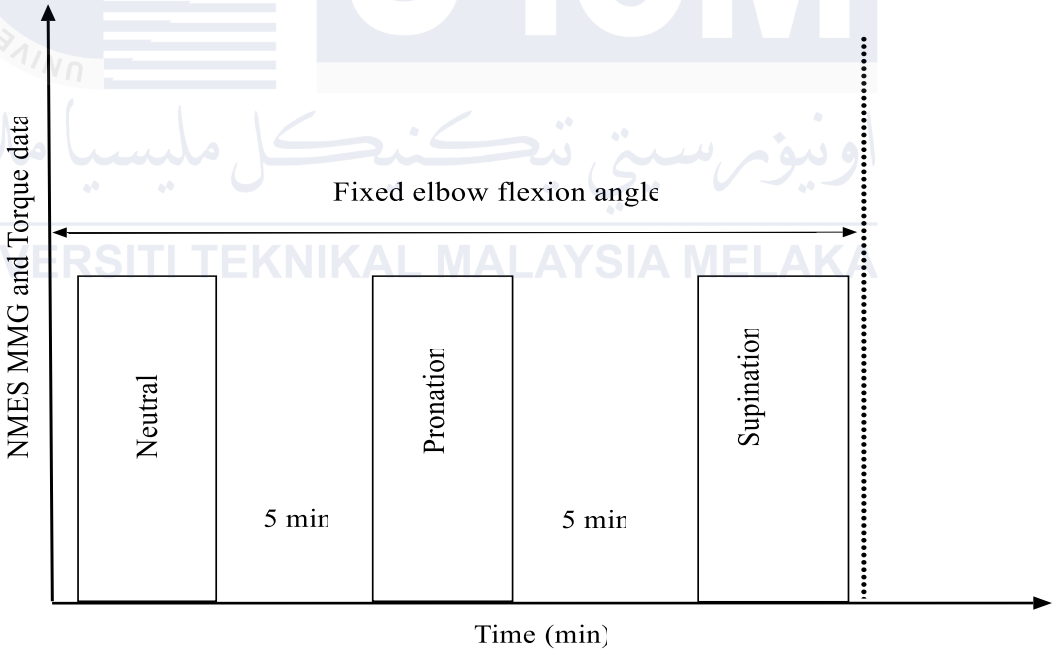

(b)

Figure 3.15: Example of one trial recording process of NMES MMG and torque data obtained from fixed forearm at joint angle at 0°, 30°, 60°, and 90° (a) with fixed elbow joint angle, with the forearm in neutral, pronation and supination postures in (b).

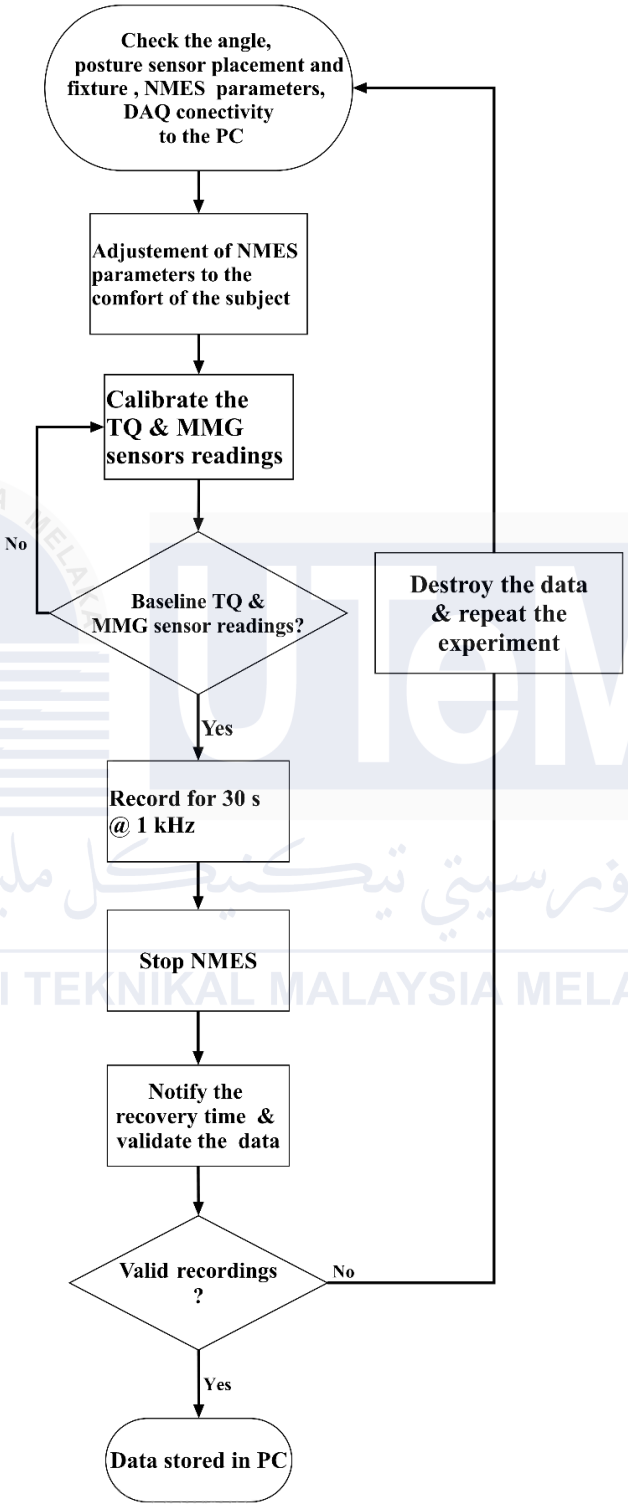

Figure 3.16: Flow chart of the steps involved for NMES MMG and TQ data recording session.

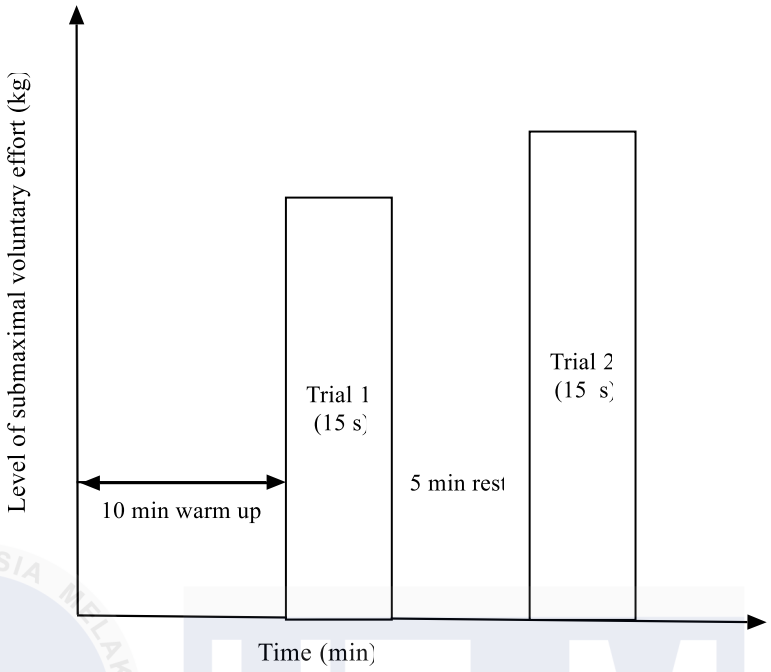

Figure 3.17:Execution of the validation protocol for submaximal muscle efforts

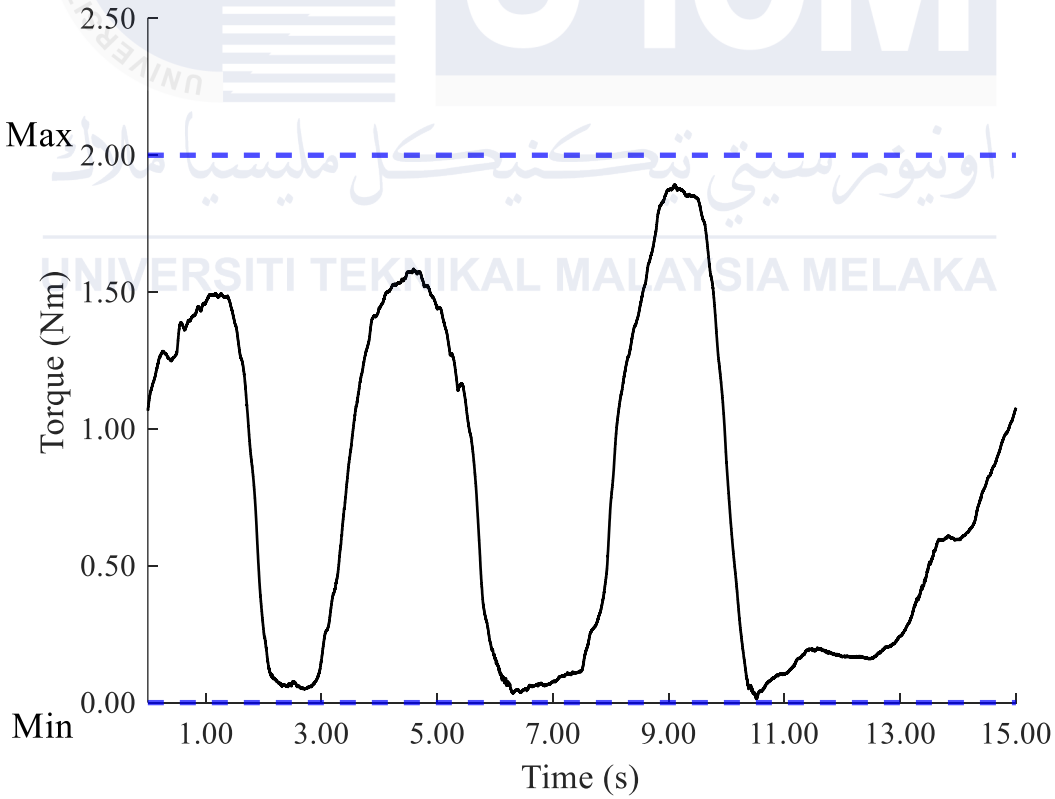

Figure 3. 18: Sample torque signal executed during the guided validation session

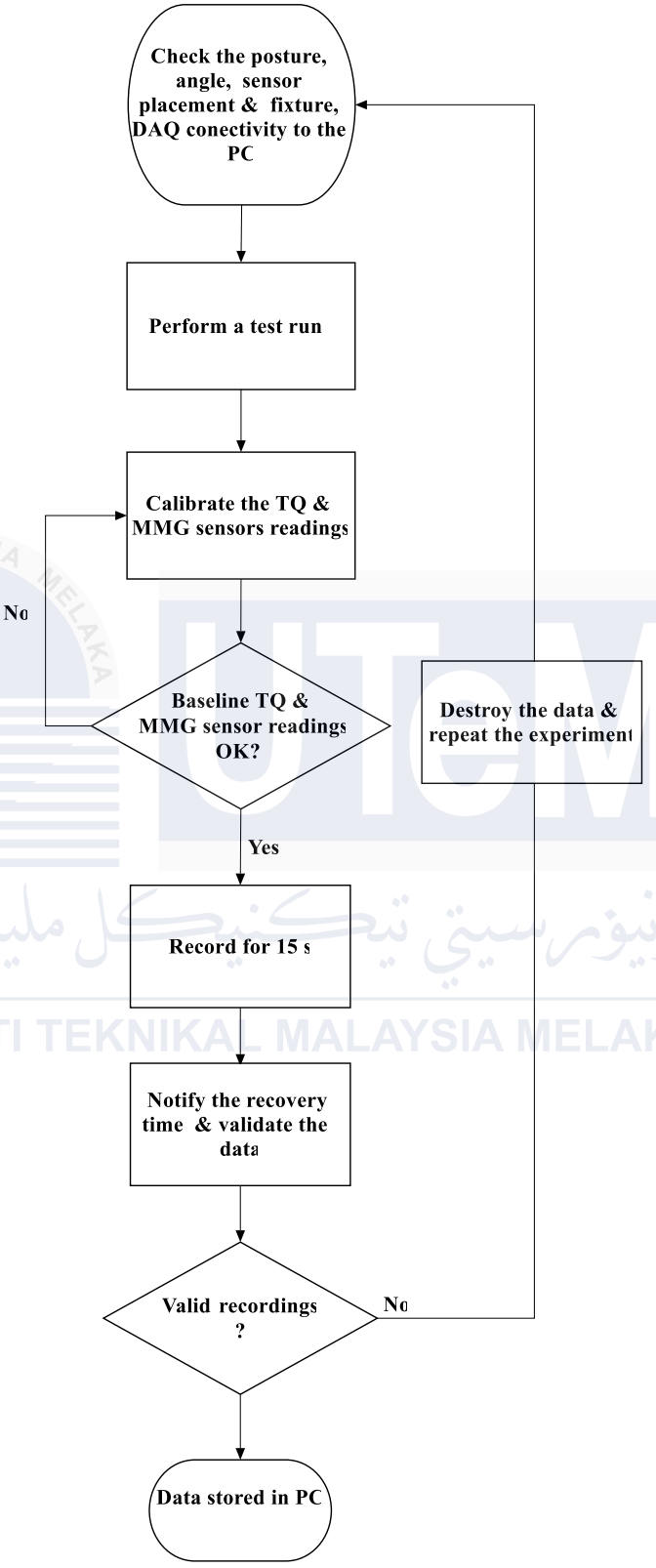

Figure 3.19: Flow diagram of the steps involved for the validation session

3.5 Data pre-processing

This section involves several interconnected steps that transform raw data into meaningful representations suitable for statistical analysis and torque estimation.

3.5.1 Filtering and segmentation

The NMES acceleration data was filtered to extract the MMG signal using a Butterworth band pass filter with cut-off frequencies of 5 Hz and 100 Hz. Torque data was processed using Butterworth low pass filtered with a 5 Hz cut-off frequency to eliminate transients caused by torque development and muscle relaxation at the end of muscle contractions.

To maintain data integrity, the first and last extreme 6-s cycles of NMES-MMG and torque were discarded. This step minimizes the influence of physiological adjustments, such as muscle warm-up, fatigue onset, or variations in muscle recruitment, which typically occur during the initial and final phases of muscle contraction. Discarding these cycles helped to avoid inconsistent signal characteristics, ensuring that the analysis focused on stable and representative muscle behaviour under electrical stimulation. For further analysis, MMG and TQ data were segmented using a 100 ms window with a 50 % overlapping window for each of the 2 recording trials per configurations of 4 elbow joint angles and 3 forearm postures. This segmentation resulted in 310176 segments providing a comprehensive dataset for assessing muscle function and torque generation.

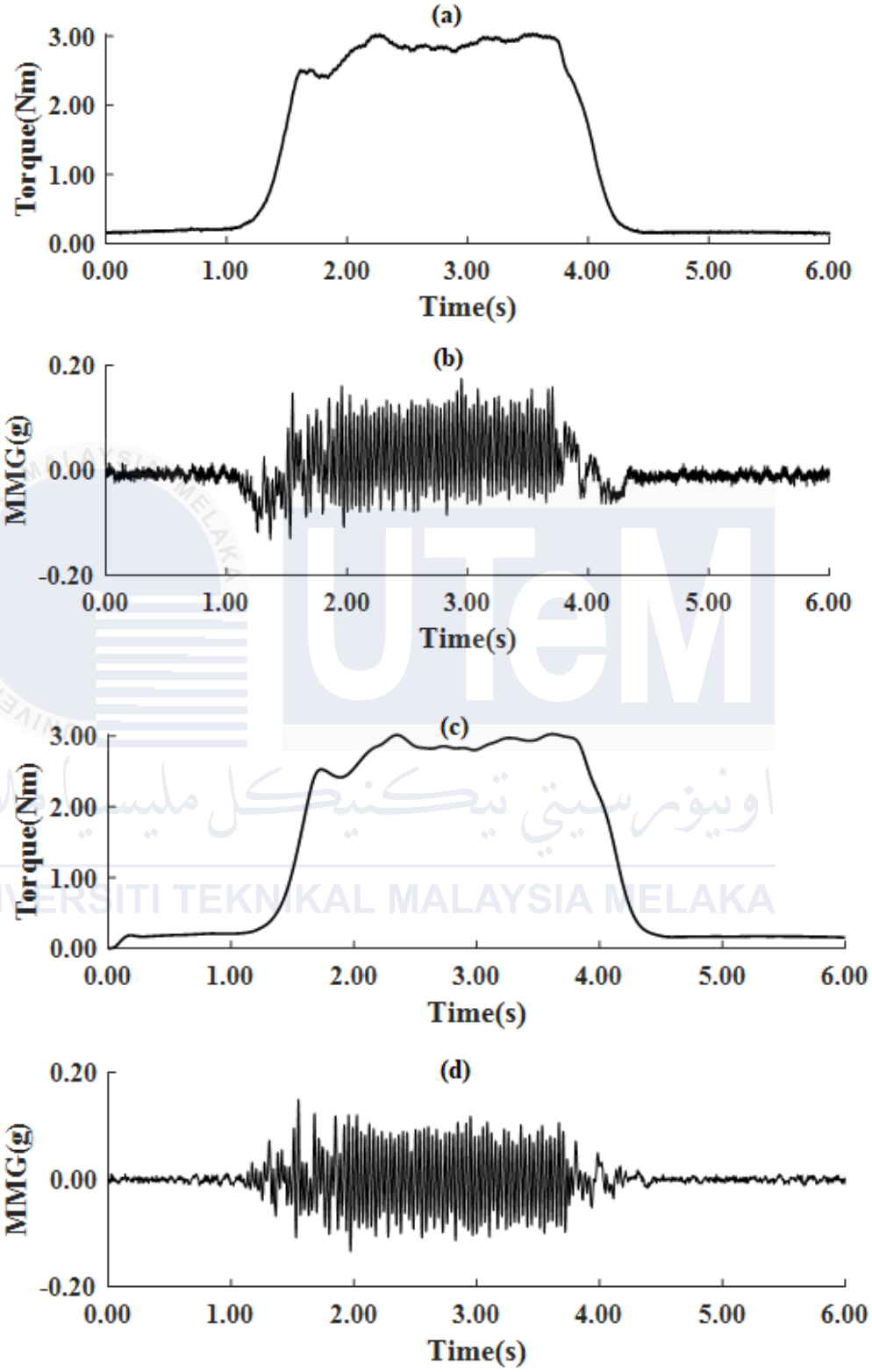

Figure 3.20: Typical representation of raw torque (a) and acceleration MMG signals (b), and filtered torque (c) and filtered MMG signals (d) during one cycle of recording (6 s).

3.5.2 Feature extraction

To characterize the muscle function and torque relationship, the following features were extracted:

3.5.2.1 Physiological features

MMG signals are inherently no-stationary, and non-linear, necessitating comprehensive analysis across time domain, frequency domain, and time-frequency domain. Time-domain analysis captures variations in the signal amplitude over time, providing insights into transient muscle activity. The frequency-domain analysis focuses on the spectral distribution of the signals, revealing dominant frequencies associated with muscle contractions. Time-frequency domain analysis, such as wavelet or short-time Fourier transform (STFT), allows for the examination of how these frequency components evolve, offering a dynamic view of muscle activity changes. Additionally, acoustic analysis computes the signal strength and energy distribution across various frequency bands, aiding in identifying the central tendencies and overall characteristics of the MMG signals (Nagineni et al., 2018).

a) Root mean square (RMS)

Root mean square (MMG RMS) was calculated using equation (3.3)

$$\mathrm{RMS} = \sqrt{\frac{1}{\mathrm{N}}\sum_{\mathrm{n}=0}^{\mathrm{N}-1}|\mathrm{x}[\mathrm{n}]|^2} \tag{3.3}$$

where x[n] is MMG signal, and N is the total number of datapoints.

b) Mean power frequency (MPF)

The MPF represents the average frequency of a signal's power spectrum. MPF was calculated using a 512-point FFT calculated with a Hamming window as determined by equation (3.4),

$$\text{MPF} = \frac{\int_{f1}^{f2} f.PS(f)df}{\int_{f1}^{f2} PS(f)df} \tag{3.4}$$

where MPF is the mean power frequency, PS(f) is power spectrum density function of MMG signal determined using FFT, f1 and f2 are the lower and upper bounds of the MMG signal bandwidth.

c) Median frequency (MDF)

The MDF is the frequency that divides the power spectrum of a signal into two equal halves, where each half contains the same amount of energy. This can be mathematically expressed using equation (3.5),

$$\int_{f1}^{f^{MDF}} \text{PS(f)df} = \int_{f^{MDF}}^{f2} \text{PS(f)df} \tag{3.5}$$

where f^{MDF} is the median frequency, PS(f) is power spectrum density function of MMG signal determined using Short Time Fourier Transform (FFT), f1 and f2 are the lower and upper bounds of the MMG signal bandwidth.

d) Zero crossing rate

The zero-crossing rate (ZCR) quantifies the frequency of muscle contractions by counting how often the MMG signal crosses the zero-amplitude level within a specified time

window. Physiologically, the ZCR correlates with the frequency content of the muscle activity detected by the MMG (Roman-Liu and Konarska, 2009). A higher ZCR suggests more frequent muscle contractions or a greater number of active motor units, which is often associated with stronger or more sustained muscle contractions. Conversely, a lower ZCR signifies less frequent contractions or fewer active motor units, often reflecting weaker or more relaxed muscle state. ZCR is computed using the following equation (3.6) (Asghar et al. 2023),

$$\mathrm{ZCR} = \frac{1}{\mathrm{N}-1}\,\mathrm{f(x)} \tag{3.6}$$

where :

$$f(x) = \sum_{i=1}^{N-1} \{1(\mathrm{x[n]}\,.\,\mathrm{x[n+1]} < 0 \;\hat{}\; |\mathrm{x[n]} - \mathrm{x[n+1]}| \geq \mathrm{T})$$

x[n] is MMG value in the segment at index n (n=1,…N) and T is the threshold deviation from the mean of 1000 ms window of muscle relaxation state.

3.5.2.2 Band energy features

3 band energy features have been determined from MMG signals, which is composed of 3 bands of which the energy of each frequency band of MMG signal, which reflects the energy associated with muscle relaxation or tremor (5–12 Hz), slow twitch (12–40 Hz) and fast twitch (40−100 Hz) muscle fibers is calculated using equation (3.7),

$$E = \sum_{k} P[k] \times \Delta f \tag{3.7}$$

where $P[k] = \frac{1}{N}|X[k]|^2$, E is the energy of MMG signal x[n], P[k] is the power spectrum, Δf is the band resolution and X[k] is the FFT of the MMG signal with length N.

3.5.2.3 Acoustic features

Four spectral frequency parameters have been extracted from pre-processed MMG signals as discussed in the following section:

Given a filtered MMG signal x[n], the magnitude spectrum X[k], k which is the total number of frequency bins in the spectrum, and the magnitude of MMG signal at k^{th} frequency bin |X[k]|,

a) Spectral centroid (SC)

The spectral centroid (SC) (equation 3.8) measures the centre of mass of the power spectrum, indicating the average frequency at which the power of MMG signal is concentrated (Nagineni et al., 2018).

$$SC = \frac{\sum_{k=0}^{N-1} k|X[k]|}{\sum_{k=0}^{N-1} |X[k]|} \tag{3.8}$$

b) Spectral spread (SS)

Spectral spread (SS) measures the distribution of frequencies around the SC or small range of frequencies, reflecting the range of uniformity of the spectral content in MMG signal (equation 3.9). It quantifies how the frequencies are spread out around the average

frequency of the MMG signal. A larger SS indicates a broader range of frequencies, suggesting more variable muscle activity. Conversely, a smaller spread implies a more consistent muscle contraction. SS in MMG under electrical stimulation provides valuable insights into the consistency and variability of muscle contraction.

$$SS = \frac{\sum_{k=0}^{N-1} (k - SC)^2 |X[k]|}{\sum_{k=0}^{N-1} |X[k]|} \tag{3.9}$$

c) Spectral flatness (SF)

Spectral flatness (SF) defined in equation 3.10 quantifies the uniformity of signal's energy distribution across different frequencies in the power spectrum. It is calculated by comparing the geometric mean to the arithmetic mean of the power spectrum. A higher SF indicates a more uniform distribution of power across different frequencies, which is typically associated with more random or complex muscle activity patterns, suggesting a mixture of different motor unit firing rates. Conversely, a lower SF indicates more synchronized or repetitive muscle activity, such as a steady contraction of muscle under NMES. SF in MMG during NMES provides insights into the muscle's response to NMES, revealing the degree of synchronization and the complexity in muscle activity.

$$SF = \frac{\prod_{k=0}^{N-1} |X[k]|^{\frac{1}{N}}}{\frac{1}{N}\sum_{k=0}^{N-1} |X[k]|} \tag{3.10}$$

d) Spectral flux (SFlx)

As shown by equation (3.11), the spectral flux (SFlx) measures the local change in

the power spectrum density between consecutive time frames, offering a measure of how quickly the frequency content of a signal changes over time (Khushaba *et al.*, 2014). In NMES MMG, SFlx provides insights into the stability and variability of muscle contractions throughout the stimulation process. It helps in understanding how the muscle reacts to changes in stimulation parameters and the overall dynamic of the muscle's mechanical response during NMES.

$$\mathrm{SFlx} = \sum_{k=0}^{N-1} \left(\sqrt{P[k]} - \sqrt{P[k_0]} \right)^2 \tag{3.11}$$

where $P[k_0]$ is a shifted frequency of P[k] , $P[k] = \frac{|X[k]|^2}{N}$, and $P[k_0] = \frac{|X[k-k_0]|^2}{N}$.

3.5.2.4 Hjorth mobility feature

The Hjorth mobility (HM) feature quantifies the deviation in the power spectrum of MMG signal (equation 3.12). HM calculates the mean frequency of the signal effectively serving as the standard deviation of the power spectrum (Shah et al., 2022).

$$\mathrm{HM} = \sqrt{\frac{\mathrm{var}(x'[n])}{\mathrm{var}\, x[n]}} \tag{3.12}$$

where $x'[n]$ denotes the derivative of the signal x.

3.5.2.5 Anthropometric features

Anthropometric features noted as weight, height, LUA, LLA, BMI, MUAC and SKT

were determined as detailed in section 3.5.

3.5.3 Construction of feature vector

Raw MMG features were transformed into a structured numerical data format employed to enable the ML model to process complex information for better prediction.

3.5.3.1 MMG feature vector

We extracted 12 MMG signal features to uncover any potential hidden relationship between the MMG signals and torque response which resulted into 310176 feature vectors as depicted in Figure 3.21.

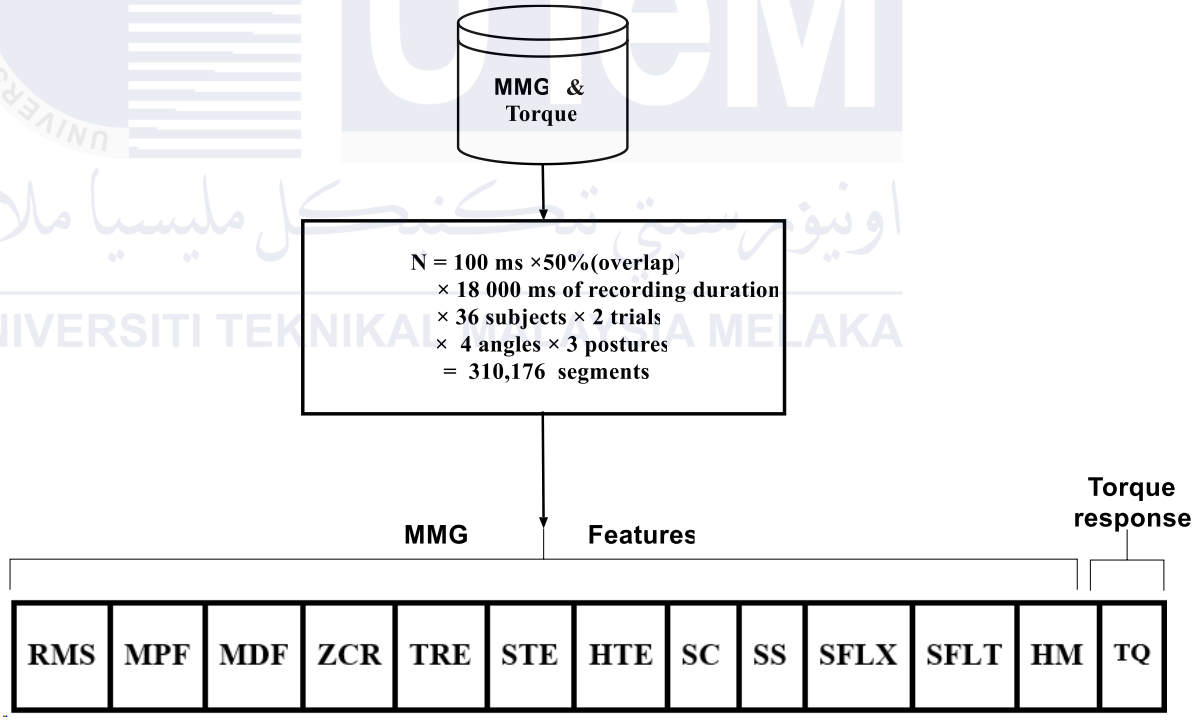

Figure 3.21:Formation of MMG feature vector.

3.5.3.2 Anthropometric++ feature vector

Recording anthropometric time series samples concurrently with torque signals is impractical due to the nature of the measurements. To address this, data augmentation was implemented for obtaining concurrent anthropometric and torque time series data using the jittering approach.

Data jittering, a technique widely used in machine learning for artificial data augmentation (Nourani *et al.*, 2021), was employed to generate synthetic anthropometric time series data. This method assumes that all anthropometric variables followed a normal distribution with a mean of zero and a standard deviation derived from three separate measurement as detailed in section 3.4.

To create the jittered data, a standard deviation δ derived from three measurements was randomized between (- δ, + δ) and added to the experimentally recorded mean of each anthropometric variable. This process generated multiple datapoints around the original measurement, simulating natural variability. The resulting synthetic anthropometric data were then scaled to match the size and temporal alignment of the torque variables, ensuring uniform patterns suitable for machine learning.

Anthropometric variables provide a strong prediction capability for the estimation of elbow flexion torque. While the addition of muscle contraction has shown a significant variation in torque estimation models, muscle contraction alone could not improve the torque estimation models (Green and Gabriel, 2012). From this observation, this thesis refers to the anthropometric++ features vectors to define the combination of 7 anthropometric and 2 MMG variables as depicted in Figure 23. Specifically, this thesis utilized 7 anthropometric variables (section 3.4) and the RMS and MPF (section 3.5) as muscle activation variables to

capture the time series relationship between anthropometric++ features and torque response, resulting in 310176 feature vectors (Figure 3.22).

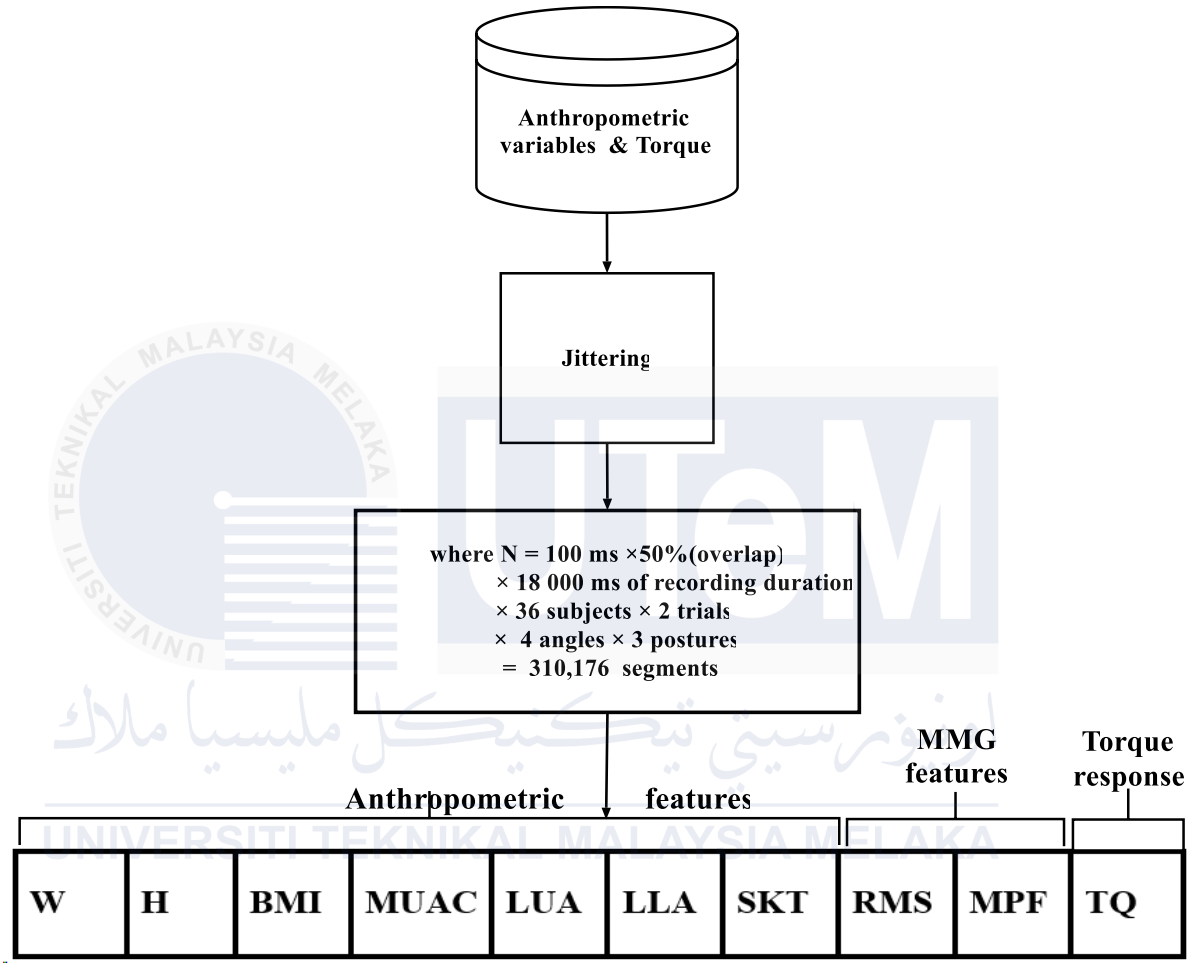

Figure 3.22: Formation of anthropometric++ feature vectors

3.5.4 Signal conditioning

The torque estimation pipeline depicted in Figure 3.23 utilizes physiological and anthropometric variables as features and requires several preprocessing steps. These include noise removal in MMG, data augmentation for anthropometric parameters, normalization to standardize extracted features on the same scale and frequency equalization of MMG and anthropometric variables through histogram-based binning for effective data learning.

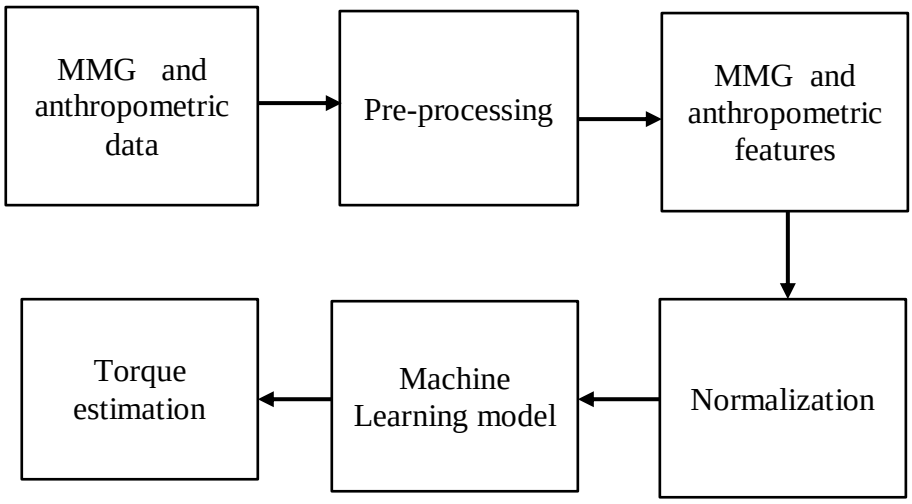

Figure 3.23: Summary of feature engineering process for elbow flexion torque estimation

3.5.4.1 Normalization and Outlier Removal

Some of the datapoints exhibit skewed distribution, which can adversely affect the machine learning algorithm. Additionally, unexpected spikes during the torque development and muscle relaxation exhibit outliers, necessitating data transformation to new standards. We applied the Z-score normalization to transform the data standardizing it to have a mean of 0 and a standard deviation of 1. This normalization brings the data to a common scale, making it more comparable reducing biases from varying distributions. However, data points with extremely high or low Z-scores, far from 0, were considered outliers and identified using equation (3.11),

$$Z = \frac{x - \bar{x}}{\sigma} \tag{3.11}$$

where $\bar{x} = \frac{1}{n}\sum_{i=1}^{n} x$, $\sigma = \sqrt{\frac{1}{n-1}\sum_{i=1}^{n} (x - \bar{x})^2}$, and $|Z|$ is the absolute value of the z-score. Datapoints within $|Z| \leq 3$ are generally considered normal and part of the underlying data

distribution. Datapoints within $|Z| > 3$ are potential outlier and are eliminated. It is a requirement to bring the new dataset to a common scale understandable by most machine learning algorithms. This is achieved by normalizing the dataset between 0 and 1 using the equation (3.12).

$$\overline{X} = \frac{X - X_{min}}{X_{max} - X_{min}} \tag{3.12}$$

where X is the original value of the feature, X_{min} is the minimum value of the feature dataset, X_{max} is the maximum value of the feature dataset, and $\overline{X}$ is the normalized value of the dataset.

3.5.4.2 Gray Relational Analysis (GRA)

Selecting features with substantial information is crucial for achieving high accuracy and generalization in machine learning models, while preserving the initial structure of the dataset. To evaluate the degree of association between MMG and anthropometric features with elbow flexion torque, we implemented an analysis of the Gray relational degree (GRD).

Consider elbow flexion torque $F = \{ F(k) \mid k = 1,2,\cdots,n \}$ and MMG or anthropometric++ features $X_i(k)) \mid k = 1,2,\cdots,n\}, i = 1,2,\ldots..m\}$ sequences, the relational degree of correlation between the elbow flexion torque and MMG or anthropometric++ features is expressed as:

$$\xi_i(k) = \frac{\min\limits_i \min\limits_k |F(k) - x_i(k)| + \rho . \max\limits_i \max\limits_k |F(k) - x_i(k)|}{|F(k) - x_i(k)| + \rho . \max\limits_i \max\limits_k |F(k) - x_i(k)|} \tag{3.13}$$

Using $\Delta_i(k) = |F(k) - x_i(k)|$, the sequence become $\Delta_i(k) = \Delta_i(1), \Delta_i(2),\ldots \Delta_i(n)$

Thus, equation (3.13) can be written as equation (3.14) :

$$\xi_i(k) = \frac{\min_i \min_k \Delta_i(k) + \rho \max_i \max_k \Delta_i(k)}{\Delta_i(k) + \rho \max_i \max_k \Delta_i(k)} \quad (3.14)$$

The value of ρ is suggested in the range between (0,1). However, the nominal value of ρ = 0.5463 was used. The mean GRD between the elbow flexion torque and MMG or anthropometric features is expressed in equation (3.15),

$$r_i = \frac{1}{n} \sum_{k=1}^{n} \xi_i(k), k = 1,2, \ldots n \quad (3.15)$$

where, *n* is total number of datapoints, *k* is the index of the datapoints considered for analysis, and *i* is the index of MMG variables.

3.5.4.3 Histogram based data binning

To mitigate the impact of uneven distribution on the correlation between MMG and elbow joint flexion torque, data was binned into a histogram based data binning. This process ensures proportional representation of all ranges of GRD, preventing bias and enhancing the generalization ability of the RFR model across varying correlation strengths (Srivastava et al., 2019). However, while the majority of GRD occupied the moderate to good correlation range, these GRD values appear dominant in bins reflecting the highest frequency distribution. A sample histogram of 2000 GRD values distributed around a mean GRD of 0.5 is depicted in Figure 3.24.

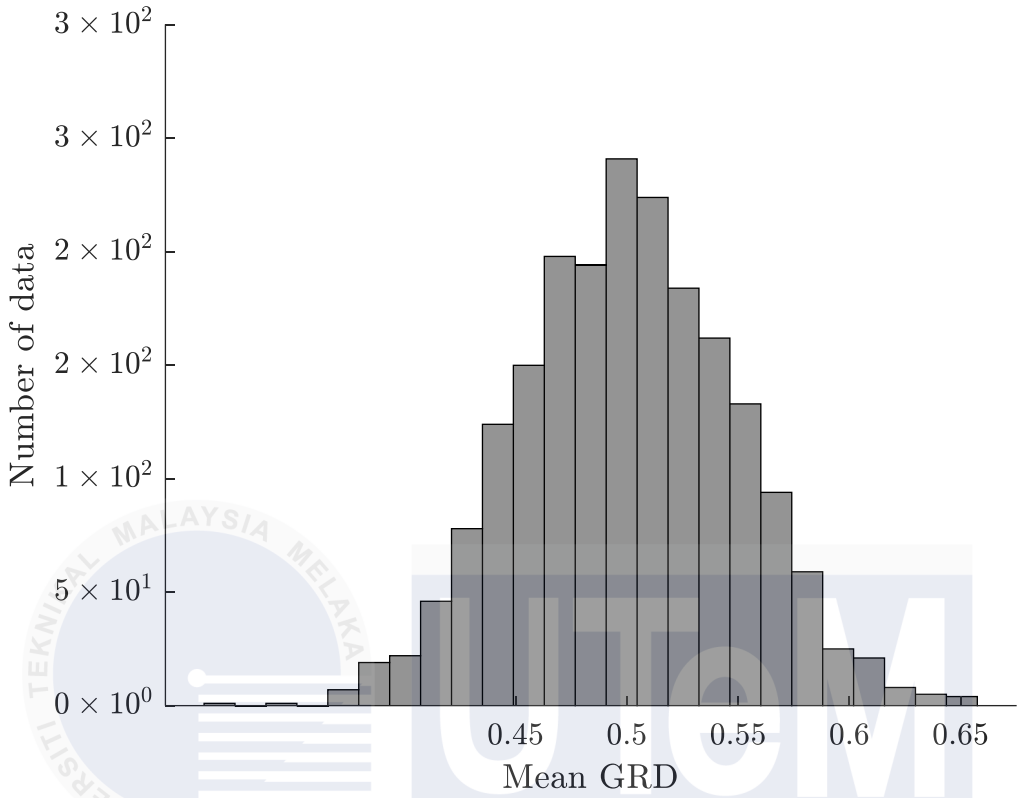

Figure 3.24: Sample Mean of GRD and dependent variables of the data representation indicates the frequency of data points within each bin per GRD value, ensuring that data is equally distributed across the bins.

3.6 Random Forest regression

For the RFR, numerous trees are employed to improve prediction accuracy and reduce the model overfitting. By averaging the output from multiple decision trees, RFR captures complex relationships between features and target output variables. This powerfulness makes it a robust tool for relating biomechanical variables.

3.6.1 Architecture and operation

RFR is a nonparametric regression that uses input random vectors $X \in X \subset R^P$ to predict a random response $Y \subset R$ by estimating the regression function $m(x) = E[Y[X| = x]$. Given the training sample of MMG and TQ, $D_n = ((X_1, Y_1),...., (X_n, Y_n))$ to construct an estimate $m_n: X \rightarrow R$ of a function of m, the regression function m_n noted as mean square error is evaluated to be consistent over X and sample D_n if $E[m_n(X) - m(X)]^2 \rightarrow 0$, $n \rightarrow \infty$.

RFR is built using randomized trees (*Mtry*), where each estimated point x , denoted as $m_n(x; \Theta_j , D_n)$, depends on independent random variables $\Theta_1, ...,\Theta_N$ which follows the same distribution as random variable Θ and the training set D_n. These trees are responsible for resampling the training set D_n and selecting successive splitting directions, as described in equation (3.15),

$$m_n(\mathbf{x}; \Theta_j, \mathcal{D}_n) = \sum_{i \in \mathcal{D}_n^{\star}(\Theta_j)} \frac{\mathbb{1}_{\mathbf{x}_i \in A_n(\mathbf{x}; \Theta_j, \mathcal{D}_n)} Y_i}{N_n(\mathbf{x}; \Theta_j, \mathcal{D}_n)} \tag{3.15}$$

where $\mathcal{D}_n^{\star}(\Theta_j)$ represent the set of data points selected before the tree construction (Bootstrap sample), N is the number of trees in the forest, $A_n(\mathbf{x}; \Theta_j, \mathcal{D}_n)$ denotes the cell containing input sample $\mathbf{x}$, $N_n(\mathbf{x}; \Theta_j, \mathcal{D}_n)$ is the number of preselected points (training sample) that fall into $A_n(\mathbf{x}; \Theta_j, \mathcal{D}_n)$. The individual Mtry are then combined to produce the overall forest estimate given by equation (3.16),

$$m_{N,n}(\mathbf{x}; \Theta_1, \dots, \Theta_N, \mathcal{D}_n) = \frac{1}{N} \sum_{j=1}^{N} m_n(\mathbf{x}; \Theta_j, \mathcal{D}_n) \tag{3.16}$$

A RFR utilizes multiple decision trees, each trained on different bootstrapped samples of the data, known as nodes. These bootstrapped samples are built with the same sample size presented in the original samples. Indeed, despite some samples being duplicates, a portion of the original samples is absent in grown trees. These omitted samples are known as out-of-bag (OOB) samples (Figure 3.25). The total number of decision trees generated in this process is denoted by the variable Ntrees.

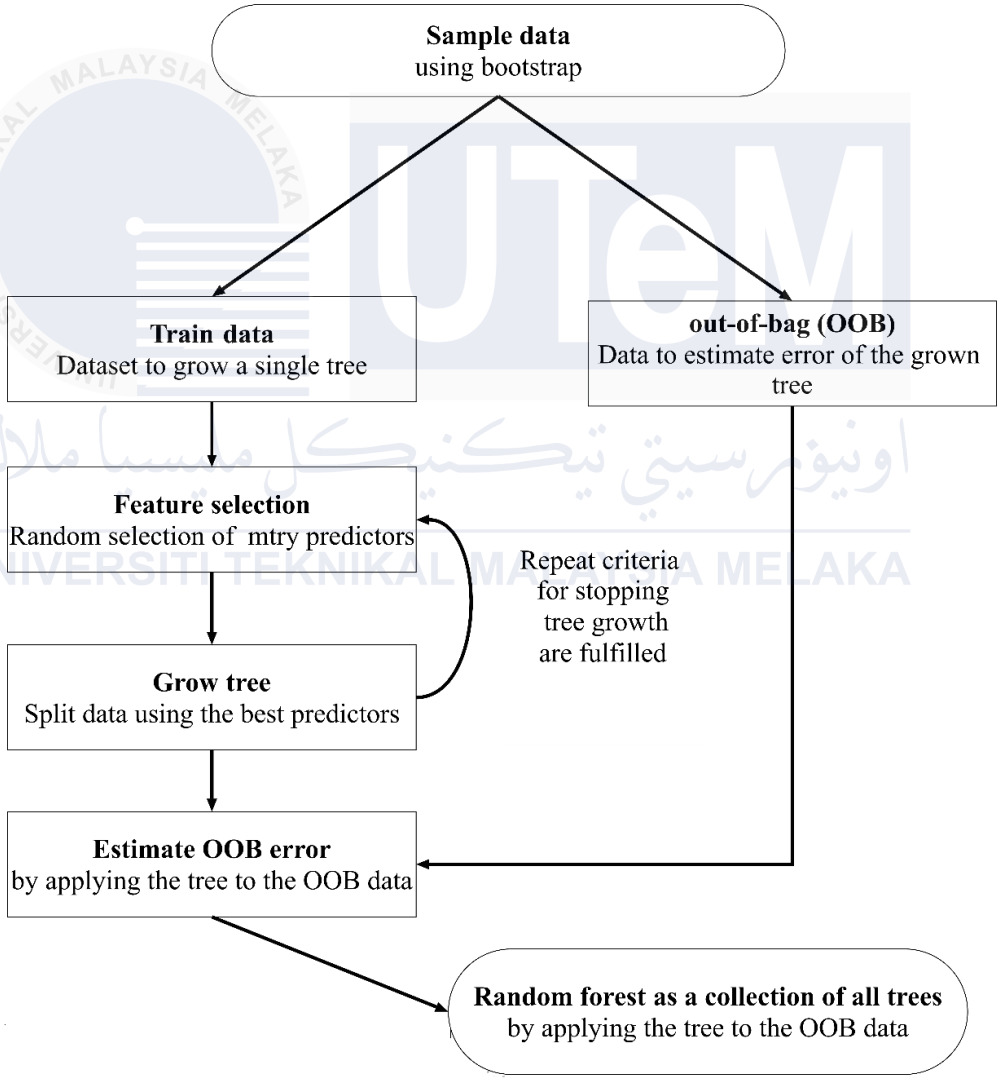

Figure 3.25: General functioning of the RFR (Boulesteix *et al.*, 2012)

Since individual trees can overfit the data, the accuracy of RFR is improved by an ensemble of bootstraps known as bagging, applied to the number of trees with high variance and low bias predictors. This ensemble method ensures that input variables to grow a tree are randomly split to overcome the correlations arising among aggregated trees. These variables are referred to as *MTry*. Based on the RMSE fitness function used in this research, the trees split data based on decision variables, aiming to improve prediction accuracy or gain in homogeneity and low OOB error. OOB predictor proportionally split into built trees to measure the prediction error, validating that RFR is parameter insensitive. However, while some studies have relied on tuning around default RFR hyperparameters, it was also reported inconsistent RFR model performance from default parameterization (Huang and Boutros, 2016). We tuned the hyperparameter of RFR and features obtained from MMG and anthropometric variables recorded for torque estimation using GLEO.

3.6.1.1 The Pseudocode of RFR

a) RFR Parameters definition

- Training dataset $D_n = [(X_1, Y_1),...., (X_{12}, Y_{12})]$: 70 %.
- Y = is the target torque value.
- Number of features = P (12 for MMG and 9 for anthropometri++ features)
- Node size $\in \{1,2,....., a_n\}$, where a_n is the number of data points in each tree.
- MaxNumSplits = Maximum number of splits allowed at each node.
- Ntrees = Number of decision trees.
- Mtry = Number of candidate features to be evaluated at each node.

b) Training

1) **for** i = 1, 2, ..., Ntrees **do**
2) Generate bootstrap samples D_i from D_n
3) Grow the decision tree using D_i
4) **for** a given node d
   (i) Choose Mtry from the feature space P.
   (ii) Select the best feature split and the cut point using Mtry.
   (iii) Divide the data, and ensure the tree splits do not exceed MaxNumSplits.
   (iv) Ensure that each node contains at least node size samples before splitting.
5) Repeat steps (i)–(iii).
   Find $m_{N,n}(\mathbf{x}; \Theta_1, \ldots, \Theta_N, \mathcal{D}_n)$ predicted per each splitting (Y_i).
6) **end for**

c) Prediction:

8) Using x_i and Ntrees, generate the predicted metric as shown in equation (3.16).
9) end for

3.6.2 Hyperparameters of RFR

To improve the generalization ability of the RFR model, several hyperparameters were considered. These include the number of learners in a forest denoted as *Ntrees*, the candidate features at each leaf-node (*Mtry*), the node size (number features in a node) denoted as *MinLeafeSize* and the maximum number of splits per tree (*Nsplits*).

Previous, approaches for optimizing the generalization of the RFR model relied on default RFR hyperparameter settings, where the *Minleafesize* was set to 5, and *Mtry* was

defined as $\frac{1}{3}$ of the total number of decision variables. However, given the complexity of the data, both *Ntrees* and *Nsplits* depend heavily on the data size and the software package involved. Consequently, the optimum generalization capability of the RFR model requires the application of metaheuristic algorithms to fine-tune both the input features and hyperparameters. As discussed in Chapter 2, while feature selection methods using both the wrapper and filter methods (Chandrashekar and Sahin, 2014), along with the general earning equilibrium optimizer (GLEO) were found crucial for identifying high informative features in biological datasets (Too and Mirjalili, 2021), this study uniquely optimized both feature and hyperparameter using GLEO.

3.6.3 Performance metrics

The statistical performance of the RFR model was evaluated using the coefficient of determination (R^2) defined by equation 3.18, the root mean square error (RMSE) and the slope (equations 3.17 and 3.19) defined as the gradient of the relationship between the measured and predicted values (Son *et al.*, 2024). The value R^2 ranges between 0 and 1, with higher values indicating better model performance. A range of slope near 0.8 to 1.05 suggests minimal bias in predictions whuich indicates that the model to fit the data.

A t-test was conducted to evaluate the repeatability of the RMSE and R^2, model's prediction metrics at 95% confidence level indicating a significance level of $\alpha = 0.05$ ($p < 0.05$).

$$\mathrm{RMSE} = \sqrt{\frac{1}{N}\sum_{i}^{N}(y_i - \hat{y}_i)^2} \tag{3.17}$$

$$R^2 = 1 - \left[\frac{\sum_i^n (y_i - \hat{y}_i)^2}{\sum_i^n (\hat{y}_i)^2}\right] \quad (3.18)$$

where N = number of experimental observations, y_i is the observed value for the i^{th} data point, and $\hat{y}_i$ is the predicted value for the i^{th} data point.

$$\text{Slope} = \frac{\sum_{i=1}^n (X_i - \overline{X})(Y_i - \overline{Y})}{\sum_{i=1}^n (X_i - \overline{X})^2} \quad (3.19)$$

Where $\overline{X}$ is the mean values in the input features variables and $\overline{Y}$ is the targetted TQ variables.

3.7 General Learning Equilibrium Optimizer

The discuusion on ML model optimization techniques in section 2.7 shows the superior perfoemance of Equilibrium Optimizer (EO) (Faramarzi *et al.*, 2020). While EO has demonstrated superiority over conventional metaheuristic algorithms for machine learning optimization, it is prone to getting trapped in local optimal. This limitation, particularly in engineering applications led to the development of an improved metaheuristic approach known as the GLEO (Too and Mirjalili, 2021). GLEO enhances separate feature selection and hyperparameter tuning by employing an improved general learning strategy. GLEO expands the search space and learns from diverse population candidates across multiple dimensions, thereby preventing particles from becoming trapped in local optima (referred to as the GLEO algorithm). In this thesis, GLEO'S performance is further compared with state-of-the-art methods such as the GRA for feature ranking and grid search algorithms for parameter optimization especially in datasets with large sample sizes but smaller feature dimensions. This comparison underscores GLEO's ability to handle vast

datasets efficiently while ensuring robust model performance.

The optimization process of the GLEO begins with the initialization of the population candidate's solutions as defined by equation (3.20),

$$X(i,d) = X_{lb} + rand_i^d(X_{ub} - X_{lb}),\ i = 1,2,3,...N,\ \text{and}\ d = 1,2,3,.....D \quad (3.20)$$

where X is the position of the candidate solution, X_{lb} and X_{ub} are the minimum and maximum values of the parameters' dimension, N is the number of particles, and D is the dimension of features and hyperparameters being tuned. Based on the fitness function defined by the RMSE in equation (3.17), the exploration strategy of GLEO (Figure 3.26) uses four potential particles with the best fitness value and their average given by equation (3.21), to form an equilibrium pool as shown in equation (3.22). This fitness value is used by the particles to update their positions by random selection among these 5 equilibrium solutions. The updating strategy of GLEO is that if the particle discovers a new position with a better fitness value than the previous best, this fitness is stored as best as shown by equation (3.23),

$$X_{eq(ave)} = \frac{X_{eq(1)} + X_{eq(2)} + X_{eq(3)} + X_{eq(4)}}{4} \quad (3.21)$$

$$X_{eq\ pool} = \{X_{eq(1)}, X_{eq(2)}, X_{eq(3)}, X_{eq(4)}, X_{eq(ave)}\} \quad (3.22)$$

$$X^d = X^d_{feq(d)} + (X^d - X^d_{feq(d)})F + \frac{G}{\lambda V}(1 - F) \quad (3.23)$$

where feq(d) = the candidate the particle should follow in dimension D.

$$G = G_0 F = \left(GCP\left(X^d_{feq\,(d)} - \lambda X^d\right)\right) \cdot F \tag{3.24}$$

$$F = \beta sign(r - 0.5)[\exp(-\lambda t) - 1] \tag{3.25}$$

$$GCP = \begin{cases} 0.5r_1 & r_2 \geq GP \\ 0 & r_1 < GP \end{cases} \tag{3.26}$$

where GP = 0.5 is the flag threshold to select a feature, λ , r_1, r_2 are random vectors between [0,1], whereas t is the time defined by equation (3.27),

$$t = \left(1 - \frac{Iter}{MaxIter}\right)^{\alpha \frac{Iter}{MaxIter}} \tag{3.27}$$

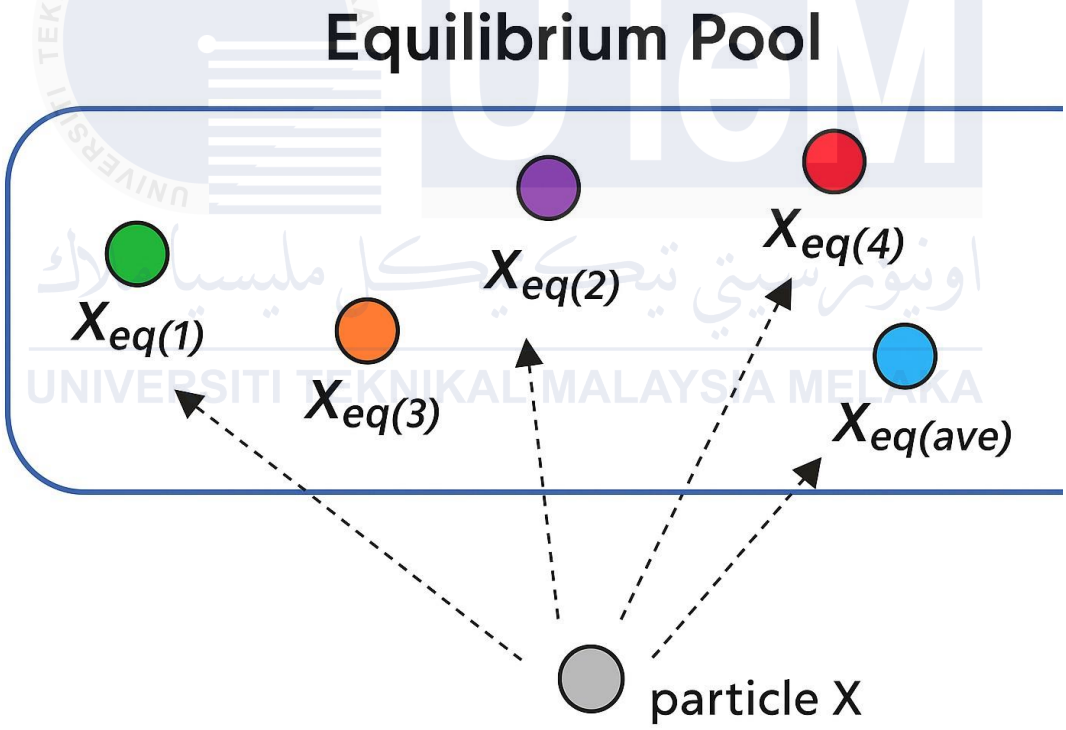

Figure 3.26: General learning Equilibrium strategy (Too and Mirjalili, 2021)

The pseudocode for the GLEO metaheuristic algorithm is defined as follows:

Input: Initialize a population of N particles using (3.20)

1) Assign the parameters $a = 1; \beta = 2;\ GP = 0.5,$ and $v = 1;$ (Faramarzi *et al.*, 2020).
2) **for** (later = 1 to Maxiter)
3) **for** i = 1 to N
4) Evaluate the fitness of X_i
5) Update four best-so-far candidates
6) **end for**
7) Compute $X_{eq(ave)}$ of $X_{eq(1)}, X_{eq(2)}, X_{eq\,(3)}, X_{eq\,(4)}$ using (3.21)
8) Construct the equilibrium pool as shown in (3.22)
9) **for** i = 1 to N
10) **if** X_i better than $pbest_i$
11) $refresh_i = 0$
12) else
13) $refresh_i = 1$
14) **end if**
15) **end for**
16) Accomplish memory saving
17) Compute t using equation (3.27)
18) **for** i = 1 to N
19) **if** $refresh_i == 1$
20) **for** d = 1 to D
21) Random one candidate from equilibrium pool
22) Store selected index in feq (i, d)
23) **end for**
24) **end if**
25) **end for**
26) **for** i = 1 to N
27) Construct F as shown in (3.25)
28) Compute G using (3.24)
29) Update the X_i using (3.23)
30) **end for**
31) **end for**

Output: Best candidate, $X_{eq\,(1)}$ (Too and Mirjalili, 2021)

3.7.1 Application of GLEO for FS, HT and FS-HT

The findings from studies on FS and ML model parameter optimizatiomn used GLEO for each process. From empirical experiement, GLEO was used for simultaneous FS and HT as indicated below:

a) Determination of the upper and lower bounds for features and hyperparameters

Using equation (3.20), the initial candidates were bounded by default ranges of features and hyperparameters, and baseline values at which the RFR obtained convergence during the preliminary experiments (Figure 3.27). The lower and upper bounds of the initial population solution of features are bounded between 0 and 1 defined by the size ($N \times D$), where N is the number of particles and D is the dimension of the features set. Each feature vector in the population contains flags of respective identification of features.

The initial solution for hyperparameters is arbitrary upper and lower bound values obtained by examining the convergence of the model around the default hyperparameters before the optimization process.

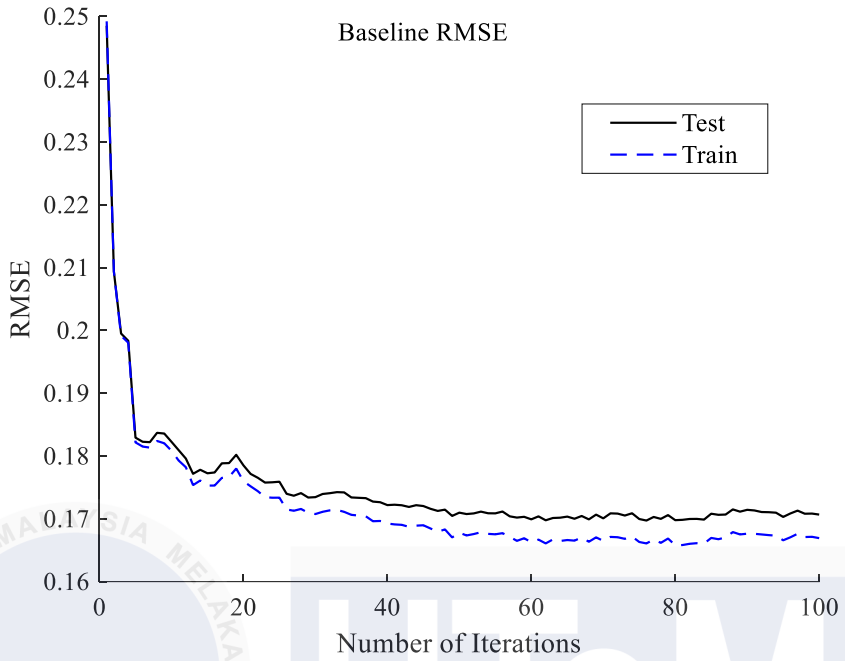

Figure 3.27: Convergence curve behavior of the baseline RFR obtained empirically from RFR configuratins at prior to RFR model optimization. The patterns show that the model successively converged during the development, supporting the expectation that optimization will further enhance its performance.

b) FS, HT and hybrid FS-HT using GLEO

The vector of candidates solution MMG and anthropometric++ feature selection is represented as a set of decision variables which are the twelve MMG or anthropometric++ features (refer to section 3.5). A feature is selected if the threshold of the corresponding flag is greater than 0.5 as defined by equation (3.26).

The initial population of the solution was random values of hyperparameters between 5 and 10 for the *MinleafeSize*, 4 and *Mtry* between the maximum number of features, *Ntrees* between 200 and 1500 and the *Nsplits* ranging between 100 and 500 determined during the initial benchmark test.

The updating function of feature selection (Figure 3.28) and hyperparameter tuning (Figure 3.29) followed the fitness function defined by the equation (3.17). Like other hyperparameters, the solution (vector of a parameter) was configured to be an infinity value at which the hyperparameter optimization of the GLEO-RFR obtained the highest fitness value (lowest RMSE) (Aljarah *et al.*, 2018).

The hybrid approach involves a single solution X_i which is mathematically represented by equation (3.29). The four first elements of the vector are RFR hyperparameters whereas the sequence F_1,.... F_{12} are feature flags for MMG and F_1,.... F_9 for anthropometric++ feature, where each feature selection is bounded by the GP value and the fitness value. The proposed model is depicted in Figure 3.30.

$$\begin{cases} X_i^d > 0.5, \text{feature is selected} \\ X_i^d \leq 0.5, \text{unselected feature} \end{cases} \quad (3.28)$$

$$X_i = [Ntrees, Mtry, MinLeafeSize, Nsplits \text{ and } F_1, \ldots, F_{12}] \quad (3.29)$$

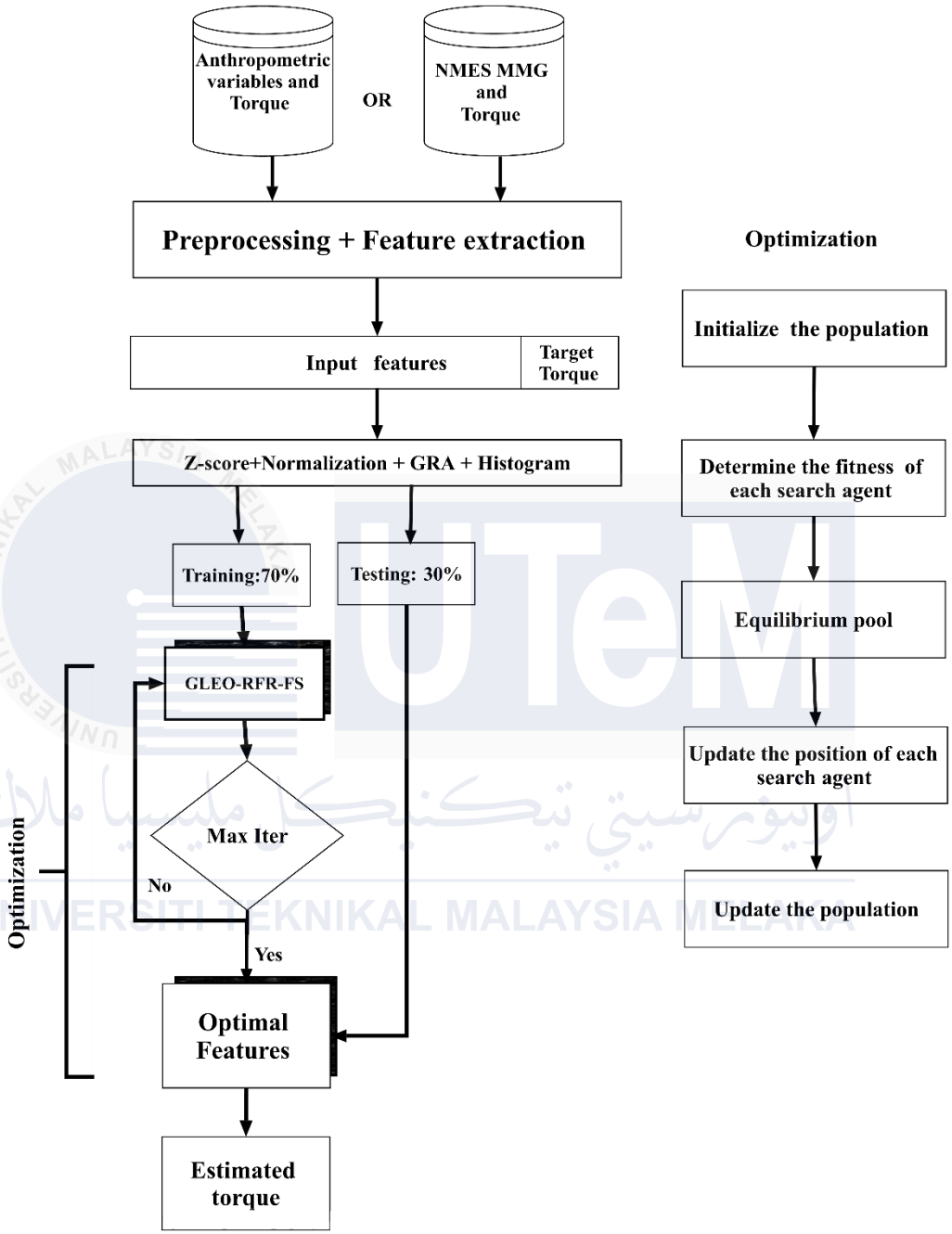

Figure 3.28:Application of GLEO for feature selection

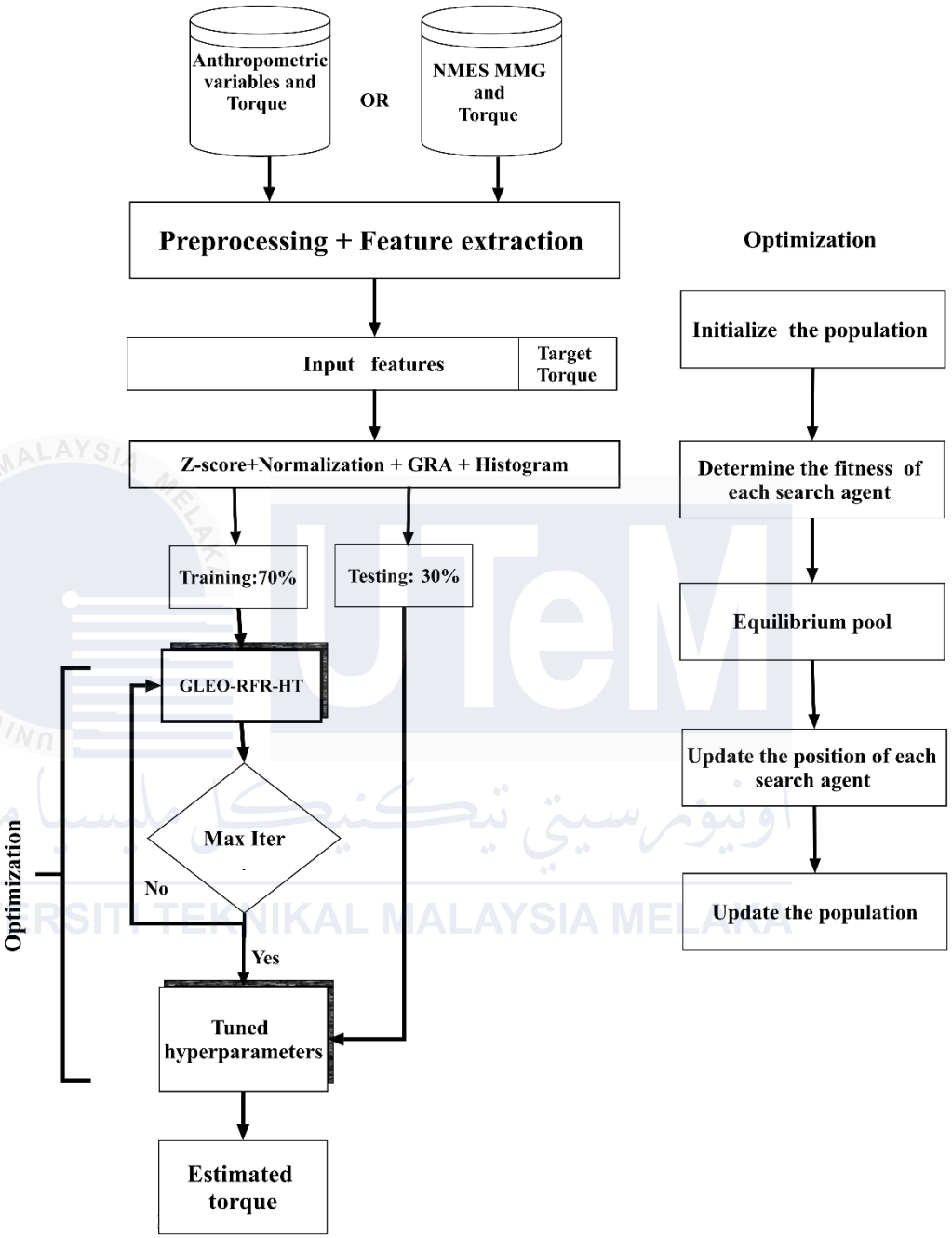

Figure 3.29: Application of GLEO for hyperparameter tuning

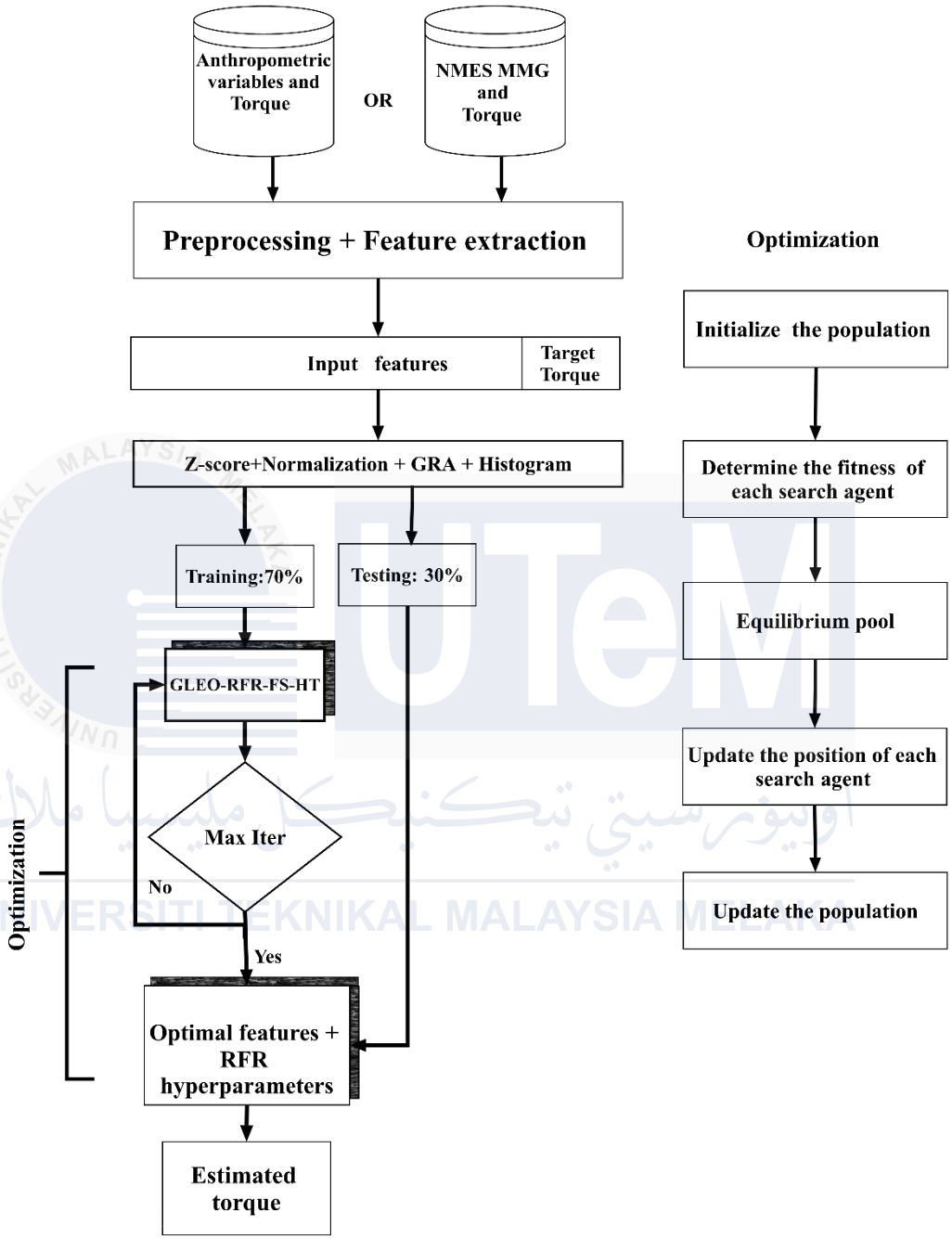

Figure 3.30: Application of GLEO for feature selection and hyperparameter tuning

3.8 Torque estimation

RFR machine learning models were developed using physiological and anthropometric++ vectors discussed in section 3.5. The generic models trained and evaluated on data collected at 12 configurations of angle and posture. Two types of models were developed and validated, namely the generic angle and forearm posture based on MMG features, and anthropometric++ feature based model. MMG feature vector were obtained from the dominant muscle fiber axis among the longitudinal, lateral and transverse axes (Figure 3.12). Anthropometric++ feature vectors were obtained as specified in section (3.5).

3.8.1 Effect of joint angle and forearm posture on MMG and TQ

Information from joint angle and forearm posture were recorded and examined for reliability before being used for torque estimation model development.

3.8.1.1 Dataset

The dataset involves three axes of acceleration signals and one TQ information for each posture and angle. Data was preprocessed for noise removal using filters detailed in section 3.5. Furthermore, the middle three cycles of 18 s were further processed for analysis. Subsequently, the middle 1s plateau of each cycle of the torque and MMG signals (Ibitoye et al., 2016) was determined using a moving window of 1000 ms at a threshold of 20% of the maximum muscle contraction above the baseline. As shown at Figure 3.31, this middle data was taken from the previously calculated segments as discussed in section 3.5.

A 512-point Short-Time Fourier Transform (STFT), with 50% window overlap was used to compute the MPF and MDF from the MMG signals. Thereafter, the TQ RMS, MMG RMS, MMG MPF, and MMG MDF were calculated for analysis using a 100 ms window

with 50% overlap. The TQ RMS, MMG RMS, MMG MPF, and MMG MDF were then normalized to their respective maximum levels of muscle contraction based on the conditions of four elbow joint angles and three forearm postures (Gonzalez *et al.*, 2018). In total, 216 TQ and MMG segments were obtained and further analyzed to understand the muscle's response to NMES in dynamic conditions.

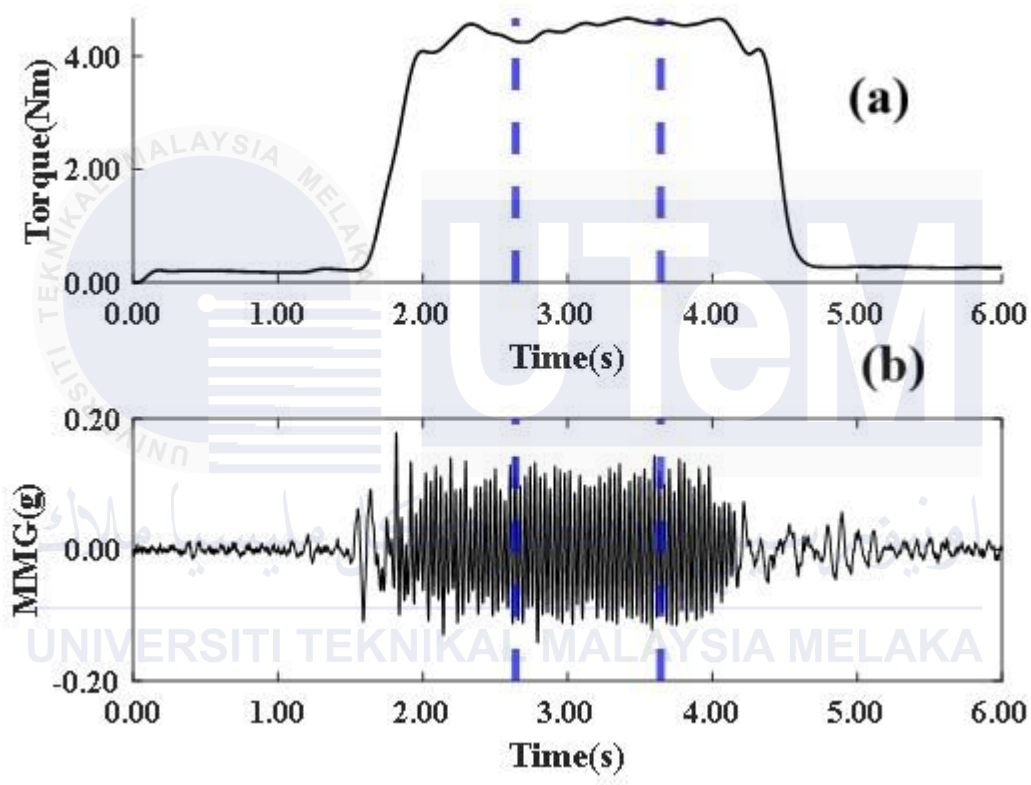

Figure 3.31: Filtered elbow joint torque **(a),** and MMG signal from the NMES of the BB muscle**.** The middle one-second data was used for the calculation of TQ RMS and MMG RMS, MMG MPF, and MMG MDF.

3.8.1.2 Statistical and reliability assessment

While the study used data collected from unconstrained elbow movements, the null hypothesis that there is no statistically significant difference among the MMG signals along the direction of propagation of these signals in the axes of muscle fibres was verified. If this

hypothesis is false, a crucial consideration is to assess the statistical association between MMG signals propagating in the muscle fiber axes and determine the dominant axis. This will mitigate overfitting, computational cost, and torque estimation accuracies.

In line with the objectives of this study, we evaluated the responsiveness of the BB muscle contractions and elbow flexion TQ with a varying elbow joint angle and forearm posture. The reliability of the MMG RMS, MMG MPF, and MMG MDF along with TQ RMS, was thoroughly analyzed before proceeding with elbow flexion torque estimation. These evaluations provide a foundation for understanding the relationship between muscle activity and torque output, which are crucial for developing accurate torque estimation models.

The relative reliability between participants's data was assessed by calculating the two-way mixed effects, absolute agreement, and single measurement intra-class correlation coefficient. ICC (2,1) with 95% confidence intervals (95%CI) defined by equation (3.30) (Latella et al., 2019) . The repeatability of NMES MMG and torque was measured employing the standard error of measurement (SEM), calculated using equation (3.32) (Atkinson and Nevill, 1998; Weir, 2005). To conclude that the observed change in torque and MMG was due to physiological effects rather than the measurements procedures, the minimal detectable change (MDC) was calculated across participants via equation (3.33) to determine the minimum difference required between trials for the change to be considered real (Weir, 2005). The within-participant coefficient of variation (CV), a measure of absolute reliability, was also calculated by using equation (3.34) and expressed as a percentage (CV%). CV % values $\leq 10\%$ were deemed to indicate low variability (Tous-Fajardo *et al.*, 2010). Within-participant CV was first calculated individually for each participant and then averaged across all participants. The reliability of the TQ RMS and MMG RMS measurement was assessed

as excellent (> 0.9), good (0.75 -0.9), moderate (0.5-0.75) and poor (< 0.05) (Latella et al., 2019). All variables represent the mean normalized (SD) of measurements.

$$\text{ICC (2,1)} = \frac{\text{MS}_\text{R} - \text{MS}_\text{E}}{\text{MS}_\text{R} + (\text{k}-1)\text{MS}_\text{E} + \frac{\text{k}}{\text{n}}(\text{MS}_\text{C} - \text{MS}_\text{E})} \tag{3.30}$$

where ICC = Intraclass correlation coefficients , MS_R = mean square for rows; = mean square for residual sources of variance; MS_E = mean square for error; MS_C = mean square for columns; n = number of subjects; k = number of raters/measurements (Latella et al., 2019).

$$\text{SDpooled} = \sqrt{\frac{(n_1 - i)SD_1{}^2 + (n_1 - i)SD_2{}^2}{n_1 + n_2 - 2}} \tag{3.31}$$

where SD_1 and SD_2 are the standard deviations of the two measurement trials, $n_1$and n_2 are the sample sizes of the two trials (typically the same if measurements were taken on the same participants).

$$\text{SEM} = \text{SDpooled}\sqrt{1 - \text{ICC}} \tag{3.32}$$

$$\text{MDC} = \text{SEM} \times 1.96 \times \sqrt{2} \tag{3.33}$$

$$\text{CV} = \text{SD}_{\text{pooled}} \,/\, \text{mean} \tag{3.34}$$

where the mean is found from the difference between the two trials, and $\text{SD}_{\text{pooled}}$ (equation 3.31) is the standard deviation of differences of the trials.

For each muscle fiber axis, we tested a null hypothesis that MMG and torque variables are not statistically significant among postures and elbow flexion angles. MMG RMS, MMG MPF, MMG MDF and TQ RMS were assessed for distribution using Shapiro-

Wilk's test (Monter-Pozos and González-Estrada, 2024). Since the data were, normally distributed, Analysis of variance (ANOVA), to evaluate the effect of BB muscle's geometry on NMES MMG and TQ across 4 elbow joints and 3 forearm postures.

A one-way ANOVA was utilized to assess the independent effect of each of the forearm postures and elbow joint angles on MMG and TQ variables. The combined effects of both posture and elbow joint angle on TQ and MMG variables were evaluated using a two-way analysis of variance (2-ways ANOVA) with repeated measurement (Sawyer, 2009). The Greenhouse-Geisser correction was applied when the assumptions of sphericity were violated, and a Bonferroni adjustment was used in post-hoc analysis to identify significant differences. A 95% confidence level was used to indicate the degree of significance ($\alpha = 0.05$), thus $p < 0.05$ was deemed statistically significant.

3.8.1.3 Determination of dominant MMG axis

The literature shows that there is a correlation between the lateral and transverse axis of muscle fibers using MMG signals (Travis W. Beck *et al.*, 2009). However, these studies used MMG sensors with low sensitivity and applied voluntary contraction which rendered the MMG signals contaminated with crosstalk. In addition, while the MMG signals from muscle contraction propagate in the three directions of muscle fibers axes, it was reported that the neural stimulation received a lower level of crosstalk in the transverse axis using ADXL 335 (Islam et al., 2014). However, these studies were carried out at a high level of submaximal MVIC, which motivated the examination of the behaviours of MMG signals from the muscle fiber axes during dynamic muscle geometry under the NMES equivalent of low levels of MVIC using the highly sensitive ADXL 313 MMG sensor. In this thesis, to observe the presence of a dominant MMG axis, MMG RMS, MMG MPF and MMG MDF

parameters from each elbow flexion joint angle and forearm postures defined in section 3.4 were statistically analyzed per the longitudinal (X), lateral (Y) and transverse (Z) axes of the muscle fibers. Thereafter, the axis exhibiting a majority of statistical significance across the investigated elbow joint angles and forearm postures indicated a dominant axis and was considered for subsequent analysis for elbow flexion torque estimation.

3.8.2 Development of torque estimation model using MMG features

MMG features obtained from the dominant MMG axis were used for subsequent RFR based torque estimation model.

3.8.2.1 Dataset

Muscle fiber activity along three axes was analyzed to determine the dominant direction of activation using MMG signals elicited from NMES applied to the biceps brachii (BB) muscle. Correspondingly, the behavior of torque (TQ) along these axes was also assessed. The axis exhibiting the highest MMG activation was selected for subsequent NMES-MMG feature extraction aimed at torque estimation. Twelve MMG features were extracted from this dominant axis and used to construct MMG feature vectors, each paired with TQ labels, resulting in 310,176 data points processed in accordance with the experimental procedures outlined in Section 3.5. These MMG-TQ feature vectors formed the basis for training the torque estimation model.

3.8.2.2 MMG feature based model

MMG feature vectors were analyzed for their correlation with the TQ RMS using GRD. The resulting GRD values were then grouped into 50 bins of width 0.02 using a histogram, as illustrated in Figure 3.25. Due to inter-subject variability in MMG feature expression, the dominant GRD feature values were observed across 24 bins, as presented in Figure 3.33. These binned GRD feature vectors were subsequently employed in the development of the torque estimation model.

To evaluate how the model behaves on unseen new data, we trained and tested the RFR model using 70% and leave out 30% of MMG features vectors. Additionally, the evaluation of the performance of RFR involves four key hyperparameters discussed in section 3.6. Hence, the GLEO −RFR − FS algorithm was used for feature selection, GLEO −RFR − HT for hyperparameter tuning, and a hybrid combination of both GLEO−RFR − FS − HT as detailed in section 3.7.

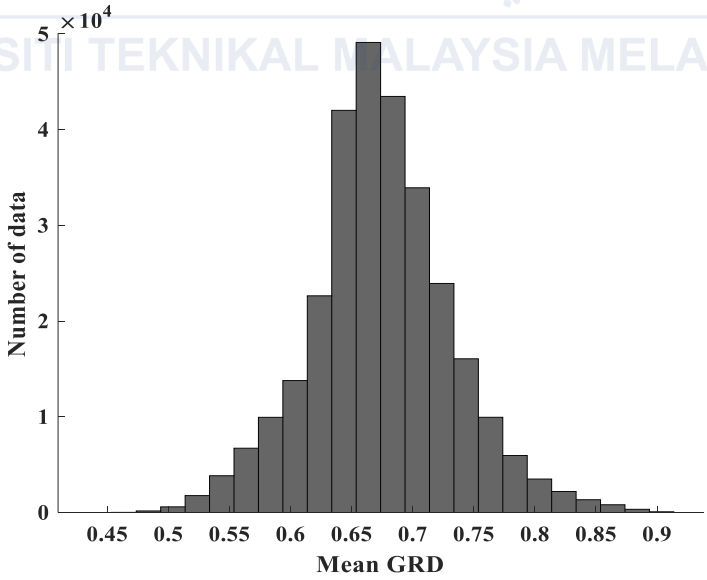

Figure 3.32: Mean of GRD MMG variables and elbow flexion torque the data representation indicates the frequency of data points within each bin per GRD value, ensuring that data is equally distributed across the bins.

3.8.2.3 Comparison of GLEO with other HT algorithms and ML

We compared the performance of the standard RFR, GLEO − RFR − FS and GLEO−RFR−FS−HT with the GRD ranking in a biological feature selection. Additionally, we compared the GLEO-RFR-HT with existing hyperparameter tuning found in the literature regardless of the estimation accuracy but focusing the improved performance. This study compared the generic RFR with other approaches hyperparameter tuning in the literature such as the semi-automated parameter adjustment, grid search, particle swarm optimization (PSWO), Salp Swarm Algorithm (SSA), genetic algorithm (GA), and the principle component analysis (PCA) alongside grid search.

The performance of both generic MMG and anthropometric++ features based models was monitored using the coefficient of determination referred to as R^2 and mathematically expressed as in equation 3.18 , the root mean square error (RMSE) in equation 3.17 , and the slope represented by equation 3.19. Additionally, the models were evaluated for performance using the convergence curve during the model training phases of the EO and GLEO algorithms.

The performance of the generic model with optimal features and hyperparameters was compared with the backpropagation neural network (BPNN) (Serbest *et al.*, 2023) with 4 hiden layer neurones and 12 inputs and support vector machine regression (SVR) models, which were also implemented in this research.

3.8.3 Development of torque estimation using anthropometric++ features

Physiological features reflecting the hughest prediction ability when combined with anthropometric variables were considered for constructing anthropometric++ features.

3.8.3.1 Dataset

Joint torque can be determined by the activation and sizes of muscles acting at a specific joint. The amount of contractile elements can be reflected by the muscle size and can be estimated by anthropometric variables. We evaluated the anthropometric and MMG-based muscle activation screening to estimate low muscle contraction. Seven anthropometric variables as well as electrically elicited MMG RMS and MMG MPF of BB muscle from 36 healthy subjects referred to as anthropometric++ features have been extracted (section 3.5). Technical Error of Measurement (TEM) was uses to assess the reliability of the anthropometric variables, and GRA assessed the correlation between NMES elicited torque with anthropometric++ features.

Athropometric feature vectors were used to develop angle and posture generic model. We used 70% for the model training and evaluated for performance exclusively on 30%.

3.8.3.2 Reliability assessment of anthropometric variables

Absolute reliability (TEM) is a measure of the precision or reliability of measurements taken by a rater or an instrument. TEM was used to quantify the degree of inconsistency or variability among repeated measurements of H, W, BMI, LUA, LLA, SKT, and the MUAC, and was determined using equation (3.35),

$$TEM_i = \sqrt{\frac{(X_i - X_j)^2}{2n}} \quad (3.35)$$

where i is the anthropometric variable, X_i and X_j are repeated measurements of the same subject's parameter, n is the number of subjects.

The reliability coefficient (%R) was obtained using equation (3.36),

$$\%R = 1 - \frac{(\sum TEM)^2}{SD^2} \times 100 \quad (3.36)$$

The relative TEM was calculated using equation (3.37),

$$\%\, TEM_i = \frac{TEM}{\bar{X}} \times 100 \quad (3.37)$$

where SD is the standard deviation of the anthropometric measurements and $\bar{X}$ is the mean of measured anthropometric variables. %R above 90% was considered reliable.

3.8.3.3 Anthropometric++ based model

The GRD was employed for assessment of the correlation between the torque with both MMG and anthropometric++ features. Although reliable, the impact of anatomical and subject characteristics on the GRD data distribution needs frequency equalization. Henceforth, GRD data was balanced using 50 bins featuring a bin size of 0.02 per each feature dimension (Figure 3.32). Thereafter, anthropometric features exhibiting the statistical significant correlation with the TQ such as the LUA and the MUAC, noted as factors of muscle activation under NMES were empirically deployed for torque estimation.

Furthermore, MMG RMS and MMG MPF were introduced to the pre-defined torque estimation models to assess the combined effectiveness of anthropometric++ on the baseline RFR models.

The RFR model was the developed anthropometric features and anthropometric++ features detailed in section 3.5. Like physiological features-based models, 70 % of data were used for model training and 30% were used for testing the model performance. Hence, optimum features and tuned hyperparameters were determined for a RFR model along the GLEO algorithm for feature selection (GLEO-RFR-FS), hyperparameter tuning (GLEO-RFR-HT), and a hybrid combination of both (GLEO-RFR-FS-HT), as detailed in section 3.7.

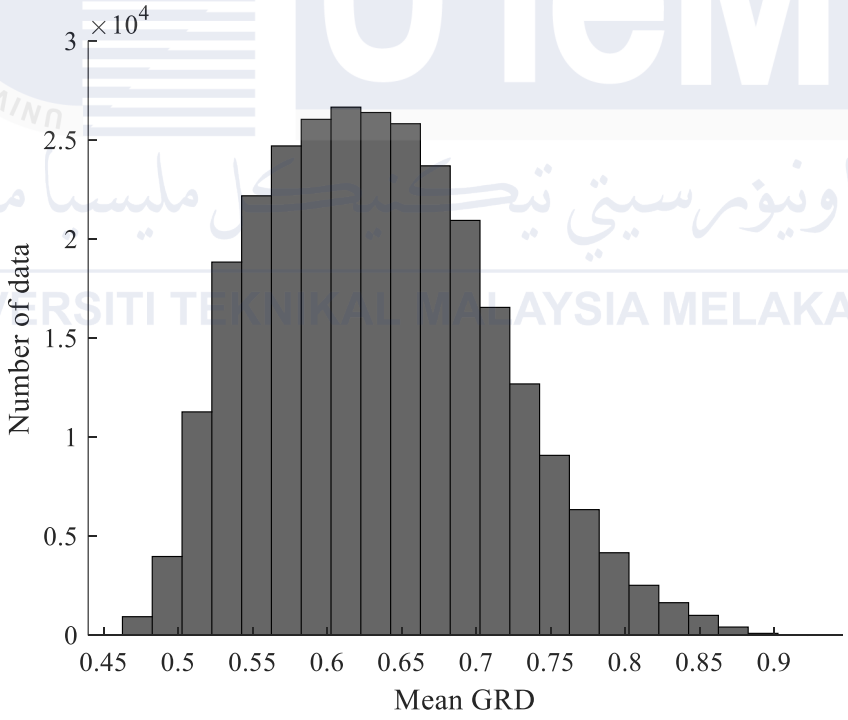

Figure 3.33: Histogram-based distribution of mean correlation (Mean GRD) between anthropometric variables and torque data is structured by binning data based on correlation levels. Each bin represents a range bounded by minimum and maximum GRD values, allowing for stratified grouping of indices where torque and anthropometric correlations fall within each specified range.

3.8.4 Validation of torque estimation models

Conventional validation and system validation have been implemented in this research using 70% for training and hold-out 30% portion of the data for testing . System validation was implemented by assessing the model performance on the real-world MMG and anthropometric++ features to deploy the model in practical conditions (Figure 3.33). The validation process involves comparing predicted torque values against experimentally measured data, ensuring the model's accuracy and generalizability. Statistical metrics, including R^2 and RMSE have been employed to evaluate prediction performance. This experimental validation investigates the responsiveness of the RFR torque estimation model developed using physiological features detailed in section 3.4. It particularly validates the predictability of the model discussed in section 3.8.2 and 3.8.3 using unseen physiological and anthropometric data obtained across the configurations of four angles and three forearm postures. Like physiological features-based models, 7 anthropometric and 2 MMG features vectors extracted from section 3.4. were used for the deployment of the developed torque estimation following the configurations of four angles and three forearm postures. This real-world validation not only verifies the robustness of the model but also highlights its potential applications in clinical and biomechanical settings.

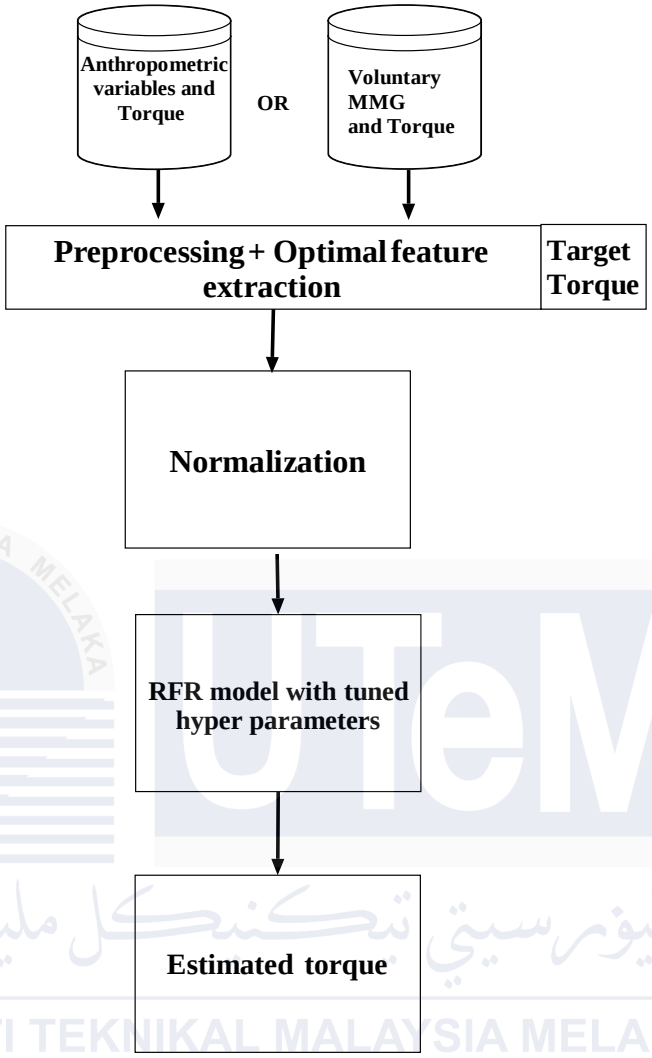

Figure 3.34: Application of the torque estimation models on real word unseen dataset.

3.9 Summary

This chapter discussed the methods and protocols used for the NMES-MMG and anthropometric data acquisition. The data validation ,the preprocessing techniques including the filtering and signal segmentation were also enclosed. Further, the feature extraction employed for RFR ML models used for the estimation of the elbow flexion torque were discussed. The next chapter presents the results obtained from these experiments along with discussion.

CHAPTER 4

RESULTS AND DISCUSSION

This chapter reports the research results and discusses the findings along with their scientific significance in relation to observations within the previous studies.

4.1 Descriptive statistics

Descriptive statistical analysis of the subjects was performed to evaluate the suitability of the sample population in relation to the research objectives.

4.1.1 Subjects' details

Table 4.1 presents the details of the 36 healthy male subjects who participated in this study. All the subjects fell within the second and third BMI quartiles, thereby excluding individual in the malnutrition and obese categories. The recruitment of subjects from two out of a total of these specific BMI quartiles clarifies that this research focussed on healthy human subjects, aligning with the outlined hypotheses of this thesis.

Table 4. 1:Descriptive variables of experimental subjects

Variables (n=36)	Mean	SD	Range
Age (Years)	22.2400	2.9400	18−28
Body Mass (Kg)	67.2080	6.8610	55.000 − 89.5400
Height (m)	1.7220	0.0540	1.630 − 1.8400
BMI $\left(\frac{\mathbf{kg}}{\mathbf{m^2}}\right)$	22.6780	2.4620	18.166−28.8140

4.1.2 Anthropometric variables

Table 4.2 presents the anthropometric variables of the subjects recruited for this study. The anthropometric variables cover a broad range of the weight, height, LUA, LLA, and SKT of the global population across various diversities.

Table 4. 2:Anthropometric variables of subjects

Variables (n=36)	Mean	SD	Range
MUAC (cm)	28.5851	1.9360	24.000 – 31.000
LUA (cm)	18.4893	1.2481	16.000 – 21.000
LLA (cm)	25.8993	2.3052	23.000 – 29.000
SKT (cm)	0.5250	0.2040	3.400 – 11.000

4.1.3 Reliability of anthropometric variables

The TEM, %TEM, and %R for three experimental sessions are shown in Table 4.3. The reliability analysis (%R) demonstrated excellent outcomes exceeding 97% for all the measurements. These measurements showed a high reliability above the acceptable %R threshold of 90%.

Table 4.3: Intra-tester reliability of anthropometric variables between familiarization, NMES, and validation sessions

Anthropometric parameter (n=36)	TEM	%TEM	%R
W(kg)	0.1430	0.2130	99.9560
H(cm)	0.0070	0.4594	97.9242
BMI$\left(\frac{kg}{m^2}\right)$	0.2061	0.9091	99.3071
MUAC (cm)	0.1192	0.6442	99.1033
LLA (cm)	0.1390	0.5380	99.6370
LUA (cm)	0.2031	0.7270	98.9040
SKT (cm)	0.2410	0.5990	98.6323

4.2 Effect of elbow joint angle and forearm posture on MMG and TQ

MMG and torque data across different elbow joint angles and forearm postures were evaluated to determine the repeatability of the experiment to meet the research objectives.

4.2.1 Dataset

Each subject performed a total of 12 NMES experimental trials, generating TQ and MMG signals as detailed in Section 3.4. Each trial produced three study segments per subject, resulting in a total of 216 MMG and TQ study segments.

4.2.2 Reliability analysis of TQ and MMG signals

The reliability ICC(2,1) of measured outcomes ranged from 0.6880 to 0.8230 for TQ RMS and from 0.5220 to 0.7610 for MMG RMS, across all investigated elbow joint angles and forearm postures. The highest CV% was observed at 60° for the neutral position. The minimum detectable change (MDC) ranged from 0.2650 to 0.4240. A paired-sample t-test revealed a non-significant difference in MMG RMS and TQ RMS across all two trials for each configuration ($p > 0.05$) (Tables 4.4 and 4.5).

Table 4.4: Test-retest reliability of torque signals (n = 36), ICC(2,1) (95% CI), $p < 0.05$

Torque	Angle	Posture	ICC(2,1)(95% CI)	*p-value*	SEM	MDC	CV (%)
Normalized TQ RMS	10^0	N	0.828 (0.746, 0.883)	*P < 0.01*	3.9630	0.2650	2.5600
		P	0.794 (0.697, 0.860)	*P < 0.01*	4.5570	0.2780	5.9100
		S	0.715 (0.576, 0.804)	*P < 0.01*	5.9620	0.3100	4.9300
	30^0	N	0.769 (0.660, 0.843)	*P < 0.01*	5.8640	0.3380	6.1110
		P	0.687(0.521, 0.779)	*P < 0.01*	6.7270	0.3270	4.0570
		S	0.823 (0.739, 0.879)	*P < 0.01*	4.5440	0.2990	13.2130
	60^0	N	0.691 (0.528, 0.639)	*P < 0.01*	11.1490	0.4240	19.2600
		P	0.715 (0.581, 0.806)	*P < 0.01*	6.0330	0.3130	4.9570
		S	0.696(0.450, 0.746)	*P < 0.01*	9.0510	0.4100	3.8400
	90^0	N	0.707(0.422, 0.733)	*P < 0.01*	9.5920	0.4240	9.4890
		P	0.688(0.539, 0.720)	*P < 0.01*	8.7940	0.3800	14.1890
		S	0.762(0.650, 0.839)	*P < 0.01*	5.8050	0.3300	3.7200

Table 4.5: Test-retest reliability of MMG signals (n = 36),ICC(2,1) (95% CI), $p < 0.05$

MMG	Angle	Posture	ICC(2,1)(95% CI)	*p value*	SEM	MDC	CV%
Normalized MMG RMS	10^0	N	0.795(0.685, 0.869)	$p < 0.001$	8.0140	0.4900	9.2960
		P	0.672(0.537, 0.677)	$p < 0.001$	9.4490	0.4570	7.1420
		S	0.438(0.323,0.643)	$p = 0.214$	10.0450	0.3710	13.8400
	30^0	N	0.622(0.495,0.675)	$p < 0.001$	7.3770	0.3320	2.1569
		P	0.716(0.583,0.807)	$p < 0.001$	9.4320	0.4900	23.304
		S	0.579(0.303,0.679)	$p < 0.001$	16.4150	0.7010	19.2370
	60^0	N	0.527(0.547,0.782)	$p < 0.001$	9.4350	0.4070	8.4920
		P	0.679(0.507,0.774)	$p < 0.001$	9.8000	0.4790	3.6290
		S	0.589(0.503,0.743)	$p=0.132$	6.8500	0.2960	2.8260
	90^0	N	0.629(0.336,0.682)	$p < 0.001$	8.8928	0.4040	3.3530
		P	0.634(0.503,0.731)	$p < 0.001$	10.7680	0.4930	5.8100
		S	0.608 (0.431,0.692)	$p < 0.001$	3.1300	0.1380	2.2470

4.2.3 Normality test

In this study, three physiological parameters MMG RMS, MMG MPF, MMG MDF and TQ RMS have been selected for the identification of the dominant MMG axis, that was latter used for the extractionof physiological features (section 3.5). Table 4.6. presents the results of the normality assessment of these parameters for four elbow joint angles at three postures of the forearm.

Table 4.6: Results for normality test of normalized TQ RMS and MMG RMS ($p < 0.05$)

Parameter	Skewness mean (SD)	Kurtosis mean (SD)
TQ RMS	0.555(0.395) − 0.618(0.395)	-0.749(0.292)−0.139(0.292)
MMG RMS	-0.473(0.219)−0.298(0.219)	-1.102(0.226)−0.313 (0.226)
MMG MDF	-0.231 (0.222) −0.494(0.222)	-0.233(0.172) −-0.538(0.172)
MMG MPF	0.323(0.265)−1.278(0.265)	-0.715(0.894)− 2.358(0.894)

The Shapiro-Wilk's Test showed that normalized values of TQ RMS, MMG-RMS, MMG-MPF, and normalized MMG-MDF were found to be normally distributed across the configurations of angles and postures groups at ($p < 0.05$). Hence, parametric analysis was

used to perform further statistical analysis of the data comprising MMG features and TQ data.

4.2.4 effect of elbow joint angle and forearm posture on tq rms

This section presents the results of experimental analysis of the biomechanical effects of angle and forearm postures on the TQ RMS.

Table 4.7: Elicited elbow flexion TQ RMS measured at the elbow joint angle of 10°, 30°, 60°, and 90° along the neutral, pronation and supination positions.

Elbow Joint Angle		**10°**		**30°**		**60°**		**90°**	
Forearm Posture		**Mean ± SD**		**Mean ± SD**		**Mean ± SD**		**Mean ± SD**	
	Neutral	0.4510	0.1770	0.5700	0.1990	0.7410	0.1830	0.6020	0.2050
	Pronation	0.4320	0.1720	0.5100	0.1700	0.6500	0.1700	0.5950	0.1790
	Supination	0.4000	0.1680	0.4520	0.1970	0.5040	0.2030	0.4630	0.1930

Table 4.7 and Figure 4.1 present the mean normalized TQ RMS (SD) obtained from neutral, pronation and supination forearm postures and at 10°, 30°, 60°, and 90° of elbow flexion. The TQ RMS in the neutral position was higher than the values obtained in the pronation and supination positions ($p < 0.05$). The mean elbow flexion TQ RMS along the neutral, pronation, and supination positions of the hand are illustrated in Table 4.7. and Figure 4.1 (a). The forearm posture had a significant effect on the TQ RMS ($p < 0.05$) at all elbow joint angles. The joint angle was found to have a significant effect on the TQ RMS in the neutral ($p < 0.05$), pronation ($p < 0.05$), and supination ($p < 0.05$) positions. The forearm posture and elbow joint angle had a significant combined main effect on the TQ RMS ($p < 0.05$; Figure 4.2). The post hoc test revealed a significant TQ RMS ($p < 0.05$) at all angles between the neutral and supination positions and among all postures at 60°.

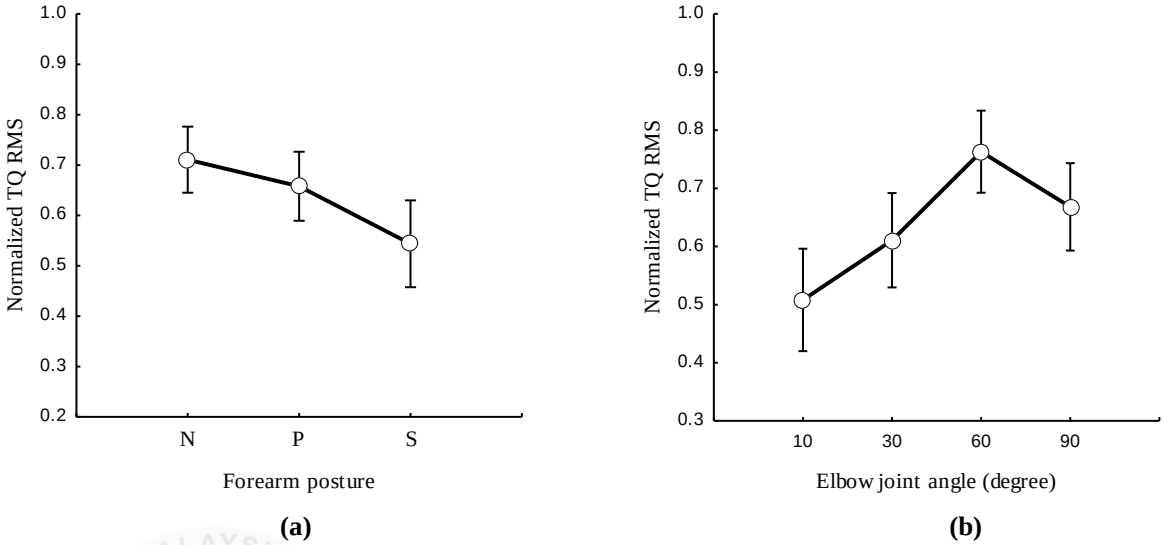

Figure 4.1: (a) Normalized TQ RMS at neutral(N), pronation(P), and supination(S) postures of the forearm and (b) the elbow flexion at 10°, 30°, 60°, and 90°.

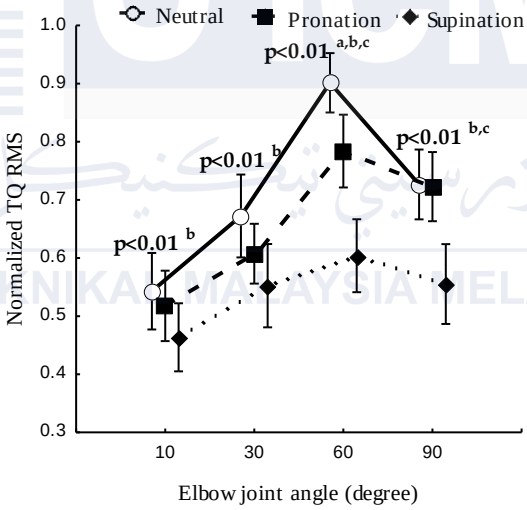

Figure 4.2: Normalized TQ RMS at the neutral, pronation, and supination positions of the forearm and at elbow joint angles of 10°, 30°, 60°, and 90°. The statistical significance between posture conditions is indicated (a-neutral and pronation, b-neutral and supination, c-pronation, and supination).

In the present study, the reliability of TQ ranges from moderate to good (ICC(2,1), $p < 0.05$). The results indicate that changes in forearm position significantly impacted the TQ RMS (Figure 4.1). This suggests that variations in forearm posture alter muscle length, shape, and size, which in turn influence the spinal excitability of the BB muscle (Forman *et*

al., 2019). These changes may also affect the BB muscle's responsiveness to NMES, implying that the effect of forearm posture on TQ RMS is linked to modifications in muscle morphology, leading to deviations from expected outcomes. Despite maintaining consistent NMES intensity, the reduction of the TQ RMS in the supination position may be due to decreased current density as the depth of the BB muscle increases, thereby limiting the recruitment of deeper muscle fibers (Paillard, 2018).

This research demonstrated that elbow joint angle significantly affected TQ RMS (Nunes *et al.*, 2020). Significant differences were observed between the neutral and supination positions across 10°, 30°, and 90° of elbow flexion, as well as across all postures at 60°. These variations are due to the disruptions in cross-bridge formation between actin and myosin, which impair force production (Petrofsky and Phillips, 1980). As the elbow flexion angle increased beyond 60°, TQ RMS showed a decreasing trend. This suggests the range of joints at which the resting muscle length optimizes cross-bridge interactions between actin and myosin filaments. The decline in TQ RMS at higher joint angles may result from mechanical interference between neighbouring actin filaments at shorter muscle lengths, and stretching of actin and myosin at longer lengths, both of which affect NMES-induced TQ RMS (Hou *et al.*, 2016).

As the BB muscle originates from the radial tuberosity, elbow flexion reduces its length due to variations in moment arms, which in turn impacts neural excitation levels (Thfipaut-Mathieu *et al.*, 1988) and influences fiber-type composition (Islam, Sundaraj, Ahmad and Ahamed, 2013; Ortega et al., 2023). NMES-induced torque is generally greater at intermediate elbow joint angles (Krueger *et al.*, 2014), reflecting variations in tendon morphological adaptations (Kubo et al., 2006) and sarcomere length changes (Kubo et al., 2006).

This study employed a consistent NMES intensity; however, during elbow flexion, some deeper motor units remained unactivated, leading to a reduction in torque output originating from fewer motor units being recruited per electrode site (Paillard, 2018). This suggests that muscle depth variations influenced by forearm posture and elbow joint angle, affect the electrical excitation of the muscle.

4.2.5 Effect of elbow joint angle and forearm posture on MMG RMS

The relationships between the forearm posture and MMG RMS (Figure 4.3, left) and between the elbow joint angle and the MMG RMS (Figure 4.3, right) and the main effect of the forearm posture and elbow joint angle on the MMG RMS (Figure 4.4) were assessed at the longitudinal, lateral, and transverse axes of BB muscle fibers.

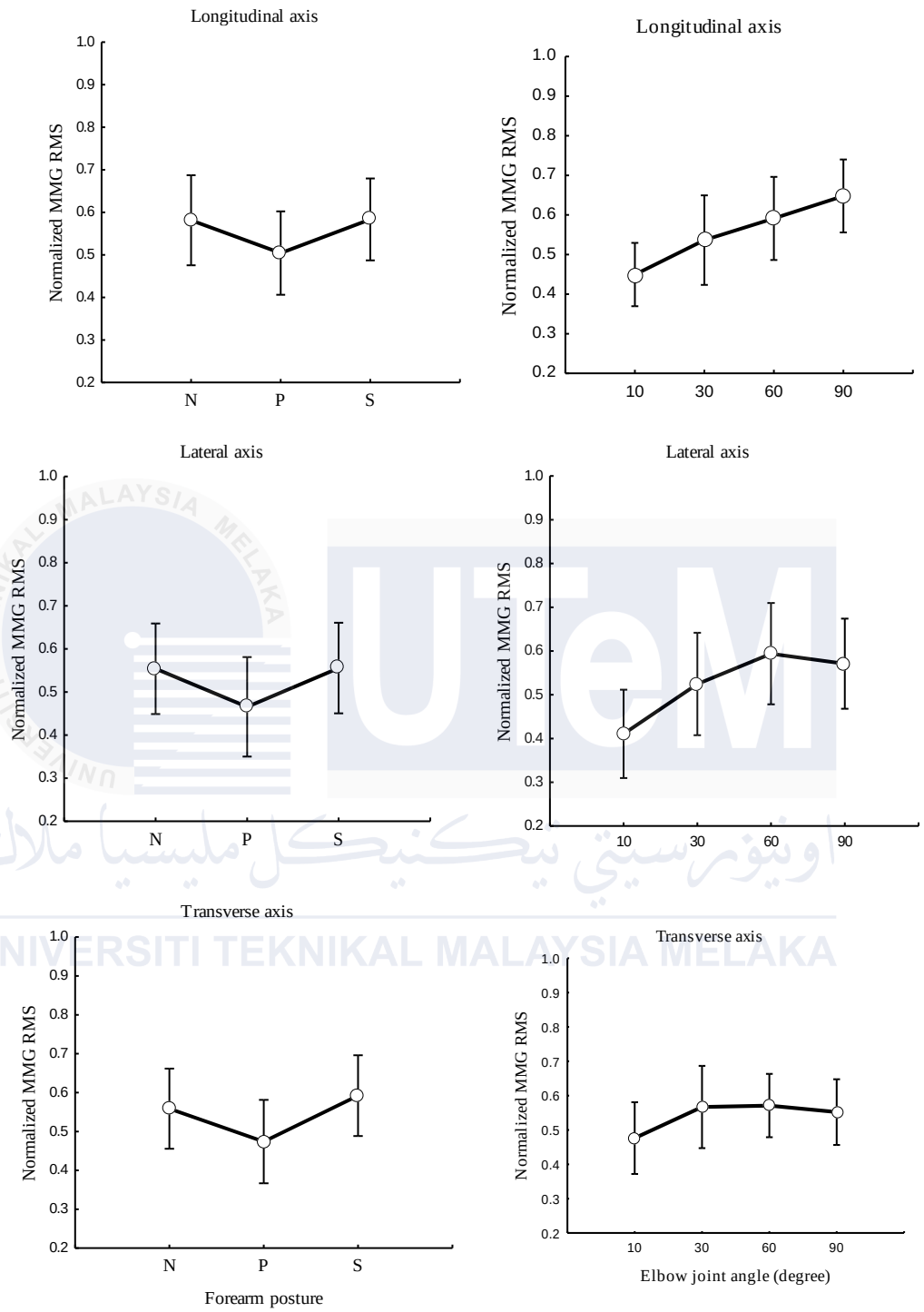

Figure 4.3:Behaviors of the normalized MMG RMS along the longitudinal, lateral, and transverse axes of the BB muscle fibers at the neutral (N), pronation (P), and supination (S) positions (left) and elbow joint at 10°, 30°, 60°, and 90° (right).

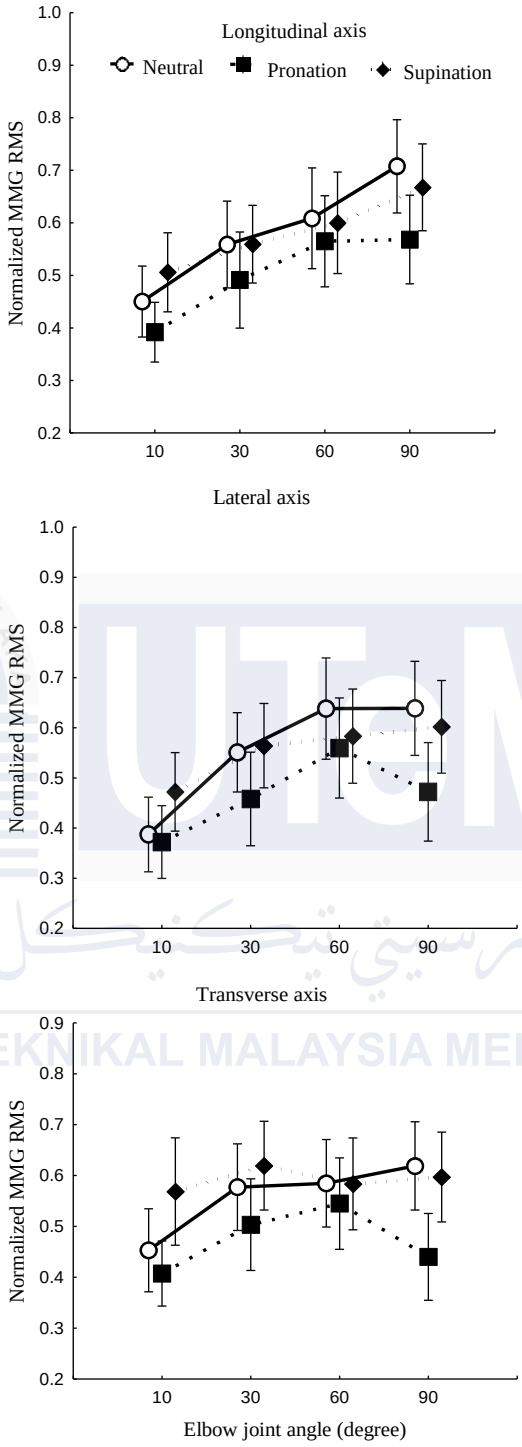

Figure 4.4: MMG RMS along the longitudinal, lateral, and transverse axes of the BB muscle with the forearm in neutral, pronation, and supination positions and the elbow joint at 10°, 30°, 60°, and 90°.

The forearm posture exhibited a significant effect on the normalized MMG RMS across the longitudinal ($p < 0.05$), lateral ($p < 0.05$), and transverse ($p < 0.05$) axes.

Similarly, the elbow joint angle significantly influenced the normalized MMG RMS along the longitudinal ($p < 0.05$), lateral ($p < 0.05$), and transverse ($p < 0.05$) axes of the BB muscle fibers. However, the interaction between forearm posture and elbow joint angle did not show significant main effects on MMG RMS along any of the axes—longitudinal ($p > 0.05$), lateral ($p > 0.05$), or transverse ($p > 0.05$).

Alterations in forearm posture significantly affect the electrophysiological properties of the BB muscle (He and Mathieu, 2018), driven by the interplay between inhibitory and excitatory circuits within spinal pathways. During elbow flexion with forearm rotation, changes in muscle fiber dimensions lead to variations in their firing rates, as captured by MMG signals (Talib *et al.*, 2018). This study found that forearm posture had a notable impact on MMG RMS across the longitudinal, lateral, and transverse axes, suggesting that posture-induced neural modulation alters the signal transmission to the BB muscle (Mogk *et al.*, 2014). The lack of significant differences in MMG RMS at 30° and 60° may be due to reduced excitability in deeper muscle fibers, stemming from a muscle length shorter than the resting length of the BB muscle (Forman *et al.*, 2019). These findings are relevant for postural correction and optimizing neural output in rehabilitation settings.

Across the elbow joint angles examined in this study, the pronation posture consistently produced the lowest MMG RMS (Figure 4.3, left, and 4.4), a result consistent with previous research (Kleiber *et al.*, 2015). This reduction in MMG RMS may arise from the inhibition of BB muscle fiber activation, which shares synaptic pathways with the brachioradialis muscle. NMES studies suggest that isolating the BB muscle from the brachialis and brachioradialis muscles can lead to a higher level of excitation, which is diminished in pronation (Kleiber *et al.*, 2015). This reduction may also be linked to increased stiffness in the muscle-tendon complex under higher torque output (Figure 4.1, left, and 4.4).

Furthermore, variations in MMG RMS across all three axes suggest that forearm posture influences muscle performance metrics.

An increase in elbow joint angle corresponded to an increase in MMG RMS, aligning with Barry's findings which demonstrated higher MMG amplitudes in electrically stimulated gastrocnemius muscles at shorter lengths (Barry, 1987). Recruitment of deeper motor units depends on the number of fibers under the stimulation electrodes, as supported by earlier research (Paillard, 2018). Altought the amplitud of MMG also may depend on the filtering capacity of the tissue between the acceleration sensor, recruited muscle fibers increases as elbow flexion angle increases (Beck *et al.*, 2005). This study also observed that MMG RMS along the lateral and transverse axes increased between 10° and 30° of elbow flexion and then decreased as the angle exceeded 60° (Figure 4.3, right). Similar to previous observations (Gobbo *et al.*, 2014), MMG amplitude peaked at 90% of muscle length and diminished at shorter or longer lengths, implying that MMG can serve as an indicator of optimal muscle strength when torque measurements are complex, such as in neurologic amputees.

The significant differences in MMG RMS across the longitudinal, lateral, and transverse axes with varying elbow angles reflect the dynamic properties of the muscle, influenced by viscosity, thickness, and stiffness, which change with muscle length. These results suggest that variations in MMG RMS along the lateral axis correspond to fiber resonance frequency, while those along the transverse axis are indicative of longitudinal stiffness (Barry, 1987).

4.2.6 Effect of elbow joint angle and forearm posture on MPF and MDF

The study investigated the relationship between forearm posture and both MPF (Figure 4.5, left) and MDF (Figure 4.6, left), as well as the effect of elbow joint angles on

MPF (Figure 4.5, right) and MDF (Figure 4.6, right). Measurements were taken along the longitudinal, lateral, and transverse axes of the BB muscle fibers. Furthermore, the interaction between forearm posture and elbow joint angles was assessed for its impact on MPF (Figure 4.7, left) and MDF (Figure 4.7, right) across all three axes, providing insight into muscle response under varied mechanical conditions.

Forearm posture significantly impacted the normalized MPF and MDF across the longitudinal ($p < 0.05$), lateral ($p < 0.05$), and transverse ($p < 0.05$) axes. Similarly, elbow joint angles showed significant effects on MPF and MDF along all BB muscle fiber axes ($p < 0.05$). However, the interaction between forearm posture and elbow joint angles did not have a significant effect on MPF and MDF along the longitudinal axis ($p > 0.05$). In contrast, a significant interaction effect was found along the lateral and transverse axes ($p < 0.05$). Notably, significant differences in MPF and MDF ($p < 0.05$) were detected across all postures at a 10° of elbow angle along the lateral and transverse axes. However, no significant differences were observed in MPF and MDF between the neutral and pronation positions ($p > 0.05$) and among all posture combinations at 30° and 60°.

This study found that increasing the elbow joint angle led to a reduction in MPF. This reduction is linked to sarcomere lengthening or shortening beyond optimal actin-myosin overlap when the muscle is isolated. As elbow flexion increases, muscle diameter expands, further impacting the interaction of actin and myosin filaments (Pasquet *et al.*, 2005).

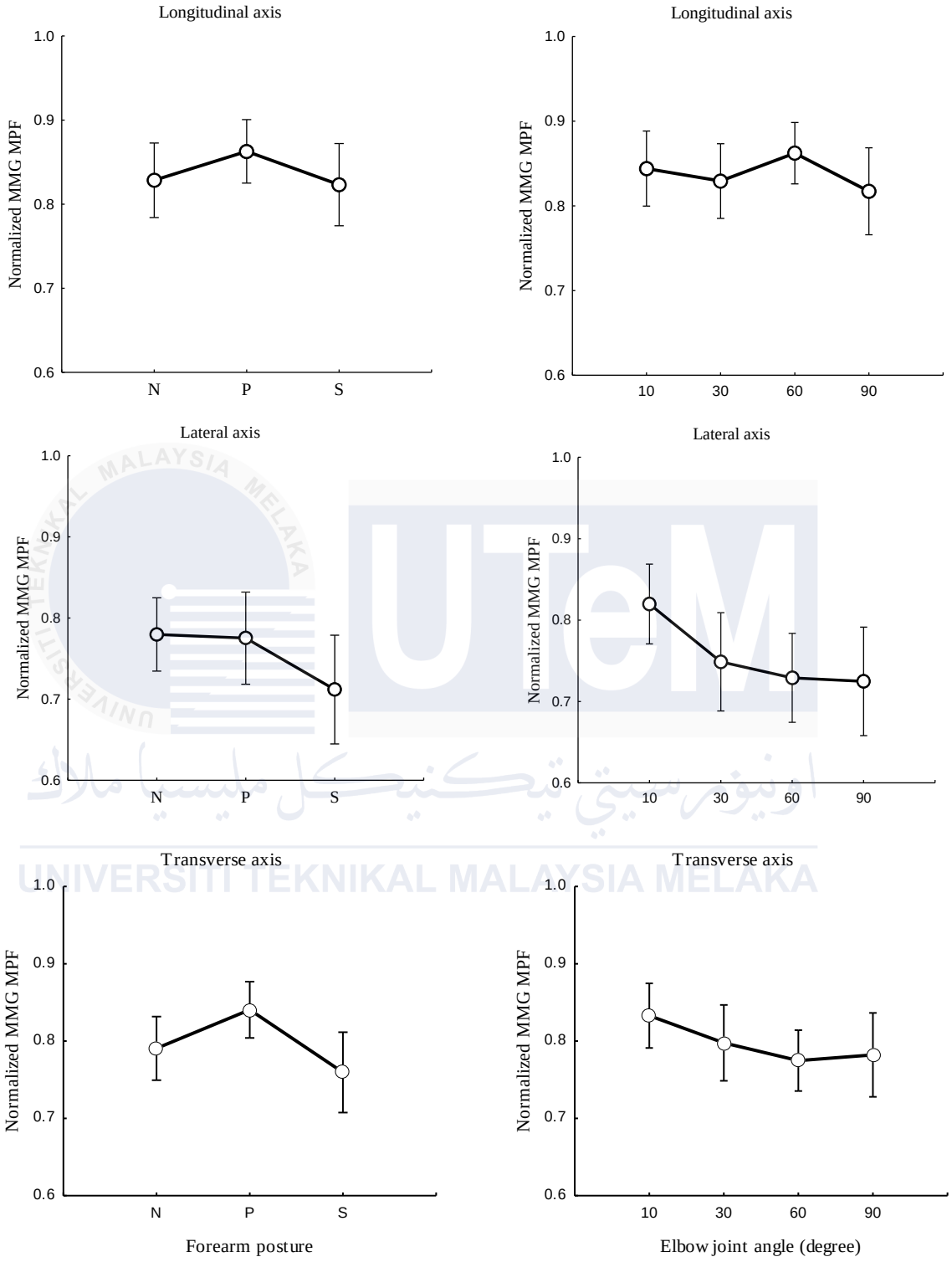

Figure 4.5:The relationship between MPF along the longitudinal, lateral, and transverse axes of the BB muscle fibers at the neutral (N), pronation (P), and supination (S) (left) positions, and elbow joint at 10°, 30°, 60°, and 90° (right).

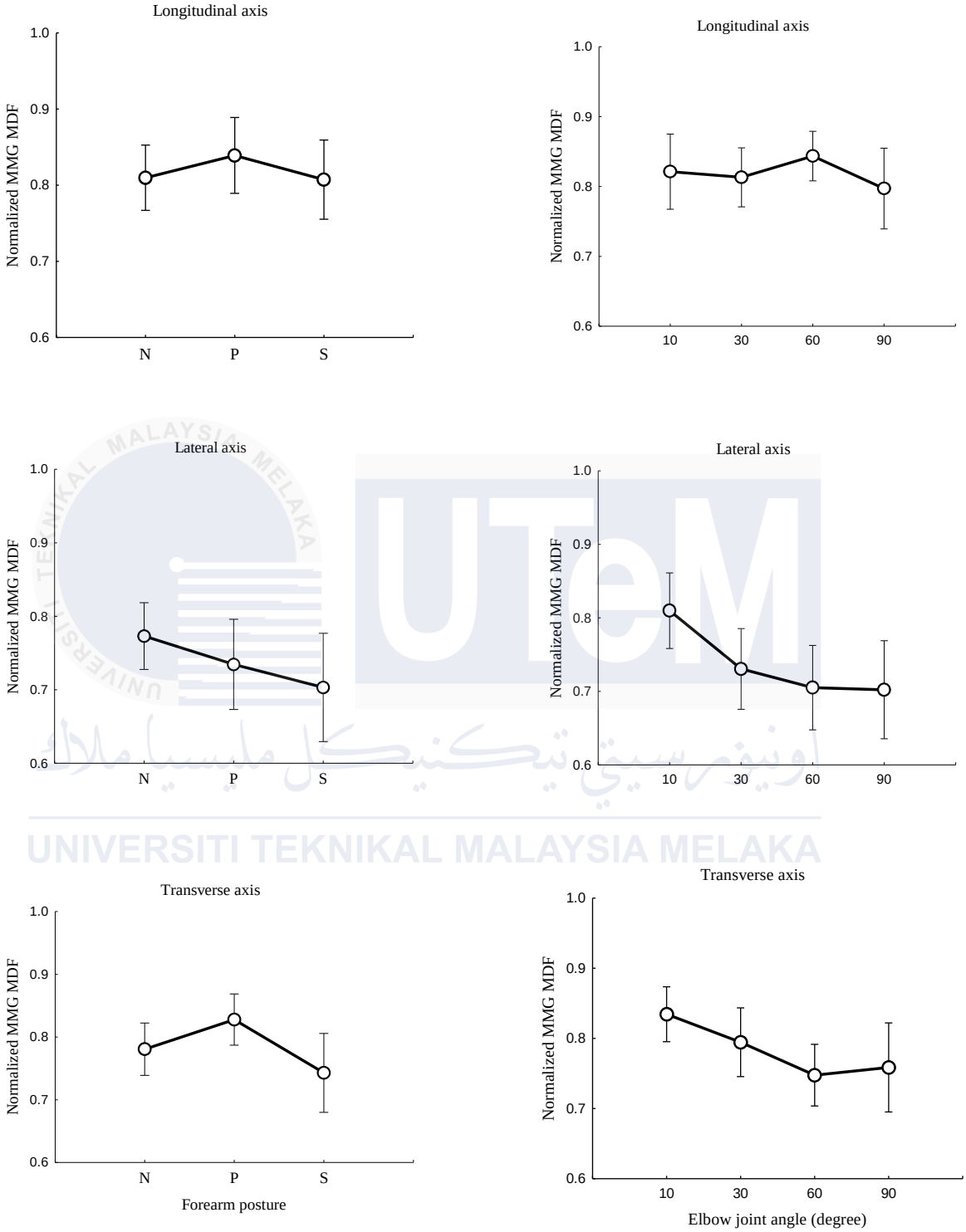

Figure 4.6: Behaviors of MDF along the longitudinal, lateral, and transverse axes of the BB muscle fibers at the neutral (N), pronation (P), and supination (S) positions (left) and at elbow joint angles of 10°, 30°, 60°, and 90° (right).

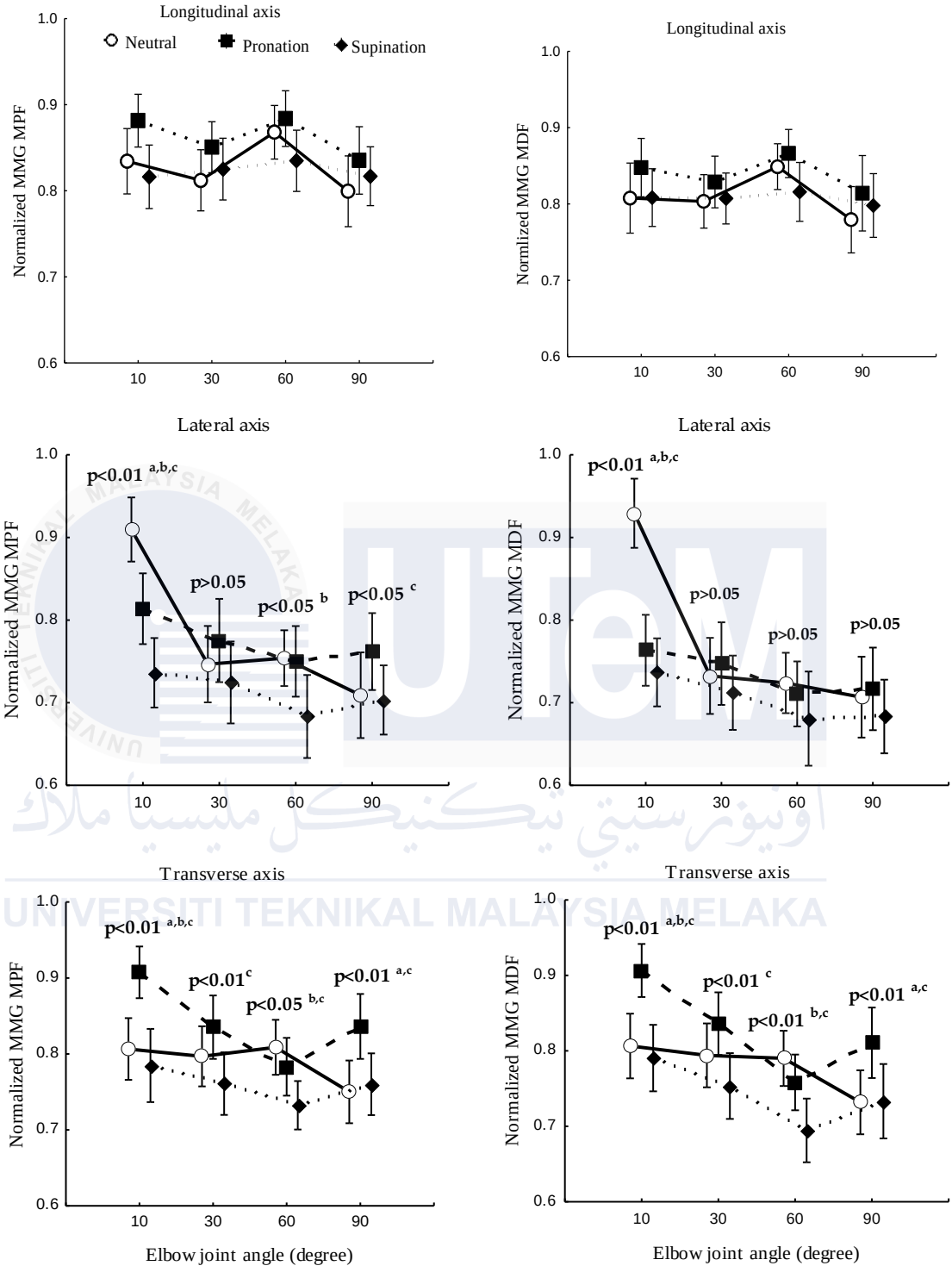

Figure 4.7: Behaviors of MDF (left) and MDF (right) along the longitudinal, lateral, and transverse axes of the BB muscle fibers at the neutral, pronation, and supination positions (left) and with the elbow joint at 10°, 30°, 60°, and 90° (right). The statistical significance between posture conditions is indicated (a-neutral and pronation, b-neutral and supination, c-pronation, and supination).

This result aligns with Frangioni's research, which demonstrated that MPF rises with increased muscle length in the electrically stimulated gastrocnemius of a frog. Studies on voluntary contractions also reported a significant decrease in MMG MPF at shorter muscle lengths (Qi *et al.*, 2011). These findings, along with previous evidence, suggest that MMG responses are governed more by muscle fiber contraction and relaxation times than motor unit firing patterns (Gobbo *et al.*, 2014).

The observed decrease in MMG MDF was also influenced by muscle length (Talib *et al.*, 2018) and increased with longer muscle lengths (Vaz *et al.*, 1997). In contrast, the decrease in MDF with greater elbow joint angles indicates the motor unit synchronization (Krishnan *et al.*, 2011). The variation in MDF across the longitudinal, lateral, and transverse axes highlights differing activation levels of muscle fibers depending on elbow joint angles and forearm postures. Specifically, MPF and MDF along the longitudinal axis exhibited patterns of increase and decrease correlating with rising TQ RMS, indicating that frequency features along this axis reflect NMES-evoked TQ patterns. However, along the lateral and transverse axes, both MPF and MDF showed a significant decline, suggesting non-linear dynamics due to muscle architecture, tendon unit behavior, and sensory feedback from muscle spindles. This non-linear relationship of MMG frequency features positions spectral parameters as promising candidates for limb TQ estimation, offering potential avenues for future exploration. Moreover, MPF, MDF, and RMS in this study surpassed the variability in multi-degree-of-freedom tasks (Kong *et al.*, 2021) and demonstrated better performance than EMG for prosthetic control in limb-amputee populations (Kim *et al.*, 2022).

A significant main effect of angle or posture on RMS and a non-significant difference of the combined main effect imply that the RMS at angle and posture alone can reflect the muscle recruitment required for the torque estimation. Overall, an increase in

elbow joint angle and TQ showed significant changes in the MPF and MDF across the transverse and lateral axes than the longitudinal axis. A significant difference in the MPF and MDF at the transverse axis (Figure 4.7) favours the transverse axis for feature extraction useful for machine learning models. Specifically, for a total of 12 configurations of muscle activation, the combined main effect of the angle and posture were found significant 8 times for both the MPF and MDF.

A limitation of the current study is its focus solely on the BB muscle. Future research should incorporate the brachioradialis and brachialis muscles to broaden understanding**.** Additionally, this study maintained a constant NMES intensity across a wide range of joint angles. Varying NMES intensity could provide further insights into neuromuscular efficiency, which may serve as a crucial metric for assessing rehabilitation efficacy in future studies.

This research is the first to investigate NMES-evoked torque variations with forearm posture and elbow joint angle at TQ levels below 15% of equivalent MVIC. The findings suggest that alterations in the lever arm, joint structure, and myosin influenced motor output, as muscle length modulates local circuit neurons (Forman *et al.*, 2019), impacting the responsiveness of the muscle to NMES, a critical factor in rehabilitation.

Previous research has shown that inter-individual NMES responses were affected by factors such as body fat, and BMI. Although this study focused on participants within a normal, healthy BMI range, upper arm circumference was found to influence muscle responsiveness to NMES (Son et al., 2014). In addition, the anthropometric parameters were found of significant elbow (Green and Gabriel, 2012) and wrist flexion torque estimation (Chimera *et al.*, 2021) in MVIC using statistical regression and were found sufficient to estimate ankle joint torque combined or not with EMG signal features input to CNN regreSsion models

(Moreira et al., 2022). These findings impress the hypothesis that (1) among all the 12 experiments trials from the transverse axis, 8 over 12 times were found to be statistically significant. Hence, it is clear that the transverse axis appear to be more reliable and should be used for torque estimation. In fact, in all the experiments, only the transverse values will be employed for MMG features computation for torque estimation. Furthermore, these findings also hypothesize that (2) a combination of anthropometric and NMES-MMG features may provide a feasible torque estimation. These findings are discussed in section 4.3 and section 4.4. of this chapter.

4.3 Development of torque estimation models using MMG features

Section 4.2 shows that RMS along the transverse axis of the muscle fiber was significant for angle and posture individually, though not statistically significant for the interaction between the two factors. In contrast, both MPF and MDF were significantly influenced by variations in elbow joint angle and forearm posture. Anthropometric variables also were found to correlate with muscle size, which in turns influences the distribution of motor nerve points and the the muscle responsiveness to NMES. The TQ RMS was also affected by the variations in elbow joint angle and forearm posture. We believe that additional spectral features extracted along the transverse axis of the muscle fiber will provide further relevance of the use of MMG for elbow joint torque estimation.

4.3.1 Dataset

In this section, twelve MMG features derived from the transverse axis of muscle fiber across the twelve angle and postures configurations, were used to develop elbow flexion

torque models. Each trial recording of 18 s was segmented at 100 ms with 50% overlap, which generated 310176 segments, yielding 292122 segments of both TQ and MMG features after outlier suppression. Initially, the GRA was applied to evaluate the degree of correlation between TQ and MMG features (Tabel 4.10). Subsequently, the dataset processed for Z-score normalization, outlier removal and histogram based binnng as discussed in section 3.5, were subsequently used for RFR torque estimation model development.

4.3.2 MMG features based model

Machine learning models was applied on the dataset discussed in section 4.3.1. We devised three distinct approaches for feature selection model , hyperparameter tuning model, and a hybrid model integrating both using EO and GLEO. To evaluate the effectiveness of these GLEO-based approaches, the baseline mean values of RMSE, R^2 and slope values were initially determined on empirically assessed RFR model configuration before feature selection and hyperparameter tuning. For the training subset, RMSE, R^2 and slope values were 0.0963, 0.8882, 0.7903, respectively. For the testing subset, the corresponding values were 0.1330, 0.7228, 0.6946. Second, the RFR was trained for features selection and hyperparameter tuning using the EO and a combination of both. Third, the data was trained using the GLEO for determining optimal features, tuned hyperparameters for all features and combination of both tasks, and further evaluated using 7:3 ratio integration histogram based frequency equalization of features among subjects' variability , following angle and posture based configuration. Hence, these strategies showed estimations with iteratively decaying RMSE and improved slope and R^2 as shown in Table 4.8 for the EO and Table 4.9 found when the GLEO was applied.

Both approches performed well (i.e model developed using EO and GLEO for feature selection and hyperparameter tuning and the hybrid combination of both). Table 4.8,4.9 and 4.10 present the performance metrics for EO and GLEO approaches applied for feature selection as also pictured at Figure 4.8(a) and hyperparameter tuning Figure 4.8(b) of the RFR model. However, altough the EO improved the estimation accuracy (Figure 4.9(a) and 4.9(b)), the hybrid approach employing GLEO for both MMG feature selection and RFR hyperparameter tuning (Figure 4.8(a) and 4.9(b)), yielded a notable RMSE of 0.0461, R^2 of 0.9665, and slope of 0.8983 respectively for the training subset and RMSE of 0.1174, R^2 of 0.7853 and slope of 0.7414 for the testing subset. The improvement in R^2 and the slope was accompanied by a significant reduction in RMSE (Figure 4.8).

The GLEO-RFR-FS-HT model demonstrated improved estimation accuracy, achieving a 33.33% reduction in the feature size (Table 4.10). These performance metrics were derived from the optimized RFR model, configured with *Ntrees* of 847, *MinLeafSize* of 1, *mTrees* of 4, and *Nsplits* of 46942.

The results were compared with those obtained from hyperparameter tuning of RFR for biological dataset (Table 4.11), and with the extended version of EO for feature selection as described in the literature (Too and Mirjalili, 2021). The comparisons encompassed various EO extensions including the EO with a divided population based on distance factor (Y. Li *et al.*, 2022), gaussian (Gupta *et al.*, 2020) and biphasic mutation (Vommi and Battula, 2023).

The literature results underscore the robustness of GLEO in performing biological feature selection through the wrapper approach. As shown inTable 4.10 highlights the GLEO's capability to identify highly informative NMES MMG features that closely correlate with elbow joint torque.Altough the GRD based correlation can rank features

according to their degree of correlation with torque, GLEO was found to select these features according to the physiological significance. Figure 4.9 offers a comparative illustration of the convergence error during training process of EO-RFR and GLEO-RFR for both feature selection and hyperparameter tuning, as well as their hybrid combination. Additionally, Figure 4.8 demonstrate that GLEO consistently achieved the lowest RMSE throughout training. Additionally, Figure 4.9 depict the training process for hybrid feature selection and hyperparameter tuning using EO and GLEO. The training curve showed smooth trend and improved RMSE with increasing training iterations, consistent with the observation in Table 4.9 and 4.8.

Taken together, Figure 4.10 indicate that the results of the proposed GLEO combined with RFR effectively address NMES feature selection and hyperparameter tuning, achieving improved accuracy in complex biological experimental datasets.

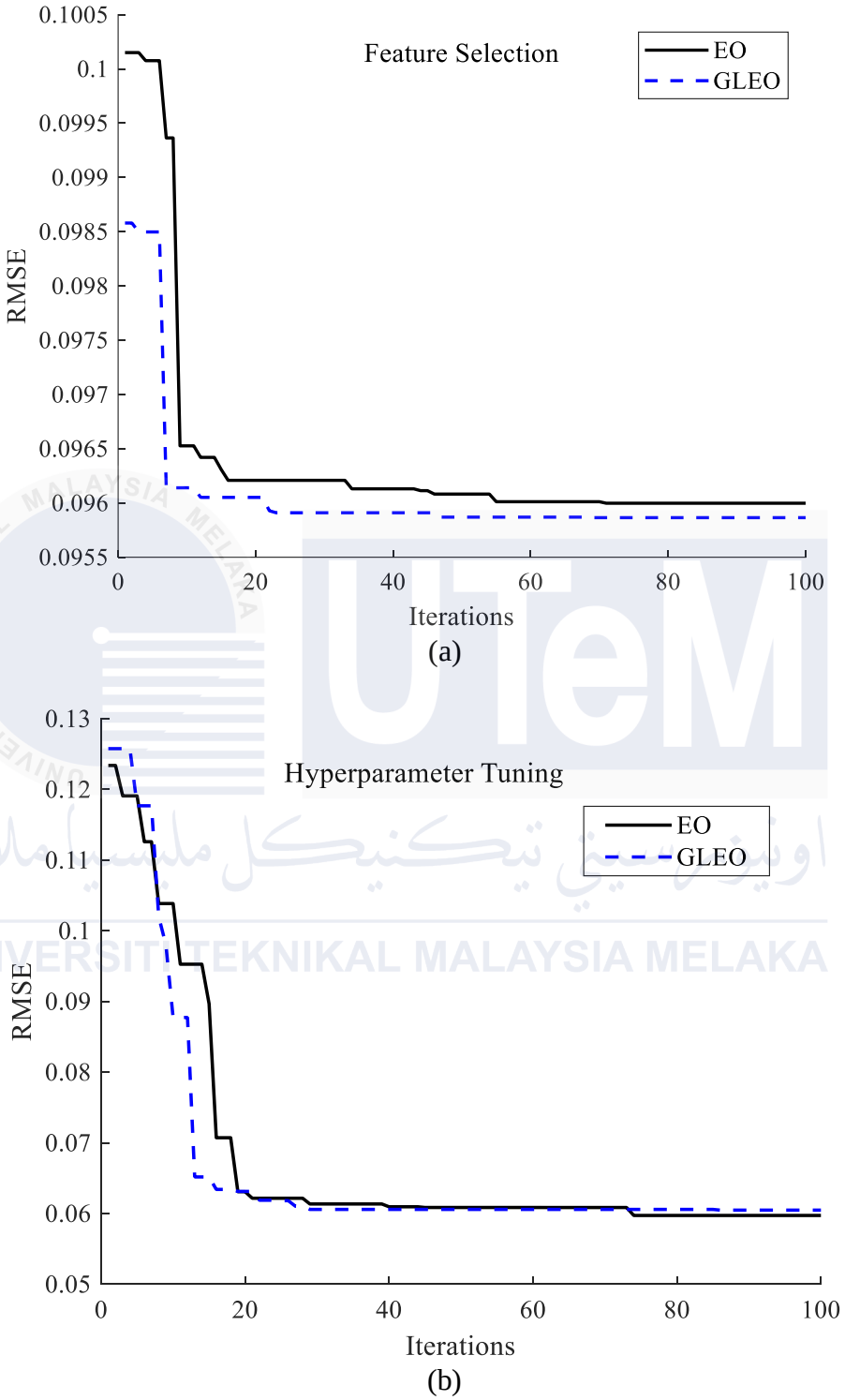

Figure 4.8: (a) Training curve of feature selection using EO and GLEO, and (b) Hyperparameter tuning using EO-RFR and GLEO-RFR.

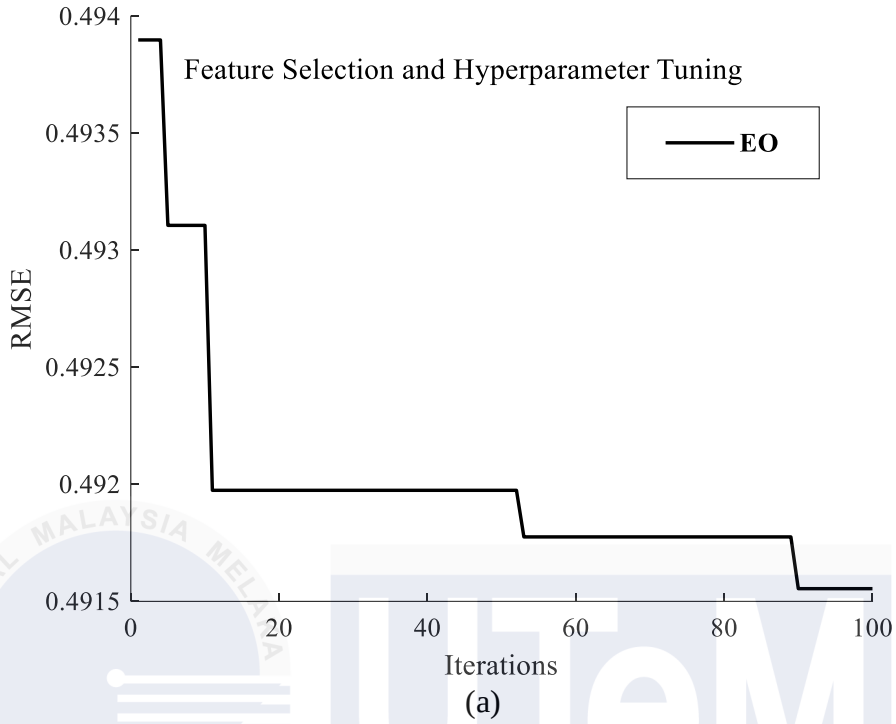

(a)

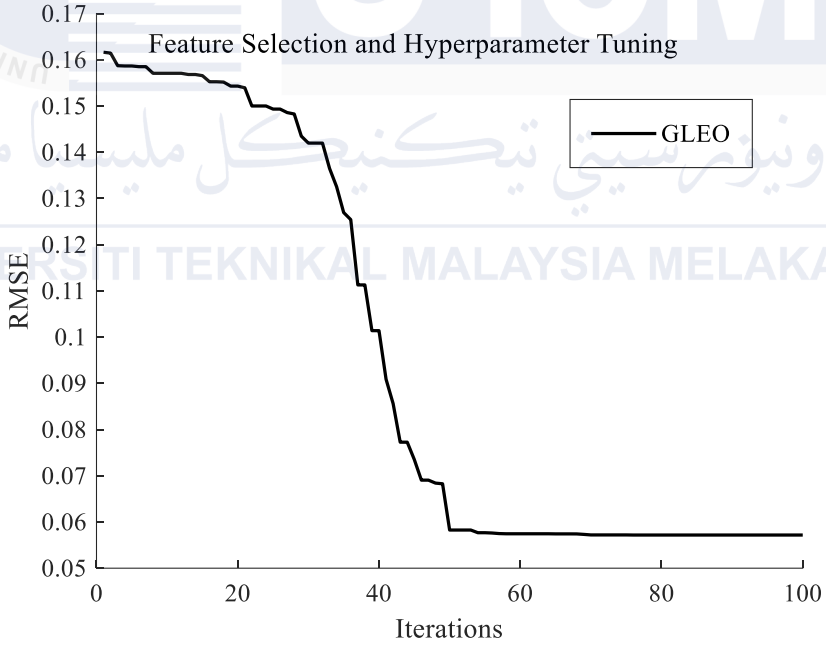

(b)

Figure 4.9: Training curve for hybrid feature selection with hyperparameter tuning using (a) EO-RFR and (b) GLEO-RFR.

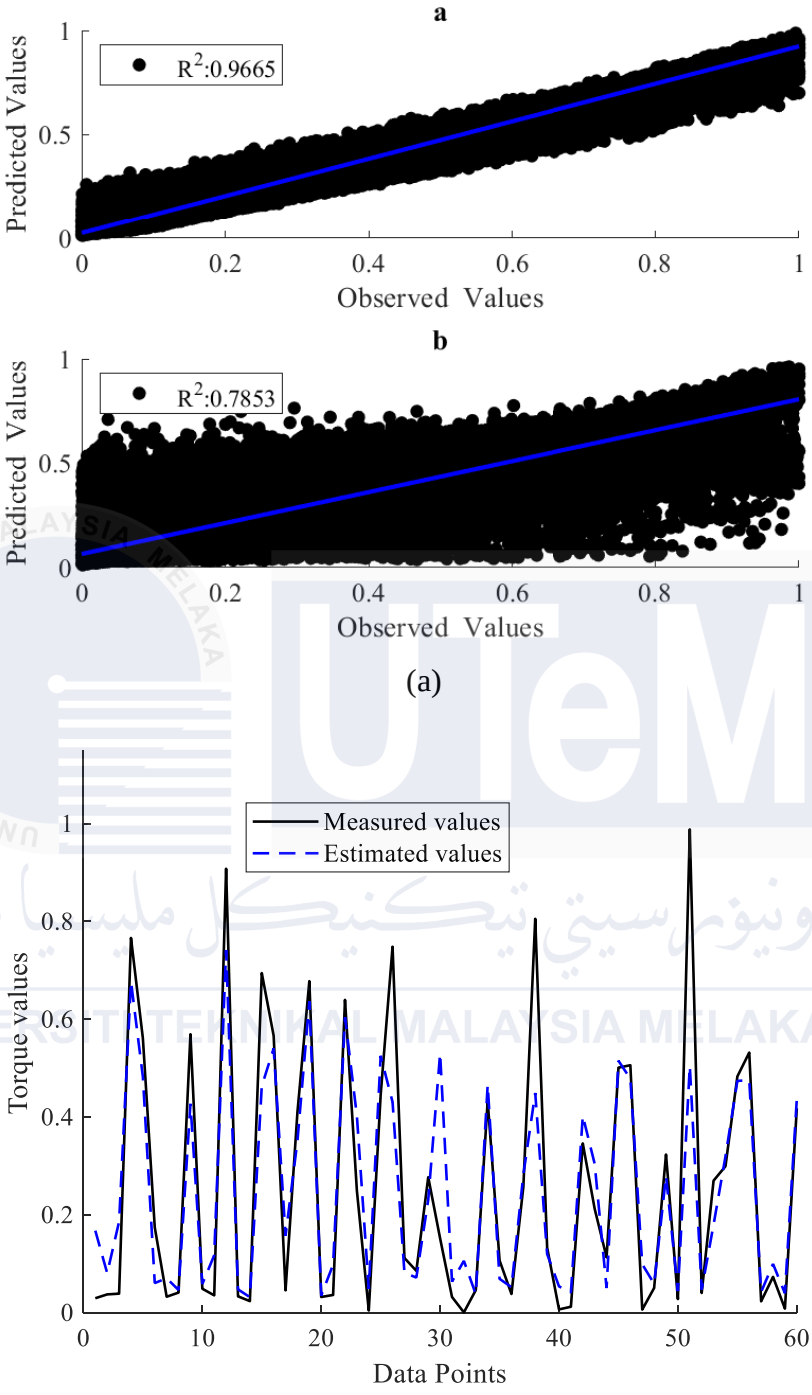

Figure 4.10:Correlation between measured and predicted torques for the (a) training and testing subsets using RFR hyperparameters with MMG features optimized through GLEO-RFR and (b) the cross plots of measured TQ versus estimated TQ for 60 test subsets.

4.3.3 Effects of integrating GLEO into MMG based RFR models

As seen in Figure 3.25, the histogram plot reveals that MMG signals features exhibited a low to moderate correlation with torque. Table 4.8 and 4.9 demonstrate that the EO-RFR-FS and GLEO-RFR-FS yielded improved performance. The GLEO feature ranking in Table 4.10 reflected the coherence between NMES MMG features and muscle physiology for estimating elbow flexion torque. The final model achieved an average R^2 of 0.7853 with a standard deviation of 0.0041.

Table 4.8: Performance of the RFR model based on EO

Model	R^2	RMSE	Slope
RFR	0.7228	0.1335	0.6910
EO-RFR-FS	0.7255	0.1298	0.6896
EO-RFR-HT	0.7443	0.1282	0.6986
EO-RFR-FS-HT	0.7625	0.1281	0.7021

HT = hyperparameter tuning, and FS = feature selection

The model with all 12 features exhibited lower performance metric compared to models with optimal features and RFR hyperparameters. The GLEO-RFR-FS-HT model outperformed the other models; achieving average metrics of 0.7853, 0.1174 and 0.7414 respectively for R^2, RMSE, and slope.

Table 4.9: Performance of the RFR model based on GLEO

Model	R^2	RMSE	Slope
RFR	0.7228	0.1335	0.6910
GLEO-RFR-FS	0.7265	0.1298	0.6896
GLEO-RFR-HT	0.7573	0.1253	0.7060
GLEO-RFR-FS-HT	0.7853	0.1174	0.7391

Table 4.10: Comparison of proposed GLEO with GRD

Feature	GRD	Ranking by correlation	Ranking by GLEO
RMS	0.8173	1	1
High band	0.7752	2	2
Lower band	0.7608	3	3
Tremor	0.7456	4	NS
SPFlx	0.7261	5	4
MDF	0.6598	6	5
SPC	0.6261	7	6
SPsp	0.6259	8	7
MPF	0.6093	9	8
ZCR	0.5947	10	NS
Mobility	0.5782	11	NS
SPFlt	0.5734	12	NS

NS = not selected

The scatter and cross plots in Figure 4.10 illustrate the correlation between measured and estimated elbow flexion torque. This correlation indicates that tuned RFR model leveraging NMES MMG signals effectively estimated the torques from unseen dataset. Based on the performance metrics, the GLEO-RFR-FS-HT model with *Ntrees* of 847 trees, *MinLeafSize* of 1, *mTrees* of 4, and *Nsplits* of 46942 emerged as the optimal configuration for achieving a considerable torque estimation.

4.4 Development of torque estimation models using anthropometric++ features

This section presents the groundwork for a generic model using anthropometric++ features. The proposed approach makes it viable to develop anatomical characteristics based RFR torque estimation model from health subjects. Each anthropometric feature's model is evaluated for torque estimation. Henceforth, a combination of length and circumferences were combined with NMES MMG to evaluate the effect of such a combination on the model's estimation capability. Thereafter, a suitable optimization combining all

anthropometric++ features is used to decide the most predictive features and hyperparameters of the RFR model.

4.4.1 Datasets

Seven anthropometric variables were collected and assessed for their reliability as demonstrated in Table 4.3. Afterwards, anthropometric features were fused with two MMG features to form anthropometric++ features (section 3.5). A total of 310176 segment lengths were extracted from each feature dimension. The outlier removal was further performed using the Z-score methods (Z. Li et al., 2022), with the Z-score value above ± 3 being suppressed before the GRD correlation analysis. The left 286232 segments for each feature were normalized between 0 and 1 before being used for torque estimation model development. The GRD analysis identified uneven distribution of anthropometric and MMG parameters, prompting to grouping of these values into bins of 0.02 to equalize frequency distribution across features (Srivastava et al., 2019) (Figure 3.33).

4.4.2 Anthropometric++ features-based model

Table 4.3 summarizes the intra-rater reliability of anthropometric variables used in this study. Of all the 7 anthropometric variables, the TEM of each parameter was 0.1435, 0.0079, 0.2063, 0.1192, 0.1395, 0.2036, and 0.2417 for the W, H, BMI, MUAC, LLA, LUA, SKT respectively. Intra-tester % R of 97.9249, 98.6322, 98.9045, 99.1036, 99.3079, 99.6379, and 99.9567 for the height, SKT, LUA, MUAC, BMI, LLA, and weight respectively were obtained.

Table 4.13 presents the GRD of correlation between torque and the anthropometric parameters, MMG RMS and MMG MPF, and among both MMG RMS and MMG MPF with

anthropometric features. The GRD between anthropometric features and elbow flexion torque was found to vary between 0.5808 to 0.6245. MMG RMS and MMG MPF were observed to be highly correlated with torque with a GRD of 0.8093 and 0.6246 respectively. A statistically significant correlation was observed between MMG RMS and TQ RMS. The value of GRD among anthropometric and MMG parameters was observed between 0.6133 and 0.8708. A statistically significant GRD was obtained between the LUA and the W, H, BMI, MUAC; between the MUAC and the height, and between the LLA and both the height and BMI. The GRD between MMG RMS and the anthropometric features was observed statistically insignificant, whereas a statistically significant correlation was identified between the RMS and MPF with GRD value of 0.6592. The statistical analysis was conducted at ($p < 0.05$).

Table 4. 11: Correlation analysis of anthropometric variables, MMG RMS and MMG MPF and torque

	TQ	**W**	**H**	**BMI**	**MUAC**	**LUA**	**LLA**	**SKT**	**RMS**	**MPF**
TQ	-									
W	0.5865	-								
H	**0.6245**	0.6873	-							
BMI	0.6032	0.7507	0.7375	-						
MUAC	0.5808	0.6747	**0.6409**	0.7543	-					
LUA	0.6189	**0.6708**	**0.7689**	**0.7611**	**0.6476**	-				
LLA	0.5995	**0.7448**	0.7793	**0.8708**	0.7467	0.7583	-			
SKT	0.6559	0.7098	0.6729	0.7033	0.7338	0.6733	0.6936	-		
RMS	**0.8093**	0.6221	0.6609	0.6170	0.6133	0.6547	0.6227	0.7027	-	
MPF	0.6246	0.7108	0.7192	0.7441	0.7043	0.7244	0.7434	0.7325	**0.6592**	-

Bold indicates a significant statistical correlation at $p < 0.05$.

Table 4.12 shows the elbow flexion torque estimated after GRD values obtained between elbow joint torque and both LUA and MUAC which define the BB muscle dimensions as well as between torque and both MMG RMS and MMG MPF which reflect muscle activation. The inclusion of MMG RMS and MMG MPF in a model defined by LUA,

MUAC, and their combination led to obtained statistically significant increase in R^2 and decrease in RMSE ($p < 0.05$).

Table 4. 12: RFR analysis for anthropometric and MMG features based torque prediction (baseline RFR model).

Models	Sequential parameters	R^2	R^2 change	RMSE	RMSE change
Model 1	LUA	0.0813	-	0.2388	-
	LUA + MPF	0.4432	0.3619	0.1869	- 0.0519
	LUA + RMS	0.5502	0.4689	0.1673	- 0.0715
	LUA + RMS + MPF	0.6209	0.5396	0.1543	- 0.0845
Model 2	MUAC	0.0767	-	0.2400	-
	MUAC + MPF	0.4430	0.3663	0.1866	- 0.0534
	MUAC + RMS	0.5448	0.4681	0.1692	- 0.0708
	MUAC + RMS + MPF	0.6212	0.5445	0.1540	- 0.0860
Model 3	LUA + MUAC	0.2116	-	0.2231	-
	LUA + MUAC + MPF	0.4643	0.2527	0.1829	- 0.0362
	LUA + MUAC + RMS	0.5716	0.3600	0.1651	- 0.0580
	LUA + MUAC + RMS + MPF	0.6425	0.4309	0.1497	- 0.0734

Anthropometric features-based models showed R^2 of 0.0813, 0.0767, 0.2116 and RMSE of 0.2383, 0.2400, 0.2231 respectively for LUA, MUAC and their combination. Adding the MMG MPF to the model containing LUA resulted in a statistically significant improvement in the estimated elbow flexion torque value ($p < 0.05$) with R^2 increasing from 0.0813 to 0.4432, and RMSE decreasing from 0.2388 to 0.1869. Including MMG RMS into the model with LUA alone yielded a statistically significant increase ($p < 0.05$), with R^2 reaching 0.5502, and RMSE decreasing to 0.1673. The addition of both MMG RMS and MMG MPF to the same model further improved the results, with R^2 increasing to 0.6209, and RMSE decreasing to 0.1543 with ($p < 0.05$).

The addition of the MMG MPF to the model defined by MUAC yielded significant increase in estimated elbow flexion torque ($p < 0.05$), at R^2 rising from 0.0767 to 0.4430, RMSE reducing from 0.2400 to 0.1866. Adding MMG RMS to the MUAC model resulted

into increasing R^2 to 0.5548, and RMSE decreasing to 0.1692. The combined addition of both MMG RMS and MMG MPF led to R^2 reaching 0.6212, and RMSE of 0.1540.

The variation in estimated elbow flexion torque from the addition of MMG MPF to the model containing LUA and MUAC was statistically significant ($p < 0.05$) with R^2 improving to 0.4643, RMSE decreasing to 0.1829. Further, the addition of MMG RMS to this model obtained R^2 increasing to 0.5716, and RMSE of 0.1651. The combined inclusion of both MMG RMS and MMG MPF yielded the highest improvement with R^2 of 0.6425, and RMSE of 0.1497.

4.4.3 Effects of integrating GLEO into anthropometric based RFR models

The baseline elbow flexion torque obtained from combined all anthropometric and MMG features showed R^2 of 0.6560 and RMSE of 0.1477. As found in Table 4.13, GRD and GLEO ranking were initially used to identify dominant features among muscle activation and anthropometric parameters. MMG RMS and MMG MPF features were found to have a significant correlation when coupled with anthropometric features. However, the GRD ranking of MMG MPF at position 3 didn't reflect the significance of physiological features.

Figures 4.11 and 4.12 present the convergence spead for feature selection and hyperparameter tuning and hybrid approach combining both using EO-RFR. Figure 4.13 illustrates the convergence patterns of the GLEO-RFR during feature selection and hyperparameter tuning, while Figure 4.14 presents the combined effect of both processes. The convergence and prediction accuracy shown at Figures 4.15 and 16 present GLEO's capability to select features and tune hyperparamter effectively. Using GLEO-RFR, for dominant feature selection, the model achieved a slight improvement with R^2 of 0.6561 and

RMSE of 0.1474 outperforming EO-RFR (refer to Figure 4.17). Similarly, hyperparameter tuning and a hybrid approach combining both feature selection and hyper-parameter tuning showed average R^2 and RMSE values of 0.6951, 0.1384, and 0.7170, 0.1333 respectively for the test dataset as shown in Figure 4.17. These results were obtained from a GLEO-RFR model configured with *Ntrees* of 333, *MinLeafSize* of 1, *Nsplits* of 40995, and *mTrees* of 4.The t-test results indicated non-significant difference between the RMSE obtained during feature selection ($p > 0.05$), hyper parameter tuning ($p > 0.05$), and hybrid combination of both ($p > 0.05$).

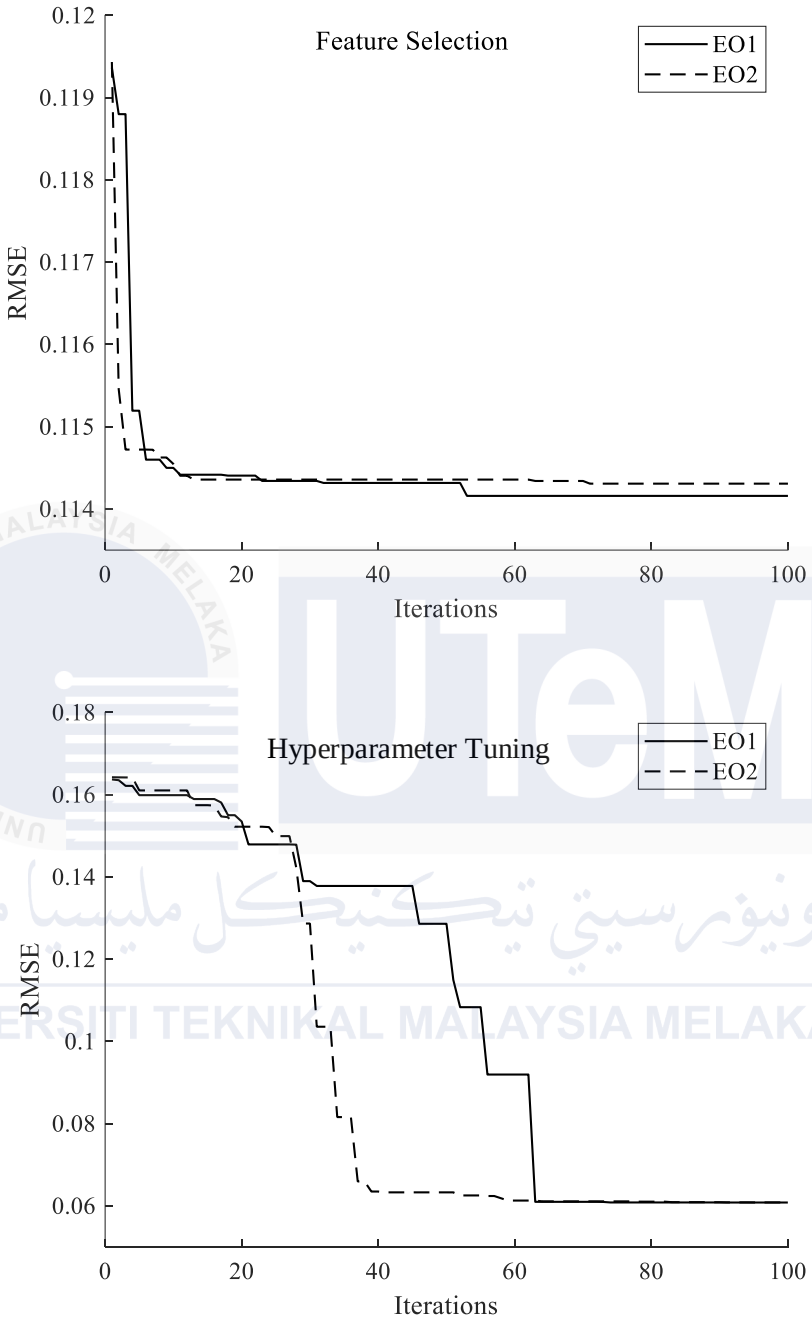

Figure 4.11:Training curves of anthropometric++ feature selection (top) and hyperparameter tuning (bottom) using EO.

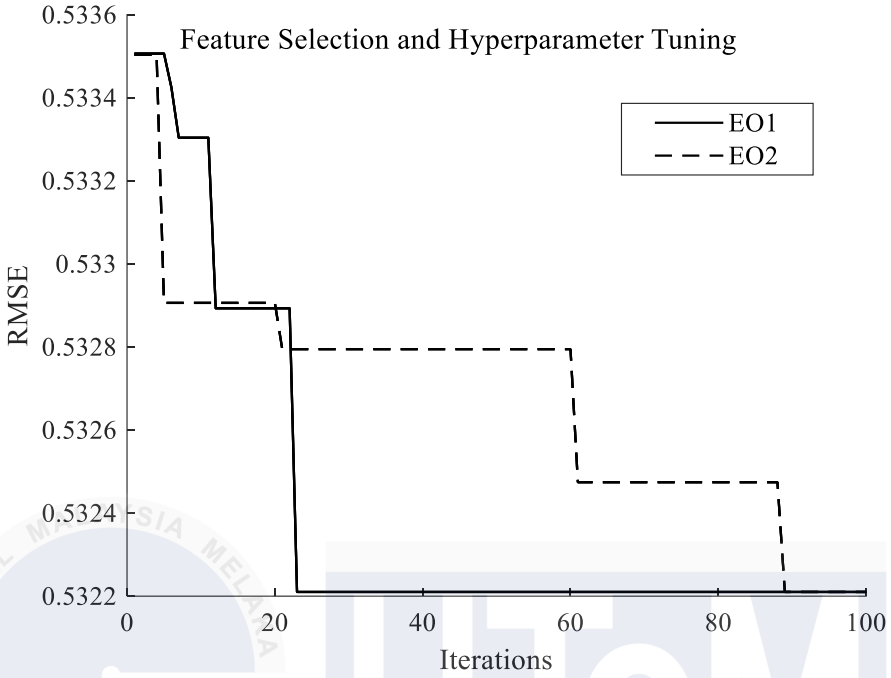

Figure 4.12:Training curves of simultaneous anthropometric++ feature selection and hyperparameter tuning using EO.

The purpose of this study was to assess the contribution of anthropometric variables and the BB muscle activation variables in predicting elbow joint flexion torque. Reliable anthropometric variables were crucial for torque estimation. The reliability analysis showed excellent consistency over 99% for the weight, BMI, MUAC, and LLA. The %R is similarly high, achieving values of 97.9248, 98.9045, and 98.6322 for the height, LUA and SKT respectively. These values exceed the %R threshold of 90% (De Miguel-Etayo *et al.*, 2014), validating the recorded variables for subsequent torque estimation model development.

Contributions to the state of the art include simulating time-series anthropometric features and further empirical analysis to establish a baseline model using both anthropometric and MMG features. Additionally, the present research introduces a GLEO to optimize feature selection and hyper-parameter tuning in RFR machine learning model, improving torque estimation accuracy.

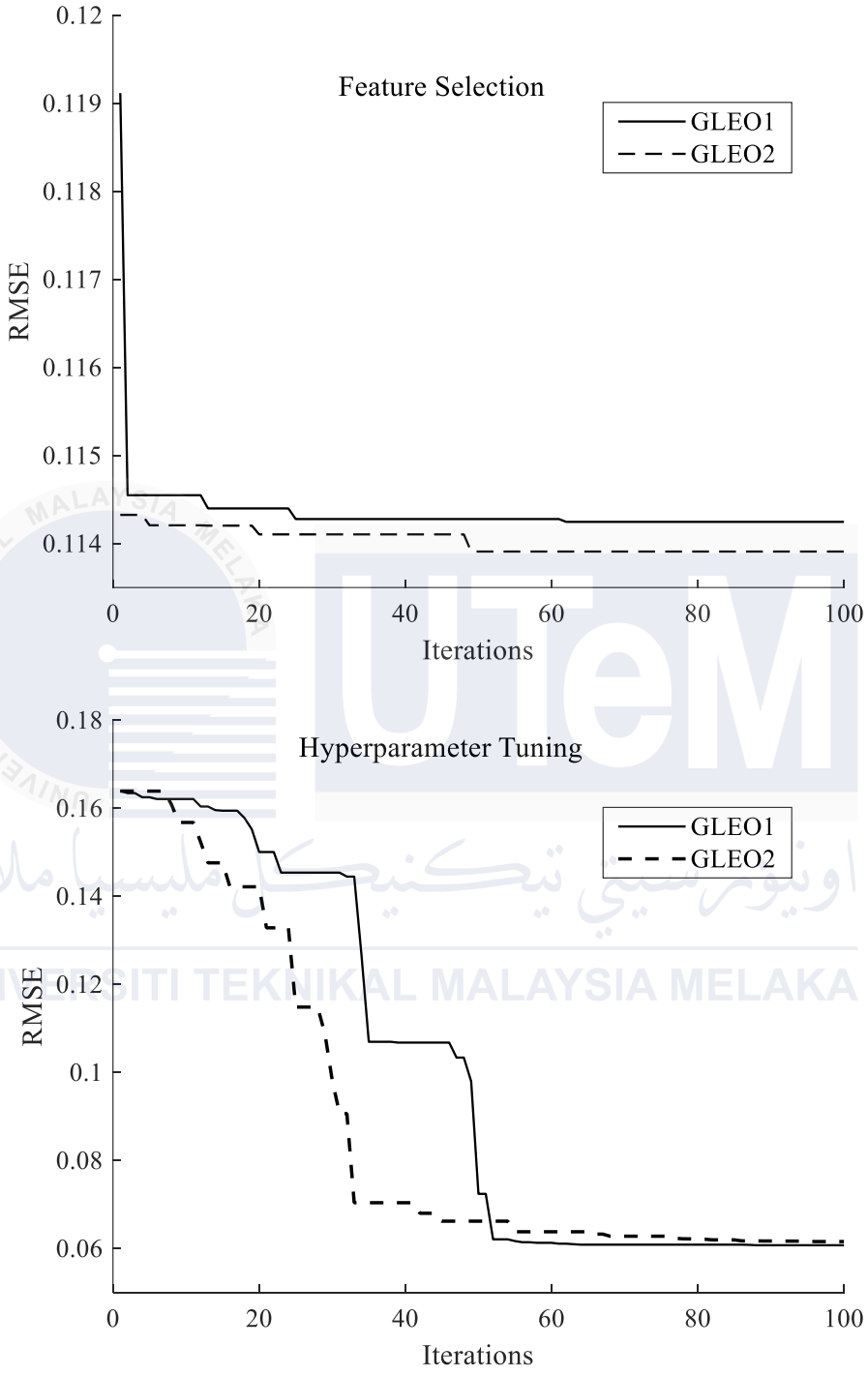

Figure 4.13:Training curves of simultaneous anthropometric++ feature selection (top) and hyperparameter tuning (bottom) using GLEO.

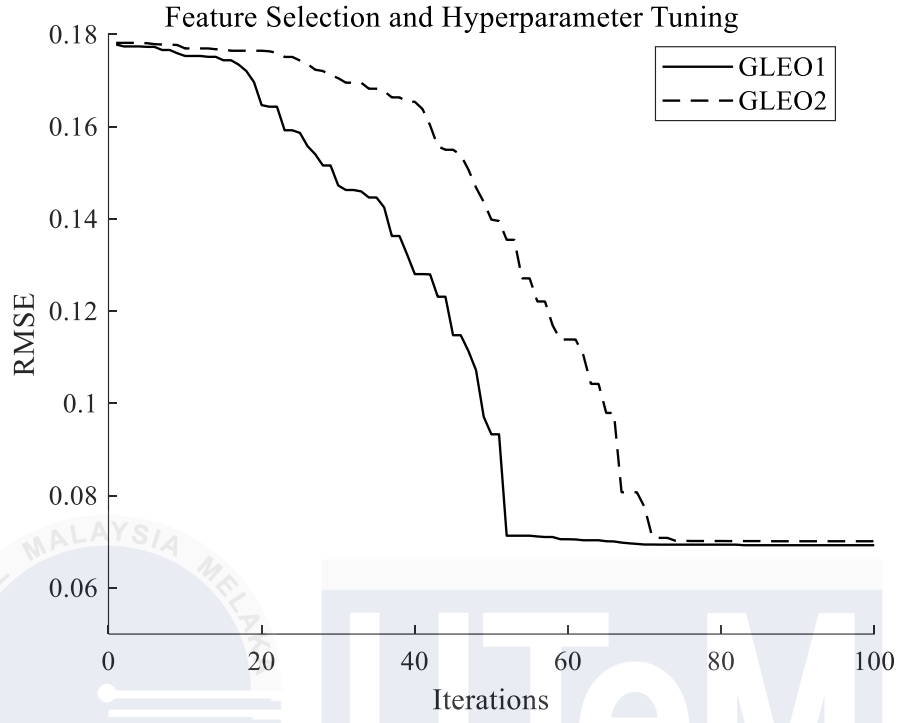

Figure 4.14:Training curves of simultaneous anthropometric++ feature selection and hyperparameter tuning using GLEO.

Table 4. 13: Comparison of proposed hybrid GLEO a and GRD for feature ranking

Feature	GRD	Ranking by correlation	Ranking by GLEO
W	0.5864	8	5
H	0.6245	4	4
BMI	0.6032	6	NS
MUAC	0.5808	9	6
LLA	0.5994	7	NS
LUA	0.6189	5	3
SKT	0.6559	2	NS
RMS	0.8093	1	1
MPF	0.6246	3	2

NS = not selected

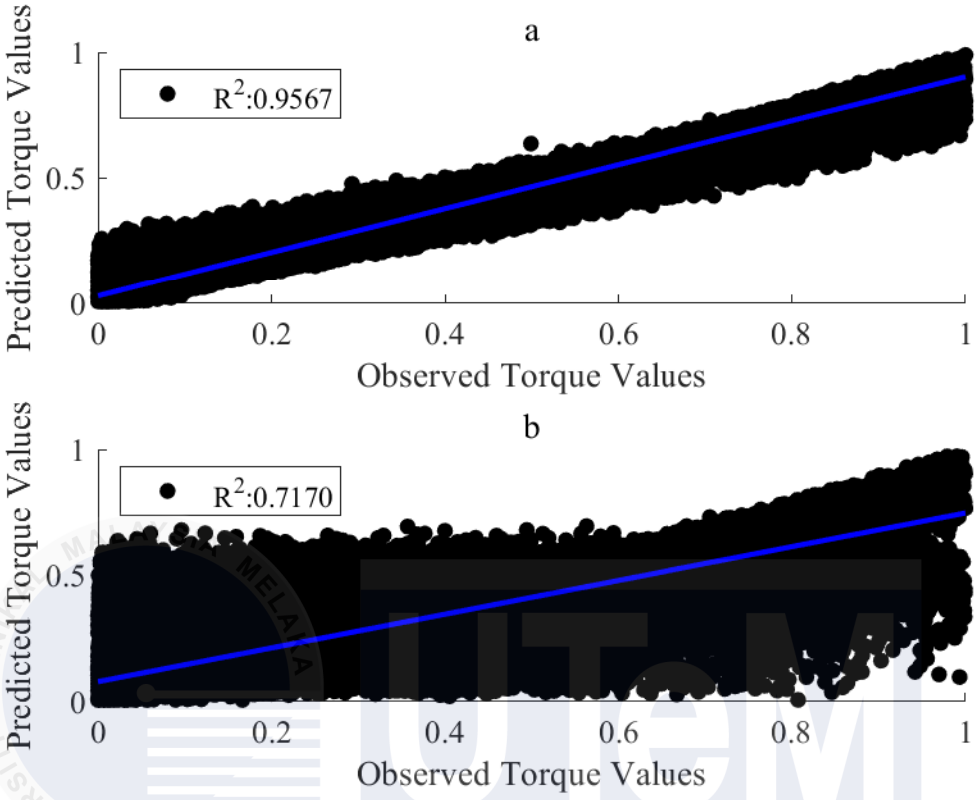

Figure 4.15:Correlation of measured and predicted torque values for the training (top) and testing (bottom) subsets.

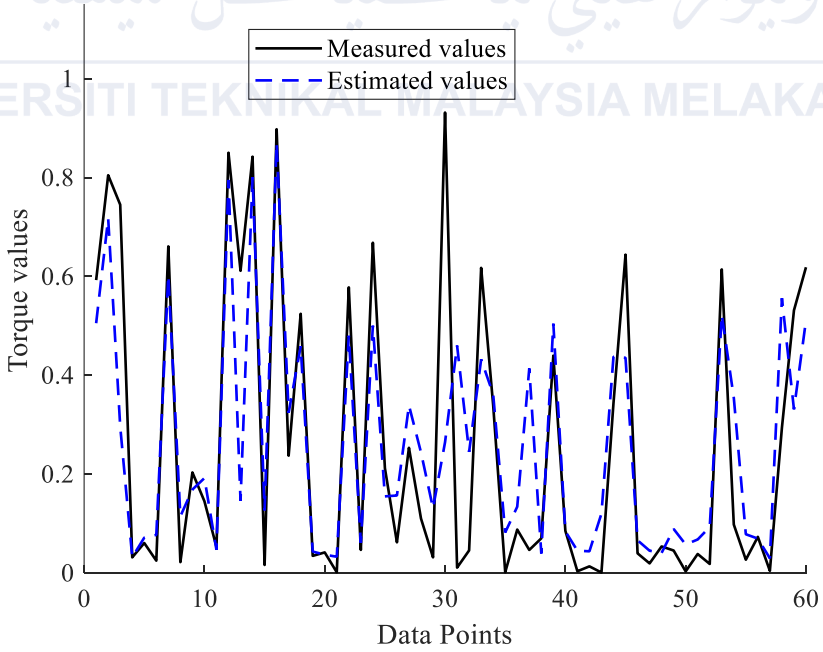

Figure 4.16:Cross-plot of measured against predicted torque.

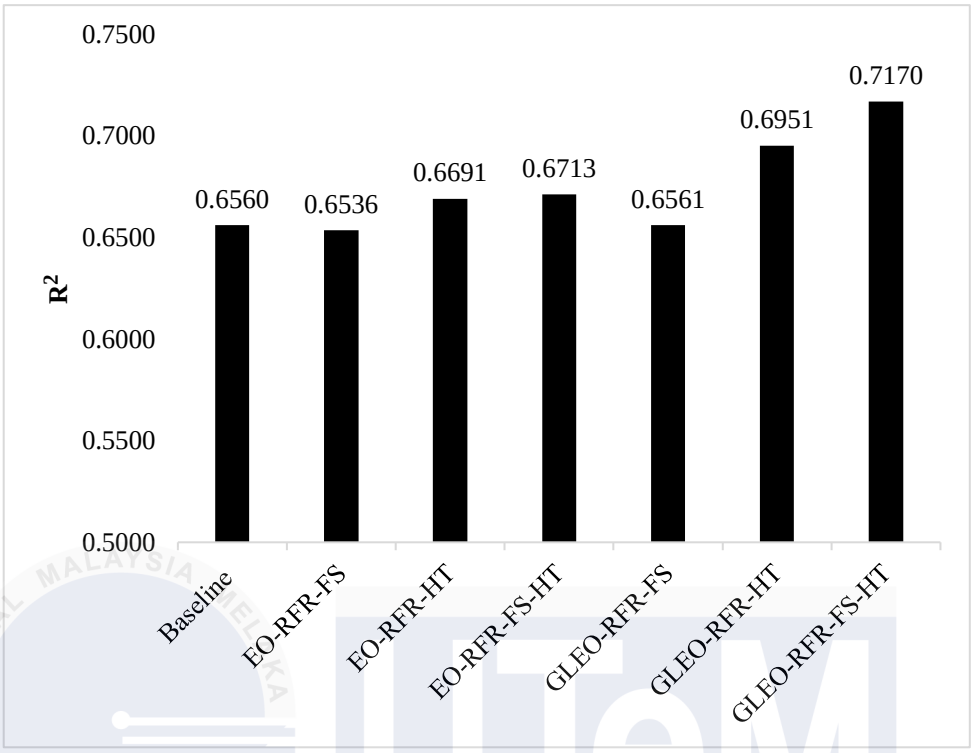

(a)

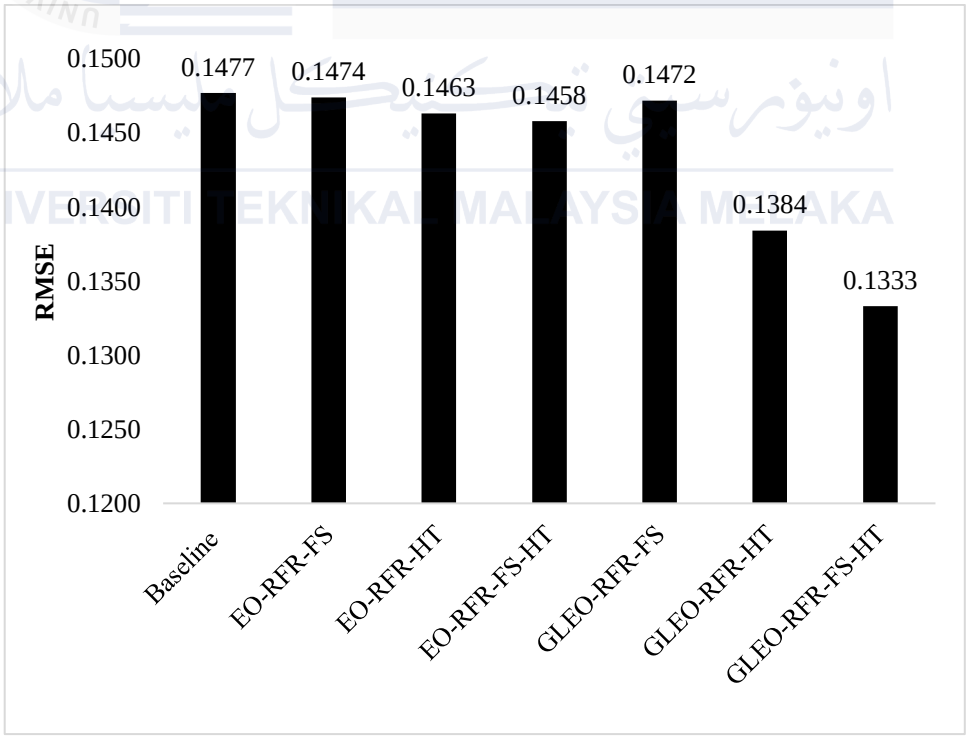

(b)

Figure 4.17: Performance measure by R^2 (a) and (b) RMSE for baseline RFR, feature selection, hyperparameter tuning and hybrid feature election and hyperparameter tuning using EO and GLEO.

The study hypothesizes that anthropometric and NMES-MMG variables will to different extents estimate the elbow flexion torque. To evaluate this, GRD correlation between anthropometric along MMG variables with elbow joint torque were analysed. The LUA and MUAC as dimensional factors of BB muscle activation were found significant for low-level muscle contraction and torque generation. Notably, LUA correlated significantly with the torque at NMES below 15% MVIC. The findings support our hypothesis that these variables contribute to torque generation, aiding in workspace design and injuries prevention in repetitive occupational tasks (Talib *et al.*, 2022).

Due to its low correlation with the torque, the LLA was excluded from the initial RFR model development. This was expected because the lever arm was maintained consistent across all subjects. MUAC, which showed a moderate correlation with the torque, has been previously reported to correlate with the torque during high (Chimera *et al.*, 2021) and low muscle contraction (Talib et al., 2019, 2022). These findings align with the hypothesis that the MUAC reflects the contractile myofibrils of the BB muscle, and that muscle activation under fixed NMES intensity depends on the muscle depth as indicated by the MUAC (Paillard, 2018).

Integrating LUA and MUAC in the RFR model improved R^2 (0.2116) and decreased RMSE (0.2231). Given that under torque generation tasks, the muscle contraction is characterized by the amplitude and frequency of MMG which reflect the number of active motor units and their firing rate, these findings support this study's hypothesis that the MUAC influences the MMG RMS and MMG MPF. These results underscore the role of muscle length and depth to influence neural activation, a vital aspect in neurophysiological research (Forman et al., 2019). Additionally, LUA and MUAC were found significant for BB muscle activation during NMES-induced isometric contraction (Ichikawa et al., 2021).

We evaluated the RFR model for NMES-induced elbow flexion torque estimation by sequentially adding MMG RMS and MMG MPF to the model with LUA and MUAC. This significantly improved R^2 and decreased RMSE ($p < 0.05$). Specifically, introducing MMG RMS and MMG MPF resulted in R^2 of 0.6425 and RMSE of 0.1497 ($p < 0.05$) improving the variance by 0.4309 and 0.0734 respectively. These results align with research findings on increased muscle activation during NMES-evoked low contractions (Flodin et al., 2022), and further support the hypothesis that there is a substantial influence of neural drive on the MMG-torque relationship in low NMES-evoked contractions of the BB muscle.

Previous studies on elbow flexion torque and anthropometric studies emphasized body weight, height, BMI, the MUAC, and the LLA. However, these studies overlooked the considerable influence of upper arm length, BB muscle depth, and subcutaneous tissue on MMG and torque variables. Additionally, these measurements are obtained from a small sample size which may restrict generalizability. Furthermore, these studies may also be biased to a large population that influence the generalization of correlation that suits the majority in the population (Chimera *et al.*, 2021). Our findings underscore the value of identifying influential anthropometric variables for optimizing designs in ergonomic tasks.

While the subcutaneous tissue acts as a low pass filter for MMG signals, its impact on torque generation was not observed in this study (Santos *et al.*, 2021). This research found that LUA and MUAC influence the elbow flexion torque more than other anthropometric features. The LUA defines the moment arm, with a longer arm having a higher proportion of available motor units recruited during movement. In addition, increased muscle length may shift optimal length tension relationship influencing the efficiency of muscle fiber recruitment (Cossich *et al.*, 2021). The effectiveness of NMES is also modulated by the muscle's thickness and length as deeper tissue activation requires higher NMES intensities.

Thicker muscles, such as the BB in some participants, demand greater NMES intensities to engage deeper motor units. Furthermore, factors like arm posture and length impact electrode placement and muscle fiber recruitment during NMES, underscoring the importance of precise electrode positioning to minimize crosstalk and target muscle fibers accurately (Talib et al., 2019; Islam et al., 2014). Although no previous study has reported on the role of LUA on torque production; the results here suggest it as a significant determinant of elbow flexion torque. This aligns with findings that BB muscle fascicles experience shifts in motor points due to changes in forearm posture and elbow flexion angle (Ichikawa et al., 2021) as well as BB muscle depth variations that consequently affect torque generation (Paillard, 2018;Anon, 2001).

Previous literature has identified the body weight as a significant predictor of elbow flexion torque under MVIC conditions (Green and Gabriel, 2012). Additionally, height has been shown to strongly predict isometric wrist flexion torque. This study also observes a significant correlation between the height and torque (Table 4.13). However, BMI did not significantly correlate with elbow joint flexion torque in our findings, contrasting with prior research linking BMI to wrist flexion torque. This discrepancy may stem from variations in the mechanical and physiological structures of the BB muscle and extensor carpi radialis, as well as the use of low muscle contraction in this study compared to MVIC in wrist flexion studies (Chimera *et al.*, 2021).

The LLA did not correlate significantly with elbow flexion torque. This should be significant, because it was consistent among all subjects. This result diverges from previous research where LLA significantly estimated elbow flexion torque. This discrepancy may be attributed to the different postures (neutral, pronation, and supination) used in this study, alongside the involvement of multiple forearm muscles and the synergistic activity of the

brachialis and brachioradialis at MVIC in past studies (Talib *et al.*, 2022).

The literature on muscle activation and joint torque highlights that calibrating non-linear models for torque estimation often requires the full muscle force range, from 0 to 100% MVIC. Prior findings indicate that torque modelling necessitates critical identification of individual muscle forces (Green and Gabriel, 2012) , which may be affected by the synergistic activation of elbow flexors at maximal efforts (Talib et al., 2019). Focusing on the BB muscle at low activation levels (below 15% MVIC) under NMES conditions in this study minimized confounding synergies and crosstalk seen in voluntary muscle -effort studies (Talib et al., 2019). Our findings align with previous research showing that the muscle length and joint angle modulate afferent pathways influencing the sEMG amplitude, while limb posture exhibits excitatory and inhibitory information from synergistic muscles (Forman et al., 2019). Although our study did not explore the impact of joint angles, future research should address how elbow joint angle and forearm posture affect MMG variables (Uwamahoro et al., 2023) alongside torque estimation.

To the best of our knowledge, this is the first study to apply RFR for NMES-based elbow joint torque estimation using MMG and anthropometric variables, achieving accuracy (R^2 = 0.7170) in estimating unseen data. These results outperform previous studies that applied sEMG and anthropometric data to estimate MVIC-based elbow flexion torque (Green and Gabriel, 2012). Figure 4.xviii demonstrate significant estimation accuracy, with R^2 and RMSE confirming a strong correlation between predicted and observed values, exceeding R^2 of 0.6560 and RMSE of 0.1477 achieved by standard RFR, not have been achieved by the mathematical modelling using the same variables. The RFR algorithm was improved by GLEO, adaptive parameter tuning techniques utilizing hybrid features and hyperparameter tuning of improved equilibrium optimizer (Too and Mirjalili, 2021). Results

in Table 4.14 further validate the feature selection and ranking capabilities of GLEO, capturing the physiological and anthropometric variables most influential on NMES-based muscle activation.

The scope of the present model is limited to elbow flexion torque estimation from a huge amount of dataset from varying elbow joint angles and forearm postures, which could have affected its performance. Future studies should focus on refining the model's performance using muscle activation and anthropometric variables of specific elbow joint angles and forearm postures.

4.5 Benchmarking with other HT algorithms and ML classifiers

In this section, we compared the performance metrics of hyperparameter tuning in RFR -based models and the performence accuracy of ML classifiers, with other biological datsests based techniques found in the literature. Table 4.14 compares GLEO with state-of-the-art hyperparameter tuning methods regardless of the estimation accuracy but focusing on their improvement. The results highlight that semi-automated mechanisms involving feature selection before hyperparameter tuning are popular. However, these techniques are often time-consuming, prone to error and constrained by the fixed space of model hyperparameters. Interestingly, despite GLEO's novelty in the literature, the results of this research underscore its ability to deliver enhanced outcomes.

Table 4.14: Hyperparameter tuning of RFR for biological dataset

Ref.	Dataset	Method	Observation
(Liu *et al.*, 2022)	Breast cancer data	Semi-automatic parameter adjustment	Pre-tuning R^2 of 0.7078 was reported. Post-tuning R^2 0.7453 was reported.
(Sakr *et al.*, 2019)	Torque and sEMG data	10-Fold cross-validation and Grid Search	Post-tuning R^2 of 0.74 ± 0.05, 0.72 ± 0.05, 0.69 ± 0.06, and 0.61 ± 0.06 respectively for four, three, two and one FMG band were reported. Pre- tuning R^2 were not reported.
(Lv *et al.*, 2023)	Forces data	PSWO, SSA, GA,	Post-tuning R^2 of 0.84 was reported. Pre-tuning R^2 was not reported.
(Shi *et al.*, 2022c)	MMG and torque data	Hilbelt 10-Fold cross-validation	Post-tuning R^2 of 0.68 was reported. Pre-tuning R^2 was not reported.
(Li *et al.*, 2020)	sEMG and joint angle data	RFR-PCA	Pre-tuning and post-tuning tuning R^2 values were not reported.
Ours	MMG and torque signal data	Grid Search	Pre-tuning R^2 of 0.7228 was reported. Post-tuning R^2 of 0.7327 was reported.
	MMG and torque signal data	**GLEO**	**Pre-tuning R^2 was 0.7228 and post-tuning R^2 was 0.7853.**

In Table 4.15, we observe the effect of integrating GLEO with the BPNN, SVR and RFR. It is evident that integrating GLEO with RFR provides higher estimation accuracy of 0.7853 compared to 0.5963 for BPNN and 0.5613 for SVR. This shows the efficacy of the RFR model for handling complex biomedical datasets.

Table 4.15: Experimental results from 3 different machine learning models

Model	R^2	RMSE	Slope
GLEO-BPNN	0.5963	0.1697	0.5917
GLEO-SVR	0.5613	0.1717	0.5514
GLEO-RFR	**0.7853**	**0.1174**	**0.7414**

BPNN = Back Propagation Neural Network; **SVR** = Support Vector Regression.
RFR = Random Forest Regression.

In this research, distinct models developed using EO-RFR (Table 4.8) and GLEO-RFR (Table 4.9) methods were evaluated for their performance in feature selection, hyperparameter tuning and hybrid approach combining both methods. The model's performance was tested on unseen data using tuned hyperparameters and selected features (Table 4.10). All models demonstrated consistent reduction in RMSE (Figures 4.8 and 4.9) alongside improvements in R^2 and slope values. The hybrid GLEO-RFR-FS-HT model exhibited superior performance evidenced by lower RMSE, higher R^2 and increasing slope trend. These results highlight the model's effectiveness in dynamic and isometric muscle contraction scenarios, where optimal hyperparameters are subject to change in response to the dynamic nature of the dataset (Yang and Shami, 2020).

Previous research has explored torque estimation using MMG features such as RMS, MPF, and ZCR of MMG signals applying artificial neural networks (ANN) model (Youn and Kim, 2011). Additionally, the SVR model has incorporated the sample entropy and reported favorable performance based on the correlation coefficient and RMSE. A wrapper-based approach using GRD has been employed to identify optimal feature combinations for MMG-based torque estimation (Z. Li et al., 2022), achieving a high estimation accuracy. However, the GRD lacks the discriminatory power to discern subtle feature differences crucial for muscle physiology. These models, however, were trained on short segments of stable muscle force and MMG, raising uncertainty about their performance in dynamic scenarios. The GLEO-RFR-FS-HT model addresses these challenging feature selection tasks and achieves improved elbow flexion torque estimation accuracy.

Machine learning models rely heavily on hyperparameters, driving the need for various optimization techniques previously deployed for torque estimation using MMG

signals features and achieving a high estimation accuracy as measured by R^2 (Z. Li et al., 2022). Conversely, study by (Hondo and Tsuji, 2022) reported lower R^2 values of 0.46 for the training and 0.44 for the testing dataset collected from one channel MMG sensor across 6 subjects. The study showed that R^2 improved with data from four additional MMG channels, though the challenge of accommodating multiple channels on small muscles persists. Furthermore, it is noteworthy that these studies utilized data from a limited number of subjects, potentially affecting the generalization of their findings.

The proposed model, developed using NMES MMG features from a cohort of 36 subjects, achieving an R^2, slope and RMSE of 0.7853, 0.7414, and 0.1174 respectively on the test dataset. This performance compares favorably to an R^2 of 0.68 reported for unseen datasets from a previous study (Shi et al., 2022). The results of the developed algorithm with SVR outperformed the study by (Hondo and Tsuji, 2022) with R^2 of 0.5613 and 0.5514 for the training and testing subset. These findings confirm the potential of the proposed approach to handle non-deterministic components in the fitness function of machine learning and dynamic muscle contraction which affect the configuration of optimal hyperparameters at each iteration (Yang and Shami, 2020). Despite relying on a high informative channel of MMG sensor, MMG might hold informative features that may have been affected by several factors.

MMG signals provides valuable insights into skeletal muscle activation levels with RMS typically indicating the intensity of motor unit recruitment (Correa *et al.*, 2023). However, conflicting findings regarding MPF variations with muscle activation levels reflect the complexity introduced by muscle fiber type composition Click or tap here to enter text. Talib et al., 2018), elbow joint angle (Uwamahoro et al., 2023), skinfold thickness (Krueger et al., 2013), muscle size, rate of recruitment and torque development, middle upper arm

circumference, upper arm length and body composition (Cooper et al., 2014). While the abovementioned studies have evaluated these factors under varying intensities of voluntary muscle activation, the use of a consistent NMES stimulation intensity at the BB muscle in this study obtained varying MPF characteristics at changing elbow joint angle (Uwamahoro et al., 2023). Given the spatial selectivity of MMG signals (Klotz *et al.*, 2022), further investigations are guaranteed to evaluate the performance of the proposed torque estimation model in relation to these factors.

While this study did not quantify crosstalk from other elbow flexor muscles such as the brachialis and brachioradialis, it is likely that NMES has minimized these effects. Given that the brachioradialis is synergetic to the elbow flexion tasks, activation of these muscles across participants and experimental trials could potentially refine torque estimations (von Werder and Disselhorst-Klug, 2016). Moreover, previous research has shown improved performance of torque estimation models from multiple sites (Hondo and Tsuji, 2022), suggesting that exploration of MMG signals using arrays of transducers could further enhance torque estimation models.

Neurological pathologies such as stroke, spinal cord injury, and neurodegenerative diseases profoundly impair skeletal muscle structure, resulting in muscle atrophy, fibrosis, altered muscle fiber type distribution, and composition in stroke survivors (Conrad *et al.*, 2017). These conditions also compromise the integrity of neuromuscular junction, further exacerbating functional deficits in the upper limbs (Sirago et al., 2023). Given that MMG signals are influenced by the physical characteristics of the muscle being assessed, these pathologies underscore the urgent need for effective intervention strategies to mitigate their defects and promote functional recovery.

Previous research demonstrated that the spinal excitability to the BB muscle is independently influenced by the joint angle and muscle length, with these effects observed when muscle length or elbow joint angle was maintained constant (Forman *et al.*, 2019). These observations suggest that MMG data used in this study could similarly be influenced by independent influence of both elbow joint angle and the forearm posture (Gerditschke *et al.*, 2024). While the existing literature showed that there is no significant difference between joint angle specific and generic torque estimation models (Wang *et al.*, 2024), this study investigated the capability of GLEO-RFR-FS-HT to select optimal feature from MMG recorded at four elbow joint angle and three forearm postures during elbow flexion tasks. Should the NMES activation of the BB muscle also have received the influence of angle and posture, the performance metrics of GLEO-RFR-FS-HT method needs to be further investigated, given independent limitations identified in this study.

Taken together, this study focused exclusively on the BB muscle and employed the transverse axis of MMG signals. The incorporation of acoustic and Hjorth mobility features to the RMS, MPF, MDF, and ZCR highlights the relevance of these features in torque estimation models. Evidence suggesting that MMG signals from multiple sites and muscles improve torque estimation performance suggests that future research should incorporate MMG data from additional elbow flexor muscles. Furthermore, the MMG signals in this study were collected from participants with relative, but not identical anthropometric characteristics, which may imply differences in muscle capacity, fiber type composition, and rate coding. Although equal proportions of data from various postures and angle-specific configurations were used, afferent pathways and individual variations in muscle responsiveness to NMES could influence the outcomes. Future studies should address these factors to further evaluate and enhance prediction performance of torque estimation models.

This study proposed GLEO-RFR-FS-HT, a novel hybrid approach for optimizing the hyperparameters of the RFR and identifying optimal subsets of MMG features for elbow flexion torque estimation. The method was tested against various models including SVR, BPNN and RF using NMES MMG signals and torque datasets. All the models were trained on a large dataset of 292122 feature vectors. The study revealed the capability of the model for selecting optimal MMG signals features and tuned hyperparameters of the RFR which yielded significant estimation accuracy, measured by R^2, slope and RMSE of 0.7853, 0.7414, and 0.1174 respectively on the test dataset. These metrics reveal that the developed model captures the underlying relationship between MMG variables and torque measurements. However, while the study's findings are promising, it is crucial to acknowledge that the data was from healthy subjects which may influence the model's generalizability. Furthermore, the study used data obtained from a single elbow flexor muscle, assessing four angles and three forearm postures. The GLEO-RFR-FS-HT model conveged at the 50th iterations, validating the superior learning capability of GLEO over EO (Figure 4.9). The model obtained a large number of predictors (*Ntrees* = 849), low best splits at 46942, and good number of best split features (*mTrees* = 4). Howeve, the low *MinLeafeSize* (1) allows the model to create deeper trees with low number of splits. A low number of mTrees also allows the model to create less correlated trees; thereby the aggregation of less correlated trees resulted into a good model generalization.

The good performance on unseen datasets was expected to happen, as the datasets was bin-stratified avoiding any bias in the data during random selection of training and testing datasets. However, joint torque depends on the muscle size, typically measured by the MUAC, which in turn reflects the density of contractile proteins, such as myosin and actin, in the muscle fibers. These activations are related to the output joint torque (Wang *et*

al., 2017). Similarly, SKT measurement is relevant for understanding how subcutaneous fat distribution affects the transmission of electrical impulses to underlying muscles, potentially impacting efficiency of muscle recruitment and torque production during NMES (Santos *et al.*, 2021). Additionally, the body weight and height may provide valuable information regarding muscle recruitment strategies and force-generating capacity in individuals undergoing NMES, as larger body dimensions may require distinct motor unit activation patterns to achieve optimal torque. Although motor unit (MU) recruitment can indeed vary with changes in posture due to shifts in neuromuscular activation patterns, the neural drive remained robust enough for consistent force predictions across postures (Kunugi *et al.*, 2021). While above mentioned findings were obtained from NMES, the next section investigates the predictability of the model developed on dataset from real-wolrd experiment.

4.6 Performance of the torque estimation models in real word senarios

Sections 4.3 and 4.4 respectively discussed the TQ estimation model development using NMES-MMG and anthropometric++ features. This section discuss the applicability of the model on dataset from real-wolrd environment.

4.6.1 MMG features based model deployment

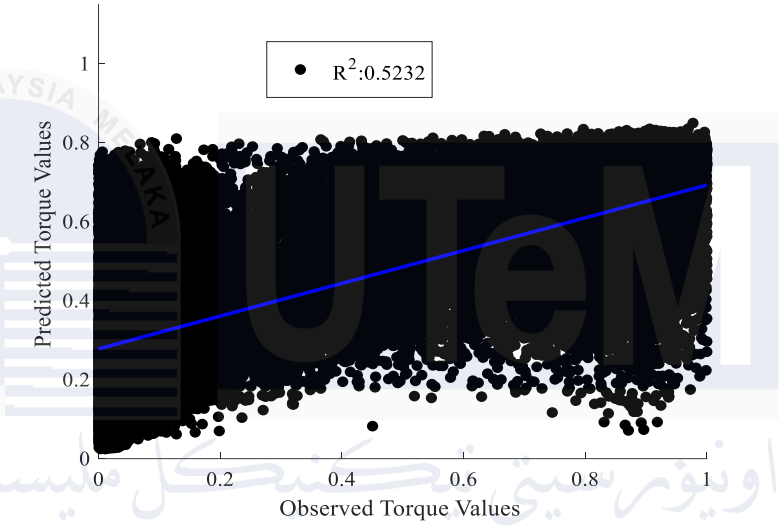

(a)

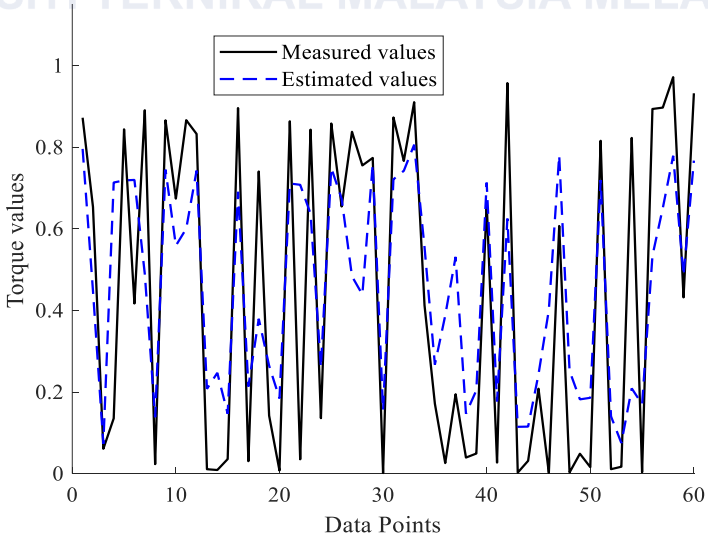

(b)

Figure 4.18:(a) Regression line and (b) cross plot for elbow joint torque estimation results from real world MMG datasets

Figure 4.18 presents the elbow joint torque estimation results based on MMG signals from the validation session (section 3.4.3). These results demonstrated an R^2 of 0.5232 and RMSE of 0.2607.

In the current study, the maximum accuracy from a lab-based experiment was measured at R^2 of 0.7853, found from RFR model developed using NMES MMG and TQ dataset. As shown in Figure 4.18, the validation data exhibited a lower RMSE than the training and testing experimental results depicted in Figure 4.10 (a). Similarly, the obtained R^2 values of the training and testing datasets indicate that the model trained on NMES MMG and TQ data achieved a higher estimation accuracy. These results align with the finding by (Shi et al., 2022), who noted a low R^2 in RFR model validation using MMG signal obtained from voluntary contraction of the brachioradialis. The results are also consistent with the research in (Youn and Kim, 2011), who observed a lower R^2 estimation accuracy in elbow flexion force model using MMG from the brachialis and brachioradialis, that was however validated by testing on the same subject's experimental dataset. Likely, some other studies (Z. Li et al., 2022; Li et al., 2021) using MMG and TQ signals on force estimation validated their model on 30% test dataset, achieving estimation accuracy over 90% with a limited number of subjects. However, these results were obtained from lab based experiments and on few datasets and subjects that may influence the results. The current research obtained a good estimation accuracy on 36 healthy subjects. A similar approach in NMES studies of the knee flexion used 70% dataset for the training and 30% for the testing and achieved comparable results using vibromyography signals from nine subjects undergoing NMES rehabilitation training (Ibitoye et al., 2016). Despite the lack of validation on unseen real word dataset in these studies, their test results align with the present research. Hence, the R^2

of 0.7853 on 30% testing experiments from NMES MMG data and validation R^2 of 0.5232 from the model deployment in real world low voluntary muscle contraction dataset is reliable.

In practical applications, torque estimation models developed on NMES data present a reduced accuracy due to several factors. Muscle activation under consistent NMES yields varying MMG and torque patterns raising from inter-subject variability. Under consistent targeted voluntary muscle contraction, the muscle activation influenced by the subcutaneous tissue and subject's specific rate coding, fiber morphology and intramuscular pressure introduces variability (Youn and Kim, 2011) . The NMES-MMG and TQ data for the training were recorded from isolated muscle. However, voluntary MMG recordings from the BB muscle under low muscle activation likely experienced crosstalk from nearby elbow flexors, such as the brachialis and brachioradialis. Additionally, NMES activates motor units non-selectively, and induced muscle activation at lower torque levels (below 20%) exhibits higher overall muscle activation than equivalent levels in voluntary contraction (Flodin et al., 2022).

The influence of anthropometric parameters such as MUAC and the LUA on torque estimation in this study align with the findings in (Green and Gabriel, 2012). Additionally, the minimal effect of skinfold thickness on torque estimation aligns with the finding in (Krueger et al.,2013), where the authors reported RMS MMG attenuation under NMES experiments. Furthermore, negligible to low negative correlation of SKT and MPF observed in (Talib *et al.*, 2022) is consistent with non-statistically significant GRD correlation observed in this study. Key anthropometric parameters, including weight, height, and BMI, which are often predictive of elbow flexion torque, showed no significant effect under low muscle activation conditions (Table 4.11). However, LLA estimation capability remained

consistent. While the study was also conducted at various four angles and three forearm postures configurations, these factors may have compromised the recording. Despite testing across four angles and three forearm postures, these configurations may have affected the recording quality. Thus, lower estimation accuracy in voluntary contractions should be based on anatomical and physiological factors unique to voluntary and NMES-induced low muscle activation.

4.6.2 Anthropometric++ features based model deployment

The performance metrics from anthropometric++ test portion showed an R^2 of 0.7170 and RMSE of 0.1333. These measurements were obtained from NMES MMG and anthropometric features fusion. The performance measurement from the validation experiments on real-world MMG and anthropometric parameters showed R^2 of 0.4437 and RMSE of 0.2317. This novel method characterized the outcome after deploying the model developed on anthropometric++ features in real world experiments, using anthropometric variables as discusses in section 3.8. While the subjects are characterized by different anthropometric features, these metrics indicated that morphological variables from healthy individuals might serve for the control of elbow joint torque output.

Apart from myographic technology, morphological features of skeletal muscles such as cross-sectional area, fascicle length have been found indexes of muscle contraction in both static and dynamic conditions (Herbert *et al.*, 2019). Study on the lower limb showed that anthropometric data alone can estimate the joint torque without considering muscle activity (Moreira et al., 2021). Particularly, cross-sectional area of the BB muscle was observed increasing during isometric contraction. This finding was confirmed by research

on the limb circumferences obtained from anthropometric measurements, reported as indexes of muscle contraction (Chimera et al., 2021). Specifically, the contraction of BB muscle has been studied with upper-arm circumferences and was found correlated with EMG as well as linearly related with the upper-arm circumference and joint torque during elbow isometric contractions especially in low muscle activity below 30% MVIC (Roman-Liu and Konarska, 2009). Despite the low torque estimation metric of the deployed model of this research, our study also used low MVIC contraction below 15% MVC, and MMG signals along anthropometric variables. While the the current study showed a significant torque estimation metric under NMES-MMG features based model (Figure 4.10), this is evident as NMES-MMG was found clean at NMES of about 20% MVC (Uwamahoro et al., 2023). Thus, the low the performance metrics were affected by the muscle morphology, and limb anthropometry (Table 4.12).

Data variability was found to improve the performance of the machine learning model (Serbest *et al.*, 2023). While some studies have used few study population subjects, the present research used 36 healthy subjects with different physical features, characterized by anthropometric variables discussed in section 3.4. As showed by Figures 4.10, 4.15 , 4.18 and 4.19 as well as Table 4.12, the torque estimation using separate anthropometric and MMG features confirm the finding of previous research that morphological and anthropometric parameters reflect the muscle activation.

Figure 4.19 (a) and (b) shows the model fit visualization and comparison plot of estimated vs true torque using anthropometric++ data from the validation in real-world experiment. A coefficient of fit of 0.4437 exhibited by the model shows that anthropometric variables are good candidates in future exploration. The regression plot also shows a

distribution of the majority data at the right and left side of the scatter. This originated from the the biomechanics of the BB muscle, rendering it to exhibit a length-tension relationship,

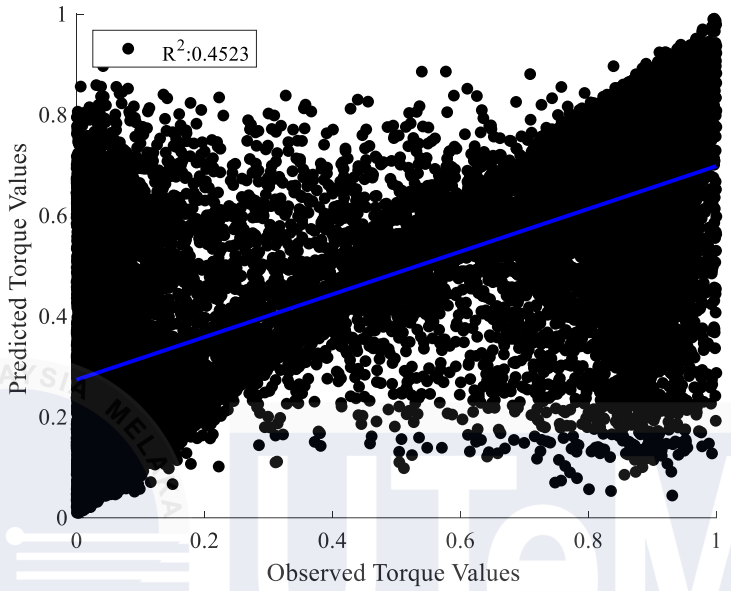

(a)

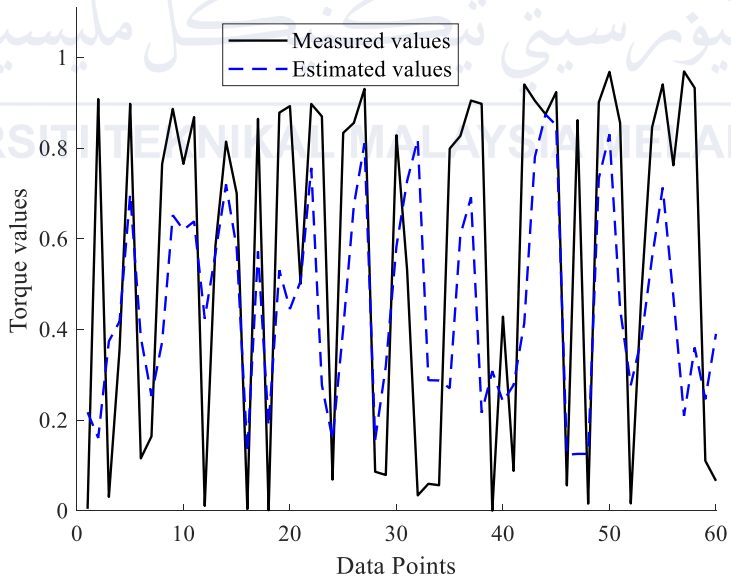

(b)

Figure 4.19: (a) Fitted regression curve and (b) agreement analysis between predicted and measured elbow torque.

to generate force varying with muscle length and joint angle. At extreme elbow positions (near full extension or full flexion), the BB muscle's mechanical advantage and fiber overlap may be suboptimal, leading to non-uniform torque output even with similar levels of muscle activation, which may confound torque prediction in those regions.

The LUA and LLA directly influence the moment arm and lever mechanics of elbow flexion. For instance, a longer forearm increases the torque demand for a given force, while upper arm length affects the alignment and insertion angle of the BB muscle. These anatomical variations can lead to subject-specific torque patterns at both low and high activation levels, potentially contributing to deviations in model predictions at the extremes, leading to the noted scatter plot bias (Figure 4.19).

Hence, further verifications are required to investigate additional anthropometric features and muscle morphology on torque production.

4.7 Summary

This chapter presents the research findings on the use of NMES MMG and voluntary signals features such as MMG RMS, MMG MPF, MMG MDF, MMG ZCR, MMG band energy, MMG SPC, MMG SS, MMG SF, MMG SFlx and Hjorth mobility to estimate NMES elbow joint torque produced from BB muscle at four elbow joint angle (0°, 30°, 60° and 90°) and three forearm postures (neutral, pronation and supination). Anthropometric parameters presented as the length of the lower arm, the length of upper arm, middle upper arm circumference, and skinfold thickness were fused with MMG RMS and MMG MPF, thus, used as anthropometric++ features to estimate dynamic elbow flexion torque. MMG features along the transverse axis were found statistically significant, thus, have been used

for torque estimation and showed R^2 of 0.7853, and 0.5352 respectively for the testing and validation datasets. Anthropometric++ features showed R^2 of 0.7170, and 0.4437 respectively for the testing and model deployment in real world. These results show that the essence of MMG alone as physiological representation of muscle activation in TQ and muscle strength simulation. Furthermore, MMG parameters alongside anthropometric variables provide information about the physiological and biomechanical function of BB muscle for TQ modelling.

CHAPTER 5

CONCLUSION

5.1 Recap of research objectives

This research presents a novel approach to estimate elbow joint torque using dynamic muscle contraction elicited by NMES and anthropometric variables reflecting the natural variability of muscle contraction. Occupational tasks, which involve changes in anatomical structure, are controlled by lower motor neurons, where the voluntary activation of muscles represents the overall contribution of muscles acting at a joint. In contrast, NMES specifically targets one or more muscles within a synergistic group. As a result, the contribution of these muscles to elbow joint torque can be computed .

Unlike the static approach, which focuses only on the maximum muscle contraction matched with the anthropometric variable based on specific event of muscle activation (Moreira et al., 2021), the proposed approach employs data augmentation simulating natural variability. It generates continuous anthropometric features that reflect the patterns of MMG and TQ data used for elbow joint torque estimation.

This research aimed to develop elbow joint torque estimation machine learning model using low muscle contraction from laboratory-based experiments and further validate it on real-world dataset. The results found that NMES MMG-based models were developed to validate the use of a low muscle contraction-based model that accounted for occupational activity of daily living. This research has three hypotheses to meet the research objectives as mentioned in section 1.4 and has been tested and validated from healthy subjects.

5.2 Summary of findings

The present research found that muscle activity was altered by the elbow joint angles as well as forearm postures, and the torque varied along the angle and posture configurations. The study found that MMG RMS increased from 10° to 30° and decreased as the joint angle expanded beyond 60°. Hence, muscle gemometry should be considered for the quantification of the patterns of MMG in muscle fiber directions.

A significant difference at 60° and a decrease in TQ at an angle beyond 60° was observed. These findings suggest that the BB muscle activation received complex morphological adaptation of muscle tendons and sarcomere lengthening.

The propagation of MMG generated by low muscle contraction exhibits different patterns of muscle contractions. MMG MPF and MMG MDF along the transverse axis produced the highest statistically significant variability across eight of all twelve configurations of elbow joint angles and forearm postures. The longitudinal axis exhibited no significant effects on both MMG MPF and MMG MDF. These results imply that the BB muscle received regular activation in the longitudinal axis and exhibited complex neural responses in the transverse axis.

Muscle geometry altered physiological responses of the muscle as reflected by MMG RMS, MMG MPF, and MMG MDF. The anatomical structure also affects the muscle's specific contraction and torque production. Consequently, the effect of muscle activation and anatomical structure on TQ may be non-overlapping, and both effects can be identified by the machine learning techniques. Indeed, anatomical structure is defined by anthropometric parameters, which in turn influence the muscle activation in both voluntary

and NMES-elicited contraction. Hence, there is a need to further validate this claim.

5.3 Research contributions

This research proposed a torque estimation model using low muscle contractions induced by NMES and validated on real-world environment datasets.

Elbow joint torque estimation using MMG features demonstrated a coefficient of determination of 0.7853. Nevertheless, anthropometric parameters exhibited different effects on muscle contraction under low muscle efforts, their features-based generic model was also developed and showed an accuracy of 0.7171. MMG features showed a high estimation but used eight features whereas six anthropometric++ features were used for model development. Both models were trained and tested on laboratory-based experiment and validated on real-world database with an accuracy of 0.5323 for voluntary MMG features and 0.4437 for anthropometric++ features. These findings are critical for prosthetic design and biomechanical devices, enabling the integration of physiologically intuitive control mechanisms and anthropometrically optimized configurations. By addressing low-effort muscle activation scenarios, the study lays a foundation for enhancing device responsiveness and muscle-specific adaptability, advancing both ergonomics and functionality in biomechanical systems.

Lastly, this research proposed a torque estimation framework integrating NMES-induced activation of elbow flexor muscles with anthropometric features, specifically tailored to estimate torque under low muscle contraction conditions in real-world datasets. This approach bridges the gap between physiological signal responsiveness and anatomical variability, providing a robust solution for accurate torque estimation in real-life applications.

5.4 Limitations and future work

The results presented in this study are beneficial. Nevertheless, some limitations need to be addressed.

First, the use of ultrasound can detect subtle changes in muscle fibers contractions factors, such as shifts in pennation angles, fascicle length, and overall muscle thickness, which are directly linked to the sliding of actin and myosin filaments during contraction (Jin *et al.*, 2024). This provides a more detailed biomechanical perspective, capturing intramuscular dynamics that surface MMG signals might overlook.

Second, there is a need to validate the proposed approach on data collected in large-scale experiments. Indeed, this study used datasets collected from homogeneous male subjects of the young age group. Further study should replicate the experiments on sex differences and a large and heterogeneous group of people.

Third, this study developed a generic torque estimation model using dataset from 36 participants with distinct biomechanical profiles, balancing anatomical and physiological variability to achieve broad applicability. However, muscle contraction dynamics are inherently subject-specific, influenced by individual neuromuscular response to NMES. These differences can significantly affect torque generation and the associated MMG signal characteristics, challenging the predictive power of a generalized model. Therefore, developing subject based model using individual specific dataset might improve the model's prediction capacity (Moreira et al., 2021).

Fourth, elbow angles and forearm postures are known to significantly influence muscle fiber recruitment patterns. Joint angle affects the muscle's length-tension relationship, altering the overlap of actin and myosin filaments and directly impacting force

production. The forearm posture (neutral, pronation, supination) shifts the contribution of individual flexor muscles due to changes in moment arms and muscle alignment relative to the joint axis (Uwamahoro et al., 2023). These biomechanical and physiological factors interplay to create complex variations in torque output that a generic model may not fully capture.

Fifth, synergistic flexors like the brachialis and brachioradialis significantly contribute to force production under varying joint angles, loads, and forearm postures. Henceforth, the recruitment patterns of these muscles vary significantly with forearm posture, further influencing torque generation. These overlapping biomechanical and related physiological effects highlight the need for muscle specific models alongwith geometric muscle configuration to clarify overall TQ contribution.

Sixth, conditions like muscular dystrophy or motor neuron diseases disrupt sarcomere integrity, ATP availability, and calcium dynamics, significantly affecting muscle contraction and force output (Sirago et al., 2023). Sarcomere misalignment reduces actin-myosin overlap, impairing tension generation, especially under NMES. Reduced ATP production in pathological muscles hampers cross-bridge cycling and accelerates fatigue. Additionally, impaired calcium release from the sarcoplasmic reticulum weakens actin-myosin binding, altering contraction strength (Dowling *et al.*, 2022) and may alter MMG signal characteristics. These physiological abnormalities result in attenuated and inconsistent MMG responses, challenging torque estimation accuracy. Future models should incorporate pathological muscle features to enhance clinical applicability, particularly for rehabilitation and assistive technologies.

REFERENCES

Adamo, D.E., Martin, B.J. and Johnson, P.W., 2002. Vibration-induced muscle fatigue, a possible contribution to musculoskeletal injury. *European Journal of Applied Physiology*, Vol. 88(1–2), pp.134–140.

Adewale, A.O. and Ahn, Y.H., 2021. Titin N2A domain and its interactions at the sarcomere. *International Journal of Molecular Sciences*, Vol. 22(14), pp.1–15.

Alawee, W.H., Basem, A. and Al-Haddad, L.A., 2023. Advancing biomedical engineering: Leveraging Hjorth features for electroencephalography signal analysis. *Journal of Electrical Bioimpedance*, Vol. 14(1), pp.66–72.

Aljarah, I., Al-Zoubi, A.M., Faris, H., Hassonah, M.A., Mirjalili, S. and Saadeh, H., 2018. Simultaneous feature selection and support vector machine optimization using the grasshopper optimization algorithm. *Cognitive Computation*, Vol. 10(3), pp.478–495.

Armstrong, W.J., 2014. Wavelet-based intensity analysis of the mechanomyograph and electromyograph during the H-reflex. *European Journal of Applied Physiology*, Vol. 114(12), pp.2571–2578.

Arrillaga, B., Miguel-Perez, M., Möller, I., Rubio, L., Blasi, J., Pérez-Bellmunt, A., Ortiz-Sagristà, J.C., Ortiz-Miguel, S. and Martinoli, C., 2024. Human shoulder anatomy: new ultrasound, anatomical, and microscopic perspectives. *Anatomical Science International*, Vol. 99(3), pp.290–304.

Asghar, A., Khan, S.J., Azim, F., Shakeel, C.S., Hussain, A. and Niazi, I.K., 2023. Intramuscular EMG feature extraction and evaluation at different arm positions and hand postures based on a statistical criterion method. *Proceedings of the Institution of Mechanical Engineers, Part H: Journal of Engineering in Medicine*, Vol. 237(1), pp.74–90.

Barry, D.T., 1987. Acoustic signals from frog skeletal muscle. *Biophysical Journal*, Vol. 51(5), pp.769–773.

Beck, T.W., Dillon, M.A., DeFreitas, J.M. and Stock, M.S., 2009. Cross-correlation analysis of mechanomyographic signals detected in two axes. *Physiological Measurement*, Vol. 30(12), p.1465.

Beck, T.W., Housh, T., Fry, A.C., Cramer, J.T., Weir, J., Schilling, B., Falvo, M. and Moore, C., 2009. MMG-EMG cross spectrum and muscle fiber type. *International Journal of Sports Medicine*, Vol. 30(7), pp.538–544.

Beck, T.W., Housh, T.J., Cramer, J.T., Weir, J.P., Johnson, G.O., Coburn, J.W., Malek, M.H. and Mielke, M., 2005. Mechanomyographic amplitude and frequency responses during dynamic muscle actions: a comprehensive review. *Biomedical Engineering Online*, Vol. 4(1), p.67.

Blangsted, A.K., Sjøgaard, G., Madeleine, P., Olsen, H.B. and Søgaard, K., 2005. Voluntary low-force contraction elicits prolonged low-frequency fatigue and changes in surface electromyography and mechanomyography. *Journal of Electromyography and Kinesiology*, Vol. 15(2), pp.138–148.

Boulesteix, A.L., Janitza, S., Kruppa, J. and König, I.R., 2012. Overview of random forest methodology and practical guidance with emphasis on computational biology and bioinformatics. *Wiley Interdisciplinary Reviews: Data Mining and Knowledge Discovery*, Vol. 2(6), pp.493–507.

Bowdle, A., Bussey, L., Michaelsen, K., Jelacic, S., Nair, B., Togashi, K. and Hulvershorn, J., 2020. A comparison of a prototype electromyograph vs. a mechanomyograph and an acceleromyograph for assessment of neuromuscular blockade. *Anaesthesia*, Vol. 75(2), pp.187–195.

Brueckner, D., Kiss, R. and Muehlbauer, T., 2018. Associations between practice-related changes in motor performance and muscle activity in healthy individuals: a systematic review. *Sports Medicine-Open*, Vol. 4(1), p.9.

Cabral, H.V., Inglis, J.G., Cudicio, A., Cogliati, M., Orizio, C., Yavuz, U.S. and Negro, F., 2024. Muscle contractile properties directly influence shared synaptic inputs to spinal motor neurons. *The Journal of Physiology*, Vol. 602(12), pp.2855–2872.

Campbell, E., Phinyomark, A. and Scheme, E., 2020. Current trends and confounding factors in myoelectric control: Limb position and contraction intensity. *Sensors*, Vol. 20(6), p.1613.

Cè, E., Paracchino, E. and Esposito, F., 2008. Electrical and mechanical response of skeletal muscle to electrical stimulation after acute passive stretching in humans: A combined electromyographic and mechanomyographic approach. *Journal of Sports Sciences*, Vol. 26(14), pp.1567–1577.

Cè, E., Rampichini, S., Limonta, E. and Esposito, F., 2013. Torque and mechanomyogram correlations during muscle relaxation: Effects of fatigue and time-course of recovery. *Journal of Electromyography and Kinesiology*, Vol. 23(6), pp.1295–1303.

Cè, E., Rampichini, S., Limonta, E. and Esposito, F., 2014. Fatigue effects on the electromechanical delay components during the relaxation phase after isometric contraction. *Acta Physiologica*, Vol. 211(1), pp.82–96.

Cè, E., Rampichini, S., Monti, E., Venturelli, M., Limonta, E. and Esposito, F., 2017. Changes in the electromechanical delay components during a fatiguing stimulation in human skeletal muscle: An EMG, MMG and force combined approach. *European Journal of Applied Physiology*, Vol. 117(1), pp.95–107.

Chandrashekar, G. and Sahin, F., 2014. A survey on feature selection methods. *Computers and Electrical Engineering*, Vol. 40(1), pp.16–28.

Cheuy, V.A., Dayton, M.R., Hogan, C.A., Graber, J., Anair, B.M., Voigt, T.B., Nelms, N.J., Stevens-Lapsley, J.E. and Toth, M.J., 2023. Neuromuscular electrical stimulation preserves muscle strength early after total knee arthroplasty: Effects on muscle fiber size. *Journal of Orthopaedic Research®*, Vol. 41(4), pp.787–792.

Chimera, N.J., Holmes, M.W.R. and Gabriel, D.A., 2021. Anthropometrics and electromyography as predictors for maximal voluntary isometric wrist torque: Considerations for ergonomists. *Applied Ergonomics*, Vol. 97, p.103525.

Chiyama, T.U. and Aito, K.S., 2018. Stiffness and viscosity of the vastus lateralis muscle in cycling exercises at low constant power output. *Advanced Biomedical Engineering*,Vol. 7, pp.124–130.

Clevert, D.A., Nyhsen, C., Ricci, P., Sidhu, P.S., Tziakouri, C. and Radziņa, M., 2020. Position statement and best practice recommendations on the imaging use of ultrasound from the European Society of Radiology ultrasound subcommittee. *Insights into Imaging*, Vol. 11(1), pp.1–12. Online Available at: https://insightsimaging.springeropen.com/ [Accessed 23 August, 2025].

Cogliati, M., Cudicio, A., Toscani, F., Gaffurini, P., Bissolotti, L.M., Orizio, C. and Negro, F., 2020. Normalized maximal rate of torque development during voluntary and stimulated static contraction in human tibialis anterior: Influence of age. *Experimental Gerontology*, Vol. 138, p.110999.

Connor, O. and McCully, K.K., 2016. Mitochondrial capacity, muscle endurance, and low energy in Friedreich ataxia. *Muscle and Nerve*, Vol. 56(4), pp.773–779.

Conrad, M.O., Qiu, D., Hoffmann, G., Zhou, P. and Kamper, D.G., 2017. Analysis of muscle fiber conduction velocity during finger flexion and extension after stroke. *Topics in Stroke Rehabilitation*, Vol. 24(4), pp.262–268.

Cooper, M.A., Herda, T.J., Vardiman, J.P., Gallagher, P.M. and Fry, A.C., 2014. Relationships between skinfold thickness and electromyographic and mechanomyographic amplitude recorded during voluntary and non-voluntary muscle actions. *Journal of Electromyography and Kinesiology*, Vol. 24(2), pp.207–213.

Correa, M., Projetti, M., Siegler, I.A. and Vignais, N., 2023. Mechanomyographic analysis for muscle activity assessment during a load-lifting task. *Sensors*, Vol. 23(18), p.7830.

Cossich, V.R., Laett, C.T., Gavilão, U.F., Blazevich, A.J. and de Oliveira, C.G., 2021. Faster intrinsic rate of torque development in elbow flexors than knee extensors: Effect of muscle architecture? *Journal of Electromyography and Kinesiology*, Vol. 59, p.102570.

Csapo, R., Gumpenberger, M. and Wessner, B., 2020. Skeletal muscle extracellular matrix – what do we know about its composition, regulation, and physiological roles? A narrative review. *Frontiers in Physiology*,Vol. 11, p.253.

De Miguel-Etayo, P., Mesana, M.I., Cardon, G., De Bourdeaudhuij, I., Góźdź, M., Socha, P., Lateva, M., Iotova, V., Koletzko, B.V., Duvinage, K. and Androutsos, O., 2014. Reliability of anthropometric measurements in European preschool children: The ToyBox-study. *Obesity Reviews*, Vol. 15, pp.67–73.

Decker, M.J., Griffin, L., Abraham, L.D. and Brandt, L., 2010. Alternating stimulation of synergistic muscles during functional electrical stimulation cycling improves endurance in persons with spinal cord injury. *Journal of Electromyography and Kinesiology*, Vol. 20(6), pp.1163–1169.

Deffieux, T., Gennisson, J., Tanter, M. and Fink, M., 2008. Assessment of the mechanical properties of the musculoskeletal system using 2-D and 3-D very high frame rate ultrasound. *IEEE Transactions on Ultrasonics, Ferroelectrics, and Frequency Control*, Vol. 55(10), pp.2177–2190.

Dowling, P., Gargan, S., Swandulla, D. and Ohlendieck, K., 2022. Proteomic profiling of impaired excitation–contraction coupling and abnormal calcium handling in muscular dystrophy. *Proteomics*, Vol. 22(23–24), p.e2200088.

Dzulkifli, M.A., Hamzaid, N.A., Davis, G.M. and Hasnan, N., 2018. Neural network-based muscle torque estimation using mechanomyography during electrically-evoked knee extension and standing in spinal cord injury. *Frontiers in Neurorobotics*, Vol. 12, p.50.

Esposito, F., Cè, E., Rampichini, S. and Veicsteinas, A., 2009. Acute passive stretching in a previously fatigued muscle: Electrical and mechanical response during tetanic stimulation. *Journal of Sports Sciences*, Vol. 27(12), pp.1347–1357.

Esposito, F., Limonta, E. and Cè, E., 2011a. Passive stretching effects on electromechanical delay and time course of recovery in human skeletal muscle: New insights from an electromyographic and mechanomyographic combined approach. *European Journal of Applied Physiology*, Vol. 111(3), pp.485–495.

Esposito, F., Limonta, E. and Cè, E., 2011b. Time course of stretching-induced changes in mechanomyogram and force characteristics. *Journal of Electromyography and Kinesiology*, Vol. 21(5), pp.795–802.

Faramarzi, A., Heidarinejad, M., Stephens, B. and Mirjalili, S., 2020. Equilibrium optimizer: A novel optimization algorithm. *Knowledge-Based Systems*, Vol. 191, p.105190.

Fidali, M., Augustyn, D., Ochmann, J. and Uchman, W., 2024. Evaluation of the diagnostic sensitivity of digital vibration sensors based on capacitive MEMS accelerometers. *Sensors*, Vol. 24(14), p.4657.

Flodin, J., Mikkelsen, C. and Ackermann, P.W., 2022. Knee extensor force production and discomfort during neuromuscular electrical stimulation of quadriceps with and without gluteal muscle co-stimulation. *European Journal of Applied Physiology*, Vol. 122(6), pp.1521–1530.

Fok, K.L., Kaneko, N., Sasaki, A., Nakagawa, K., Nakazawa, K. and Masani, K., 2020. Motor point stimulation in spinal paired associative stimulation can facilitate spinal cord excitability. *Frontiers in Human Neuroscience*, Vol. 14, p.593806.

Forman, D.A., Abdel-Malek, D., Bunce, C.M. and Holmes, M.W., 2019. Muscle length and joint angle influence spinal but not corticospinal excitability to the biceps brachii across forearm postures. *Journal of Neurophysiology*, Vol. 122(1), pp.413–423.

Frangioni, J.V., Kwan-Gett, T.S., Dobrunz, L.E. and McMahon, T.A., 1987. The mechanism of low-frequency sound production in muscle. *Biophysical Journal*, Vol. 51(5), pp.775–783.

Fukunaga, T., Miyatani, M., Tachi, M., Kouzaki, M., Kawakami, Y. and Kanehisa, H., 2001. Muscle volume is a major determinant of joint torque in humans. *Acta Physiologica Scandinavica*, Vol. 172(4), pp.249–255.

Gerditschke, L., Schrattner, J.S. and Forman, D.A., 2024. Upper arm muscle activity is influenced by both forearm posture and wrist exertion direction during isometric wrist flexion and extension. *Journal of Electromyography and Kinesiology*, Vol. 79, p.102919.

Gobbo, M., Cè, E., Diemont, B., Esposito, F. and Orizio, C., 2006. Torque and surface mechanomyogram parallel reduction during fatiguing stimulation in human muscles. *European Journal of Applied Physiology*, 97(1), pp.9–15.

Gobbo, M., Maffiuletti, N.A., Orizio, C. and Minetto, M.A., 2014. Muscle motor point identification is essential for optimizing neuromuscular electrical stimulation use. *Journal of neuroengineering and rehabilitation*, Vol. 11(1), p.17.

Gonzalez, E.J., Downey, R.J., Rouse, C.A. and Dixon, W.E., 2018. Influence of Elbow Flexion and Stimulation Site on Neuromuscular Electrical Stimulation of the Biceps Brachii. *IEEE Transactions on Neural Systems and Rehabilitation Engineering*, Vol. 26(4), pp.904–910.

Green, L.A. and Gabriel, D.A., 2012. Anthropometrics and electromyography as predictors for maximal voluntary isometric arm strength. *Journal of Sport and Health Science*, Vol. 1(2), pp.107–113.

Guo, J.Y., Zheng, Y.P., Xie, H.B. and Chen, X., 2010. Continuous monitoring of electromyography (EMG), mechanomyography (MMG), sonomyography (SMG) and torque output during ramp and step isometric contractions. *Medical Engineering and Physics*, Vol. 32(9), pp.1032–1042.

Gupta, S., Deep, K. and Mirjalili, S., 2020. An efficient equilibrium optimizer with mutation strategy for numerical optimization. *Applied Soft Computing Journal*, Vol. 96, pp.1–15.

Gwak, G.T., Lee, S.Y., Kim, H.J., Park, J.S. and Yoo, W.G., 2021. Comparison of maximal isometric forearm supination torque in two elbow positions between subjects with and without limited forearm supination range of motion. *Physiotherapy Theory and Practice*, Vol. 37(1), pp.99–105.

He, L. and Mathieu, P.A., 2018. Static hand posture classification based on the biceps brachii muscle synergy features. *Journal of Electromyography and Kinesiology*, Vol. 43, pp.201–208.

Hemmerling, T., 2015. Monitoring neuromuscular blockade at the vastus medialis muscle using phonomyography. *Canadian Journal of Anesthesia*, Vol. 52(8), pp.795–800.

Herbert, R.D., Bolsterlee, B.B. and Gandevia, S.C., 2019. Passive changes in muscle length. *Journal of Applied Physiology*, Vol. 126, pp.1445–1453.

Herold, F., Wiegel, P., Scholkmann, F. and Müller, N.G., 2018. Applications of functional near-infrared spectroscopy (fNIRS) neuroimaging in exercise–cognition science: A systematic, methodology-focused review. *Journal of Clinical Medicine*, Vol. 7(12), pp.1–26.

Hondo, N. and Tsuji, T., 2022. Torque estimation of knee flexion and extension movements from a mechanomyogram of the femoral muscle. *IEEE Transactions on Neural Systems and Rehabilitation Engineering*, Vol. 30, pp.1120–1126.

Hou, J., Sun, Y., Sun, L., Pan, B., Huang, Z., Wu, J. and Zhang, Z., 2016. A pilot study of individual muscle force prediction during elbow flexion and extension in the neurorehabilitation field. *Sensors*, Vol. 16(12), p.2018.

Huang, B.F.F. and Boutros, P.C., 2016. The parameter sensitivity of random forests. *BMC Bioinformatics*, Vol. 17(1), pp.1–10.

Hunter, A.M., Galloway, S.D., Smith, I.J., Tallent, J., Ditroilo, M., Fairweather, M.M. and Howatson, G., 2012. Assessment of eccentric exercise-induced muscle damage of the elbow flexors by tensiomyography. *Journal of Electromyography and Kinesiology*, Vol. 22(3), pp.334–341.

Ibitoye, M.O., Hamzaid, N.A., Abdul Wahab, A.K., Hasnan, N., Olatunji, S.O. and Davis, G.M., 2016. Estimation of electrically-evoked knee torque from mechanomyography using support vector regression. *Sensors*, Vol. 16(7), p.1115.

Ibitoye, M.O., Hamzaid, N.A., Hasnan, N., Wahab, A.K.A., Islam, M.A., Kean, V.S. and Davis, G.M., 2016. Torque and mechanomyogram relationships during electrically-evoked isometric quadriceps contractions in persons with spinal cord injury. *Medical Engineering and Physics*, Vol. 38(8), pp.767-775.

Ibitoye, M.O., Hamzaid, N.A., Hasnan, N., Wahab, A.K.A., Islam, M.A., Kean, V.S. and Davis, G.M., 2016. Torque and mechanomyogram relationships during electrically evoked isometric quadriceps contractions in persons with spinal cord injury. *Medical Engineering and Physics*, Vol. 38(8), pp.767–775.

Ibrahim, S.N., Rahman, F.A. and Rosli, S., 2017. Characterization of screen printed Ag-PDMS flexible electrode for electrical muscle stimulation (EMS). *Indonesian Journal of Electrical Engineering and Informatics*, Vol. 5(4), pp.295–303.

Ichikawa, K., Jiang, Y., Sugi, M., Togo, S. and Yokoi, H., 2021. Joint angle based motor point tracking stimulation for surface FES: A Study on biceps brachii. *Medical Engineering and Physics*, Vol. 88, pp.9-18.

Islam, M.A., Hamzaid, N.A., Ibitoye, M.O., Hasnan, N., Wahab, A.K.A. and Davis, G.M., 2018. Mechanomyography responses characterize altered muscle function during electrical stimulation-evoked cycling in individuals with spinal cord injury. *Clinical Biomechanics*, Vol. 58, pp.21–27.

Islam, M.A., Sundaraj, K., Ahmad, R.B. and Ahamed, N.U., 2013. Mechanomyogram for muscle function assessment: a review. *PLoS ONE*, Vol. 8(3), pp.1–14.

Islam, M.A., Sundaraj, K., Ahmad, R.B., Ahamed, N.U. and Ali, M.A., 2013. Mechanomyography sensor development, related signal processing, and applications: a systematic review. *IEEE Sensors Journal*, Vol. 13(7), pp.2499–2516.

Islam, M.A., Sundaraj, K., Ahmad, R.B., Sundaraj, S., Ahamed, N.U. and Ali, M.A., 2014. Cross-talk in mechanomyographic signals from the forearm muscles during sub-maximal to maximal isometric grip force. *PLoS ONE*, Vol. 9(5), p.e96628.

Islam, M.A., Sundaraj, K., Ahmad, R.B., Sundaraj, S., Ahamed, N.U. and Ali, M.A., 2014. Longitudinal, lateral and transverse axes of forearm muscles influence the crosstalk in the mechanomyographic signals during isometric wrist postures. *PLoS ONE*, Vol. 9(8), p.e104280.

Jarocka, E., Marusiak, J., Kumorek, M., Jaskólska, A. and Jaskólski, A., 2011. Muscle stiffness at different force levels measured with two myotonometric devices. *Physiological Measurement*, Vol. 33(1), p.65.

Jiang, D., Li, G., Sun, Y., Kong, J., Tao, B. and Chen, D., 2022. Grip strength forecast and rehabilitative guidance based on adaptive neural fuzzy inference system using sEMG. *Personal and Ubiquitous Computing*, Vol. 26(4), pp.1215–1224.

Jin, Y., Alvarez, J.T., Suitor, E.L., Swaminathan, K., Chin, A., Civici, U.S., Nuckols, R.W., Howe, R.D. and Walsh, C.J., 2024. Estimation of joint torque in dynamic activities using wearable A-mode ultrasound. *Nature Communications*, Vol. 15(1), p.5756.

Jo, M., Ahn, S., Kim, J., Koo, B., Jeong, Y., Kim, S. and Kim, Y., 2018. Mechanomyography for the measurement of muscle fatigue caused by repeated functional electrical stimulation. *International Journal of Precision Engineering and Manufacturing*, Vol. 19(9), pp.1405–1410.

Karamian, B.A., Siegel, N., Nourie, B., Serruya, M.D., Heary, R.F., Harrop, J.S. and Vaccaro, A.R., 2022. The role of electrical stimulation for rehabilitation and regeneration after spinal cord injury. *Journal of Orthopaedics and Traumatology*, Vol. 23(1), p.2.

Khushaba, R.N., Takruri, M., Miro, J.V. and Kodagoda, S., 2014. Towards limb position invariant myoelectric pattern recognition using time-dependent spectral features. *Neural Networks*, Vol. 55, pp.42–58.

Kim, J., Yang, S., Koo, B., Lee, S., Park, S., Kim, S., Cho, K.H. and Kim, Y., 2022. SEMG-based hand posture recognition and visual feedback training for the forearm amputee. *Sensors*, Vol. 22(20), p.7984.

Kim, W.S., Lee, H.D., Lim, D.H., Han, J.S., Shin, K.S. and Han, C.S., 2014. Development of a muscle circumference sensor to estimate torque of the human elbow joint. *Sensors and Actuators : Physical*, Vol. 208, pp.95–103.

Kimura, T., Hamada, T., Ueno, L.M. and Moritani, T., 2003. Changes in contractile properties and neuromuscular propagation evaluated by simultaneous mechanomyogram

and electromyogram during experimentally induced hypothermia. *Journal of Electromyography and Kinesiology*, Vol. 13(5), pp.433–440.

Kleiber, T., Kunz, L. and Disselhorst-Klug, C., 2015. Muscular coordination of biceps brachii and brachioradialis in elbow flexion with respect to hand position. *Frontiers in Physiology*, Vol. 6, p.215.

Klotz, T., Gizzi, L. and Röhrle, O., 2022. Investigating the spatial resolution of EMG and MMG based on a systemic multi-scale model. *Biomechanics and Modeling in Mechanobiology*, Vol. 21(3), pp.983–997.

Kong, P.W., Pan, J., Chu, D.P., Cheung, P.M. and Lau, P.W.C., 2021. Acquiring expertise in precision sport: What can we learn from an elite snooker player?. *Physical Activity and Health.*

Koren, K., Rejc, E. and Lazzer, S., 2015. Differences between skeletal muscle contractile parameters estimated from transversal tensiomyographic and longitudinal torque twitch response. *International Journal of Fundamental and Applied Kinesiology*, Vol. 47(1), pp.19–26.

Kozlowska, K., Scher, S. and Helgeland, H., 2020. Functional somatic symptoms in children and adolescents: A stress-system approach to assessment and treatment. *Springer Nature*, p.383.

Krishnan, C., Allen, E.J. and Williams, G.N., 2011. Effect of knee position on quadriceps muscle force steadiness and activation strategies. *Muscle and Nerve*, Vol. 43(4), pp.563–573.

Krueger, E., Scheeren, E.M., Nogueira-Neto, G.N., Button, V.L.D.S.N. and Nohama, P., 2014. Advances and perspectives of mechanomyography. *Revista Brasileira de Engenharia Biomédica*, Vol. 30, pp.384–401.

Krueger, E., Scheeren, E.M., Nogueira-Neto, G.N., Button, V.L.D.S.N. and Nohama, P., 2016. Correlation between spectral and temporal mechanomyography features during functional electrical stimulation. *Research on Biomedical Engineering*, Vol. 32(1), pp.85–91.

Krueger, E., Scheeren, E.M., Nogueira-Neto, G.N., Neves, E.B., Button, V.L.S. and Nohama, P., 2013. Influence of skinfold thickness in mechanomyography features. *In: World Congress on Medical Physics and Biomedical Engineering* May 26–31, 2012, Beijing, China, pp.2030–2033.

Kubo, K., Ohgo, K., Takeishi, R., Yoshinaga, K., Tsunoda, N., Kanehisa, H. and Fukunaga, T., 2006. Effects of isometric training at different knee angles on the muscle–tendon complex in vivo. *Scandinavian Journal of Medicine and Science in Sports*, Vol. 16(3), pp.159–167.

Kunugi, S., Holobar, A., Kodera, T., Toyoda, H. and Watanabe, K., 2021. Motor unit firing patterns on increasing force during force and position tasks. *Journal of Neurophysiology*, Vol. 126(5), pp.1653–1659.

Latella, C., Ruas, C.V., Mesquita, R.N., Nosaka, K. and Taylor, J.L., 2019. Test-retest reliability of elbow flexor contraction characteristics with tensiomyography for different elbow joint angles. *Journal of Electromyography and Kinesiology*, Vol. 45, pp.26–32.

Li, J., Zhang, N., Xu, Y., Wang, J., Kang, X., Ji, R., Li, K. and Hou, Y., 2024. Dynamical network-based evaluation for neuromuscular dysfunction in stroke-induced hemiplegia during standing. *Journal of NeuroEngineering and Rehabilitation*, Vol. 21(1), p.190.

Li, Y., Chen, W., Chen, J., Chen, X., Liang, J. and Du, M., 2019. Neural network based modeling and control of elbow joint motion under functional electrical stimulation. *Neurocomputing*, Vol. 340, pp.171–179.

Li, Y., Wang, W., Liu, J. and Zhou, H., 2022. Equilibrium optimizer with divided population based on distance and its application in feature selection problems. *Knowledge-Based Systems*, Vol. 256, p.109842.

Li, Z., Gao, L., Lu, W., Wang, D., Cao, H. and Zhang, G., 2022. Estimation of knee extension force using mechanomyography signals based on GRA and ICS-SVR. *Sensors*, Vol. 22(12), p.4651.

Li, Z., Gao, L., Lu, W., Wang, D., Xie, C. and Cao, H., 2021. Estimation of knee joint extension force using mechanomyography based on IGWO-SVR algorithm. *Electronics*, Vol. 10(23), p.2972.

Li, Z., Gao, L., Zhang, G., Lu, W., Wang, D., Zhang, J. and Cao, H., 2024. MMG-based knee dynamic extension force estimation using cross-talk and IGWO-LSTM. *Bioengineering*, Vol. 11(5), p.470.

Li, Z., Guan, X., Zou, K. and Xu, C., 2019. Estimation of knee movement from surface EMG using random forest with principal component analysis. *Electronics*, Vol. 9(1), p.43.

Liu, J., Zhou, Z., Kong, S. and Ma, Z., 2022. Application of random forest based on semi-automatic parameter adjustment for optimization of anti-breast cancer drugs. *Frontiers in Oncology*, Vol. 12, p.956705.

Longo, S., Cè, E., Rampichini, S., Devoto, M., Limonta, E. and Esposito, F., 2014. Mechanomyogram amplitude correlates with human gastrocnemius medialis muscle and tendon stiffness both before and after acute passive stretching. *Experimental Physiology*, Vol. 99(10), pp.1359–1369.

Longo, S., Devoto, M., Monti, E., Venturelli, M., Limonta, E., Rampichini, S. and Valentina, A., 2016. Acute effects of static stretching on skeletal muscle relaxation at different ankle joint angles. *Sport Sci Health*, 12, pp.429–436.

Lv, J., Yang, Y., Niu, L., Sun, X., Wang, L., Lin, W., Rong, H. and Zou, L., 2023. Prediction of hand grip strength based on surface electromyographic signals. *Journal of King Saud University-Computer and Information Sciences*, Vol. 35(5), p.101548.

Macgregor, L.J., Ditroilo, M., Smith, I.J., Fairweather, M.M. and Hunter, A.M., 2016. Reduced radial displacement of the gastrocnemius medialis muscle after electrically elicited fatigue. *Journal of Sport Rehabilitation*, Vol. 25(3), pp.241–247.

Mallegni, N., Molinari, G., Ricci, C., Lazzeri, A., La Rosa, D., Crivello, A. and Milazzo, M., 2022. Sensing devices for detecting and processing acoustic signals in healthcare. *Biosensors*, Vol. 12(10), p.835.

Matsue, Y. and T.U., 2000. Medial gastrocnemius muscle stiffness dependent on gait speed. *Transactions of Japanese Society for Medical and Biological Engineering*, Vol. 55, pp.534–535.

Mazzinari, G., Errando, C.L., Díaz-Cambronero, O. and Martin-Flores, M., 2019. Influence of tetanic stimulation on the staircase phenomenon and the acceleromyographic time-course of neuromuscular block: a randomized controlled trial. *Journal of Clinical Monitoring and Computing*, Vol. 33(2), pp.325–332.

McCully, K.K., Moraes, C., Patel, S.V., Green, M. and Willingham, T.B., 2019. Muscle-specific endurance of the lower back erectors using electrical twitch mechanomyography. *Journal of Functional Morphology and Kinesiology*, Vol. 4(1), p.12.

Menon, P. and Vucic, S., 2021. The upper motor neuron—improved knowledge from ALS and related clinical disorders. *Brain Sciences*, 11(8), p.958.

Miyamoto, N. and Oda, S., 2005. Effect of joint angle on mechanomyographic amplitude during unfused and fused tetani in the human biceps brachii muscle. *European Journal of Applied Physiology*, Vol. 95(2–3), pp.221–228.

Miyamoto, N., Mitsukawa, N., Sugisaki, N., Fukunaga, T. and Kawakami, Y., 2010. Joint angle dependence of intermuscle difference in postactivation potentiation. *Muscle and Nerve*, Vol. 41(4), pp.519–523.

Mogk, J.P., Rogers, L.M., Murray, W.M., Perreault, E.J. and Stinear, J.W., 2014. Corticomotor excitability of arm muscles modulates according to static position and orientation of the upper limb. *Clinical Neurophysiology*, Vol. 125(10), pp.2046–2054.

Mohamad, N.Z., Hamzaid, N.A., Davis, G.M., Abdul Wahab, A.K. and Hasnan, N., 2017. Mechanomyography and torque during FES-evoked muscle contractions to fatigue in individuals with spinal cord injury. *Sensors*, Vol. 17(7), p.1627.

Monter-Pozos, A. and González-Estrada, E., 2024. On testing the skew normal distribution by using Shapiro–Wilk test. *Journal of Computational and Applied Mathematics*, Vol. 440, p.115649.

Moreira, L., Figueiredo, J., Vilas-Boas, J.P. and Santos, C.P., 2021. Kinematics, speed, and anthropometry-based ankle joint torque estimation: a deep learning regression approach. *Machines*, Vol. 9(8), p.154.

Naeem, J., Hamzaid, N.A., Islam, M.A., Azman, A.W. and Bijak, M., 2019. Mechanomyography-based muscle fatigue detection during electrically elicited cycling in patients with spinal cord injury. *Medical and Biological Engineering and Computing*, Vol. 57(6), pp.1199–1211.

Nagineni, S., Taran, S. and Bajaj, V., 2018. Features based on variational mode decomposition for identification of neuromuscular disorder using EMG signals. *Health Information Science and Systems*, Vol. 6(1), p.13.

Ng, M.Y., Pourmajidian, M. and Hamzaid, N.A., 2014. Mechanomyography sensors for detection of muscle activities and fatigue during FES-evoked contraction. In *the 19th IEEE*

International Functional Electrical Stimulation Society Annual Conference (IFESS), 2014. pp.1–3.

Norali, A.N., 2017. Human breathing classification using electromyography signal with features based on mel-frequency cepstral coefficients. *International Journal of Integrated Engineering*, Vol. 9(4).

Nourani, V., Asghari, P. and Sharghi, E., 2021. Artificial intelligence based ensemble modeling of wastewater treatment plant using jittered data. *Journal of Cleaner Production*, Vol. 291, p.125772.

Nunes, J.P., Jacinto, J.L., Ribeiro, A.S., Mayhew, J.L., Nakamura, M., Capel, D.M., Santos, L.R., Santos, L., Cyrino, E.S. and Aguiar, A.F., 2020. Placing greater torque at shorter or longer muscle lengths? Effects of cable vs. barbell preacher curl training on muscular strength and hypertrophy in young adults. *International Journal of Environmental Research and Public Health*, Vol. 17(16), p.5859.

Ohta, Y.2013. The relationship between changes in joint kinematics parameters and mechanomyographic signals during non-isometric contraction in human skeletal muscle. *Acta of Bioengineering and Biomechanics*, Vol. 15(2), pp.97–104.

Ohta, Y., Shima, N. and Yabe, K., 2009. In vivo behaviour of human muscle architecture and mechanomyographic response using the interpolated twitch technique. *Journal of Electromyography and Kinesiology*, Vol. 19(3), pp.e154–e161.

Orizio, C., Celichowski, J., Toscani, F., Calabretto, C., Bissolotti, L. and Gobbo, M., 2013. Extra-torque of human tibialis anterior during electrical stimulation with linearly varying frequency and amplitude trains. *Journal of Electromyography and Kinesiology*, Vol. 23(6), pp.1375–1383.

Orizio, C., Solomonow, M., Diemont, B. and Gobbo, M., 2008. Muscle-joint unit transfer function derived from torque and surface mechanomyogram in humans using different stimulation protocols. *Journal of Neuroscience Methods*, Vol. 173(1), pp.59–66.

Ortega, D.G., Housh, T.J., Smith, R.W., Arnett, J.E., Neltner, T.J., Anders, J.P.V., Schmidt, R.J. and Johnson, G.O., 2023. Fatiguing joint angle does not influence torque and neuromuscular responses following sustained, isometric forearm flexion tasks anchored to perceptual intensity in men. *Journal of Functional Morphology and Kinesiology*, Vol. 8(3), p.114.

Miramonti, A.A., Jenkins, N.D., Oza, P.D., Weir, J.P. and Cramer, J.T., 2017. Mechanomyographic responses during recruitment curves in the soleus muscle. *Muscle and nerve*, Vol. *56*(1), pp.107-116.

Paillard, T., 2018. Training based on electrical stimulation superimposed onto voluntary contraction would be relevant only as part of submaximal contractions in healthy subjects. *Frontiers in Physiology*, Vol. 9, p.1428.

Papcke, C., Krueger, E., Olandoski, M., Nogueira-Neto, G.N., Nohama, P. and Scheeren, E.M., 2018. Investigation of the relationship between electrical stimulation frequency and muscle frequency response under submaximal contractions. *Artificial Organs*, Vol. 42(6), pp.655–663.

Park, B.K., Shin, Y.B., Ko, H.Y., Park, J.H. and Baek, S.Y., 2007. Anatomic motor point localization of the biceps brachii and brachialis muscles. *Journal of Korean Medical Science*, Vol. 22(3), pp.459–464.

Parums, D.V., 2024. The 2024 revision of the declaration of Helsinki and its continued role as a code of ethics to guide medical research. *Medical Science Monitor: International Medical Journal of Experimental and Clinical Research*, Vol. 30, p.e947428.

Pasquet, B., Carpentier, A. and Duchateau, J., 2005. Change in muscle fascicle length influences the recruitment and discharge rate of motor units during isometric contractions. *Journal of Neurophysiology*, Vol. 94(5), pp.3126–3133.

Perrey, S., Quaresima, V. and Ferrari, M., 2024. Muscle oximetry in sports science: An updated systematic review. *Sports Medicine*, Vol. 54(4), pp.975–996.

Pertici, I., Bongini, L., Caremani, M., Reconditi, M., Linari, M., Piazzesi, G., Lombardi, V. and Bianco, P., 2023. Matching mechanics and energetics of muscle contraction suggests unconventional chemomechanical coupling during the actin–myosin interaction. *International Journal of Molecular Sciences*, Vol. 24(15), p.12324.

Petrofsky, J.S. and Phillips, C.A., 1980. The effect of elbow angle on the isometric strength and endurance of the elbow flexors in men and women. *Journal of Human Ergology*, Vol. 9(2), pp.125–131.

Plotkin, D.L., Roberts, M.D., Haun, C.T. and Schoenfeld, B.J., 2021. Muscle fiber type transitions with exercise training: shifting perspectives. *Sports*, Vol. 9(9), p.127.

Podgórski, M., Olewnik, Ł., Rusinek, M., Cichosz, M., Polguj, M. and Topol, M., 2019. 'Superior biceps aponeurosis'—morphological characteristics of the origin of the short head of the biceps brachii muscle. *Annals of Anatomy-Anatomischer Anzeiger*, Vol. 223, pp.85–89.

Popesco, T., Bet da Rosa Orssatto, L., Hug, F., Blazevich, A.J., Trajano, G.S. and Place, N., 2024. Motoneuron persistent inward current contribution to increased torque responses to wide-pulse high-frequency neuromuscular electrical stimulation. *European Journal of Applied Physiology*, Vol. 124(11), pp.3377–3386.

Qi, L., Wakeling, J.M. and Ferguson-Pell, M., 2011. Spectral properties of electromyographic and mechanomyographic signals during dynamic concentric and

eccentric contractions of the human biceps brachii muscle. *Journal of Electromyography and Kinesiology*, Vol. 21(6), pp.1056–1063.

Rafolt, D. and Gallasch, E., 2002. Surface myomechanical responses recorded on a scanner galvanometer. *Medical and Biological Engineering and Computing*, Vol. 40(5), pp.594–599.

Rampichini, S., Cè, E., Limonta, E. and Esposito, F., 2014. Effects of fatigue on the electromechanical delay components in gastrocnemius medialis muscle. *European Journal of Applied Physiology*, Vol. 114(3), pp.639–651.

Roman-Liu, D. and Konarska, M., 2009. Characteristics of power spectrum density function of EMG during muscle contraction below 30%MVC. *Journal of Electromyography and Kinesiology*, Vol. 19(5), pp.864–874.

Sakr, M., Jiang, X. and Menon, C., 2019. Estimation of user-applied isometric force/torque using upper extremity force myography. *Frontiers in Robotics and AI*, 6, p.120.

Salminen, J., van Gils, M., Paloheimo, M. and Yli-Hankala, A., 2016. Comparison of train-of-four ratios measured with Datex-Ohmeda's M-NMT MechanoSensorTM and M-NMT ElectroSensorTM. *Journal of Clinical Monitoring and Computing*, Vol. 30(3), pp.295–300.

Santos, E., Vara, M.D.F.F., Ranciaro, M., Neto, G.N.N. and Nohama, P., 2021. Influence of sensor mass and adipose tissue on the mechanomyography signal of elbow flexor muscles. *Journal of Biomechanics*, Vol. 122, p.110456.

Sawyer, S.F., 2009. Analysis of variance: The fundamental concepts. *Journal of Manual and Manipulative Therapy*, Vol. 17(2), pp.27E–38E.

Scarapicchia, V., Brown, C., Mayo, C. and Gawryluk, J.R., 2017. Functional magnetic resonance imaging and functional near-infrared spectroscopy: insights from combined recording studies. *Frontiers in Human Neuroscience*, Vol. 11, p.419.

Seidl, L., Tosovic, D. and Brown, J.M., 2017. Test-retest reliability and reproducibility of laser- vs contact-displacement sensors in mechanomyography: Implications for musculoskeletal research. *Journal of Applied Biomechanics*, Vol. 33(2), pp.130–136.

Serbest, K., Ozkan, M.T. and Cilli, M., 2023. Estimation of joint torques using an artificial neural network model based on kinematic and anthropometric data. *Neural Computing and Applications*, Vol. 35(17), pp.12513–12529.

Shah, D., Gopan, K.G. and Sinha, N., 2022. An investigation of the multi-dimensional (1D vs. 2D vs. 3D) analyses of EEG signals using traditional methods and deep learning-based methods. *Frontiers in Signal Processing*, Vol. 2, p.936790.

Shcherbynina, M.B., Gladun, V.M. and Sarana, V.M., 2020. Acoustic myography as a noninvasive technique for assessing muscle function: Historical aspects and possibilities for application in clinical practice. *Neurophysiology*, Vol. 52(4), pp.298–307.

Shi, F., Rymer, W.Z. and Son, J., 2021. Mechanomyogram amplitude vs. isometric ankle plantarflexion torque of human medial gastrocnemius muscle at different ankle joint angles. *Journal of Electromyography and Kinesiology*,Vol. 61, p.102609.

Shi, Y., Dong, W., Lin, W., He, L., Wang, X., Li, P. and Gao, Y., 2022. Human joint torque estimation based on mechanomyography for upper extremity exosuit. *Electronics*, Vol. 11(9), p.1335.

Shideler, B.L., Bulea, T.C., Chen, J., Stanley, C.J., Gravunder, A.J. and Damiano, D.L., 2020. Toward a hybrid exoskeleton for crouch gait in children with cerebral palsy: Neuromuscular electrical stimulation for improved knee extension. *Journal of NeuroEngineering and Rehabilitation*, Vol. 17(1), p.121.

Shima, N., McNeil, C.J. and Rice, C.L., 2007. Mechanomyographic and electromyographic responses to stimulated and voluntary contractions in the dorsiflexors of young and old men. *Muscle and Nerve*, Vol. 35(3), pp.371–378.

Shima, N., Rice, C.L., Ota, Y. and Yabe, K., 2006. The effect of postactivation potentiation on the mechanomyogram. *European Journal of Applied Physiology*, Vol. 96(1), pp.17–23.

Šimunič, B., Koren, K., Rittweger, J., Lazzer, S., Reggiani, C., Rejc, E., Pišot, R., Narici, M. and Degens, H., 2019. Tensiomyography detects early hallmarks of bed-rest-induced atrophy before changes in muscle architecture. *Journal of Applied Physiology*, Vol. 126(4), pp.815–822.

Sirago, G., Pellegrino, M.A., Bottinelli, R., Franchi, M.V. and Narici, M.V., 2023. Loss of neuromuscular junction integrity and muscle atrophy in skeletal muscle disuse. *Ageing Research Reviews*, Vol. 83, p.101810.

Snow, E.L. and Lanik, W.E., 2024. Structural and functional analysis of bilateral five-headed biceps brachii muscles with clinical insights. *Translational Research in Anatomy*, Vol. 35, p.100289.

Son, J., Lee, D. and Kim, Y., 2014. Effects of involuntary eccentric contraction training by neuromuscular electrical stimulation on the enhancement of muscle strength. *Clinical Biomechanics*, Vol. 29(7), pp.767–772.

Son, J., Shi, F. and Rymer, W.Z., 2024. BiLSTM-based joint torque prediction from mechanomyogram during isometric contractions: A proof of concept study. *IEEE Transactions on Neural Systems and Rehabilitation Engineering*, Vol. 32, pp.1926–1933.

Talib, I., Sundaraj, K. and Lam, C.K., 2018. Choice of mechanomyography sensors for diverse types of muscle activities. *Journal of Telecommunication, Electronic and Computer Engineering (JTEC)*, Vol. 10(1–13), pp.79–82.

Talib, I., Sundaraj, K. and Lam, C.K., 2019. Association of anthropometric parameters with amplitude and crosstalk of mechanomyographic signals during forearm flexion, pronation and supination torque tasks. *Scientific Reports*, Vol. 9(1), p.16166.

Talib, I., Sundaraj, K. and Lam, C.K., 2020. Analysis of the crosstalk in mechanomyographic signals along the longitudinal, lateral and transverse axes of elbow flexor muscles during sustained isometric forearm flexion, supination and pronation exercises. *Journal of Musculoskeletal and Neuronal Interactions*, Vol. 20(2), p.194.

Talib, I., Sundaraj, K., Hussain, J., Lam, C.K. and Ahmad, Z., 2022. Analysis of anthropometrics and mechanomyography signals as forearm flexion, pronation and supination torque predictors. *Scientific Reports*, Vol. 12(1), p.16086.

Talib, I., Sundaraj, K., Lam, C.K. and Sundaraj, S., 2018. A systematic review of muscle activity assessment of the biceps brachii muscle using mechanomyography. *Journal of Musculoskeletal and Neuronal Interactions*, Vol. 18(4), p.446.

Thepaut-Mathieu, C., Van Hoecke, J. and Maton, B., 1988. Myoelectrical and mechanical changes linked to length specificity during isometric training. *Journal of Applied Physiology*, Vol. 64(4), pp.1500–1505.

Toca-Herrera, J.L., Gallach, J.E., Gómis, M. and González, L.M., 2008. Cross-education after one session of unilateral surface electrical stimulation of the rectus femoris. *The Journal of Strength and Conditioning Research*, Vol. 22(2), pp.614–618.

Too, J. and Mirjalili, S., 2021. General learning equilibrium optimizer: A new feature selection method for biological data classification. *Applied Artificial Intelligence*, Vol. 35(3), pp.247–263.

Trager, G., Michaud, G., Deschamps, S. and Hemmerling, T.M., 2006. Comparison of phonomyography, kinemyography and mechanomyography for neuromuscular monitoring. *Canadian Journal of Anesthesia*, Vol. 53(2), pp.130–135.

Travnik, L., Djordjevič, S., Rozman, S., Hribernik, M. and Dahmane, R., 2013. Retracted: Muscles within muscles: A tensiomyographic and histochemical analysis of the normal human vastus medialis longus and vastus medialis obliquus muscles. *Journal of Anatomy*, Vol. 222(6), pp.580–587.

Trovato, F.M., Imbesi, R., Conway, N. and Castrogiovanni, P., 2016. Morphological and functional aspects of human skeletal muscle. *Journal of Functional Morphology and Kinesiology*, Vol. 1(3), pp.289–302.

Truong, M.T.N., Ali, A.E.A., Owaki, D. and Hayashibe, M., 2023. EMG-based estimation of lower limb joint angles and moments using long short-term memory network. *Sensors*, Vol. 23(6), p.3331.

Uchiyama, T. and Sakai, H., 2013. System identification of evoked mechanomyogram from abductor pollicis brevis muscle in isometric contraction. *Medical and Biological Engineering and Computing*, Vol. 51(12), pp.1349–1355.

Uchiyama, T. and Shinohara, K., 2013. Comparison of displacement and acceleration transducers for the characterization of mechanics of muscle and subcutaneous tissues by system identification of a mechanomyogram. *Medical and Biological Engineering and Computing*, Vol. 51(1–2), pp.165–173.

Uchiyama, T. and Tomoshige, T., 2017. System identification of velocity mechanomyogram measured with a capacitor microphone for muscle stiffness estimation. *Journal of Electromyography and Kinesiology*, Vol. 33, pp.57–63.

Uchiyama, T., Saito, K. and Shinjo, K., 2015. Muscle stiffness estimation using a system identification technique applied to evoked mechanomyogram during cycling exercise. *Journal of Electromyography and Kinesiology*, Vol. 25(6), pp.847–852.

Udahemuka, G., Djouani, K. and Kurien, A.M., 2024. Multimodal emotion recognition using visual, vocal and physiological signals: A review. *Applied Sciences*, Vol. 14(17), p.8071.

Ukawa, T.F. and Chiyama, T.U., 2016. System identification of evoked mechanomyogram to clarify lower limb muscle stiffness in treadmill walking. *Transactions of Japanese Society for Medical and Biological Engineering*, Vol. 52, pp.160–161.

Uwamahoro, R., Sundaraj, K. and Feroz, F.S., 2023. Effect of forearm postures and elbow joint angles on elbow flexion torque and mechanomyography in neuromuscular electrical stimulation of the biceps brachii. *Sensors*, Vol. 23(19), p.8165.

Uwamahoro, R., Sundaraj, K. and Subramaniam, I.D., 2019, November. Analysis of upper limb rehabilitation using muscle mechanics: Current and future perspectives using mechanomyography signals. *In 12th Biomedical Engineering International Conference (BMEiCON), of IEEE, 2019*, pp.1–5.

Uwamahoro, R., Sundaraj, K. and Subramaniam, I.D., 2021. Assessment of muscle activity using electrical stimulation and mechanomyography: A systematic review. *BioMedical Engineering Online*, 20(1), p.1.

Vaz, M.A., Herzog, W., Zhang, Y.T., Leonard, T.R. and Nguyen, H., 1997. The effect of muscle length on electrically elicited muscle vibrations in the in-situ cat soleus muscle. *Journal of Electromyography and Kinesiology*, Vol. 7(2), pp.113–121.

Vommi, A.M. and Battula, T.K., 2023. A binary Bi-phase mutation-based hybrid equilibrium optimizer for feature selection in medical datasets classification. *Computers and Electrical Engineering*, Vol. 105, p.108553.

von Werder, S.C.F.A. and Disselhorst-Klug, C., 2016. The role of biceps brachii and brachioradialis for the control of elbow flexion and extension movements. *Journal of Electromyography and Kinesiology*, Vol. 28, pp.67–75.

Wang, H., Bardizbanian, B., Zhu, Z., Wang, H., Dai, C. and Clancy, E.A., 2024. Evaluation of generic EMG-Torque models across two Upper-Limb joints. *Journal of Electromyography and Kinesiology*, Vol. 75, p.102864.

Wang, X., Tao, X. and So, R.C., 2017. A bio-mechanical model for elbow isokinetic and isotonic flexions. *Scientific Reports*, Vol. 7(1), p.8919.

Watanabe, S., Nojima, I., Agarie, Y., Watanabe, T., Fukuhara, S., Fujinaga, T. and Oka, H., 2016. Electrically induced mechanomyograms reflect inspiratory muscle strength in young or elderly subjects. *Respiratory Investigation*, Vol. 54(6), pp.436-444.

Wessell, A.N., Khalil, J., Zavatsky, J. and Ghacham, W., 2016. Verification of nerve decompression using mechanomyography. *The Spine Journal*, Vol. 16(6), pp.679–686.

Willingham, T.B., Melbourn, J., Moldavskiy, M., McCully, K.K. and Backus, D., 2018. Case report: Effect of antigravity treadmill training on muscle oxidative capacity, muscle endurance, and walking function in a person with multiple sclerosis. *International Journal of MS Care*, Vol. 20(4), pp.186–190.

Wilson, H.V., Jones, A., Johnson, M.I. and Francis, P., 2019. The effect of inter-electrode distance on radial muscle displacement and contraction time of the biceps femoris, gastrocnemius medialis and biceps brachii, using tensiomyography in healthy participants. *Physiological Measurement*, Vol. 40(7), p.075007.

Xie, J., Zhang, Y., Yang, K. and Xia, C., 2020, May. Estimation of triceps muscle strength based on mechanomyography. In *Journal of Physics: Conference Series, IOP Publishing*, p.012055, Vol.1544(1).

Yamamoto, M., Kojyo, U., Yanagisawa, N., Mitomo, K., Takayama, T., Sakiyama, K. and Abe, S., 2018. Morphology and relationships of the biceps brachii and brachialis with the musculocutaneous nerve. *Surgical and Radiologic Anatomy*, Vol. 40(3), pp.303–311.

Yang, J. and Yin, Y., 2020. Dependent-Gaussian-process-based learning of joint torques using wearable smart shoes for exoskeleton. *Sensors* (Switzerland), Vol. 20(13), pp.1–17.

Yang, L. and Shami, A., 2020. On hyperparameter optimization of machine learning algorithms: Theory and practice. *Neurocomputing*, Vol. 415, pp.295–316.

Youn, W. and Kim, J., 2011. Feasibility of using an artificial neural network model to estimate the elbow flexion force from mechanomyography. Journal of Neuroscience Methods, Vol. 194(2), pp.386–393.

Yu, L. and Liu, H., 2004. Efficient feature selection via analysis of relevance and redundancy. *Journal of Machine Learning Research*, Vol. 5, pp.1205–1224.

Yung, M., Erik, S. and Wells, R.P., 2012. Variation of force amplitude and its effects on local fatigue. *European Journal of Applied Physiology*, Vol. 112(11), pp.3865–3879.

Žagar, T. and Križaj, D., 2005. Validation of an accelerometer for determination of muscle belly radial displacement. *Medical and Biological Engineering and Computing*, Vol. 43(1), pp.78–84.

Zimmermann, H.B., Macintosh, B.R. and Pupo, J.D., 2025. The relationship between length and active force for submaximal skeletal muscle contractions: A review. *Sports Medicine*, Vol. 55(1), pp.37–47.

APPENDICES

APPENDIX A

Evaluation of the elbow flexor muscles' function using Electrical Stimulation and Mechanomyographic signals

Principal Investigator: Prof. Ir. Dr. Kenneth Sundaraj
Sub-investigator: Mr. Uwamahoro Raphael

SUBJECT'S CONSENT FORM

- I confirm that I have been given oral and written information for this study and have read and understood the purpose of conducting this research.
- I have had sufficient time to consider participation in the study and have had the opportunity to ask questions and all have been answered satisfactorily.
- I understand that my participation is voluntary, and I can at any time withdraw from the study without giving a reason and this will in any way affect me.
- I understand that study staff, qualified monitors and auditors, the sponsor, or its affiliates, and governmental or regulatory authorities, may have direct access to the recording of this experiment to make sure that the study is conducted correctly. I understand that the recordings of this study will be only used for the research purpose and will be handled by investigators.
- I agree to participate in this study.

I hereby provide my consent to be the subject of this research.

Subject number:

Signature: ID number:

Name:

Investigator conducting informed consent:

Signature: ID number:

Name:

Impartial witness:

Signature: ID number:

APPENDIX B: SUBJECT'S INFORMATION SHEET

Evaluation of the elbow flexor muscle function using Electrical Stimulation and Mechanomyographic signals

Principal Investigator: Prof. Ir. Dr. Kenneth Sundaraj
Co-investigator: Uwamahoro Raphael

Subject Bio-data Form

Name	
Age	
Gender	
ID Number	
Nationality	
Current Address	
Occupation	
Email Address	
Contact Number	

APPENDIX C: DATA COLLECTION FORM

Evaluation of the elbow flexor muscle function using Electrical Stimulation and Mechanomyographic signals

Principal Investigator: Prof. Ir. Dr. Kenneth Sundaraj
Co-investigator: Uwamahoro Raphael

DATA COLLECTION FORM

Session 1: General Subject's covid-19 information checkup from MySejahetra.
Duration: 1 minutes
Session 2: Briefing of the experiment and signing informed consent.
Duration: 10 minutes
Session 3: **Anthropometric details**
Duration: 15 minutes

Gender		Weight (kg)	
Age (years)		Height (m)	
Landmark	Experiment recording	Measurement (Cm)	Average
Length of the lower arm (from **olecranon process to styloid process of the ulna**)	Trial 1		
	Trial 2		
	Trial 3		
Length of upper arm (**deltoid tubercle to olecranon process**)	Trial 1		
	Trial 2		
	Trial 3		
Diameter of the upper arm at full elbow extension (mid-point obtained at elbow flexed to 90 degree)	Trial 1		
	Trial 2		
	Trial 3		
Skinfold Thickness (At the level of the mid-point between the acromial and the radiale, and the mid-line of the anterior (front) surface of the arm.)	Trial 1		
	Trial 2		
	Trial 3		

Session 4: Determination and recording of MVIC

Body position: the subject sits in a chair with the arm parallel to their torso, chest and lower leg immobilized with straps, the subject's forearm positioned to the long axis of the dynamometer and making 90 degree of elbow flexion.
Duration :15 minutes.

Hand position	Trial	Unit (Kg)	Max	10%MVC	15%MVC
Neutral	1st trial				
	2nd trial				
	3rd trial				
Pronation	1st trial				
	2nd trial				
	3rd trial				
Supination	1st trial				
	2nd trial				
	3rd trial				

Guided session (recording of the validation data): Use the random angle and hand posture combination to perform 0<=10<= 15% MVC as being shown on the computer screen.

Angle (°)	Forearm posture		
	Neutral	Pronation	Supination
10			
30			
60			
90			

Duration: 5 minutes rest after MVC determination + 30 seconds for recording.

Day 2: Recording of the MMG and elbow flexion torque

Warm up: the subject holding no weight of 2 kg dumbbell flexing the elbow and randomly changing into supination, pronation and neutral.
Duration = 5 minutes

Body position: The subject's hand is maintained parallel to the body torso maintaining a shoulder abduction of about 3^0 using a goniometer. The elbow flexion is ensured by a custom-made adjustable arm rest with mechanical fixtures.
Choice of posture and elbow flexion: A pre-programmed function is developed to randomize angles and postures as follows:

Angle (°)	Forearm posture		
	Neutral	Pronation	Supination
10			
30			
60			
90			

Familiarization with NMES:

The subject's conform maximum electrical stimulation intensity to flex his arm at 10 to 15% MVC while the elbow fixed at 90^0 same point of MVC determined while the hand fixed into supination, pronation and neutral position.

Time = 5 minutes for the warmup session, 5 minutes rest following NMES delivery at each posture + 30 s minutes of NMES stimulation for each posture delivery.

Duration = 5 minutes +30 seconds ×3 + 5 minutes (3-1) = 16 minutes 30 seconds.

APPENDIX D: MEDICAL DEVICE APPROVAL FOR NMES EMS 7500

No. Siri:
Serial No.: 030129

ASAL
ORIGINAL

PIHAK BERKUASA
PERANTI PERUBATAN

MEDICAL DEVICE AUTHORITY

PIHAK BERKUASA PERANTI PERUBATAN
MEDICAL DEVICE AUTHORITY
AKTA PERANTI PERUBATAN 2012 (AKTA 737)
MEDICAL DEVICE ACT 2012 (ACT 737)
SIJIL PENDAFTARAN PERANTI PERUBATAN
MEDICAL DEVICE REGISTRATION CERTIFICATE
Seksyen 5(1) Akta 737
Section 5(1) of Act 737

No. Pendaftaran: **GA4919519-31333**
Registration No.:

Tarikh Sah Laku Pendaftaran: **22/07/2019 -**
Registration Validity Date: **21/07/2024**

Sijil ini adalah dengan ini diberi kepada: **CHYROMED WORKS SDN BHD**
This certificate is hereby issued to:

yang beralamat di:
which is located at:

LEVEL 11, MENARA KEN TTDI, 37, JALAN BURHANUDDIN HELMI, TAMAN TUN DR ISMAIL, 60000 KUALA LUMPUR

bagi mengesahkan peranti perubatan seperti yang dinyatakan dalam Lampiran 1 adalah berdaftar di bawah Seksyen 5(1) Akta 737.
to confirm that the medical device as detailed out in Attachment 1 is registered under Section 5(1) of Act 737.

Pendaftaran ini diberikan tertakluk kepada peruntukan-peruntukan di bawah Akta 737 dan peraturan-peraturan yang dibuat dibawahnya serta syarat-syarat seperti di Lampiran 2.
This registration is granted subject to the provisions under Act 737 and its subsidiary legislations and the conditions as in Attachment 2.

AHMAD SHARIFF BIN HAMBALI
KETUA EKSEKUTIF
CHIEF EXECUTIVE
PIHAK BERKUASA PERANTI PERUBATAN
MEDICAL DEVICE AUTHORITY

APPENDIX E: MEDICAL DEVICE APPROVAL FOR NMES ELECTRODES

NO	NAME AS PER DEVICE LABEL	IDENTIFIER	BRIEF DESCRIPTION OF ITEM
1	TENS Electrode LW1	LW1	48 x 47 mm, Non-woven fabric material, Button connector
2	TENS Electrode LP1	LP1	48 x 47 mm, Foam material, Button connector
3	TENS Electrode LW2	LW2	42 x 42 mm, Non-woven fabric material, Button connector
4	TENS Electrode LP2	LP2	42 x 42 mm, Foam material, Button connector
5	TENS Electrode LW3	LW3	12 x 66 mm, Non-woven fabric material, Button connector
6	TENS Electrode LP3	LP3	23 x 34 mm, PET material, PET-Tab connector
7	TENS Electrode LW4	LW4	42 x 24 mm, Non-woven fabric material, Button connector
8	TENS Electrode LP4	LP4	42 x 24 mm, Foam material, Button connector
9	TENS Electrode LW5	LW5	40 x 40 mm, Non-woven fabric material, Button connector
10	TENS Electrode LW6	LW6	40 x 40 mm, Non-woven fabric material, Wire connector
11	TENS Electrode LW7	LW7	50 x 50 mm, Non-woven fabric material, Button connector
12	TENS Electrode LW8	LW8	50 x 50 mm, Non-woven fabric material, Wire connector
13	TENS Electrode LW9	LW9	40 x 80 mm, Non-woven fabric material, Button connector

APPENDIX F: ETHICAL APPROVAL OF THE RESEARCH

JAWATANKUASA ETIKA & PENYELIDIKAN PERUBATAN
(*MEDICAL RESEARCH & ETHICS COMMITTEE*)
KEMENTERIAN KESIHATAN MALAYSIA
MINISTRY OF HEALTH MALAYSIA
Kompleks Institut Kesihatan Negara (NIH)
No.1, Jalan Setia Murni U13/52,
Seksyen U13 Bandar Setia Alam,
40170 Shah Alam, Selangor.
Tel.: +(6)03-33628888/ 33628205

Ref. : KKM/NIHSEC/P20-2454(8)
Date : **7-December-2020**

PROF. EURING. IR. DR. KENNETH SUNDARAJ
UNIVERSITI TEKNIKAL MALAYSIA MELAKA (UTEM)

Dear Dato'/ Dr/ Sir/ Madam,

LETTER OF ETHICAL APPROVAL:

NMRR-20-2613-56796 (IIR)
ESTIMATION OF ELBOW JOINT FLEXION TORQUE FROM MECHANOMYOGRAPHY SIGNALS OF THE BICEPS BRACHIUM UNDER ELECTRICAL STIMULATION USING MACHINE LEARNING

This letter is made in reference to the matter above.

2. The Medical Research and Ethics Committee (MREC), Ministry of Health Malaysia (MOH) has provided ethical approval for this study. Please take note that all records and data are to be kept strictly **CONFIDENTIAL** and can only be used for the purpose of this study. All precautions are be taken to maintain data confidentiality. Permission from the District Health Officer / Hospital Administrator/ Hospital Director and all relevant heads of departments /units where the study will be carried out must be obtained prior to the study. You are required to follow and comply with their decision and all other relevant regulations including the Access to the Biological and Benefit Sharing Act 2017.

3. The investigators and sites involved in this study are:

Universiti Teknikal Malaysia Melaka (UTEM)
Prof. Euring. Ir. Dr. Kenneth Sundaraj (Principal / Coordinating Investigator)
Dr. Sebastian Sundaraj
Raphael Uwamahoro

4. The following study documents have been received and reviewed with reference to the above study:

Documents received and reviewed with reference to the above study:

1. Cover letter to MREC (Version 1, dated 22-11-2020)
2. Declaration of Conflict of Interest (COI) (Version 1, dated 22-11-2020)
3. Protocol (Version 1, dated 20-11-2020)
4. English: Patient Information Sheet/ Informed Consent Form (Version 1, dated 20-11-2020)
5. Malay: Patient Information Sheet/ Informed Consent Form (Version 1, dated 20-11-2020)
6. Data Collection Form (Version 1, dated 20-11-2020)
7. IA-HOD-IA, CV and GCP Certification of:
   - Prof. Euring. Ir. Dr. Kenneth Sundaraj
8. IA-HOD-IA and CV of:
   - Raphael Uwamahoro
9. CV and GCP Certification of:
   - Dr. Sebastian Sundaraj

.../2-

JAWATANKUASA ETIKA & PENYELIDIKAN PERUBATAN
(*Medical Research & Ethics Committee*)
KEMENTERIAN KESIHATAN MALAYSIA
d/a Kompleks Institut Kesihatan Negara
Blok A, No 1, Jalan Setia Murni U13/52,
Seksyen U13, Bandar Setia Alam,
40170 Shah Alam, Selangor.
Tel: 03-3362 8888/8205

Ruj.Kami: KKM/NIHSEC/ P20-2454
Tarikh: 15-November-2022

PROF. EURING. IR. DR. KENNETH SUNDARAJ
UNIVERSITI TEKNIKAL MALAYSIA MELAKA (UTEM)

Dato'/ Tuan/ Puan,

Annual Ethical Renewal for 2022

NMRR-20-2613-56796 (IIR)
Protocol No :
Estimation of Elbow Joint Flexion Torque from Mechanomyography Signals of the Biceps Brachium Under Electrical Stimulation using Machine Learning

With reference to the 'Continuing Review Form' submitted 10-November-2022, we are pleased to inform that the conduct of the above study has been granted approval (via Expedited Review by Chairperson) for a year by the Medical Research & Ethics Comittee, Ministry of Health Malaysia. Please note that the approval is valid until 6-December-2023. To renew the approval, a completed 'Continuing Review Form' has to be submitted to MREC **within 2 months** before the expiry of the approval.

The Medical Research & Ethics Committee, Ministry of Health Malaysia operates in accordance with The International Council for Harmonization of Technical Requirement for Pharmaceutical for Human Use (ICH) dan Malaysia Guidelines for Good Clinical Practice.

Effective date: 7-December-2022 Until 6-December-2023

Comments (if any): NIL

"WAWASAN KEMAKMURAN BERSAMA 2030"

"BERKHIDMAT UNTUK NEGARA"

Yours sincerely,

(DR NURAIN BINTI MOHD NOOR)
Chairman
Medical Research & Ethics Committee
Ministry of Health Malaysia